Ministry of Education and Science of the Russian Federation
Saint Petersburg National Research University of Information
Technologies, Mechanics, and Optics

NANOSYSTEMS:
PHYSICS, CHEMISTRY, MATHEMATICS

2020, volume 11(2)

Наносистемы: физика, химия, математика

2020, том 11, № 2

NANOSYSTEMS:

PHYSICS, CHEMISTRY, MATHEMATICS

ADVISORY BOARD MEMBERS

Chairman: V.N. Vasiliev *(St. Petersburg, Russia)*,
V.M. Buznik *(Moscow, Russia)*; V.M. Ievlev *(Voronezh, Russia)*, P.S. Kop'ev*(St. Petersburg, Russia)*, N.F. Morozov *(St. Petersburg, Russia)*, V.N. Parmon *(Novosibirsk, Russia)*, A.I. Rusanov *(St. Petersburg, Russia)*,

EDITORIAL BOARD

Editor-in-Chief: I.Yu. Popov *(St. Petersburg, Russia)*

Section Co-Editors:
Physics – V.M. Uzdin *(St. Petersburg, Russia)*,
Chemistry, material science –V.V. Gusarov *(St. Petersburg, Russia)*,
Mathematics – I.Yu. Popov *(St. Petersburg, Russia)*.

Editorial Board Members:
V.M. Adamyan *(Odessa, Ukraine)*; O.V. Al'myasheva *(St. Petersburg, Russia)*; A.P. Alodjants *(Vladimir, Russia)*; S. Bechta *(Stockholm, Sweden)*; J. Behrndt *(Graz, Austria)*; M.B. Belonenko *(Volgograd, Russia)*; A. Chatterjee (*Hyderabad, India)*; S.A. Chivilikhin *(St. Petersburg, Russia)*; A.V. Chizhov *(Dubna, Russia)*; A.N. Enyashin *(Ekaterinburg, Russia)*, P.P. Fedorov *(Moscow, Russia)*; E.A. Gudilin *(Moscow, Russia)*; V.K. Ivanov *(Moscow, Russia)*, H. Jónsson *(Reykjavik, Iceland)*; A.A. Kiselev *(Durham, USA)*; Yu.S. Kivshar *(Canberra, Australia)*; S.A. Kozlov *(St. Petersburg, Russia)*; P.A. Kurasov *(Stockholm, Sweden)*; A.V. Lukashin *(Moscow, Russia)*; I.V. Melikhov *(Moscow, Russia)*; G.P. Miroshnichenko *(St. Petersburg, Russia)*; I.Ya. Mittova *(Voronezh, Russia)*; Nguyen Anh Tien *(Ho Chi Minh, Vietnam)*; V.V. Pankov *(Minsk, Belarus)*; K. Pankrashkin *(Orsay, France)*; A.V. Ragulya *(Kiev, Ukraine)*; V. Rajendran *(Tamil Nadu, India)*; A.A. Rempel *(Ekaterinburg, Russia)*; V.Ya. Rudyak *(Novosibirsk, Russia)*; D Shoikhet *(Karmiel, Israel)*; P Stovicek *(Prague, Czech Republic)*; V.M. Talanov *(Novocherkassk, Russia)*; A.Ya. Vul' *(St. Petersburg, Russia)*; A.V. Yakimansky (*St. Petersburg, Russia*), V.A. Zagrebnov *(Marseille, France)*.

Editors:
I.V. Blinova; A.I. Popov; A.I. Trifanov; E.S. Trifanova *(St. Petersburg, Russia)*,
R. Simoneaux *(Philadelphia, Pennsylvania, USA)*.

Address: University ITMO, Kronverkskiy pr., 49, St. Petersburg 197101, Russia.
Phone: +7(812)312-61-31, **Journal site:** http://nanojournal.ifmo.ru/,
E-mail: popov1955@gmail.com

AIM AND SCOPE

The scope of the journal includes all areas of nano-sciences. Papers devoted to basic problems of physics, chemistry, material science and mathematics inspired by nanosystems investigations are welcomed. Both theoretical and experimental works concerning the properties and behavior of nanosystems, problems of its creation and application, mathematical methods of nanosystem studies are considered.

The journal publishes scientific reviews (up to 30 journal pages), research papers (up to 15 pages) and letters (up to 5 pages). All manuscripts are peer-reviewed. Authors are informed about the referee opinion and the Editorial decision.

CONTENT

MATHEMATICS

PHYSICS

CHEMISTRY AND MATERIAL SCIENCE

NANOSYSTEMS: PHYSICS, CHEMISTRY, MATHEMATICS, 2020, 11 (2), P. 131–137

Reduced second Zagreb index of product graphs

N. De

Department of Basic Sciences and Humanities (Mathematics),
Calcutta Institute of Engineering and Management, Kolkata, India
de.nilanjan@rediffmail.com

DOI 10.17586/2220-8054-2020-11-2-131-137

The reduced second Zagreb index of a graph G is defined as $RM_2(G) = \sum\limits_{uv\in E(G)} (d_G(u) - 1)(d_G(v) - 1)$, where $d_G(v)$ denotes the degree of the vertex v of graph G. Recently Furtula et al. (Furtula B., Gutman I., Ediz S. *Discrete Appl. Math.*, 2014) characterized the maximum trees with respect to reduced second Zagreb index. The aim of this paper is to compute reduced second Zagreb index of the Cartesian product of k (≥ 2) number of graphs and hence as a consequence the reduced second Zagreb index of some special graphs applicable in various real world problems are computed. Topological properties of different nanomaterials like nanotube, nanotorus etc. are studied here graphically in terms of the aforesaid aforementioned index.

Keywords: Reduced second Zagreb index, cartesian product of graphs, nanotube, nanotorus, Hamming graphs, Ladder graphs, Rook's graph.

Received: 15 January 2020

Revised: 5 March 2020

1. Introduction

Let G be a simple connected graph with vertex set $V(G)$ and edge set $E(G)$. For a graph G, let $d_G(v)$ denote the degree of a vertex v in G, that is, the number of vertices adjacent with v. Throughout this article, we consider chemical graph [1, 2]. By chemical graph we mean a simple connected graph where vertices and edges are supposed to be atoms and chemical bonds between them respectively.

Topological indices, also called molecular structure descriptors are used in theoretical chemistry for design of chemical compounds with given physico-chemical properties and also to model chemical biological and pharmacological properties of the molecules. A topological index is a real number and it does not depend on the labelling of a graph and must be a structural invariant. The first topological index, Wiener index, was published in 1947 [3]. Due to the importance of topological indices in chemical research, lots of topological indices are developed in the chemical graph theory. Degree based topological indices are one of them that is applicable in quantitative structure property relationship and quantitative structure activity relationship [4, 5]. Among them Zagreb indices are most popular indices. First and second Zagreb indices are introduced by Gutman and Trinajestić [6], defined as follows:

$$M_1(G) = \sum_{u\in V(G)} d_G(u)^2,$$
$$M_2(G) = \sum_{uv\in E(G)} d_G(u)d_G(v).$$

These graph invariants were proposed to measure the branching of carbon-atom skeleton [7]. For detail discussion on these indices, see [8–14]. Furtula et al. [15] proposed the reduced second Zagreb index of a graph G to study the difference between M_1 and M_2, which is defined as follows:

$$RM_2(G) = \sum_{uv\in E(G)} (d_G(u) - 1)(d_G(v) - 1).$$

The graphs having maximum and minimum reduced second Zagreb index in the class of cyclic graphs with cut edges are studied in [16]. Mahanta et al. [17] obtained Reduced the reduced second Zagreb index of four new graph operations based on tensor product. Several useful composite graphs can be obtained by operations of different graphs. The Cartesian product is one of that the operations and which is considered in the present work.

The Cartesian product $G_1 \otimes G_2$ of graphs G_1 and G_2 has the vertex set $V(G) \times V(G_2)$ and $(a, x)(b, y)$ is an edge of $G_1 \otimes G_2$ if $a = b$ and $xy \in E(H)$ or $ab \in E(G)$ and $x = y$. Using the Cartesian product of two graphs, the structure of several nanomaterials can be designed such as C_4-nanotube, C_4-nanotorus, multi-walled nanotorus etc. Carbon nanotube has diverse applications in cancer treatment, cardiac autonomic regulation, tissue regeneration etc. As topological index can predict different physico-chemical properties, it is worthy to compute that for different structures of real world application. First and second Zagreb indices of the Cartesian product graph is presented in [18]. The PI index of the Cartesian product of bipartite graphs is computed in [19]. Klavzar et al. [20] computed the Szeged index of Cartesian product graph. In [21], the Wiener index of Cartesian product graphs are studied. The present author [22–24] studied F-index, F-coindex and reformulated first Zagreb index for Cartesian product graphs. The goal of this work is to obtain the reduced second Zagreb index of Cartesian product graphs. Using that results, RM_2 index of some chemical graphs is also derived.

2. Main results

Let G_i $(i = 1, 2, ..., k)$ be a connected graph with vertex set $V(G_i)$ and $E(G_i)$, so that, $|V(G_i)| = n_i$ and $|E(G_i)| = m_i$. In this section, we derive the reduced second Zagreb index of Cartesian product of k-number of connected graphs $G_1,\ G_2, ..., G_k$. To do this first we prove the result for two connected graphs G_1 and G_2.

Lemma 1. *[18] Let G_1 and G_2 be two connected graphs, then:*

$$\begin{aligned}(i)\ |V(G_1 \otimes G_2)| &= |V(G_1)| \times |V(G_2)|,\\ (ii)\ |E(G_1 \otimes G_2)| &= |E(G_1)||V(G_2)| + |E(G_2)||V(G_1)|,\\ (iii)\ d_{G_1 \otimes G_2}(a,b) &= d_{G_1}(a) + d_{G_2}(b).\end{aligned}$$

Lemma 2. *[18] Let $G_1,\ G_2, ..., G_k$ be k-number of graphs, then*

$$M_1(\bigotimes_{i=1}^{k} G_i) = n\sum_{i=1}^{k}\frac{M_1(G_i)}{n_i} + 4n\sum_{i\neq j,\ i,j=1}^{k}\frac{m_i m_j}{n_i n_j}.$$

Lemma 3. *[18] Let $G_1,\ G_2, ..., G_k$ be k-number of graphs, then*

$$\begin{aligned}(i)\ |V(\bigotimes_{i=1}^{k} G_i)| &= \prod_{i=1}^{k} n_i,\\ (ii)\ |E(\bigotimes_{i=1}^{k} G_i)| &= \prod_{i=1}^{k} n_i \sum_{i=1}^{k}\frac{m_i}{n_i}.\end{aligned}$$

Theorem 1. *Let G_1 and G_2 be two connected graphs with n_1 and n_2 number of vertices and, m_1 and m_2 number of edges respectively, then:*

$$RM_2(G_1 \otimes G_2) = n_1 RM_2(G_2) + n_2 RM_2(G_1) + 3m_1 M_1(G_2) + 3m_2 M_1(G_1) - 8m_1 m_2.$$

Proof. From definition of Cartesian product of two graphs, we have:

$$\begin{aligned}RM_2(G_1 \otimes G_2) &= \sum_{(a,b)(c,d)\in E(G_1\otimes G_2)} (d_{G_1}(a,b) - 1)(d_{G_2}(c,d) - 1)\\ &= \sum_{u\in V(G_1)}\sum_{bd\in E(G_2)} (d_{G_1}(u) + d_{G_2}(b) - 1)(d_{G_1}(u) + d_{G_2}(d) - 1)\\ &\quad + \sum_{v\in V(G_2)}\sum_{ac\in E(G_1)} (d_{G_1}(a) + d_{G_2}(v) - 1)(d_{G_1}(c) + d_{G_2}(v) - 1)\\ &= C_1 + C_2,\ (Say).\end{aligned}$$

Where,

$$\begin{aligned}C_1 &= \sum_{u\in V(G_1)}\sum_{bd\in E(G_2)} (d_{G_1}(u) + d_{G_2}(b) - 1)(d_{G_1}(u) + d_{G_2}(d) - 1)\\ &= \sum_{u\in V(G_1)}\sum_{bd\in E(G_2)} (d_{G_2}(b) - 1)(d_{G_2}(d) - 1) + \sum_{bd\in E(G_2)}\sum_{u\in V(G_1)} d_{G_1}(u)^2\\ &\quad + \sum_{bd\in E(G_2)}\sum_{u\in V(G_1)} d_{G_1}(u)(d_{G_2}(b) + d_{G_2}(d) - 2)\\ &= n_1 RM_2(G_2) + m_2 M_1(G_1) + 2m_1 M_1(G_2) - 4m_1 m_2.\end{aligned}$$

Similarly,

$$\begin{aligned}
C_2 &= \sum_{v\in V(G_2)}\sum_{ac\in E(G_1)}(d_{G_1}(a)+d_{G_2}(v)-1)(d_{G_1}(c)+d_{G_2}(v)-1)\\
&= \sum_{v\in V(G_2)}\sum_{ac\in E(G_1)}(d_{G_1}(a)-1)(d_{G_1}(c)-1)+\sum_{ac\in E(G_1)}\sum_{v\in V(G_2)}d_{G_1}(v)^2\\
&\quad+\sum_{ac\in E(G_1)}(d_{G_1}(a)+d_{G_1}(c)-2)\sum_{v\in V(G_2)}d_{G_1}(v)\\
&= n_2RM_2(G_1)+m_1M_1(G_2)+2m_2M_1(G_1)-4m_1m_2.
\end{aligned}$$

Therefore, combining the contributions of C_1 and C_2 we get the desired results. □

In the following, we calculate reduced second Zagreb index of the Cartesian product of k-number of graphs G_i for $i=1,2,....,k$.

Theorem 2. *Let G_1, G_2,.....,G_k be k-number of connected graphs, then*

$$\begin{aligned}
RM_2(\bigotimes_{i=1}^{k}G_i) &= n\sum_{i=1}^{k}\frac{RM_2(G_i)}{n_i}+3\sum_{i=1}^{k}(\frac{m}{n_i}-\frac{nm_i}{n_i^2})M_1(G_i)\\
&\quad+4n\sum_{p,q,r=1,\ p\neq q\neq r}\frac{m_pm_qm_r}{n_pn_qn_r}-4n\sum_{i,j=1,\ i\neq j}\frac{m_im_j}{n_in_j}.
\end{aligned}$$

Where, $n=|V(\bigotimes_{i=1}^{k}G_i)|$ and $m=|E(\bigotimes_{i=1}^{k}G_i)|$.

Proof. Let us assume that, $n'=|V(\bigotimes_{i=1}^{k-1}G_i)|$ and $m'=|E(\bigotimes_{i=1}^{k-1}G_i)|$ so that, $n'=\dfrac{n}{n_k}$ and $m'=\dfrac{mn_k-nm_k}{n_k^2}$. Now by Theorem 1 and an inductive argument, we can have

$$\begin{aligned}
RM_2(\bigotimes_{i=1}^{k}G_i) &= RM_2(\bigotimes_{i=1}^{k-1}G_i\otimes G_k)\\
&= n_kRM_2(\bigotimes_{i=1}^{k-1}G_i)+|V(\bigotimes_{i=1}^{k-1}G_i)|RM_2(G_k)+3m_kM_1(\bigotimes_{i=1}^{k-1}G_i)\\
&\quad+3|E(\bigotimes_{i=1}^{k-1}G_i)|M_1(G_k)-8|E(\bigotimes_{i=1}^{k-1}G_i)||E(G_k)|
\end{aligned}$$

Using Lemmas 1, 2, and 3 on the above result, we obtain:

$$\begin{aligned}
RM_2(\bigotimes_{i=1}^{k}G_i) &= n_k[n'\sum_{i=1}^{k-1}\frac{RM_2(G_i)}{n_i}+3\sum_{i=1}^{k-1}(\frac{m'}{n_i}-\frac{n'm_i}{n_i^2})M_1(G_i)\\
&\quad+4n'\sum_{p,q,r=1,\ p\neq q\neq r}^{k-1}\frac{m_pm_qm_r}{n_pn_qn_r}-4n'\sum_{i,j=1}^{k-1}\frac{m_im_j}{n_in_j}]+n'RM_2(G_k)\\
&\quad+3m_k[n'\sum_{i=1}^{k-1}\frac{M_1(G_i)}{n_i}+4n'\sum_{i,j=1}^{k-1}\frac{m_im_j}{n_in_j}]+3n'\sum_{i=1}^{k-1}(\frac{m_i}{n_i}M_1(G_k)\\
&\quad-8m_kn'\sum_{i=1}^{k}\frac{m_i}{n_i}
\end{aligned}$$

After arranging the terms, we have:

$$\begin{aligned} RM_2(\bigotimes_{i=1}^{k} G_i) &= [n_k n' \sum_{i=1}^{k-1} \frac{RM_2(G_i)}{n_i} + n' RM_2(G_k)] + [3n_k \sum_{i=1}^{k-1} (\frac{m'}{n_i} - \frac{n' m_i}{n_i^2}) M_1(G_i) \\ &\quad + 3m_k n' \sum_{i=1}^{k-1} \frac{M_1(G_i)}{n_i} + 3n' \sum_{i=1}^{k-1} (\frac{m_i}{n_i} M_1(G_k))] \\ &\quad + [4n_k n' \sum_{p,q,r=1,\ p\neq q\neq r}^{k-1} \frac{m_p m_q m_r}{n_p n_q n_r} + 12 n' m_k \sum_{i,j=1}^{k-1} \frac{m_i m_j}{n_i n_j}] \\ &\quad - [4n \sum_{i,j=1}^{k-1} \frac{m_i m_j}{n_i n_j} + 8 m_k n' \sum_{i=1}^{k} \frac{m_i}{n_i}] \end{aligned}$$

After some calculations, we get:

$$\begin{aligned} RM_2(\bigotimes_{i=1}^{k} G_i) &= [n \sum_{i=1}^{k-1} \frac{RM_2(G_i)}{n_i} + n \frac{RM_2(G_k)}{n_k}] + [3 \sum_{i=1}^{k-1} (\frac{m' n_k + m_k n'}{n_i} \\ &\quad - \frac{n' n_k m_i}{n_i^2}) M_1(G_i) + 3(\frac{m n_k - n m_k}{n_k^2}) M_1(G_k)] \\ &\quad + [4n \sum_{p,q,r=1,\ p\neq q\neq r}^{k-1} \frac{m_p m_q m_r}{n_p n_q n_r} + 12 n \frac{m_k}{n_k} \sum_{i,j=1, i\neq j}^{k-1} \frac{m_i m_j}{n_i n_j}] \\ &\quad - [4n \sum_{i,j=1}^{k-1} \frac{m_i m_j}{n_i n_j} + 8n \frac{m_k}{n_k} \sum_{i=1}^{k} \frac{m_i}{n_i}] \\ &= n \sum_{i=1}^{k} \frac{RM_2(G_i)}{n_i} + 3 \sum_{i=1}^{k} (\frac{m}{n_i} - \frac{n m_i}{n_i^2}) M_1(G_i) \\ &\quad + 4n \sum_{p,q,r=1, p\neq q\neq r} \frac{m_p m_q m_r}{n_p n_q n_r} - 4n \sum_{i,j=1}^{k} \frac{m_i m_j}{n_i n_j}], \end{aligned}$$

which is the desired result. □

If $G_1 = G_2 = ... = G_k = G$ then $\bigotimes_{i=1}^{k} G_i = G^k$. Hence from the above theorem, the following corollary follows:

Corollary 1. *If G be connected graph, then*

$$\begin{aligned} RM_2(G^k) &= k|V(G)|^{k-3}[|V(G)|^2 RM_2(G) + 3(k-1)|V(G)||E(G)|M_1(G) \\ &\quad + 4(k-1)(k-2)|E(G)|^3 - 4(k-1)|V(G)||E(G)|^2]. \end{aligned}$$

3. Applications

Using various unary and binary graph operations on different elementary graphs, such as the path graph, cycle graph, complete graph etc, we can obtain several significant composite graphs having excellent usage in modern science and technology. The Cartesian product is one of that binary operations capable to construct different special structure. Using Cartesian product of two graphs, one can get ladder graph, C_4-nanotube and nanotorus, rectangular grid, rook's graph, hamming graph etc. The Hamming graphs are interesting in connection with error-correcting codes and association schemes. The rook's graph represents all legal moves of rook on the chess board. So it is worth to investigate investigating topological indices for the above structures. In this section, the reduced second Zagreb index of aforesaid graphs is derived. For path, cycle, and complete graph of n vertices, the notations P_n, C_n, and K_n are used.

Example 1. *The Ladder graph L_n (Fig. 1) is the Cartesian product of P_2 and P_{n+1}, made by n sequences and $(2n+2)$ vertices. So, using theorem 1, the reduced second Zagreb index of L_n is given by*

$$RM_2(L_n) = 12n - 10.$$

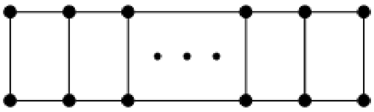

FIG. 1. The ladder graph L_n

Example 2. *The Cartesian product of* P_n $(n \geq 2)$ *and* C_m $(m \geq 2)$ *is a* C_4*-nanotube* $TUC_4(m,n)$*, whose reduced second Zagreb index can be calculated using theorem 1 as follows:*

$$RM_2(P_n \otimes C_m) = 18mn - 25m.$$

Example 3. *The Cartesian product of* C_n $(n \geq 3)$ *and* C_m $(m \geq 3)$ *is a* C_4*-nanotorus* $TC_4(m,n)$*, whose reduced second Zagreb index is calculated from Theorem 1 as follows:*

$$RM_2(C_n \otimes C_m) = 18mn.$$

Example 4. *The rectangular grid (Fig.2) is the Cartesian product of the* P_n $(n \geq 2)$ *and* P_m $(m \geq 2)$*. So, using Theorem 1, its reduced second Zagreb index is given by*

$$RM_2(P_n \otimes P_m) = 18mn - 25m - 25n + 28.$$

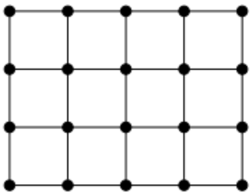

FIG. 2. The grid graph $P_5 \otimes P_4$

Example 5. *The Cartesian product of* K_n *and* K_m *yields the rook's graph (Fig. 3). So, using Theorem 1, its reduced second Zagreb index is given by*

$$RM_2(K_m \otimes K_n) = \frac{mn}{2}[(m+n)^3 - 8m^2 - 8n^2 - 16mn + 21m + 21n - 14].$$

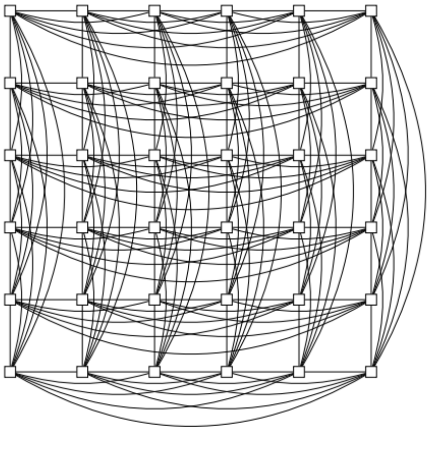

FIG. 3. The rook's graph $K_6 \otimes K_6$

Example 6. *The graph* $G = \bigotimes_{i=1}^{N} K_{n_i}$ *is known as a Hamming graph and is denoted by* $H_{n_1,n_2,\ldots,n_N}$. *so, applying previous theorem to compute reduced second Zagreb index of a Hamming graph as follows:*

$$\begin{aligned} RM_2(H_{n_1,n_2,\ldots,n_N}) &= RM_2(\bigotimes_{i=1}^{N} K_{n_i}) \\ &= \frac{1}{2}\prod_{i=1}^{N} n_i \sum_{i=1}^{N}(n_i-1)[\sum_{i=1}^{N}(n_i-1)-1]^2. \end{aligned}$$

If $n_1 = n_2 = \ldots\ldots = n_N = 2$*, then the graph G is known as a hypercube of dimension N and denoted by* Q_n *(Fig. 4). Thus from above, we directly get*

$$RM_2(Q_n) = \frac{1}{2}N2^N(N-1)^2.$$

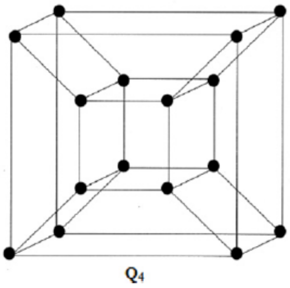

FIG. 4. Example of Hypercube

Example 7. *The reduced second Zagreb index of the torus* $C_{n_1} \otimes C_{n_2} \otimes \ldots\ldots \otimes C_{n_k}$ *is given by*

$$RM_2(C_{n_1} \otimes C_{n_2} \otimes \ldots\ldots \otimes C_{n_k}) = k(2k-1)^2 \prod_{i=1}^{k} n_i.$$

Example 8. *Let* $T = T[p,q]$ *be the molecular graph of a nanotorus (Fig. 5). Then* $|V(T)| = pq$, $|E(T)| = \frac{9pq}{2}$, $M_1(T) = 9pq$. *We consider a q-multi-walled nanotorus* $G_n = P_n \otimes T$. *It is easy to find that* $RM_2(P_n) = n-3$, $RM_2(T) = 6pq$, *and* $M_1(P_n) = 4n-6$. *Thus from theorem 1, we have the following result.*

$$RM_2(G_n) = 5pq(8n-9).$$

We have plotted the result in Fig. 6

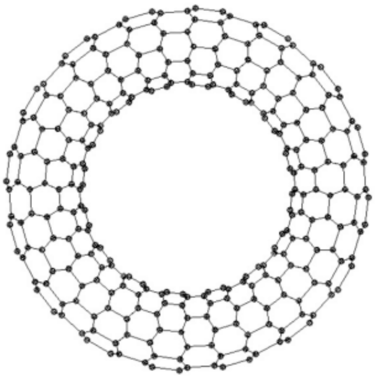

FIG. 5. The graph of a nanotorus

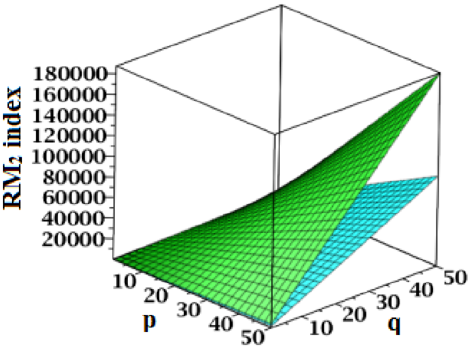

FIG. 6. Plotting of the RM_2 index for G_n, $n = 2, 3$. Cyan and green colors are used for $n = 2, 3$ respectively

4. Conclusion

In this article, reduced second Zagreb index of Cartesian product graph is studied. Firstly RM_2 index is obtained for the product of two graphs and then the general case is considered. Applying that results, RM_2 index is investigated for some special structures. As future work, some other graph operations like composition, tensor product, corona product, strong product, splice, link etc. can be discussed in terms of the reduced second Zagreb index.

References

[1] Trinajstić N. *Chemical Graph Theory*. CRC Press, Boca Raton, 1993.

[2] Gutman I., Polansky O.E. *Mathematical Concepts in Organic Chemistry*. Springer, Berlin, 1986.

[3] Wiener H. Structural determination of paraffin boiling points. *J. Am. Chem. Soc.*, 1947, **69**, P. 7–20.

[4] Randić M. Quantitative Structure – Property Relationship: boiling points and planar benzenoids. *New. J. Chem.*, 1996, **20**(10), P. 1001–1009.

[5] Hawkins D.M., Basak S.C., Mills D. Assessing Model Fit by Cross Validation. *J. Chem. Inf. Comput. Sci.*, 2003, **43**, P. 579–586.

[6] Gutman I, Trinajstić N. Graph theory and molecular orbitals. Total π-electron energy of alternate hydrocarbons. *Chem. Phys. Lett.*, 1972, **17**, P. 535–538.

[7] Gutman I, Rućić B, Trinajstić N, Wilcox C.F. Graph theory and molecular orbitals. XII. Acyclic polyenes. *J. Chem. Phys.*, 1975, **62**, P. 3399–3405.

[8] Das K.C., Xu K., Gutman I. On Zagreb and Harary indices. *MATCH Commun. Math. Comput Chem.*, 2013, **70**, P. 301–314.

[9] Azari M., Iranmanesh A., Gutman I. Zagreb indices of bridge and chain graphs. *MATCH Commun. Math. Comput. Chem.*, 2013, **70**, P. 921–938.

[10] Hamzeh A., Reti T. An analogue of Zagreb index inequality obtained from graph ir-regularity measures. *MATCH Commun. Math. Comput. Chem.*, 2014, **72**, P. 669–683.

[11] Li S., Zhang M.J. Sharp upper bounds for the Zagreb indices of bipartite graphs with a given diameter. *Appl. Math. Lett.*, 2011, **24**, P. 131–137.

[12] Fonseca C.M.D., Stevanovic D. Further properties of the second Zagreb index. *MATCH Commun. Math. Comput. Chem.*, 2014, **72**, P. 655–668.

[13] Gutman I., Das K.C. The first Zagreb index 30 years after. *MATCH Commun. Math. Comput. Chem.*, 2004, **50**, P. 83–92.

[14] Mondal S., Bhosale A., De N., Pal A. Topological properties of some nanostructures. *Nanosystems: Physics, Chemistry, Mathematics*, 2020, **11** (1), P. 14–24.

[15] Furtula B., Gutman I., Ediz S. On difference of Zagreb indices. *Discrete Appl. Math.*, 2014, **178**, P. 83–88.

[16] Horoldagva H., Buyantogtokh L., Dorjsembe S. Difference of Zagreb indices andreduced second Zagreb index of cyclic graphs with cut edges. *MATCH Commun. Math.Comput. Chem.*, 2017, **78**, P. 337–349.

[17] Mahanta A., Buragohain J., Bharali A. Reduced first Zagreb index, Reduced second Zagreb index and hyper-Zagreb index of four new sums based on tensor product of graphs. *Global journal of engineering science and researches*, 2018, **5** (11), P. 12–19.

[18] Khalifeh M.H., Azari H.Y, Ashrafi A.R. The first and second Zagreb indices of some graph operations. *Discrete Appl. Math.*, 2009, **157**, P. 804–811.

[19] Azari H.Y, Manoochehrian B, Ashrafi A.R. The PI index of product graphs. *Appl. Math. Lett.*, 2008, **21**, P. 624–627.

[20] Klavzar S., Rajapakse A., Gutman I. The Szeged and the Wiener index of graphs. *Appl. Math. Lett.*, 1996, **9**, P. 45–49.

[21] Graovac A., Pisanski T. On the Wiener index of a graph. *J. Math. Chem.*, 1991, **8**, P. 53–62.

[22] De N., Nayeem S.M.A., Pal A. F-Index of some graph operations. 2016, *Discrete Math. Algorithm Appl.*, **8**, Article ID: 1650025.

[23] De N., Nayeem S.M.A., Pal A. The F-coindex of some graph operations. 2016, *Springer Plus*, **5**, P. 221–233.

[24] De N., Nayeem S.M.A., Pal A. Reformulated First Zagreb Index of Some Graph Operations. *Mathematics*, 2015, **3**(4), P. 945–960.

[25] De N., Pal A., Nayeem S.M.A. On some bounds and exact formulae for connective eccentric indices of graphs under some graph operations. *Int. J. Comb.*, 2014, **2014**, Article ID 579257.

NANOSYSTEMS: PHYSICS, CHEMISTRY, MATHEMATICS, 2020, 11 (2), P. 138–144

Analysis of the spectrum of a 2×2 operator matrix. Discrete spectrum asymptotics

T. H. Rasulov, E. B. Dilmurodov

Faculty of Physics and Mathematics, Bukhara State University
M. Ikbol str. 11, 200100 Bukhara, Uzbekistan
rth@mail.ru, elyor.dilmurodov@mail.ru

DOI 10.17586/2220-8054-2020-11-2-138-144

We consider a 2×2 operator matrix $\mathcal{A}_\mu$, $\mu > 0$ related with the lattice systems describing two identical bosons and one particle, another nature in interactions, without conservation of the number of particles. We obtain an analog of the Faddeev equation and its symmetric version for the eigenfunctions of $\mathcal{A}_\mu$. We describe the new branches of the essential spectrum of $\mathcal{A}_\mu$ via the spectrum of a family of generalized Friedrichs models. It is established that the essential spectrum of $\mathcal{A}_\mu$ consists the union of at most three bounded closed intervals and their location is studied. For the critical value μ_0 of the coupling constant μ we establish the existence of infinitely many eigenvalues, which are located in the both sides of the essential spectrum of $\mathcal{A}_\mu$. In this case, an asymptotic formula for the discrete spectrum of $\mathcal{A}_\mu$ is found.

Keywords: operator matrix, bosonic Fock space, coupling constant, dispersion function, essential and discrete spectrum, Birman–Schwinger principle, spectral subspace, Weyl creterion.

Received: 30 December 2019

Revised: 17 February 2020

1. Introduction and statement of the problem

It is well-known that [1], if H is a bounded linear operator in a Hilbert space $\mathcal{H}$ and a decomposition $\mathcal{H} = \mathcal{H}_1 \oplus \mathcal{H}_2$ into two Hilbert spaces $\mathcal{H}_1$, $\mathcal{H}_2$ is given, then H always admits a block operator matrix representation

$$H = \begin{pmatrix} H_{11} & H_{12} \\ H_{21} & H_{22} \end{pmatrix}$$

with bounded linear operators $H_{ij} : \mathcal{H}_j \to \mathcal{H}_i$, $i, j = 1, 2$. In addition, $H = H^*$ if and only if $H_{ii} = H_{ii}^*$, $i = 1, 2$ and $H_{21} = H_{12}^*$. Such operator matrices often arise in mathematical physics, e.g., in quantum field theory, condensed matter physics, fluid mechanics, magnetohydrodynamics and quantum mechanics. One of the special class of 2×2 block operator matrices is the Hamiltonians acting in the one- and two-particle subspaces of a Fock space. It is related with a system describing three-particles in interaction without conservation of the number of particles in Fock space. Here, off-diagonal entries of such block operator matrices are annihilation and creation operators.

Operator matrices of this form play a key role for the study of the energy operator of the spin-boson Hamiltonian with two bosons on the torus. In fact, the latter is a 6×6 operator matrix which is unitarily equivalent to a 2×2 block diagonal operator with two copies of a particular case of H on the diagonal, see e.g. [2]. Consequently, the location of the essential spectrum and finiteness of discrete eigenvalues of the spin-boson Hamiltonian are determined by the corresponding spectral information on the operator matrix H. We recall that the spin-boson model is a well-known quantum-mechanical model which describes the interaction between a two-level atom and a photon field. We refer to [3] and [4] for excellent reviews from physical and mathematical perspectives, respectively. Independently of whether the underlying domain is a torus $\mathbb{T}^{\mathrm{d}}$ or the whole space $\mathbb{R}^{\mathrm{d}}$, the full spin-boson Hamiltonian is an infinite operator matrix in Fock space for which rigorous results are very hard to obtain. One line of attack is to consider the compression to the truncated Fock space with a finite number N of bosons, and in fact most of the existing literature concentrates on the case $N \leq 2$. For the case of $\mathbb{R}^{\mathrm{d}}$ there are some exceptions, e.g. [5, 6] for arbitrary finite N and [7] for $N = 3$, where a rigorous scattering theory was developed for small coupling constants.

For the case when the underlying domain is a torus, the spectral properties of some versions of H were investigated in [8–11]. An important problem of the spectral theory of such matrix operators is the infiniteness of the number of eigenvalues located outside the essential spectrum. We mention that, the infiniteness of the discrete eigenvalues below the bottom of the essential spectrum of the Hamiltonian in Fock space, which has a block operator matrix representation, and corresponding eigenvalue asymptotics were discussed in [8]. These results were obtained using the machinery developed in [12] by Sobolev.

In the present paper we consider a 2×2 operator matrix $\mathcal{A}_\mu$, ($\mu > 0$ is a coupling constant) related with the lattice systems describing two identical bosons and one particle, another nature in interactions, without conservation of the number of particles. This operator acts in the direct sum of one- and two-particle subspaces of the bosonic Fock space and it is related with the lattice spin-boson Hamiltonian [2,13]. We find the critical value μ_0 of the coupling constant μ, to establish the existence of infinitely many eigenvalues lying in **both** sides of essential spectrum of $\mathcal{A}_{\mu_0}$ and to obtain an asymptotics for the number of these eigenvalues.

We point out that the latter assertion seems to be quite new for the discrete models and similar result have not been obtained yet for the three-particle discrete Schrödinger operators and operator matrices in Fock space. In all papers devoted to the infiniteness of the number of eigenvalues (Efimov's effects), the situation on the neighborhood of the left edge of essential spectrum are discussed, see for example [8–10, 14–16]. Since the essential spectrum of the three-particle continuous Schrödinger operators [12, 17, 18] and standard spin-boson model with at most two photons [19, 20] coincides with half-axis $[\kappa; +\infty)$, the main results of the present paper are typical only for lattice case, and they do not have analogs in the continues case.

Now, we formulate the problem. Let $\mathbb{T}^3$ be the three-dimensional torus, the cube $(-\pi, \pi]^3$ with appropriately identified sides equipped with its Haar measure. Let $L_2(\mathbb{T}^3)$ be the Hilbert space of square integrable (complex) functions defined on $\mathbb{T}^3$ and $L_2^{\mathrm{s}}((\mathbb{T}^3)^2)$ be the Hilbert space of square integrable (complex) symmetric functions defined on $(\mathbb{T}^3)^2$. Denote by $\mathcal{H}$ the direct sum of spaces $\mathcal{H}_1 := L_2(\mathbb{T}^3)$ and $\mathcal{H}_2 := L_2^{\mathrm{s}}((\mathbb{T}^3)^2)$, that is, $\mathcal{H} := \mathcal{H}_1 \oplus \mathcal{H}_2$. The spaces $\mathcal{H}_1$ and $\mathcal{H}_2$ are called one- and two-particle subspaces of a bosonic Fock space $\mathcal{F}_{\mathrm{s}}(L_2(\mathbb{T}^3))$ over $L_2(\mathbb{T}^3)$, respectively.

Let us consider a 2×2 operator matrix $\mathcal{A}_\mu$ acting in the Hilbert space $\mathcal{H}$ as:

$$\mathcal{A}_\mu := \begin{pmatrix} A_{11} & \mu A_{12} \\ \mu A_{12}^* & A_{22} \end{pmatrix}$$

with the entries

$$(A_{11} f_1)(k) = w_1(k) f_1(k), \quad (A_{12} f_2)(k) = \int_{\mathbb{T}^3} f_2(k, s) ds,$$
$$(A_{22} f_2)(k, p) = w_2(k, p) f_2(k, p), \quad f_i \in \mathcal{H}_i, \quad i = 1, 2.$$

Here, $\mu > 0$ is a coupling constant, the functions $w_1(\cdot)$ and $w_2(\cdot, \cdot)$ have the form

$$w_1(k) := \varepsilon(k) + \gamma, \quad w_2(k, p) := \varepsilon(k) + \varepsilon(\frac{1}{2}(k + p)) + \varepsilon(p)$$

with $\gamma \in \mathbb{R}$ and the dispersion function $\varepsilon(\cdot)$ is defined by:

$$\varepsilon(k) := \sum_{i=1}^{3} (1 - \cos k_i), \; k = (k_1, k_2, k_3) \in \mathbb{T}^3, \tag{1.1}$$

A_{12}^* denotes the adjoint operator to A_{12} and

$$(A_{12}^* f_1)(k, p) = \frac{1}{2}(f_1(k) + f_1(p)), \quad f_1 \in \mathcal{H}_1.$$

Under these assumptions, the operator $\mathcal{A}_\mu$ is bounded and self-adjoint.

We remark that the operators A_{12} and A_{12}^* are called annihilation and creation operators [21], respectively. In physics, an annihilation operator is an operator that lowers the number of particles in a given state by one, a creation operator is an operator that increases the number of particles in a given state by one, and it is the adjoint of the annihilation operator.

2. Faddeev's equation and essential spectrum of $\mathcal{A}_\mu$

In this section, we obtain an analog of the Faddeev type integral equation for eigenvectors of $\mathcal{A}_\mu$ and investigate the location and structure of the essential spectrum of $\mathcal{A}_\mu$.

Throughout the present paper we adopt the following conventions: Denote by $\sigma(\cdot)$, $\sigma_{\mathrm{ess}}(\cdot)$ and $\sigma_{\mathrm{disc}}(\cdot)$, respectively, the spectrum, the essential spectrum, and the discrete spectrum of a bounded self-adjoint operator.

Let $H_0 := \mathbb{C}$. To study the spectral properties of the operator $\mathcal{A}_\mu$, we introduce a family of bounded self-adjoint operators (generalized Friedrichs models) $\mathcal{A}_\mu(k)$, $k \in \mathbb{T}^3$ which acts in $\mathcal{H}_0 \oplus \mathcal{H}_1$ as 2×2 operator matrices:

$$\mathcal{A}_\mu(k) := \begin{pmatrix} A_{00}(k) & \frac{\mu}{\sqrt{2}} A_{01} \\ \frac{\mu}{\sqrt{2}} A_{01}^* & A_{11}(k) \end{pmatrix},$$

with matrix elements:

$$A_{00}(k)f_0 = w_1(k)f_0, \ (A_{01}f_1) = \int\limits_{\mathbb{T}^3} f_1(t)dt,$$
$$(A_{11}(k)f_2)(p) = w_2(k,p)f_1(p), \quad f_i \in \mathcal{H}_i, \quad i=1,2.$$

From the simple discussions it follows that $\sigma_{\text{ess}}(\mathcal{A}_\mu(k)) = [m(k), M(k)]$, where the numbers $m(k)$ and $M(k)$ are defined by:

$$m(k) := \min_{p\in\mathbb{T}^3} w_2(k,p), \quad M(k) := \max_{p\in\mathbb{T}^3} w_2(k,p). \tag{2.1}$$

For any $k \in \mathbb{T}^3$ we define an analytic function: $I(k\,;\cdot)$ in $\mathbb{C}\setminus\sigma_{\text{ess}}(\mathcal{A}_\mu(k))$ by

$$I(k\,;z) := \int\limits_{\mathbb{T}^3} \frac{dt}{w_2(k,t)-z}.$$

Then the Fredholm determinant associated to the operator $\mathcal{A}_\mu(k)$ is defined by:

$$\Delta_\mu(k\,;z) := w_1(k) - z - \frac{\mu^2}{2}\, I(k\,;z), \ z \in \mathbb{C}\setminus\sigma_{\text{ess}}(\mathcal{A}_\mu(k)).$$

A simple consequence of the Birman–Schwinger principle and the Fredholm theorem implies that for the discrete spectrum of $\mathcal{A}_\mu(k)$, the equality:

$$\sigma_{\text{disc}}(\mathcal{A}_\mu(k)) = \{z \in \mathbb{C}\setminus[m(k); M(k)] : \ \Delta_\mu(k\,;z) = 0\}$$

holds.

We set:

$$m := \min_{k,p\in\mathbb{T}^3} w_2(k,p), \quad M := \max_{k,p\in\mathbb{T}^3} w_2(k,p),$$
$$\Lambda_\mu := \bigcup_{k\in\mathbb{T}^3} \sigma_{\text{disc}}(\mathcal{A}_\mu(k)), \quad \Sigma_\mu := [m; M] \cup \Lambda_\mu.$$

For each $\mu > 0$ and $z \in \mathbb{C}\setminus\Sigma_\mu$ we define the integral operator $T_\mu(z)$ acting in the Hilbert spaces $L_2(\mathbb{T}^3)$ by

$$(T_\mu(z)g)(p) = \frac{\mu^2}{2\Delta_\mu(p;\,z)} \int\limits_{\mathbb{T}^3} \frac{g(t)dt}{w_2(p,t)-z}.$$

The following theorem is an analog of the well-known Faddeev's result for the operator $\mathcal{A}_\mu$ and establishes a connection between eigenvalues of $\mathcal{A}_\mu$ and $T_\mu(z)$.

Theorem 2.1. *The number* $z \in \mathbb{C} \setminus \Sigma_\mu$ *is an eigenvalue of the operator* $\mathcal{A}_\mu$ *if and only if the number* $\lambda = 1$ *is an eigenvalue of the operator* $T_\mu(z)$. *Moreover, the eigenvalues* z *and* 1 *have the same multiplicities.*

We point out that the integral equation $g = T_\mu(z)g$ is an analog of the Faddeev type system of integral equations for eigenfunctions of the operator $\mathcal{A}_\mu$ and it is played crucial role in the analysis of the spectrum of $\mathcal{A}_\mu$. For the proof of Theorem 2.1 we show the equivalence of the eigenvalue problem $\mathcal{A}_\mu f = zf$ to the equation $g = T_\mu(z)g$.

The following theorem describes the location of the essential spectrum of the operator $\mathcal{A}_\mu$ by the spectrum of the family of generalized Friedrichs models $\mathcal{A}_\mu(k)$.

Theorem 2.2. *For the essential spectrum of* $\mathcal{A}_\mu$, *the equality* $\sigma_{\mathrm{ess}}(\mathcal{A}_\mu) = \Sigma_\mu$ *holds. Moreover, the set* Σ_μ *consists of no more than three bounded closed intervals.*

The inclusion $\Sigma_\mu \subset \sigma_{\mathrm{ess}}(\mathcal{A}_\mu)$ in the proof of Theorem 2.2 is established with the use of a well-known Weyl creterion, see for example [11]. An application of Theorem 2.1 and analytic Fredholm theorem (see, e.g., Theorem VI.14 in [18]) proves inclusion $\sigma_{\mathrm{ess}}(\mathcal{A}_\mu) \subset \Sigma_\mu$.

In the following we introduce the new subsets of the essential spectrum of $\mathcal{A}_\mu$.

Definition 2.3. *The sets* Λ_μ *and* $[m; M]$ *are called two- and three-particle branches of the essential spectrum of* $\mathcal{A}_\mu$, *respectively.*

The definition of the set Λ_μ and the equality

$$\bigcup_{k \in \mathbb{T}^3} [m(k); M(k)] = [m; M]$$

together with Theorem 2.2 give the equality

$$\sigma_{\mathrm{ess}}(\mathcal{A}_\mu) = \bigcup_{k \in \mathbb{T}^3} \sigma(\mathcal{A}_\mu(k)). \tag{2.2}$$

Here the family of operators $\mathcal{A}_\mu(k)$ have a simpler structure than the operator $\mathcal{A}_\mu$. Hence, in many instances, (2.2) provides an effective tool for the description of the essential spectrum.

Using the extremal properties of the function $w_2(\cdot,\cdot)$, and the Lebesgue dominated convergence theorem one can show that the integral $I(\overline{0}; 0)$ is finite, where $\overline{0} := (0,0,0) \in \mathbb{T}^3$, see [22,23].

For the next investigations we introduce the following quantities

$$\mu_l^0(\gamma) := \sqrt{2\gamma}\,\big(I(\overline{0},0)\big)^{-1/2} \ \text{ for } \gamma > 0;$$
$$\mu_r^0(\gamma) := \sqrt{24 - 2\gamma}\,\big(I(\overline{0},0)\big)^{-1/2} \ \text{ for } \gamma < 12.$$

Since $\mathbb{T}^3$ is compact, and the functions $\Delta_\mu(\cdot; 0)$ and $\Delta_\mu(\cdot; 18)$ are continuous on $\mathbb{T}^3$, there exist points $k_0, k_1 \in \mathbb{T}^3$ such that the equalities

$$\max_{k \in \mathbb{T}^3} \Delta_\mu(k; 0) = \Delta_\mu(k_0; 0), \quad \min_{k \in \mathbb{T}^3} \Delta_\mu(k; 18) = \Delta_\mu(k_1; 18)$$

hold.

Let us define the following notations:

$$\gamma_0 := \left(12\frac{I(k_0; 0)}{I(\overline{0}; 0)} - \varepsilon(k_0)\right)\left(1 + \frac{I(k_0; 0)}{I(\overline{0}; 0)}\right)^{-1};$$
$$\gamma_1 := (18 - \varepsilon(k_1))\left(1 - \frac{I(k_1; 18)}{I(\overline{0}; 0)}\right).$$

We denote:

$$E_\mu^{(1)} := \min\{\Lambda_\mu \cap (-\infty; 0]\};\ E_\mu^{(2)} := \max\{\Lambda_\mu \cap (-\infty; 0]\};$$
$$E_\mu^{(3)} := \min\{\Lambda_\mu \cap [18; \infty)\};\ E_\mu^{(4)} := \max\{\Lambda_\mu \cap [18; \infty)\}.$$

We formulate the results, which precisely describe the structure of the essential spectrum of $\mathcal{A}_\mu$. The structure of the essential spectrum depends on the location of the parameters $\mu > 0$ and $\gamma \in \mathbb{R}$.

Theorem 2.4. *Let* $\mu = \mu_r^0(\gamma)$, *with* $\gamma < 12$. *The following equality holds*

$$\sigma_{\text{ess}}(\mathcal{A}_\mu) = \begin{cases} [E_1; E_2] \bigcup [0; 18], & \text{if } \gamma < \gamma_0; \\ [E_1; 18], & \text{if } \gamma_0 \le \gamma < 6; \\ [0; 18], & \text{if } 6 \le \gamma < 12. \end{cases}$$

Theorem 2.5. *Let* $\mu = \mu_l^0(\gamma)$, *with* $\gamma > 0$. *The following equality holds:*

$$\sigma_{\text{ess}}(\mathcal{A}_\mu) = \begin{cases} [0; 18], & \text{if } 0 < \gamma \le 6; \\ [0; E_\mu^{(4)}], & \text{if } 6 < \gamma \le \gamma_1; \\ [0; 18] \bigcup [E_\mu^{(3)}; E_\mu^{(4)}], & \text{if } \gamma > \gamma_1. \end{cases}$$

The proof of these two theorems are based on the existence conditions of the eigenvalue $z_\mu(k)$ of the operator $\mathcal{A}_\mu(\cdot)$ and the continuity of $z_\mu(\cdot)$ on its domain.

3. Birman–Schwinger principle and discrete spectrum asymptotics of the operator $\mathcal{A}_\mu$

Let us denote by $\tau_{\min}(\mathcal{A}_\mu)$ and $\tau_{\max}(\mathcal{A}_\mu)$ the lower and upper bounds of the essential spectrum $\sigma_{\text{ess}}(\mathcal{A}_\mu)$ of the operator $\mathcal{A}_\mu$, respectively, that is,

$$\tau_{\min}(\mathcal{A}_\mu) :\equiv \min \sigma_{\text{ess}}(\mathcal{A}_\mu), \quad \tau_{\max}(\mathcal{A}_\mu) :\equiv \max \sigma_{\text{ess}}(\mathcal{A}_\mu).$$

For an interval $\Delta \subset \mathbb{R}$, $E_\Delta(\mathcal{A}_\mu)$ stands for the spectral subspace of $\mathcal{A}_\mu$ corresponding to Δ. Let us denote by $\sharp\{\cdot\}$ the cardinality of a set and by $N_{(a,b)}(\mathcal{A}_\mu)$ the number of eigenvalues of the operator $\mathcal{A}_\mu$, including multiplicities, lying in $(a, b) \subset \mathbb{R} \setminus \sigma_{\text{ess}}(\mathcal{A}_\mu)$, that is,

$$N_{(a,b)}(\mathcal{A}_\mu) := \dim E_{(a,b)}(\mathcal{A}_\mu).$$

For a $\lambda \in \mathbb{R}$, we define the number $n(\lambda, A_\mu)$ as follows

$$n(\lambda, A_\mu) := \sup\{\dim F : (A_\mu u, u) > \lambda,\ u \in F \subset \mathcal{H},\ ||u|| = 1\}.$$

The number $n(\lambda, A_\mu)$ is equal to the infinity if $\lambda < \max \sigma_{\text{ess}}(A_\mu)$; if $n(\lambda, A_\mu)$ is finite, then it is equal to the number of the eigenvalues of A_μ bigger than λ.

By the definition of $N_{(a;b)}(\mathcal{A}_\mu)$, we have

$$N_{(-\infty;z)}(\mathcal{A}_\mu) = n(-z, -\mathcal{A}_\mu),\ -z > -\tau_{\min}(\mathcal{A}_\mu),$$
$$N_{(z;+\infty)}(\mathcal{A}_\mu) = n(z, \mathcal{A}_\mu),\ z > \tau_{\max}(\mathcal{A}_\mu).$$

In our analysis of the discrete spectrum of $\mathcal{A}_\mu$, the crucial role is played by the compact operator $\widehat{T}_\mu(z)$, $z \in \mathbb{R} \setminus [\tau_{\min}(\mathcal{A}_\mu); \tau_{\max}(\mathcal{A}_\mu)]$ in the space $L_2(\mathbb{T}^3)$ as integral operator

$$(\widehat{T}_\mu(z)g)(p) = \frac{\mu^2}{2\sqrt{\Delta_\mu(p;\, z)}} \int_{\mathbb{T}^3} \frac{g(t)dt}{\sqrt{\Delta_\mu(t;\, z)}(w_2(p,t) - z)}, \quad \text{for} \quad z < \tau_{\min}(\mathcal{A}_\mu),$$
$$(\widehat{T}_\mu(z)g)(p) = -\frac{\mu^2}{2\sqrt{-\Delta_\mu(p;\, z)}} \int_{\mathbb{T}^3} \frac{g(t)dt}{\sqrt{-\Delta_\mu(t;\, z)}(w_2(p,t) - z)}, \quad \text{for} \quad z > \tau_{\max}(\mathcal{A}_\mu).$$

The following lemma is a realization of the well-known Birman–Schwinger principle for the operator $\mathcal{A}_\mu$ (see [8]).

Lemma 3.1. *For* $z \in \mathbb{R} \setminus [\tau_{\min}(\mathcal{A}_\mu); \tau_{\max}(\mathcal{A}_\mu)]$ *the operator* $\widehat{T}_\mu(z)$ *is compact and continuous in* z *and*

$$N_{(-\infty;z)}(\mathcal{A}_\mu) = n(1, \widehat{T}_\mu(z)) \quad \textit{for} \quad z < \tau_{\min}(\mathcal{A}_\mu),$$

$$N_{(z;+\infty)}(\mathcal{A}_\mu) = n(1, \widehat{T}_\mu(z)) \quad \textit{for} \quad z > \tau_{\max}(\mathcal{A}_\mu).$$

This lemma can be proven quite similarly to the corresponding result of [8].

Let $\mathbb{S}^2$ being the unit sphere in $\mathbb{R}^3$ and

$$S_r : L_2((0,r),\sigma_0) \to L_2((0,r),\sigma_0), \quad r > 0, \quad \sigma_0 = L_2(\mathbb{S}^2)$$

be the integral operator with the kernel

$$S(t;y) = \frac{25}{8\pi^2\sqrt{6}} \frac{1}{5\cos(hy)+t},$$

$$y = x - x', \quad x, x' \in (0,r), \quad t = (\xi, \eta), \quad \xi, \eta \in \mathbb{S}^2.$$

For $\lambda > 0$, define

$$U(\lambda) = \frac{1}{2} \lim_{r\to\infty} r^{-1} n(\lambda, S_r).$$

The existence of the latter limit and the fact $U(1) > 0$ shown in [12].

From the definitions of the quantities $\mu_l^0(\gamma)$ and $\mu_r^0(\gamma)$, it is easy to see that $\mu_l^0(6) = \mu_r^0(6)$. We set $\mu_0 := \mu_l^0(6)$. We can now formulate our last main result.

Theorem 3.2. *The following relations hold:*

$$\sharp(\sigma_{\rm disc}(\mathcal{A}_{\mu_0}) \cap (-\infty, 0)) = \sharp(\sigma_{\rm disc}(\mathcal{A}_{\mu_0}) \cap (18, \infty)) = \infty;$$

$$\lim_{z \nearrow 0} \frac{N_{(-\infty,\, z)}(\mathcal{A}_{\mu_0})}{|\log|z||} = \lim_{z \searrow 18} \frac{N_{(z,\, \infty)}(\mathcal{A}_{\mu_0})}{|\log|z-18||} = U(1). \tag{3.1}$$

Clearly, by equality (3.1), the infinite cardinality of the parts of discrete spectrum of $\mathcal{A}_{\mu_0}$ in $(-\infty; 0)$ and $(18; +\infty)$ follows automatically from the positivity of $U(1)$.

Acknowledgements

The authors thank the anonymous referee for reading the manuscript carefully and for making valuable suggestions.

References

[1] Tretter C. *Spectral theory of block operator matrices and applications*. Imperial College Press, 2008.

[2] Muminov M., Neidhardt H., Rasulov T. On the spectrum of the lattice spin-boson Hamiltonian for any coupling: 1D case. *Journal of Mathematical Physics*, 2015, **56**, 053507.

[3] Leggett A.J., Chakravarty S., et al. Dynamics of the dissipative two-state system. *Rev. Mod. Phys.*, 1987, **59**, P. 1–85.

[4] Hübner M., Spohn H. Radiative decay: nonperturbative approaches. *Rev. Math. Phys.*, 1995, **7** (3), P. 363–387.

[5] Gérard C. Asymptotic completeness for the spin-boson model with a particle number cutoff. *Rev. in Math. Phys.*, 1996, **8** (4), P. 549–589.

[6] Hübner M., Spohn H. Spectral properties of spin-boson Hamiltonian. *Annl. Inst. Poincare*, 1995, **62** (3), P. 289–323.

[7] Zhukov Y.V., Minlos R.A. The spectrum and scattering in the 'spin-boson' model with at most three photons. *Theor. Math. Phys.*, 1995, **103** (1), P. 63–81.

[8] Albeverio S., Lakaev S.N., Rasulov T.H. On the spectrum of an Hamiltonian in Fock space. Discrete spectrum asymptotics. *J. Stat. Phys.*, 2007, **127** (2), P. 191–220.

[9] Albeverio S., Lakaev S.N., Rasulov T.H. The Efimov effect for a model operator associated with the Hamiltonian of a non conserved number of particles. *Methods Funct. Anal. Topology*, 2007, **13** (1), P. 1–16.

[10] Muminov M.I., Rasulov T.H. On the number of eigenvalues of the family of operator matrices. *Nanosystems: Physics, Chemistry, Mathematics*, 2014, **5** (5), P. 619–626.

[11] Rasulov T.H., Tosheva N.A. Analytic description of the essential spectrum of a family of 3×3 operator matrices. *Nanosystems: Physics, Chemistry, Mathematics*, 2019, **10** (5), P. 511–519.

[12] Sobolev A.V. The Efimov effect. Discrete spectrum asymptotics. *Comm. Math. Phys.*, 1993, **156**, P. 101–126.

[13] Rasulov T.Kh. Branches of the essential spectrum of the lattice spin-boson model with at most two photons. *Theoretical and Mathematical Physics*, 2016, **186** (2), P. 251–267.

[14] Abdullaev Zh.I., Lakaev S.N. Asymptotics of the discrete spectrum of the three-particle Schrödinger difference operator on a lattice. *Theor. Math. Phys.*, 2003, **136** (2), P. 1096–1109.

[15] Albeverio S., Lakaev S.N., Muminov Z.I. Schrödinger operators on lattices. The Efimov effect and discrete spectrum asymptotics. *Ann. Henri Poincaré*, 2004, **5**, P. 743–772.

[16] Lakaev S.N., Muminov M.É. Essential and discrete spectra of the three-particle Schrödinger operator on a lattices. *Theor. Math. Phys.*, 2003, **135** (3), P. 849–871.

[17] Mogilner A.I. Hamiltonians in solid state physics as multiparticle discrete Schrödinger operators: problems and results. *Advances in Sov. Math.*, 1991, **5**, P. 139–194.

[18] Reed M., Simon B. *Methods of modern mathematical physics. IV: Analysis of Operators*. Academic Press, New York, 1979.

[19] Malishev V.A., Minlos R.A. *Linear infinite-particle operators*. Translations of Mathematical Monographs. 143, AMS, Providence, RI, 1995.

[20] Minlos R.A., Spohn H. The three-body problem in radioactive decay: the case of one atom and at most two photons. *Topics in Statistical and Theoretical Physics. Amer. Math. Soc. Transl.*, 1996, **177** (2), AMS, Providence, RI, P. 159–193.

[21] Friedrichs K.O. *Perturbation of spectra in Hilbert space*. Amer. Math. Soc. Providence, Rhole Island, 1965.

[22] Rasulov T.H., Dilmurodov E.B. Threshold analysis for a 2×2 operator matrix. *Nanosystems: Physics, Chemistry, Mathematics*, 2019, **10** (6), P. 616–622.

[23] Rasulov T.H., Dilmurodov E.B. Eigenvalues and virtual levels of a family of 2×2 operator matrices. *Methods of Functional Analysis and Topology*, 2019, **25** (3), P. 273–281.

NANOSYSTEMS: PHYSICS, CHEMISTRY, MATHEMATICS, 2020, 11 (2), P. 145–152

Particle transport in a network of quantum harmonic oscillators

J. R. Yusupov[1], Kh. Sh. Matyokubov[2], K. K. Sabirov[3]

[1]Turin Polytechnic University in Tashkent, 17 Niyazov Str., 100095, Tashkent, Uzbekistan

[2]Urgench State University, 14 H. Olimjon Str., 220100, Urgench, Uzbekistan

[3]Tashkent University of Information Technologies, 108 Amir Temur Str., 100200, Tashkent Uzbekistan

jambul.yusupov@gmail.com

PACS 03.65.Aa, 02.60.Cb, 05.60.Gg **DOI 10.17586/2220-8054-2020-11-2-145-152**

In this paper, we address the problem of a particle dynamics in a network of quantum harmonic oscillators by solving the stationary Schrödinger equation on metric graphs in the presence of harmonic oscillator potential with bond-dependent frequency. Particle transport is analyzed by considering wave packet dynamics in such a system modeled in terms of quantum graph.

Keywords: quantum graph, harmonic oscillator, particle transport, wave packet dynamics.

Received: 13 February 2020

Revised: 24 February 2020

1. Introduction

Quantum transport in low-dimensional branched structures and networks is of importance for a broad variety of problems in condensed matter physics, polymers, optics and biophysics. For of sub-micron scales, particle and wave dynamics in networks can be described in terms of so-called quantum graphs. The latter is a set of quantum wires connected to each other at the nodes (vertices) according to a rule, which is called the topology of a graph. Recently quantum graphs have attracted much attention in the contexts as powerful model for studying quantum transport in low-dimensional branched systems. Initially, quantum mechanical description of particle transport in networks dates back to Refs. [1, 2], where electron motion in organic molecules was studied. Strict formulation of quantum graph concept was first introduced by Exner, Seba and Stovicek to describe free quantum motion on branched wires [3]. Later, Kostrykin and Schrader derived the general boundary conditions providing self-adjointness of the Schrödinger operator on graphs [4]. Earlier, the quantum graph concept was applied to microwave optical fiber networks [5], quantum chaos theory [6–8] and condensed matter physics [9, 10]. Relativistic quantum mechanics described by Dirac [11] and Bogoliubov-de Gennes operators [12] on graphs have been studied recently. Very recent application of quantum graphs to optical network lasers (LANER) problem can be found in the Ref. [13]. The problem for designing of transparent quantum graphs has been discussed in [14, 15]. A version of PT-symmetric quantum graph was introduced in [16]. Tunable transport in quantum graphs has been studied in [17, 18]. Different aspects of the linear and nonlinear wave equations on metric graphs are considered in the Refs. [19–28].

Here, we address the problem of a particle dynamics in a network of quantum harmonic oscillators by solving the stationary Schrödinger equation on metric graphs in the presence of harmonic oscillator potential with bond-dependent frequency. To solve Schrödinger equation on harmonic oscillator network we impose for confined harmonic oscillator wave functions the vertex boundary conditions providing continuity of wave function and Kirchhoff rule at the vertex. Such boundary conditions lead to spectral equations in the form of transcendental algebraic equation.

Network of quantum harmonic oscillators can be used for modeling of vibrations and oscillations in discrete or branched systems, such as crystal lattices, molecular chains, polymers, etc. [5,9,10]. Also, since crystal lattices can be considered as branched structures, one can use quantum harmonic oscillator network for modeling lattice vibrations in solid state. Our approach for the study of quantum harmonic oscillator network is based on considering it as a set of confined harmonic oscillators connected at vertices. Confined, or bounded harmonic oscillator presents parabolic potential given at finite interval (see, Fig.1). Quantum mechanical bounded oscillator was studied earlier in detail in the Refs. [29–31]. Main motivation for the study of network of quantum harmonic oscillators comes from their potential applications in the physics of conducting polymers, where polymer chain (e.g., in polyacetylene) can be considered as a branched structure, where lattice of the chain forms graph. Charge carriers in such structure are localized (trapped) near one bond of the lattice. Depending on the type of exciton the trapping potential well can be different. For all cases, such a well has a cutoff near the branching point. If one also considers lattice vibrations, most realistic form of the well can be in the form of harmonic oscillators. Thus, exciton moving along the polymer chain behaves itself as a particle moving in the quantum harmonic oscillator network.

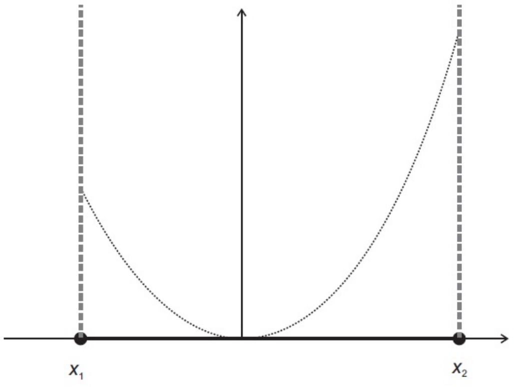

FIG. 1. Parabolic potential given at finite interval

This paper is organized as follows. In the next section, we will provide a brief description of the corresponding problem on a finite interval, i.e., particle dynamics in confined quantum harmonic oscillator potential well. Section 3 presents description of the main problem, quantum harmonic oscillator network. Section 4 provides some concluding remarks.

2. Confined quantum harmonic oscillator

Before discussing harmonic oscillator network, we briefly recall the problem of confined quantum harmonic oscillator described by harmonic oscillator potential on a finite interval. Consider a quantum particle confined in a 1D box $[x_1, x_2]$ under influence of harmonic potential. Such potential represent parabolic well with the cut-off on the box walls. The Hamiltonian of the system can be written as (in the units $\hbar = m = 1$):

$$H = -\frac{1}{2}\frac{d^2}{dx^2} + \frac{1}{2}\omega^2 x^2. \tag{1}$$

Complete solution of the time-independent Schrödinger equation

$$H\phi = E\phi \tag{2}$$

can be written in terms of the confluent hypergeometric function of the first kind:

$$\phi(x) = \exp\left(-\frac{1}{2}\omega x^2\right)\left[AM\left(\frac{1}{4} - \frac{E}{2\omega}; \frac{1}{2}; \omega x^2\right) + B\omega^{\frac{1}{2}} x M\left(\frac{3}{4} - \frac{E}{2\omega}; \frac{3}{2}; \omega x^2\right)\right], \tag{3}$$

where A and B are constants and $M(\cdot;\cdot;\cdot)$ is the Kummer's function.

The boundary conditions $\phi(x_1) = \phi(x_2) = 0$ result in a system of linear algebraic equations with respect to coefficients A and B:

$$\mathbf{h}(E)\begin{pmatrix} A \\ B \end{pmatrix} = 0, \tag{4}$$

where

$$\mathbf{h}(E) = \begin{pmatrix} M\left(\frac{1}{4} - \frac{E}{2\omega}; \frac{1}{2}; \omega x_1^2\right) & \omega^{1/2} x_1 M\left(\frac{3}{4} - \frac{E}{2\omega}; \frac{3}{2}; \omega x_1^2\right) \\ M\left(\frac{1}{4} - \frac{E}{2\omega}; \frac{1}{2}; \omega x_2^2\right) & \omega^{1/2} x_2 M\left(\frac{3}{4} - \frac{E}{2\omega}; \frac{3}{2}; \omega x_2^2\right) \end{pmatrix}. \tag{5}$$

Existence of the non-trivial solutions of the above algebraic system leads to the following secular equation with respect to E:

$$\det(\mathbf{h}(E)) = 0. \tag{6}$$

Roots of this equation give the eigenvalues of the confined quantum harmonic oscillator. In Fig. 2 the first few eigenvalues obtained in this way are plotted for the parameters $\omega = 1$, $x_1 = 0$, $x_2 = 5$. It is clear that when the size of the box is very large, the eigenvalues coincide with those of bulk (unbound) harmonic oscillator becoming equidistant.

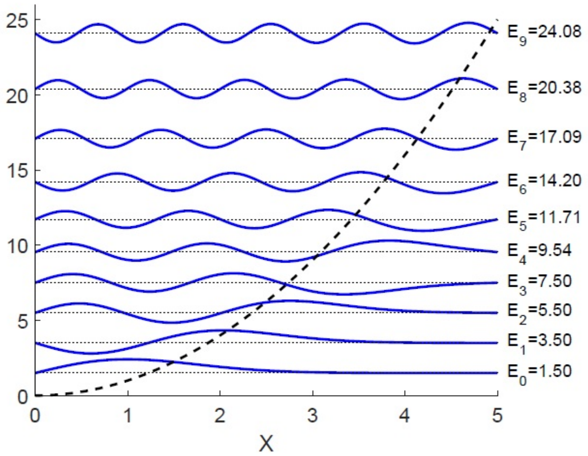

FIG. 2. Oscillator potential (dashed line), energy levels (dotted line) and corresponding eigenfunctions (solid line) for $\omega = 1$ and $x \in [0, 5]$

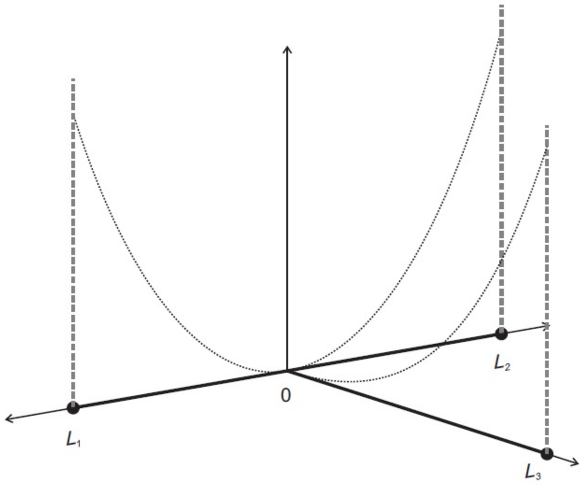

FIG. 3. Considered case: Harmonic oscillators on a star graph with 3 bonds

3. Harmonic oscillator on a star graph

The system we are interested to study is a network of quantum harmonic oscillators. Since a star graph can be considered as a building block for any complex networks we limit our study to the simplest graph topology, a star graph presented in Fig. 3. In the absence of external time-dependent forces, such system can be described by the stationary Schrödinger equation on metric graphs that includes harmonic oscillator potential, which is given as (in the units $\hbar = m = 1$):

$$\left[-\frac{1}{2}\frac{d^2}{dx^2} + \frac{1}{2}\omega_j^2 x^2\right]\phi_j = E\phi_j, \tag{7}$$

where ϕ_j is the wave function of jth bond and (in general) $j = 1, 2, 3, ...N$.

The vertex boundary conditions for a star graph are imposed as the wave function continuity [6]:

$$\phi_1|_{x=0} = \phi_2|_{x=0} = \cdots = \phi_N|_{x=0}, \tag{8}$$

and current conservation [6]:

$$\sum_{j=1}^{N} \frac{d\phi_j}{dx}\bigg|_{x=0} = 0. \tag{9}$$

TABLE 1. The first 20 energy levels of the star graph in Fig. 4

n	0	1	2	3	4
E_n	0.70710	2.12132	2.12132	3.53554	4.94981
n	5	6	7	8	9
E_n	4.94993	6.36492	7.78123	7.78573	9.21454
n	10	11	12	13	14
E_n	10.65426	10.70381	12.20934	13.74315	13.95672
n	15	16	17	18	19
E_n	15.62432	17.32891	17.82647	19.68142	21.57984

The boundary conditions at the bond edges can be imposed as Dirichlet ones:

$$\phi_j|_{x=L_j} = 0, \tag{10}$$

where L_j are the bond lengths.

Solution of Eq. (7) can be written as

$$\phi_j(x) = \exp\left(-\frac{1}{2}\omega_j x^2\right)\left[A_j M\left(\frac{1}{4}-\frac{E}{2\omega_j},\frac{1}{2},\omega_j x^2\right) + B_j\omega_j^{1/2} x M\left(\frac{3}{4}-\frac{E}{2\omega_j},\frac{3}{2},\omega_j x^2\right)\right], \tag{11}$$

where A_j and B_j are the constants to be found from normalization conditions and $M(\cdot;\cdot;\cdot)$ is the confluent hypergeometric function. From the boundary conditions given by Eqs. (8)–(10) one can find energy eigenvalues, E_n and constants, A_j and B_j.

The continuity condition (8) leads to:

$$A_1 = A_2 = \cdots = A_N := A. \tag{12}$$

From the current conservation condition given by Eq. (9) we have

$$\sum_{j=1}^{N} B_j\omega_j^{1/2} = 0. \tag{13}$$

Finally, from the Dirichlet boundary conditions on the bonds edges, Eq. (10) we get the following system of linear algebraic equations with respect to coefficients A and B_j, $(j = 1, 2, ..., N)$:

$$\mathbf{h}(E)\begin{pmatrix} A \\ B_1 \\ \vdots \\ B_N \end{pmatrix} = 0, \tag{14}$$

where

$$\mathbf{h}(E) = \begin{pmatrix} 0 & \omega_1^{1/2} & \omega_2^{1/2} & \dots & \omega_N^{1/2} \\ \mu_1 & \eta_1 & 0 & \dots & 0 \\ \mu_2 & 0 & \eta_2 & \dots & 0 \\ \vdots & \vdots & \vdots & \ddots & \vdots \\ \mu_N & 0 & 0 & \dots & \eta_N \end{pmatrix} \tag{15}$$

with $\mu_j = M\left(\frac{1}{4}-\frac{E}{2\omega_j},\frac{1}{2},\omega_j L_j^2\right)$ and $\eta_j = \omega_j^{1/2} L_j M\left(\frac{3}{4}-\frac{E}{2\omega_j},\frac{3}{2},\omega_j L_j^2\right)$.

Existence of non-trivial solutions of this system yields the following secular equation:

$$\det(\mathbf{h}(E)) = 0. \tag{16}$$

The first ten eigenfunctions are plotted in Fig.4 and the first twenty energy levels are presented in Table 1. Calculations have been done for $N = 3$ and parameters $\omega_1 = \omega_2 = \omega_3 = 1$ and $L_1 = 5.31$, $L_2 = 5.53$, $L_3 = 5.18$. Bond lengths of the star graph have been chosen such in order to avoid degeneracy in numerical calculations. Although the energy grows by growing of n, unlike to usual harmonic oscillator, the levels are not equidistant. Moreover, the level spacing distances are strongly non-uniform for such a system.

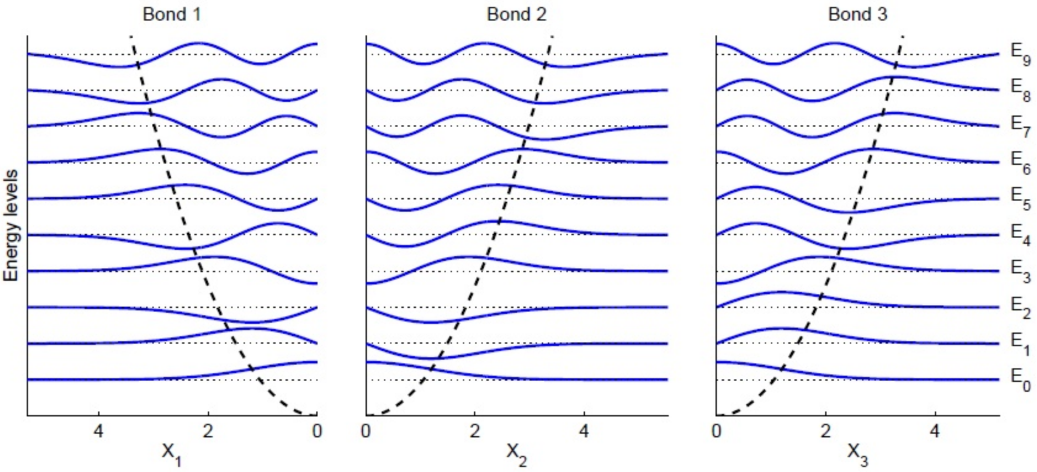

FIG. 4. Oscillator potential (dashed line), energy levels (dotted line) and corresponding eigenfunctions (solid line) for $\omega_1 = \omega_2 = \omega_3 = 1$ and $L_1 = 5.31$, $L_2 = 5.53$, $L_3 = 5.18$. The three columns correspond to the bonds of the star graph. The x-coordinate of the first arm is reversed

Having found eigenfunctions and eigenvalues of such a network, one can study particle transport in it by considering wave packet dynamics. This means that one needs to solve the time-dependent Schrödinger equation (in the units $\hbar = m = 1$) given as:

$$i\frac{\partial}{\partial t}\Psi_j(x,t) = \left(-\frac{1}{2}\frac{\partial^2}{\partial x^2} + \frac{1}{2}\omega_j^2 x^2\right)\Psi_j(x,t),\ j = 1,2,3. \tag{17}$$

The wave function of the system can be written in terms of the complete set of eigenfunctions as:

$$\Psi_j(x,t) = \sum_n c_n e^{-iE_n t}\phi_{j,n}(x), \tag{18}$$

where $\phi_{j,n}(x)$ and E_n are given by Eqs. (11) and (16). Wave packet dynamics can be studied by imposing initial condition in the form of Gaussian wave packet given by:

$$f(x) = \frac{1}{d\sqrt{\pi}}\exp\left[-\frac{(x-x_0)^2}{2d^2} + iv_0 x\right], \tag{19}$$

and determining expansion coefficients, c_n in terms of $f(x)$ as

$$c_n = \sum_j \int_0^{L_j} \phi_{j,n}^*(x) f(x) dx. \tag{20}$$

In the following numerical calculations, we consider quantum star graph with bond lengths $L_1 = 5.31$, $L_2 = 5.53$, $L_3 = 5.18$ and Gaussian wave packet initially located in the first bond at $x_0 = L_1/2$ at rest, that is with initial group velocity $v_0 = 0$ and width $d = L_1/10$. This setup can be approximated by choosing expansion coefficients in the form:

$$c_n = \int_0^{L_1} \phi_{1,n}^*(x) f(x) dx.$$

Then, the numerical solution requires to limit the number of expansion terms. In our calculations, we limit ourselves to 300 terms, which have been enough for controlling the deviation from unity in the normalization condition,

$$\sum_n |C_n|^2 = 1.$$

Thus, space-time evolution of Gaussian wave packet in a network of quantum harmonic oscillators having similar (for all bonds) frequencies is plotted in Fig. 5. Fig. 6 presents similar plots for the case when frequencies of harmonic oscillators are different for different bonds: $\omega_1 = 1$, $\omega_2 = 2$, $\omega_3 = 3$. As it can be seen from these plots, dispersion of the wave packet is much stronger in the case of different frequencies.

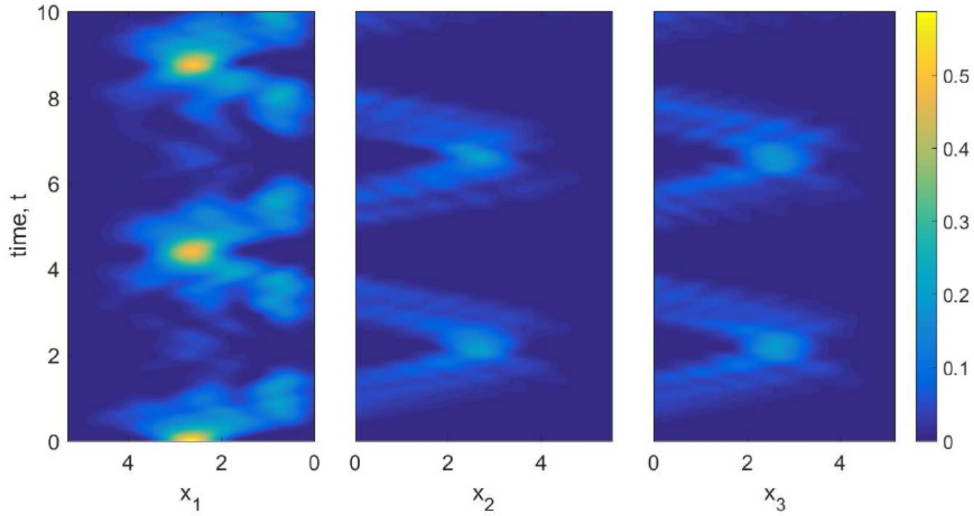

FIG. 5. Space-time evolution of Gaussian wave packet in a network of quantum harmonic oscillators. Frequencies of oscillators in all bonds are equal: $\omega_1 = \omega_1 = \omega_3 = 1$

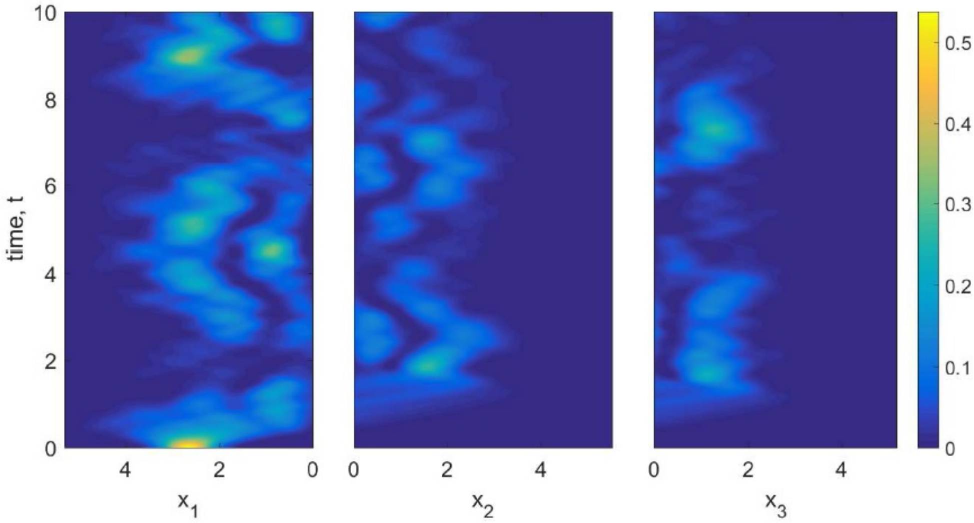

FIG. 6. Space-time evolution of Gaussian wave packet in a network of quantum harmonic oscillators for frequencies, $\omega_1 = 1, \omega_2 = 2, \omega_3 = 3$

An important characteristics of the particle and wave transport in quantum graphs is probability current. Current on each bond of the graph is given by:

$$J_j(x,t) = \frac{i}{2}\left[\Psi_j(x,t)\frac{\partial \Psi_j^*(x,t)}{\partial x} - \frac{\partial \Psi_j(x,t)}{\partial x}\Psi_j^*(x,t)\right]. \tag{21}$$

In Fig. 7 and Fig. 8 time-dependence of current on each bond is plotted for the cases presented in Fig. 5 and Fig. 6, respectively.

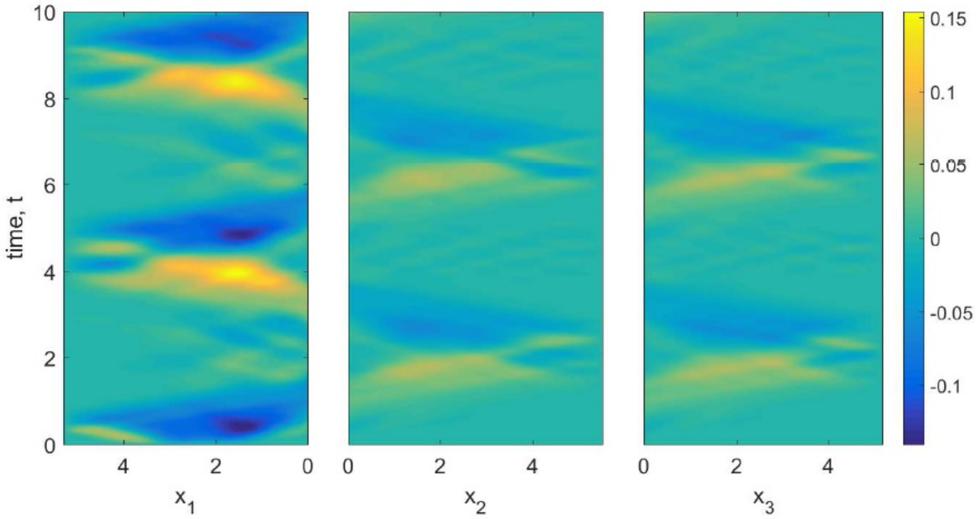

FIG. 7. Time-dependence of the current for equal frequencies, $\omega_1 = 1, \omega_2 = 1, \omega_3 = 1$

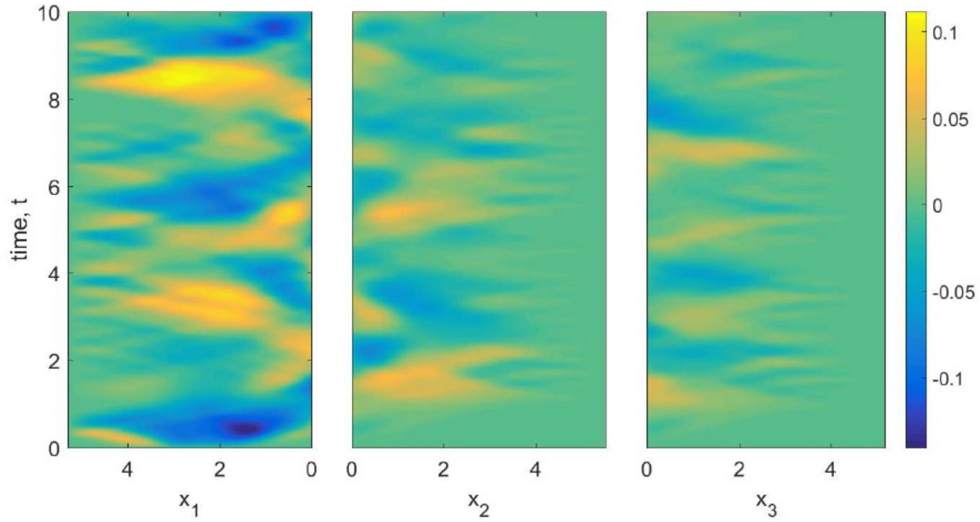

FIG. 8. Time-dependence of the current. Frequencies of oscillators are different: $\omega_1 = 1, \omega_2 = 2$, $\omega_3 = 3$

4. Conclusions

In this paper we studied quantum harmonic oscillator network with the focus on energy spectrum and particle transport. The system is modeled in terms of the stationary Schrödinger equation on metric graphs by imposing continuity and current conservation boundary conditions at the graph nodes. The energy spectrum is calculated numerically from the secular equation following from the vertex boundary conditions. Particle transport is studied by analyzing the evolution of Gaussian wave packet at different parameters and spatio-temporal evolution of the current on each bond of the graph. The model can have practical application in different systems arising in condensed matter physics and polymers. In condensed matter, the realization of the model comes from the fact that crystal lattices can be considered as branched structures, where the atoms in the lattice nodes exhibit harmonic vibrations. Such structure can be considered as a network of quantum harmonic oscillators. Very attractive application of the model is related to charge carrier transport in conducting polymers [32–38]. These latter can be considered as a network, where each branch is affected by external confining potential, which makes particle motion localized. Then the charge transport along such a network of potential wells will be reduced to its traveling from one well to another one.

References

[1] Pauling L. The Diamagnetic Anisotropy of Aromatic Molecules, *J. Chem. Phys.*, 1936, **4**, P. 673.

[2] Ruedenberg K. and Scherr C.W. Free-Electron Network Model for Conjugated Systems. I. Theory, *J. Chem. Phys.*, 1953, **21** P. 1565.

[3] Exner P. and Seba P. Free quantum motion on a branching graph. *Rep. Math. Phys.*, 1989, **28**(1) P. 26.

[4] Kostrykin R. and Schrader R. Kirchhoff's rule for quantum wires. *J. Phys. A: Math. Gen.*, 1999, **32**, P. 595.

[5] Hul O., Bauch S., Pakonski P., Savytskyy N., Zyczkowski K. and Sirko L. Experimental simulation of quantum graphs by microwave networks, *Phys. Rev. E*, 2004, **69**, P. 056205.

[6] Kottos T. and Smilansky U. Periodic Orbit Theory and Spectral Statistics for Quantum Graphs. *Ann.Phys.*, 1999, **274**(1), P. 124.

[7] Gnutzmann S. and Smilansky U. Quantum graphs: Applications to quantum chaos and universal spectral statistics. *Adv.Phys.*, 2006, **55**(5-6) P. 527–625.

[8] Gnutzmann S., Keating J.P. and Piotet F. Eigenfunction statistics on quantum graphs. *Ann.Phys.*, 2010, **325**(12) P. 2595–2640.

[9] Goldman N. and Gaspard P. Quantum graphs and the integer quantum Hall effect, *Phys. Rev. B*, 2008, **77**, P. 024302.

[10] Russo A., Barnes E., Economou S.E. Photonic graph state generation from quantum dots and color centers for quantum communications, *Phys. Rev. B*, 2018, **98**, P. 085303.

[11] Bolte J. and Harrison J. The spin contribution to the form factor of quantum graphs. *J. Phys. A: Math. Gen.*, 2003, **36**, P. L433.

[12] Sabirov K., Yusupov J., Jumanazarov D., Matrasulov D. Bogoliubov de Gennes equation on metric graphs. *Phys. Lett. A*, 2018, **382**, P. 2856.

[13] Giacomelli G., Lepri S., Trono C. Optical networks as complex lasers, *Phys. Rev. A*, 2019, **99**, P. 023841.

[14] Yusupov J.R., Sabirov K.K., Ehrhardt M. and Matrasulov D.U. Transparent quantum graphs. *Phys. Lett. A*, 2019, **383**, P. 2382.

[15] Aripov M.M., Sabirov K.K., Yusupov J.R. Transparent vertex boundary conditions for quantum graphs: simplified approach. *Nanosystems: physics, chemistry, mathematics*, 2019, **10**(5), P. 501–602.

[16] Matrasulov D.U., Sabirov K.K. and Yusupov J.R. PT-symmetric quantum graphs. *J. Phys. A: Math. Gen.*, 2019, **52**, P. 155302.

[17] Yusupov J., Dolgushev M., Blumen A. and Mülken O. Directed transport in quantum star graphs. *Quantum Inf Process*, 2016, **15**, P. 1765.

[18] Yusupov J. Tunable wave packet transport in branched periodic lattices with time-dependent external field. *Nanosystems: physics, chemistry, mathematics*, 2017, **8**(1), P. 42–47.

[19] Naimark K. and Solomyak M. Eigenvalue estimates for the weighted Laplacian on metric trees. *Proc. London Math. Soc.*, 2000, **80**, P. 690.

[20] Keating J.P. Fluctuation statistics for quantum star graphs. Quantum graphs and their applications. *Contemp. Math.*, 2006, **415**, P. 191–200.

[21] Harrison J.M., Smilansky U. and Winn B. Quantum graphs where back-scattering is prohibited. *J. Phys. A: Math. Gen.*, 2007, **40**, P. 14181.

[22] Exner P. and Lipovský J. On the absence of absolutely continuous spectra for Schrödinger operators on radial tree graphs. *J. Math. Phys.*, 2010, **51**, P. 122107.

[23] Berkolaiko G., Kuchment P. *Introduction to Quantum Graphs, Mathematical Surveys and Monographs*, AMS, 2013.

[24] Mugnolo D. *Semigroup Methods for Evolution Equations on Networks*. Springer-Verlag, Berlin, 2014.

[25] Kurasov P., Ogik R. and Rauf A. On reflectionless equi-transmitting matrices. *Opuscula Math.*, 2014, **34**, P. 483.

[26] P. Exner and H. Kovarik, *Quantum waveguides*. Springer, 2015.

[27] Joly P., Kachanovska M. and Semin A. Wave propagation in fractal trees. Mathematical and Numerical Issues. *hal-01801394*, 2018.

[28] Yusupov J.R., Sabirov K.K., Ehrhardt M. and Matrasulov D.U. Transparent nonlinear networks. *Phys. Rev. E*, 2019, **100**, P. 032204.

[29] Aquino N. The isotropic bounded oscillators. *J. Phys. A: Math. Gen.*, 1997, **30**(7) P. 2403.

[30] Stevanović L. and Sen K.D. Eigenspectrum properties of the confined 3D harmonic oscillator. *J. Phys. B: At.Mol.*, 2008, **41** P. 225002.

[31] Amore P. and Fernández F.M. One-dimensional oscillator in a box. *Eur. J. Phys.*, 2010, **31**, P. 69.

[32] Rice M.J., Gartstein Yu.N. Excitons and Interband Excitations in Conducting Polymers Based on Phenylene. *Phys. Rev. Lett.*, 1994, **73**, P. 2504.

[33] Brazovskii S., Kirova N., Bishop A.R. Theory of electronic states and excitations in PPV. *Opt. Mat.*, 1998, **9** P. 465–471.

[34] Moses D., Wang J., Heeger A.J., Kirova N., Brazovski S. Electric field induced ionization of the exciton in poly(phenylene vinylene). *Synth. Met.*, 2001, **119**, P. 503.

[35] Kirova N., Brazovskii S. Optical and electrooptical absorption in conducting polymers. *Thin Solid Films*, 2002, **403**, P. 419.

[36] Kirova N., Brazovskii S. Conjugated polymers at the verge of strongly correlated systems and 1d semiconductors, *Synth. Met.*, 2004, **141**, P. 139.

[37] Kirova N., Brazovskii S. Electronic interactions and excitons in conducting polymers, *Current Appl. Phys.*, 2004, **4** P. 473–478.

[38] Kobrak M.N., Bittner E.R. A dynamic model for exciton self-trapping in conjugated polymers. I. Theory, *J. Chem. Phys.*, 2000, **112** P. 5399.

NANOSYSTEMS: PHYSICS, CHEMISTRY, MATHEMATICS, 2020, 11 (2), P. 153–160

Model of destruction of montmorillonite crystal structure in a microwave field

V. N. Makarov*, O. N. Kanygina
Orenburg State University, Victory Ave. 13, Orenburg, 460018, Russia
*makarsvet13@gmail.com

PACS 61.43.Er **DOI 10.17586/2220-8054-2020-11-2-153-160**

We address amorphization of montmorillonite crystal structure. Powdered montmorillonite samples with an effective particle diameter $D \leq 630\,\mu m$ were treated by microwave field with the frequency 2.45 GHz and power 750 W for ten minutes in different environments. The first sample was treated in an air environment, the second one in a humid environment. The third sample was a ceramic mass with 10% concentration of mixing water (with respect to the total mass). The model describing amorphization is based on results of X-ray analysis. Activation energies were evaluated for covalently and ionically bound oxygen ions, hydroxyl groups, and silicon (aluminum) ions. It is shown that the amorphization is carried out in four stages. In fractions of the energy consumption of the last stage the first one consumes $7 \div 9\%$, the second one takes $13 \div 15\%$, and the third one takes $49 \div 59\%$.

Keywords: model, amorphization, crystal structure, montmorillonite, microwave field.

Received: 26 December 2019

Revised: 4 March 2020

1. Introduction

High frequency electromagnetic field treatment is a new approach to modifications of structure of non-organic materials [1–3]. Structure changes of nature-occurring aluminosilicates are of a special interest as aluminosilicates are widely considered to be a perspective raw material for production of new functional materials via microwave field treatment [4]. Recently montmorillonite-containing and montmorillonite clays were used as raw products for new fictional materials. For dioctahedral aluminuos smectites the corresponding chemical formula reads:

$$(\mathrm{Al}_{2-y}\mathrm{Mg}_y)(\mathrm{Si}_{4-x}\,\mathrm{Al}_x)\mathrm{O}_{10}(\mathrm{OH})_2\,\mathrm{E}_{x+y}\cdot n\mathrm{H}_2\mathrm{O}, \quad \text{if } y > x,$$

then the smectite is called montmorillonite. Its particles are nature-occurring two-dimensional nanoparticles sensitive to structural changes which makes them suitable for various realizations of structure evolution. Montmorillonite unite cell with an iron ion occupying one of oxygen octahedra (which is a common feature for Orenburg region clays) is presented on Fig. 1 [5].

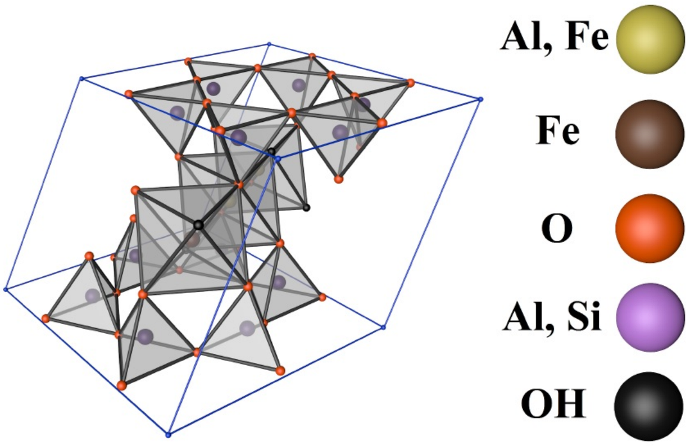

FIG. 1. The unit cell of montmorillonite. Aluminum and iron ions are located in centers of oxygen octahedra; aluminum and silicon ions are located in centers of oxygen tetrahedra. At vertices of oxygen octahedra, a hydroxyl group may be located

Adsorption, interplanar, and lattice (the hydroxyl group in the lattice) waters are of a special interest for study of montmorillonite structure evolution. Results of the previous thermodynamic studies point to sophisticated interactions between montmorillonite particles and water which are indicated by three endothermic effects associated with the extraction of water of various types. Adsorption water molecules are placed at the boundary of crystal particles and the mechanism responsible for their extraction due to heating, also known as the first endothermic effect, is well-studied both theoretically and empirically [6]. Interplanar water molecules are placed between neutral layers of the lattice. The correspondent activation mechanism, also known as the second endothermic effect, is also well-studied. For instance, in paper [7], a model was studied which is capable to connect the dehydration temperature, positions of Al^{3+} ions, and their transitions to different parts of oxygen octahedra. The model successfully describes the second endothermic effect.

The lattice water which is a hydroxyl group located within the montmorillonite unit cell is of a special interest. Extraction of hydroxyl groups from montmorillonite unite cells is called the third endothermic effect. In paper [8], the influence of a 10-minute-long microwave field irradiation on morphology and phase structure of montmorillonite clays was studied. The particle dispersion effect was found which enhances system adsorption features while keeping the phase structure almost unaffected. The description of enhanced adsorption properties of layered aluminosilicates (montmorillonite and kaolin) was given in papers [9, 10]. Further study of the third endothermic effect induced by the microwave treatment is relevant, as it allows one to predict montmorillonite clays adsorption features and to design functional materials with enhanced adsorption properties.

In paper [11], it was proven empirically that the degree of montmorillonite amortization is defined by conditions of the high-frequency microwave field treatment. Namely, the microwave treatment of powdered samples resulted in a few effects. Firstly, the intensity of diffraction peaks is decreased. Secondly, interplanar distances of montmorillonite lattice are also decreased due to extraction of water molecules located in between three-layered packages of crystal plane. The present paper presents an attempt to evaluate and to visualize amorphization (destruction) of the montmorillonite crystal structure (the unit cell) after the third endothermic effect.

2. Materials and experiments

We use empirical data about destruction of montmorillonite lattice induced by a microwave field treatment for the sake of illustration. A more detailed discussion of these results can be found in [11]. The object of the empirical study was a nature-occurring montmorillonite clay, its chemical composition is discussed in [12]. Powdered samples (P0) were subjected to 10-minute-long microwave treatment (frequency is 2.45 GHz, power is 750 W) in various conditions. In the first case (P1) 10mm thick powdered sample was placed in a vessel and treated in an aerobic environment. In the second case the sample (P2) was treated in a humid environment (the partial pressure of the water vapor was increased a factor 2). The third sample (P3) was a uniform soft mud consisting of the same clay minerals and 10% (in mass) of mixing water. The diffractogram peaks were measured with DROM-3M apparatus in the refraction regime (Bragg-Brentano geometry) via $\mathrm{CuK}\alpha$ radiation with the angular velocity 1 angular degree/min. The particles effective diameter is $D \leq 630\,\mu m$. As a result, it was established that the montmorillonite unit cell is destroyed and the intensity of the process is defined by the conditions of the experiment. Values of interplanar distances d and the correspondent diffraction peak intensities I are given in Table 1. In the first column the diffractogram line numbers are given (Fig. 2).

TABLE 1. Structural changes in the crystal structure of montmorillonite induced by the radiation treatment [11]

No.	**hkl**	**P0**		**P1**		**P2**		**P3**	
		d, nm	**I, %**	**d, nm**	**I, %**	**d, nm**	**I, %**	**d, nm**	**I, %**
1	001	1.22	100	1.08	80	0.95	70	1.41	70
2	100	0.51	20	0.51	10	-	0	-	0
3	110, 020	0.44	80	0.44	30	0.44	30	0.44	30
4	002	0.32	60	0.32	40	0.31	20	0.32	30
5	200, 130	0.26	80	0.26	50	0.25	30	0.25	10
6	210	0.25	40	-	0	-	0	-	0
7	003	0.21	30	0.21	10	-	0	0.21	20
8	300, 222	0.17	70	0.17	30	0.17	20	0.17	30
9	310, 142	0.17	70	0.17	50	-	0	0.17	20
10	060, 213	0.15	80	0.15	50	0.15	10	0.15	20

Lined diffraction patterns for all samples are given on Fig. 2, where we present 9 out of 10 diffractogram lines for sample P0. They are required for a study of montmorillonite lattice destruction. For sample P1 8 out 10 lines are given (plane (210) vanishes) that can be observe in the discussed range. For sample P2 5 lines are presented (planes (100), (210), (003), and (310,142) vanish). For sample P3 7 out 10 lines are presented (planes (100) and (210) vanish).

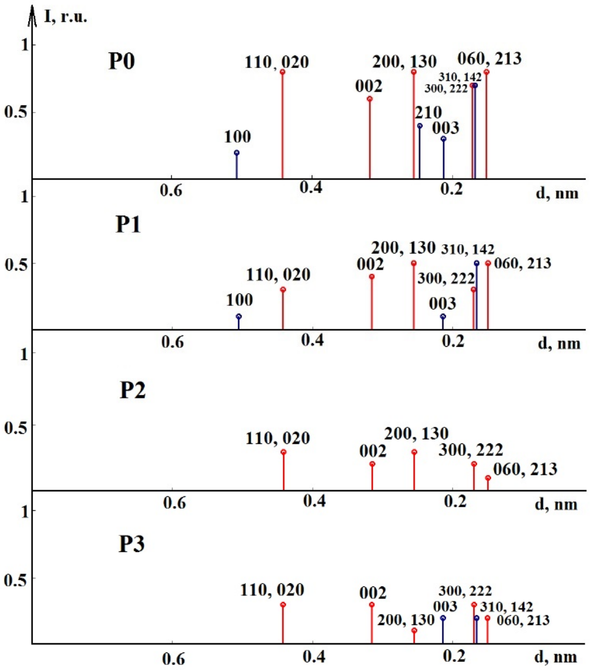

FIG. 2. Diffraction patterns for P0, P1, P2, and P3. After the microwave field irradiation, the following occurred: for sample P1, the intensity of diffraction maxima decreased and the plane (210) disappeared; for sample P2, the intensity of diffraction maxima decreased significantly and planes with indices (100), (210), (003), and (310,142) disappeared; for P3, the intensity of diffraction maxima decreased (and become comparable with sample P1) and planes (100) and (210) disappeared

3. Discussion of results

In order to describe amorphization (destruction) of the montmorillonite unit cell, it is necessary to evaluate the ions' bound energy with respect to various crystallographic directions. It is equal to the activation energy required by ions to be removed from the unit cell. Calculations were made for a unit cell in an equilibrium state. The evaluation method is based on a calculation of the activation energy for ions located within the crystal plane destroyed after the microwave irradiation(see Fig. 2). These energies were compared with the empirical data [11]. It should be noted, that we have found a rough estimation of the activation energy. This is due of the fact that the activation energy is a difference between the peak of an activation barrier and the energy of an initial state. The difference between the obtained estimation and the true activation energy can be up to a few orders of magnitude.

Preliminary results were presented in [13]. The activation energy required by a particle to leave the unit cell can be calculated with the linear muffin-tin orbitals in the strong coupling regime [14]. In the present paper an evaluation of the extraction activation energy for hydroxyl groups and other ions of the unit cell is given based on the aforementioned empirical data.

3.1. Extraction activation energy for the hydroxyl group and the oxygen atom

Evidence of amorphization can be found in samples P2 and P3 when the crystallographic plane (100) vanishes (Table 1, line No. 2). At this stage the hydroxyl group and the oxygen cation are removed from oxygen octahedra. Visualization of this amorphization stage presented on Fig. 3. Atoms that cross the plane and leave the crystal due to the high frequency electromagnetic field treatment are marked green.

Extraction activation energies for the hydroxyl group and the oxygen atom depend on the ion situated in the center of the oxygen octahedra:

$$\sum U_{Fe}(100) = \sum U_{Fe-O}(100) + \sum U_{Fe-OH}(100), \tag{1}$$

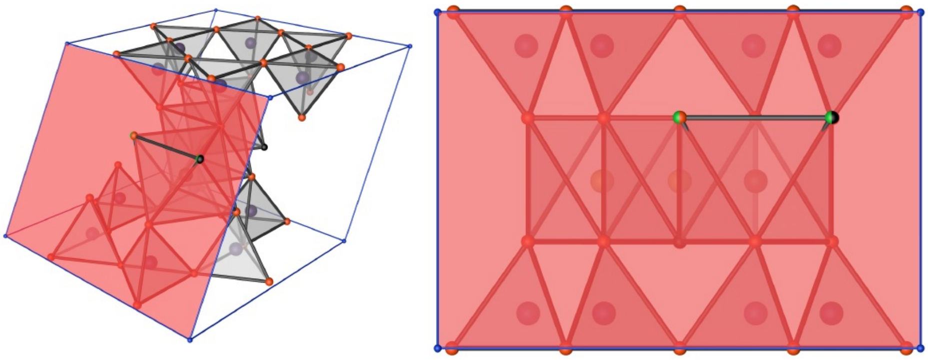

FIG. 3. The crystallographic plane (100) for the unit cell of montmorillonite (two projections)

$$\text{or } \sum U_{Al}(100) = \sum U_{Al-O}(100) + \sum U_{Al-OH}(100), \tag{2}$$

where $\sum U_{Fe}(100)$ s the extraction activation energy for the hydroxyl group and the oxygen ion when an *iron* ion is placed in the center of an oxygen octahedron;

$\sum U_{Al}(100)$ is the extraction activation energy for the hydroxyl group and the oxygen ion when an *aluminium* ion occupies the center of the oxygen octahedron.

Extraction activation energy of an oxygen when an *iron* ion occupies the center of an oxygen octahedron is given by the following expression:

$$\sum U_{Fe-O}(100) = \frac{U_{Fe-O(O)} + 2 \cdot E_{O-O(O)} + 2 \cdot E_{OH-O}}{5}, \tag{3}$$

where $E_{O-O(O)}$ is the bound energy between oxygen cations inside the oxygen octahedron;

E_{OH-O} is the bound energy between cations and the hydroxyl group;

$U_{Fe-O(O)}$ is the bound energy between an oxygen cation and the iron ion in an oxygen octahedron.

The bound energy between oxygen cations in an oxygen octahedron can be evaluated with approximate values defined in [15, 16, p. 221], so it reads $E_{O-O(O)} = 234.256$ kJ/mol. The bound energy between an oxygen ion and the hydroxyl group is obtained with approximate values given in [17], and it reads $E_{OH-O} = 20.287$ kJ/mol. The bound energy between an oxygen and the iron ions can be evaluated based on electronegativity [18]:

$$U_{Fe-O(O)} = \frac{1}{2} Z_{(O)} \cdot e \cdot N_a \cdot (\chi_O - \chi_{Fe})^2 = 740.662 \text{ kJ/mol}. \tag{4}$$

Here N_a is the Avogadro constant,

e is the electron charge,

$Z_{(O)}$ is the number of nearest neighbors,

χ_O is the oxygen electronegativity;

χ_{Fe} is the iron electronegativity.

The data was used to evaluate the iron activation energy via (3). The energy is $\sum U_{Fe-O}(100) = 249.950$ kJ/mol.

If an aluminum atom occupies the center of an oxygen octahedron, then the extraction activation energy for an oxygen ion is given by the following expression:

$$\sum U_{Al-O}(100) = \frac{U_{Al-O(O)} + 2 \cdot E_{O-O(O)} + 2 \cdot E_{OH-O}}{5}. \tag{5}$$

Here $U_{Al-O(O)}$ is the bound energy between oxygen and aluminum ions in an oxygen octahedron. The bound energy between an oxygen cation and the aluminum ion in the oxygen octahedron can be evaluated via electronegativity [18]:

$$U_{Al-O(O)} = \frac{1}{2} Z_{(O)} \cdot e \cdot N_a \cdot (\chi_O - \chi_{Al})^2 = 831.227 \text{ kJ/mol} \tag{6}$$

here $\chi_{Al} = 1.640$ is the iron electronegativity. Thus,

$$\sum U_{Al-O}(100) = 268.063 \text{ kJ/mol}.$$

If an iron ion is located in the center of an oxygen octahedron, the extraction activation energy for a hydroxyl group reads:

$$\sum U_{Fe-OH}(100) = \frac{E_{Fe-OH} + 4 \cdot E_{OH-O}}{5}. \tag{7}$$

Here E_{Fe-OH} is the bound energy between the hydroxyl group and the iron ion. The bound energy between the hydroxyl group and the iron ion can be obtained with the approximation data [15,19–21], so the energy reads $E_{Fe-OH} = 186.942$ kJ/mol. This allows one to obtain the energy given by (7) which reads $\sum U_{Fe-OH}(100) = 53.618$ kJ/mol.

If an aluminum ion is located in the center of an oxygen octahedron, the extraction activation energy for a thehydroxyl group is given by the following expression:

$$\sum U_{Al-OH}(100) = \frac{E_{Al-OH} + 4 \cdot E_{OH-O}}{5}. \tag{8}$$

Here E_{Al-OH} is the bound energy between the hydroxyl group and the aluminum ion. The bound energy between the hydroxyl group and the aluminum ion can be found via approximate data [15, 19, 20], thus it reads $E_{Al-OH} = 209.800$ kJ/mol. With these values, the energy (8) can be evaluated and reads $\sum U_{Al-OH}(100) = 58.190$ kJ/mol. Finally, extraction activation energies for a hydroxyl group and an oxygen cation in cases when an iron ion is located the center of an oxygen octahedron is given by (1) and reads $\sum U_{Fe}(100) = 303.568$ kJ/mol; in case when an aluminum ion occupies the place the energy is given by (2) and reads $\sum U_{Al}(100) = 326.253$ kJ/mol.

In a similar way, semi-quantitative calculations can be performed for bonds which then are destroyed within planes (100), (210), (003). When the activation energy for a hydroxyl group placed within (003) plane, it was assumed that $E_{OH-OH} \approx E_{OH-O}$ as the hydrogen bound can be neglected within the studied setup.

3.2. Intensity dynamics for lines No. 9 (310, 142) in P2

During the discussed stage of the experiment, oxygen cations are extracted from a tetrahedral ring within plane (142). During this stage planes (310) lose oxygen cations and cations of tetrahedral rings (aluminum and silicon) which results in strong crystal amorphization. Visualization of this stage presented on Fig. 4. These results are in agreement with the theoretical results, but they do not fit the extraction activation condition for ions in octahedral silicon packages [22].

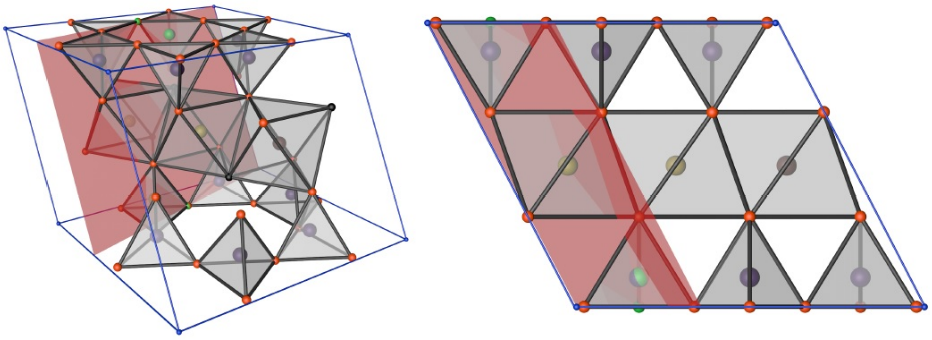

FIG. 4. The crystallographic plane (310) for the unit cell of montmorillonite (two projections)

Let us study the plane (310). Within an oxygen tetrahedron the extraction activation energy for oxygen cations and an ion reads:

$$\sum U^{Si}(310) = \sum U_{Si-O}(310) + \sum U_{Si}(310), \tag{9}$$

$$\text{or} \sum U^{Al}(310) = \sum U_{Al-O}(310) + \sum U_{Al}(310), \tag{10}$$

$$\text{or} \sum U^{Si,Al}(310) = \sum U_{Si-O,Al-O}(310) + \sum U_{Si,Al}(310). \tag{11}$$

Formulae (9) and (10) describe maximal and minimal values of the energy correspondingly.

When a *silicon* ion is located in the center of an oxygen tetrahedron the extraction activation energy for oxygen cations reads:

$$\sum U_{Si-O}(310) = 2 \cdot \frac{2 \cdot U_{Si-O(T)} + 6 \cdot E_{O-O(T)}}{8} = 482.235 \text{ kJ/mol}. \tag{12}$$

When an *aluminium* ion is located in the center of an oxygen tetrahedron the extraction activation energy for oxygen cations is:

$$\sum U_{Al-O}(310) = 2 \cdot \frac{2 \cdot U_{Al-O(T)} + 6 \cdot E_{O-O(T)}}{8} = 609.826 \text{ kJ/mol}. \tag{13}$$

Finally, when an *aluminium* ion occupies the center of one tetrahedron and a *silicon* ion occupies another, then the extraction activation energy of oxygen cations reads:

$$\sum U_{Si-O,Al-O}(310) = 2 \cdot \frac{U_{Si-O(T)} + U_{Al-O(T)} + 6 \cdot E_{O-O(T)}}{8} = 546.030 \text{ kJ/mol.} \tag{14}$$

Calculations of the extraction activation energy should account not only for ion bounds, but also for covalent bounds. Ratios [23] between metallic, ion, and covalent bounds that holds between the oxygen and the other elements were used. Thus, the covalent bound reads:

$$U^C_{Si(T)}(310) = \frac{100 \cdot U_{Si-O(T)}}{22,93} = 1303.838 \text{ kJ/mol,} \tag{15}$$

$$U^C_{Al(T)}(310) = \frac{100 \cdot U_{Al-O(T)}}{30,19} = 1835.546 \text{ kJ/mol.} \tag{16}$$

Here $U^C_{Si(T)}$ is the covalent bound energy for the silicon ion inside an oxygen tetrahedron.

$U^C_{Al(T)}$ is the covalent bound energy for the aluminum ion in an oxygen tetrahedron. The extraction activation energies for the (silicon or aluminum) ion inside an oxygen tetrahedron are given by the following formulae:

$$\sum U_{Si}(310) = 2 \cdot U^C_{Si(T)} = 2607.676 \text{ kJ/mol,} \tag{17}$$

$$\sum U_{Al}(310) = 2 \cdot U^C_{Al(T)} = 3671.092 \text{ kJ/mol,} \tag{18}$$

$$\sum U_{Si,Al}(310) = U^C_{Si(T)} + U^C_{Al(T)} = 3139.384 \text{ kJ/mol.} \tag{19}$$

Extraction activation energies for an oxygen cation and the (silicon or aluminum) ion inside an oxygen tetrahedron for formulae (9), (10), (11) read:

$$\sum U^{Si}(310) = 3089.911 \text{ kJ/mol,}$$

$$\text{or } \sum U^{Al}(310) = 4280.918 \text{ kJ/mol,}$$

$$\text{or } \sum U^{Si,Al}(310) = 3685.414 \text{ kJ/mol.}$$

The general value of the particle extraction activation energy for a unit cell within planes (310, 142) read:

$\sum U^{Si}(310, 142) = 3331.029$ kJ/mol is the ion extraction activation energy if a silicon ion is placed in an oxygen tetrahedron.

$\sum U^{Al}(310, 142) = 4845.831$ kJ/mol is the ion extraction activation energy if an aluminium ion is placed in an oxygen tetrahedron.

Maximal and minimal values of the ion extraction activation energy for planes (310, 142) depend on the position of ions within the montmorillonite lattice.

3.3. Maximal and minimal values of the ion extraction activation energy for planes (310, 142) depend on positions of ions within the montmorillonite lattice

Values of ion extraction activation energies for the studied planes are given in Tabel 2.

TABLE 2. Activation energies of ion extraction from crystallographic plane

Indices of the plane, (hkl)	Ions leaving the unit cell	The activation energy of ions, kJ/mol
100	O, OH	$304 \div 326$
210	O	$482 \div 610$
003	O, OH	$1948 \div 2260$
310, 142	O, (Si, Al)	$3331 \div 4586$

Results show that ion extraction activation energies for planes (100) and (210) are very close to each other. Destruction of planes (003) and (310,142) requires an increase of the energy by an order of magnitude. According to the X-ray diffraction data and to the numerical calculations the amorphization takes four stages. Visualization of these stages is given on Fig. 5–8.

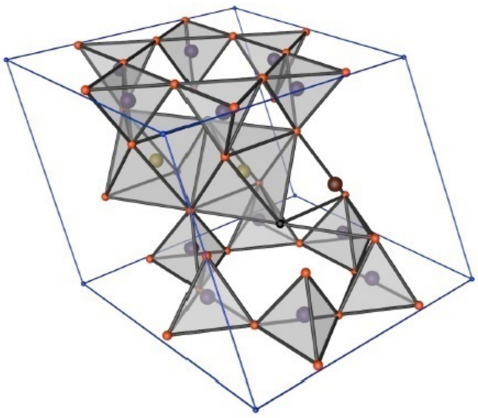

FIG. 5. The first stage of amorphization of the montmorillonite cell; ion activation at (100)

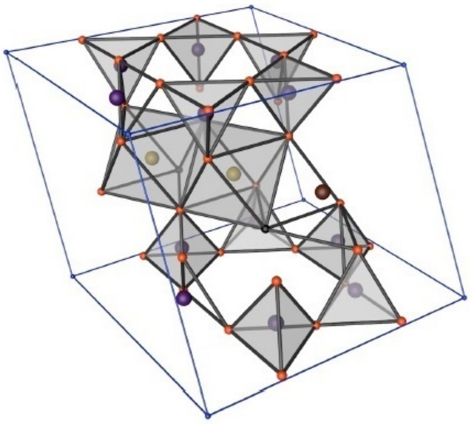

FIG. 6. The second stage of the amorphization of the montmorillonite cell; ion activation at (210)

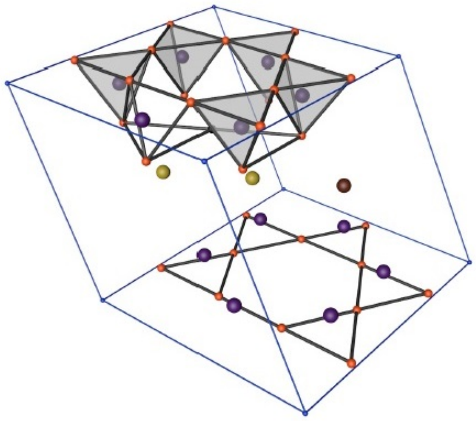

FIG. 7. The third stage of the amorphization of the montmorillonite cell; ion activation at (003)

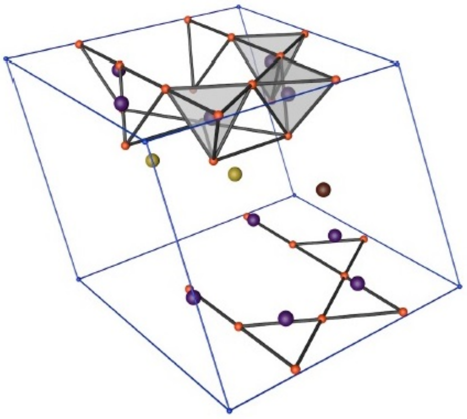

FIG. 8. The fourth stage of the amorphization of the montmorillonite cell; ion activation at (310, 142)

4. Conclusion

Montmorillonite unit cell amorphization induced by high-frequency electromagnetic field treatment can be split in four stages.

During the first stage, the oxygen octahedron in the plane (100) is destroyed due to extraction of oxygen ions and hydroxyl group ions (Fig. 5). During the second stage, oxygen tetrahedra are destroyed in planes (210) due to extraction of oxygen ions (Fig. 6). Because ion extraction activation energies for ions place in planes (100) and (210) are similar, first and second stages of the amorphization are equally probable. For sample P1 the ion extraction occured in the plane (210) while the diffraction maximum intensity (100) decreased down to 10%. For sample P3 ions were extracted from planes (100) and (210) which proves that ion extraction activation energies have comparable values for these planes.

During the third stage an intensive lattice destruction takes place along planes (003) due to extraction of oxygen ions and hydroxyl groups (Fig. 7). This results in a destruction of oxygen tetrahedra and octahedra.

During the fourth stage the lattice is destroyed along planes (310,142) because of the extraction of oxygen and aluminum or silicon ions (Fig. 8). The fourth stage in the most energy intensive as it requires destruction of covalent bound.

References

[1] Clark D. E., Sutton W. H. Microwave processing of materials. *Annu. Rev. Mater. Sci.*, 1996, **26**(299), P. 299–331.

[2] Egorov S. V., Rubakov K. I., Semenov V. E. and etc. Role of convective heat removal and electromagnetic field structure in the microwave heating of materials. *Journal of Materials Science*, 2007, **42**(6), P. 2097–2104.

[3] Kitchen H. J. et al. Modern microwave methods in solid-state inorganic materials chemistry: from fundamentals to manufacturing. *Chem. Rev.*, 2014, **114**(2), P. 1170–1206.

[4] Kozhevnikov V. Y. Sintering of ceramic materials in a microwave electromagnetic field. *Bulletin of the Saratov State Technical University*, 2007, **1**(10), P. 99–104.

[5] Eitel V. *Physical chemistry of silicates*. M.: Publishing house of foreign countries literature, 1962, 1056 p.

[6] Deryagin B. V. et al. *Water in dispersed systems*. M.: Chemistry, 1989. 288 p.

[7] Drits V. A., Besson G., Muller F. An improved model for structural transformations of heat-treated aluminous dioctahedral 2:1 layer silicates. *Clays and Clay Minerals*, 1995, **43**(6), P. 718–731.

[8] Prokhina A. V., Shapovalov N. A., Latypova M. M. Surface modification of clay minerals with a high content of montmorillonite in a high frequency electromagnetic field. *Modern high technology*, 2011, **1**, P. 135–136.

[9] Belchinskaya L. I. et al. The effect of salt modification on the adsorption characteristics of acid-activated montmorillonite and kaolinite. *Journal of Applied Chemistry*, 2008, **81**(6), P. 926–930.

[10] Belchinskaya L. I. et al. The influence of various mechanisms of heating layered aluminosilicate on sorption processes. Communication 1. Sorption of water during thermal and electromagnetic (microwave) heating of montmorillonite. *Sorption and chromatographic processes*, 2017, **17**(5), P. 781–791.

[11] Chetverikova A. G. et al. Structural and morphological features of montmorillonite treated with a high-frequency microwave field. *Physics and Chemistry of Materials Processing*, 2019, **3**, P. 5–12.

[12] Kanygina O. N. et al. High-temperature phase transformations in iron-containing clays of the Orenburg region. *Bulletin of the Orenburg State University*, 2010, **6**(112), P. 113–118.

[13] Makarov V. N., Kanygina O. N. On the question of amorphization of a unit cell of montmorillonite in a microwave field. Proceedings of Physical Materials: IX International School with elements of a scientific school for youth; Actual problems of strength: LXI International Conference dedicated to the 90th anniversary of the processor M.A. Cristal: collection of materials, 2019.

[14] Zaynullina V. M., Leonidov I. A., Kozhevnikov V. L. Features of the formation of oxygen defects in $\mathrm{SrFeO}_{2.5}$ ferrate with brownmillerite structure. *SSP*, 2002, **44**(11), P. 1970–1973.

[15] Shefer K. et al. Features of the real structure of pseudoboehmites: disturbances in the structure and packing of layers associated with crystallized water. *Journal of structural chemistry*, 2010, **51**(1), P. 137–147.

[16] Bobkova N. M. *Physical chemistry of refractory non-metallic and silicate materials*. Minsk: The Highest School, 2007, 301 p.

[17] Olivella S. et al. Mechanism of the hydrogen transfer from the OH group to oxygen-centered radicals: proton-coupled electron-transfer versus radical hydrogen abstraction. *Chemistry A European Journal*, 2004, **10**(14), P. 3404–3410.

[18] Little E. J., Jones M.M. A complete table of electronegativities. *Journal of Chemical Education*. 1960, **37**(5), P. 231–233.

[19] Gorlov Y. I., Konoplya M. M., Chuyko A. A. On the mechanism of de- and rehydration of krimnemoz. *Theoretical and experimental chemistry*, 1980, **16**(3), P. 333–338.

[20] Gorlov Y. I. et al. Field desorption of water from the surface of silica with the structure of its hydration cover. *Theoretical and experimental chemistry*, 1980, **16**(2), P. 202–206.

[21] Yurova I. V. et al. The interaction of the Fe3O4 cluster with monohydrates of hydroxide, hydroxide ions and water molecules. *News of higher educational institutions. Series: chemistry and chemical technology*, 2008, **51**(5), P. 37–40.

[22] Mikheev V. I. *Radiometric determinant of minerals.* M.: State. scientific and technical publishing house lit. in geology and mineral protection, 1957, 868 p.

[23] Sirotkin O. S. et al. The ratio of the components of the element-oxygen bonds (EO) as the basis for predicting their ability to form chains in polymer oxides and evaluating their certain properties. *Bulletin of Kazan Technological University*, 2012, **15**(13), P. 31–35.

NANOSYSTEMS: PHYSICS, CHEMISTRY, MATHEMATICS, 2020, 11 (2), P. 161–170

Comparison of non classical effects: quantum phase fluctuation, antibunching and minimum total noise in various non linear optical processes

Priyanka, Savita Gill*

Department of Applied Science, University Institute of Engineering and Technology,
Kurukshetra 136119, India

*savita2015@kuk.ac.in

DOI 10.17586/2220-8054-2020-11-2-161-170

We study various non classical effects of light like reduction of quantum phase fluctuation, antibunching and minimum total noise present in various nonlinear optical processes. Further, we have shown that depth of non-classicality can be directly measured using all these parameters. We have done the comparative study to correlate these non-classical effects in seven wave mixing, eight wave mixing and third harmonic generation.

Keywords: phase fluctuation, photon number, antibunching, minimum total noise.

Received: 26 January 2020

Revised: 20 February 2020

1. Introduction

For being a non-classical quantum state, negativities of Glauber–Sudarshan P-function may appear. However, this function may be strongly singular [1, 2]. Generally we use standard deviation as the most natural measure to study quantum fluctuation [3]. Non classical effects of radiation field like reduction of quantum fluctuation, antibunching and minimum total noise were recently attracted a great interest in quantum optics. Quantum phase can be considered as a main feature to differentiate between classical and quantum physics. Antibunching and squeezing has no classical correlation and are called non classical states. In Sub-Poissonian (antibunching) photon statistics the variance of photon number is less than the mean value. The Hermitian quantum phase operators have some uncertainty [4–6] which leads to a lot of adverse formalism [7–9] of phase problem. Out of all these formalisms, Barnett–Pegg(BP) [8] and Susskind–Glogower(SG) [9] has contributed a considerable role in phase fluctuation and have been used by various researchers [10–18]. Study of phase fluctuation of coherent light coupled to a nonlinear medium and in intermediate state have already been studied [19, 20]. The development of nanotechnology and nanoscience has provided new opportunities for nonlinear optics. In the last few decades, numerous studies on the nonlinear optical properties of novel materials have been performed because of the potential of these materials in optical device applications [21–25]. Strong optical nonlinearities in nanoparticles are observed due to quantum confinement, such as nonlinear optical absorption and second and third order optical nonlinearities; these can be studied for making optical modulators, optical limiters and laser second and third harmonic generators [23, 24]. To study the optical nonlinearity of nanoparticles, there is a significant body of research concerning the measurements of third order nonlinear susceptibility χ^3 which can be used as a source for the generation of third harmonic generation process [26]. With the role of quantum phase fluctuation in quantum cryptography [27], super conductivity [28, 29] and with the success in experimental study of phase fluctuation [30], there has been a significant increase in importance of study of non-classical parameters.

In the present work, Carruther and Nieto phase parameters [16] are used to study phase fluctuation parameters in nonlinear processes like seven and eight wave interaction process and in third harmonic generation using Barnett–Pegg (BP) formalism [7]. We have reported in the paper that reduction of phase parameters not only directly implies antibunching but also increases with an increase in antibunching. We have also found minimum total noise in terms of number operators and observed that the greater the sub-Poissonian (antibunched) state, the greater will be the minimum total noise in the system.

2. Measurement of quantum phase fluctuation parameters

Barnett and Pegg [7] defined the exponential of phase operator E and its Hermitian conjugate $E^\dagger$ as:

$$\begin{aligned} E &= \left(\overline{N} + \frac{1}{2}\right)^{-\frac{1}{2}} a(t), \\ E^\dagger &= \left(\overline{N} + \frac{1}{2}\right)^{-\frac{1}{2}} a^\dagger(t), \end{aligned} \tag{1}$$

where $\overline{N}$is the mean photon number in the coherent state. Cosine and sine operators are defined as [7]:

$$\begin{aligned} C &= \frac{1}{2}(E + E^{\dagger}), \\ S &= -\frac{i}{2}(E - E^{\dagger}), \end{aligned} \tag{2}$$

and satisfy the following relations:

$$\langle C\rangle^2 + \langle S\rangle^2 = 1, \tag{3}$$

and

$$[C, S] = \frac{i}{2}\left(\overline{N} + \frac{1}{2}\right)^{-\frac{1}{2}}, \tag{4}$$

and, we get

$$(\Delta C)^2 (\Delta S)^2 \geq \frac{1}{16}\frac{1}{(\overline{N} + \frac{1}{2})}. \tag{5}$$

To measure quantum phase fluctuation, Carruthers and Nieto [16] had introduced U, S and Q parameters in the following way:

$$U\left(\theta, t, |\alpha|^2\right) = (\Delta N)^2 \frac{(\Delta S)^2 + (\Delta C)^2}{\langle S\rangle^2 + \langle C\rangle^2}, \tag{6}$$

$$S(\theta, t, |\alpha|^2) = (\Delta N)^2 (\Delta S)^2, \tag{7}$$

and

$$Q(\theta, t, |\alpha|^2) = \frac{S(\theta, t, |\alpha|^2)}{\langle C\rangle^2}, \tag{8}$$

where θ is the phase of input Poissonian state, t is interaction time and $|\alpha|^2$ is mean photon number in coherent state.

2.1. Seven wave interaction process

In seven wave mixing process, the interaction takes place in such a way that the absorption of two photons of frequency ω_1 each and the emission of two photons of frequency ω_2 each and other two photons of frequency ω_3. The Hamiltonian represents total energy for the system and is given as (taking $\hbar = 1$):

$$H = \omega_1 a^+ a + \omega_2 b^+ b + \omega_3 c^+ c + g\left(a^2 b^{+2} c^{+3} + a^{+2} b^2 c^3\right), \tag{9}$$

where g is a coupling constant, $a\left(a^+\right)$, $b\left(b^+\right)$, $c\left(c^+\right)$ are the annihilation(creation) operators respectively. $A = a \exp i\omega_1 t$, $B = b \exp i\omega_2 t$, $C = c \exp i\omega_3 t$ are slowly varying operators at frequencies ω_1, ω_2 and ω_3.

To study quantum phase fluctuation, a coherent state $|\alpha\rangle$ is used as pump for mode A and before the interaction process there was no photon in signal mode B and stokes mode C i.e.,

$$|\psi\rangle = |\alpha\rangle|0\rangle|0\rangle. \tag{10}$$

The Heisenberg equation of motion for fundamental mode A is given as $(\hbar = 1)$:

$$\frac{dA}{dt} = \frac{\partial A}{\partial t} + i\,[H, A], \tag{11}$$

in this process, we assume the interaction time t to be very small. Using short time approximation technique, expand $A\,(t)$ by using Taylor's series expansion and retain the terms up to second order in $g^2 t^2$:

$$A(t) = A(0) + \frac{t}{1!}\frac{dA(0)}{dt} + \frac{t^2}{2!}\frac{d^2A(0)}{dt^2},$$

and we get:

$$\begin{aligned} A(t) = A - 2igtA^{\dagger}B^2C^3 + g^2t^2\Big(&2AN_B^2N_C^3 - 9A^{\dagger}A^2N_B^2N_C^2 - 18A^{\dagger}A^2N_B^2N_C \\ &-6A^{\dagger}A^2N_B^2 - 4A^{\dagger}A^2N_BN_C^3 - 36A^{\dagger}A^2N_BN_C^2 - 72A^{\dagger}A^2N_BN_C - 24A^{\dagger}A^2N_B \\ &-2A^{\dagger}A^2N_C^3 - 18A^{\dagger}A^2N_C^2 - 36A^{\dagger}A^2N_C - 12A^{\dagger}A^2\Big), \end{aligned} \tag{12}$$

where $N_B = B^{\dagger}B$ and $N_C = C^{\dagger}C$.

From equation (12), the mean number of photons i.e. $N(t) = A^{\dagger}(t) \times A(t)$ can be expressed as:

$$\begin{aligned} N(t) = A^{\dagger}A - 2igt\left(A^{\dagger 2}B^{2}C - A^{2}B^{\dagger 2}C^{\dagger}\right) + 4g^{2}t^{2}\left(2A^{\dagger}AN_{B}^{2}N_{C} + N_{B}^{2}N_{C}\right) \\ -2g^{2}t^{2}\left(A^{\dagger 2}A^{2}N_{B}^{2} + 4A^{\dagger 2}A^{2}N_{B}N_{C} + 4A^{\dagger 2}A^{2}N_{B} + 2A^{\dagger 2}A^{2}N_{C} + 12A^{\dagger 2}A^{2}\right), \end{aligned} \tag{13}$$

the expectation value of $N(t)$ using condition (10) is:

$$\langle N\rangle = |\alpha|^{2} - 24g^{2}t^{2}|\alpha|^{4}. \tag{14}$$

The squaring of expectation value of number operator is given as:

$$\langle N\rangle^{2} = |\alpha|^{4} - 48g^{2}t^{2}|\alpha|^{6} + 576g^{4}t^{4}|\alpha|^{8},$$

as the interaction time is small, we are taking terms up to $g^{2}t^{2}$ and above equation is written as:

$$\langle N\rangle^{2} = |\alpha|^{4} - 48g^{2}t^{2}|\alpha|^{6}, \tag{15}$$

$$\left\langle N^{2}\right\rangle = |\alpha|^{4} + |\alpha|^{2} - g^{2}t^{2}\left(48|\alpha|^{6} + 96|\alpha|^{4}\right). \tag{16}$$

Using equation (15) and (16), we get:

$$\begin{aligned} (\Delta N)^{2} &= \left\langle N^{2}\right\rangle - \langle N\rangle^{2}, \\ (\Delta N)^{2} &= |\alpha|^{2} - g^{2}t^{2}\left(96|\alpha|^{4}\right). \end{aligned} \tag{17}$$

The condition of sub-Poissonian photon statistics is given as:

$$d = (\Delta N)^{2} - \langle N\rangle < 0. \tag{18}$$

Using (14) and (17), we get:

$$d = -72g^{2}t^{2}|\alpha|^{4}. \tag{19}$$

We obtained a negative value, which shows that the photon statistics is sub-Poissonian or antibunched light. By substituting (13) in (2), we obtain:

$$\begin{aligned} C = \frac{1}{2}\left(N + \frac{1}{2}\right)^{-\frac{1}{2}} \Big[A + A^{\dagger} - 2igtA^{\dagger}B^{2}C^{3} + 2igtAB^{\dagger 2}C^{\dagger 3} + g^{2}t^{2}\Big(2AN_{B}^{2}N_{C}^{3} - 9A^{\dagger}A^{2}N_{B}^{2}N_{C}^{2} \\ -18A^{\dagger}A^{2}N_{B}^{2}N_{C} - 6A^{\dagger}A^{2}N_{B}^{2} - 4A^{\dagger}A^{2}N_{B}N_{C}^{3} - 36A^{\dagger}A^{2}N_{B}N_{C}^{2} - 72A^{\dagger 2}A^{2}N_{B}N_{C} \\ -24A^{\dagger 2}AN_{B} - 2A^{\dagger}A^{2}N_{C}^{3} - 18A^{\dagger}A^{2}N_{C}^{2} - 36A^{\dagger}A^{2}N_{C} - 12A^{\dagger}A^{2} + 2A^{\dagger}N_{B}^{2}N_{C}^{3} \\ -9A^{\dagger 2}AN_{B}^{2}N_{C}^{2} - 18A^{\dagger 2}AN_{B}^{2}N_{C} - 6A^{\dagger 2}AN_{B}^{2} - 4A^{\dagger 2}AN_{B}N_{C}^{3} - 36A^{\dagger 2}AN_{B}N_{C}^{2} \\ -72A^{\dagger 2}A^{2}N_{B}N_{C} - 24A^{\dagger}A^{2}N_{B} - 2A^{\dagger 2}AN_{C}^{3} - 18A^{\dagger 2}AN_{C}^{2} - 36A^{\dagger 2}AN_{C} - 12A^{\dagger 2}A\Big)\Big] \end{aligned} \tag{20}$$

and

$$\begin{aligned} lS = -\frac{i}{2}\left(N + \frac{1}{2}\right)^{-\frac{1}{2}} \Big[A - A^{\dagger} - 2igtA^{\dagger}B^{2}C^{3} - 2igtAB^{\dagger 2}C^{\dagger 3} + g^{2}t^{2}\Big(2AN_{B}^{2}N_{C}^{3} - 9A^{\dagger}A^{2}N_{B}^{2}N_{C}^{2} \\ -18A^{\dagger}A^{2}N_{B}^{2}N_{C} - 6A^{\dagger}A^{2}N_{B}^{2} - 4A^{\dagger}A^{2}N_{B}N_{C}^{3} - 36A^{\dagger}A^{2}N_{B}N_{C}^{2} - 72A^{\dagger 2}A^{2}N_{B}N_{C} \\ -24A^{\dagger 2}AN_{B} - 2A^{\dagger}A^{2}N_{C}^{3} - 18A^{\dagger}A^{2}N_{C}^{2} - 36A^{\dagger}A^{2}N_{C} - 12A^{\dagger}A^{2} - 2A^{\dagger}N_{B}^{2}N_{C}^{3} \\ +9A^{\dagger 2}AN_{B}^{2}N_{C}^{2} + 18A^{\dagger 2}AN_{B}^{2}N_{C} + 6A^{\dagger 2}AN_{B}^{2} + 4A^{\dagger 2}AN_{B}N_{C}^{3} + 36A^{\dagger 2}AN_{B}N_{C}^{2} \\ +72A^{\dagger 2}A^{2}N_{B}N_{C} + 24A^{\dagger}A^{2}N_{B} + 2A^{\dagger 2}AN_{C}^{3} + 18A^{\dagger 2}AN_{C}^{2} + 36A^{\dagger 2}AN_{C} + 12A^{\dagger 2}A\Big)\Big]. \end{aligned} \tag{21}$$

The expectation value of C and S operators of equation (20) and (21) by applying condition (10) are:

$$\langle C\rangle = \frac{1}{2}\left[\left(N + \frac{1}{2}\right)^{-\frac{1}{2}}\left\{\alpha + \alpha^{*} - g^{2}t^{2}\left(12|\alpha|^{2}\alpha + 12|\alpha|^{2}\alpha^{*}\right)\right\}\right], \tag{22}$$

$$\langle S\rangle = -\frac{i}{2}\left[\left(\overline{N} + \frac{1}{2}\right)^{-\frac{1}{2}}\left\{\alpha - \alpha^{*} - g^{2}t^{2}(12|\alpha|^{2}\alpha - 12|\alpha|^{2}\alpha^{*})\right\}\right]. \tag{23}$$

Then square of expectation value of C and S are:

$$\langle C\rangle^{2} = \frac{1}{4}\left(N + \frac{1}{2}\right)^{-1}\left[\alpha^{2} + \alpha^{*2} + 2|\alpha|^{2} - 24g^{2}t^{2}\left(|\alpha|^{2}\alpha^{2} + |\alpha|^{2}\alpha^{*2} + 2|\alpha|^{4}\right)\right], \tag{24}$$

$$\langle S\rangle^2 = -\frac{1}{4}\left(N+\frac{1}{2}\right)^{-1}\left[\alpha^2+\alpha^{*2}-2|\alpha|^2-24g^2t^2\left(|\alpha|^2\alpha^2+|\alpha|^2\alpha^{*2}-2|\alpha|^4\right)\right]. \tag{25}$$

Similarly:

$$\langle C^2\rangle = \frac{1}{4}\left(N+\frac{1}{2}\right)^{-1}\left[\alpha^2+\alpha^{*2}+2|\alpha|^2+1-12g^2t^2\Big(\alpha^2+\alpha^{*2}+2|\alpha|^2\alpha^2 +2|\alpha|^2\alpha^{*2}+4|\alpha|^4+4|\alpha|^2\Big)\right], \tag{26}$$

$$\langle S^2\rangle = -\frac{1}{4}\left(N+\frac{1}{2}\right)^{-1}\left[\alpha^2+\alpha^{*2}-2|\alpha|^2-1-12g^2t^2\Big(\alpha^2+\alpha^{*2}+2|\alpha|^2\alpha^2 +2|\alpha|^2\alpha^{*2}-4|\alpha|^4-4|\alpha|^2\Big)\right]. \tag{27}$$

.

Using equations (24)–(27), second order variances is expressed as:

$$(\Delta C)^2 = \langle C^2\rangle - \langle C\rangle^2 = \frac{1}{4}\left(N+\frac{1}{2}\right)^{-1}\left[1-12g^2t^2\left(\alpha^2+\alpha^{*2}+4|\alpha|^2\right)\right], \tag{28}$$

and

$$(\Delta S)^2 = \langle S^2\rangle - \langle S\rangle^2 = -\frac{1}{4}\left(\overline{N}+\frac{1}{2}\right)^{-1}\left[-1-12g^2t^2\left(\alpha^2+\alpha^{*2}-4|\alpha|^2\right)\right]. \tag{29}$$

Now equations (6)–(8) can be expressed as:

$$U(\theta,t,|\alpha|^2) = \frac{1}{2}\left\{\frac{1-144g^2t^2|\alpha|^2}{1-24g^2t^2|\alpha|^2}\right\}, \tag{30}$$

$$S(\theta,t,|\alpha|^2) = \frac{1}{4}\left(|\alpha|^2-24g^2t^2|\alpha|^4+\frac{1}{2}\right)^{-1}\left[|\alpha|^2+24|\alpha|^4g^2t^2(\cos2\theta-6)\right], \tag{31}$$

and

$$Q(\theta,t,|\alpha|^2) = \frac{1+24|\alpha|^2g^2t^2(\cos2\theta-6)}{2(\cos2\theta+1)(1-24|\alpha|^2g^2t^2)}. \tag{32}$$

From equation (19) and (30), it is clear that the reduction of phase parameter U increases withan increase in the number of photons and is associated with antibunching.

2.2. Eight wave interaction process

In an eight wave mixing process, the interaction takes place in such a way that the absorption of two photons of frequency ω_1 each and the emission of four photons of frequency ω_2 each and another two photons of frequency ω_3.

The Hamiltonian for the given process is:

$$H = \omega_1a^+a+\omega_2b^+b+\omega_3c^+c+g\left(a^2b^{+4}c^{+2}+a^{+2}b^4c^2\right), \tag{33}$$

where g is a coupling constant, $a\left(a^+\right)$, $b\left(b^+\right)$, $c\left(c^+\right)$ are the annihilation(creation) operators, respectively. $A = a\exp i\omega_1t$, $B = b\exp i\omega_2t$, $C = c\exp i\omega_3t$ are slowly varying operators at frequencies ω_1, ω_2 and ω_3.

Now, using the short time approximation technique, Taylor's series expansion of $A\left(t\right)$ can be expressed as:

$$\begin{aligned} A(t) = {} & A-2igtA^\dagger B^4C^2+g^2t^2(2AN_B^4N_C^2-16A^\dagger A^2N_B^3N_C^2-72A^\dagger A^2N_B^2N_C^2 \\ & -96A^\dagger A^2N_BN_C^2-24A^\dagger A^2N_C^2-4A^\dagger A^2N_B^4N_C-64A^\dagger A^2N_B^3N_C-288A^\dagger A^2N_B^2N_C \\ & -384A^\dagger A^2N_BN_C-96A^\dagger A^2N_C-2A^\dagger A^2N_B^4-32A^\dagger A^2N_B^3-144A^\dagger A^2N_B^2 \\ & -192A^\dagger A^2N_B-48A^\dagger A^2, \end{aligned} \tag{34}$$

where $N_B = B^\dagger B$ and $N_C = C^\dagger C$.

From equation (33), mean number of photons using condition (10) can be written as:

$$N(t) = A^\dagger A-96g^2t^2(A^{\dagger2}A^2). \tag{35}$$

The expectation value of $N(t)$ is:

$$\langle N\rangle = |\alpha|^2-96g^2t^2|\alpha|^4. \tag{36}$$

Using equation (35), we get:

$$(\Delta N)^2 = |\alpha|^2 - 192g^2t^2 \left(2\,|\alpha|^4\right). \tag{37}$$

The condition of sub-Poissonian photon statistics is given as:

$$d = (\Delta N)^2 - \langle N \rangle < 0. \tag{38}$$

Using equations (36) and (37), we get:

$$d = -288g^2t^2\,|\alpha|^4\,, \tag{39}$$

as d is negative, and thus, we achieve an antibunched state.

Now, by substituting equation (34) in equation (2), we obtain:

$$\begin{aligned} C = \frac{1}{2}\left(N+\frac{1}{2}\right)^{-\frac{1}{2}} \Big[&A + A^\dagger - 2igtA^\dagger B^4C^2 + 2igtAB^{\dagger 4}C^{\dagger 2} + g^2t^2\Big(2AN_B^4N_C^2 \\ &-16A^\dagger A^2N_B^3N_C^2 - 72A^\dagger A^2N_B^2N_C^2 - 96A^\dagger A^2N_BN_C^2 - 24A^\dagger A^2N_C^2 \\ &-4A^\dagger A^2N_B^4N_C - 64A^\dagger A^2N_B^3N_C - 288A^\dagger A^2N_B^2N_C - 384A^\dagger A^2N_BN_C \\ &-96A^\dagger A^2N_C - 2A^\dagger A^2N_B^4 - 32A^\dagger A^2N_B^3 - 144A^\dagger A^2N_B^2 - 192A^\dagger A^2N_B \\ &-48A^\dagger A^2 + 2A^\dagger N_B^4N_C^2 - 16A^{\dagger 2}AN_B^3N_C^2 - 72A^{\dagger 2}AN_B^2N_C^2 - 96A^{\dagger 2}AN_BN_C^2 \\ &-24A^{\dagger 2}AN_C^2 - 4A^{\dagger 2}AN_B^4N_C - 64A^{\dagger 2}AN_B^3N_C - 288A^{\dagger 2}AN_B^2N_C - 384A^{\dagger 2}AN_BN_C \\ &-96A^{\dagger 2}AN_C - 2A^{\dagger 2}AN_B^4 - 32A^{\dagger 2}AN_B^3 - 144A^{\dagger 2}AN_B^2 - 192A^{\dagger 2}AN_B - 48A^{\dagger 2}A\Big)\Big] \end{aligned} \tag{40}$$

and

$$\begin{aligned} S = -\frac{i}{2}\left(N+\frac{1}{2}\right)^{-\frac{1}{2}} \Big[&A - A^\dagger - 2igtA^\dagger B^4C^2 - 2igtAB^{\dagger 4}C^{\dagger 2} + g^2t^2\Big(2AN_B^4N_C^2 - 16A^\dagger A^2N_B^3N_C^2 \\ &-72A^\dagger A^2N_B^2N_C^2 - 96A^\dagger A^2N_BN_C^2 - 24A^\dagger A^2N_C^2 - 4A^\dagger A^2N_B^4N_C - 64A^\dagger A^2N_B^3N_C \\ &-288A^\dagger A^2N_B^2N_C - 384A^\dagger A^2N_BN_C - 96A^\dagger A^2N_C - 2A^\dagger A^2N_B^4 - 32A^\dagger A^2N_B^3 - 144A^\dagger A^2N_B^2 \\ &-192A^\dagger A^2N_B - 48A^\dagger A^2 - 2A^\dagger N_B^4N_C^2 + 16A^{\dagger 2}AN_B^3N_C^2 + 72A^{\dagger 2}AN_B^2N_C^2 + 96A^{\dagger 2}AN_BN_C^2 \\ &+24A^{\dagger 2}AN_C^2 + 4A^{\dagger 2}AN_B^4N_C + 64A^{\dagger 2}AN_B^3N_C + 288A^{\dagger 2}AN_B^2N_C + 384A^{\dagger 2}AN_BN_C \\ &+96A^{\dagger 2}AN_C + 2A^{\dagger 2}AN_B^4 + 32A^{\dagger 2}AN_B^3 + 144A^{\dagger 2}AN_B^2 + 192A^{\dagger 2}AN_B + 48A^{\dagger 2}A\Big)\Big]. \end{aligned} \tag{41}$$

Using equations (40) and (41), second order variance is expressed as

$$(\Delta C)^2 = \langle C^2\rangle - \langle C\rangle^2 = \frac{1}{4}\left(N+\frac{1}{2}\right)^{-1}\Big[1 - 48g^2t^2(\alpha^2 + \alpha^{*2} + 4\,|\alpha|^2)\Big] \tag{42}$$

and

$$(\Delta S)^2 = \langle S^2\rangle - \langle S\rangle^2 = -\frac{1}{4}\left(\overline{N}+\frac{1}{2}\right)^{-1}\Big[-1 - 48g^2t^2(\alpha^2 + \alpha^{*2} - 4\,|\alpha|^2)\Big]. \tag{43}$$

Now, equations (6)–(8) can be expressed as:

$$U(\theta, t, |\alpha|^2) = \frac{1}{2}\left\{\frac{1 - 576g^2t^2\,|\alpha|^2}{1 - 96g^2t^2\,|\alpha|^2}\right\}, \tag{44}$$

$$S(\theta, t, |\alpha|^2) = \frac{1}{4}\left(|\alpha|^2 - 96g^2t^2\,|\alpha|^4 + \frac{1}{2}\right)^{-1}\Big[|\alpha|^2 + 96\,|\alpha|^4\,g^2t^2(\cos 2\theta - 6)\Big], \tag{45}$$

and

$$Q(\theta, t, |\alpha|^2) = \frac{1 + 96\,|\alpha|^2\,g^2t^2(\cos 2\theta - 6)}{2(\cos 2\theta + 1)(1 - 96\,|\alpha|^2\,g^2t^2)}. \tag{46}$$

From equation (38) and (44), we can correlate reduction of U with sub-Poissonian state.

2.3. Third harmonic generation process

In third harmonic generation process, the interaction takes place in such a way that the absorption of three photons of frequency ω_1 each and the emission of one photon of frequency ω_2 such that $\omega_2 = 3\omega_1$. The Hamiltonian for the given process is:

$$H = \omega_1 a^+ a + \omega_2 b^+ b + g\left(a^3 b^+ + a^{+3} b\right), \tag{47}$$

where g is a coupling constant, $a\left(a^+\right)$, $b\left(b^+\right)$ are the annihilation(creation) operators, respectively. $A = a \exp i\omega_1 t$, $B = b \exp i\omega_2 t$ are slowly varying operators at frequencies ω_1, ω_2.

By using the same techniques used in above interaction process, we get;

$$A(t) = A - 3igtA^{\dagger 2}B + \frac{3}{2}g^2t^2\left(6A^\dagger A^2 N_B + 6AN_B - A^{\dagger 2}A^3\right), \tag{48}$$

where $N_B = B^\dagger B$ and $N_C = C^\dagger C$.

From equation (48), the mean number of photons using condition (10) can be simplified as:

$$N(t) = A^\dagger A - 3g^2t^2\left(A^{\dagger 3}A^3\right). \tag{49}$$

The expectation value of $N(t)$ is:

$$\langle N\rangle = |\alpha|^2 - 3g^2t^2|\alpha|^6. \tag{50}$$

Using equation (48), we get:

$$(\Delta N)^2 = |\alpha|^2 - 18g^2t^2\left(|\alpha|^6\right). \tag{51}$$

The condition of sub-Poissonian photon statistics is given as:

$$d = (\Delta N)^2 - \langle N\rangle < 0. \tag{52}$$

Using (50) and (51), we get:

$$d = -15g^2t^2|\alpha|^6, \tag{53}$$

as d is negative and thus we achieve a non-classical state.

By substituting (48) in (2), we obtain:

$$C = \frac{1}{2}\left(N + \frac{1}{2}\right)^{-\frac{1}{2}}\left[A + A^\dagger - 3igtA^{\dagger 2}B + 3igtA^3B^\dagger - \frac{3}{2}g^2t^2\left(A^{\dagger 2}A^3 + A^{\dagger 3}A^2\right)\right] \tag{54}$$

and

$$S = -\frac{i}{2}\left(\overline{N} + \frac{1}{2}\right)^{-\frac{1}{2}}\left[A - A^\dagger - 3igtA^{\dagger 2}B - 3igtA^2B^\dagger - \frac{3}{2}g^2t^2\left(A^{\dagger 2}A^3 - A^{\dagger 3}A^2\right)\right], \tag{55}$$

Using equations (54)–(55), second order variance is expressed as:

$$(\Delta C)^2 = \langle C^2\rangle - \langle C\rangle^2 = \frac{1}{4}\left(N + \frac{1}{2}\right)^{-1}\left[1 - \frac{3}{2}g^2t^2\left(2|\alpha|^2\alpha^2 + 2|\alpha|^2\alpha^{*2} + 6|\alpha|^4\right)\right], \tag{56}$$

and

$$(\Delta S)^2 = \langle S^2\rangle - \langle S\rangle^2 = -\frac{1}{4}\left(\overline{N} + \frac{1}{2}\right)^{-1}\left[-1 - \frac{3}{2}g^2t^2\left(2|\alpha|^2\alpha^2 + 2|\alpha|^2\alpha^{*2} - 6|\alpha|^4\right)\right]. \tag{57}$$

Now equations (6)–(8) can be expressed as:

$$U(\theta, t, |\alpha|^2) = \frac{1}{2}\left\{\frac{1 - 27g^2t^2|\alpha|^4}{1 - 3g^2t^2|\alpha|^4}\right\}, \tag{58}$$

$$S(\theta, t, |\alpha|^2) = \frac{1}{4}\left(|\alpha|^2 - 3g^2t^2|\alpha|^6 + \frac{1}{2}\right)^{-1}\left[|\alpha|^2 + 3|\alpha|^6 g^2t^2(2\cos 2\theta - 9)\right], \tag{59}$$

and

$$Q(\theta, t, |\alpha|^2) = \frac{1 + 3|\alpha|^4 g^2t^2(2\cos 2\theta - 9)}{2(\cos 2\theta + 1)(1 - 3|\alpha|^4 g^2t^2)}, \tag{60}$$

equations (53) and (58) indicate the presence of non-classicality.

3. Minimum total noise in terms of number operator

The minimum total noise of a single mode with density matrix ρ can be stated in terms of A and $A^\dagger$ as [31]:

$$X_1 = \frac{1}{2}[A + A^\dagger] \quad \text{and} \quad X_2 = \frac{1}{2i}[A - A^\dagger]. \tag{61}$$

From equation (60), we get:

$$\left\langle X_1^2 \right\rangle + \langle X_2 \rangle^2 = \left\langle N + \frac{1}{2} \right\rangle. \tag{62}$$

In order to find out the minimum total noise of state in terms of number operator we use Schwartz inequality:

$$\Big| \left\langle \left(X_2 - \langle X_2 \rangle\right) \left(N - \langle N \rangle\right) \right\rangle \Big|^2 \leq \left\langle \left(X_2 - \langle X_2 \rangle\right)^2 \right\rangle \left\langle \left(N - \langle N \rangle\right)^2 \right\rangle \leq \left(\Delta X_2\right)^2 \left(\Delta N\right)^2. \tag{63}$$

Equation (63) is simplified as:

$$\left(\Delta X_2\right)^2 \left(\Delta N\right)^2 \geq \frac{1}{4} \Big| \left\langle [X_2, N] \right\rangle \Big|^2 \geq \frac{1}{4} \left| \left\langle X_1 \right\rangle \right|^2, \tag{64}$$

where $[X_2, N] = iX_1$.

Similarly,we can achieve for X_1 is:

$$\left(\Delta X_1\right)^2 \left(\Delta N\right)^2 \geq \frac{1}{4} \left| \left\langle X_2 \right\rangle \right|^2. \tag{65}$$

Using equation (64) and (65), we get:

$$\left\langle X_1 \right\rangle^2 + \left\langle X_2 \right\rangle^2 \leq 4 \left(\Delta N\right)^2 \left[\left(\Delta X_1\right)^2 + \left(\Delta X_2\right)^2 \right]. \tag{66}$$

Using equation (62), we obtain:

$$\left\langle N + \frac{1}{2} \right\rangle \leq \left[4 \left(\Delta N\right)^2 + 1 \right] \left[\left(\Delta X_1\right)^2 + \left(\Delta X_2\right)^2 \right], \tag{67}$$

thus minimum total noise in terms of number operator is:

$$T_{\min} = \left[(\Delta X_1)^2 + (\Delta X_2)^2 \right].$$

Substituting equation (67) in above relation, we get:

$$T_{\min} \geq \frac{\langle N + \frac{1}{2} \rangle}{[4(\Delta N)^2 + 1]}, \tag{68}$$

equation (68) shows that as the value of $(\Delta N)^2$ decreases, minimum total noise increases.

3.1. Seven wave mixing process

Minimum total noise in seven wave interaction process can be obtained by substituting equation (14) and (17) in equation (68):

$$T_N \geq \frac{|\alpha|^2 - 24 g^2 t^2 |\alpha|^4 + \frac{1}{2}}{4 |\alpha|^2 + 1 - 384 g^2 t^2 |\alpha|^4}. \tag{69}$$

3.2. Eight wave mixing process

In this case we substitute equation (36) and (37) in equation (68) to obtain the expression for minimum total noise and is given as:

$$T_N \geq \frac{|\alpha|^2 - 96 g^2 t^2 |\alpha|^4 + \frac{1}{2}}{4 |\alpha|^2 + 1 - 1536 g^2 t^2 |\alpha|^4}. \tag{70}$$

3.3. Third harmonic generation process

After substituting equation (50) and (51) in equation (68), we get expression of minimum total noise as:

$$T_N \geq \frac{|\alpha|^2 - 3 g^2 t^2 |\alpha|^6 + \frac{1}{2}}{4 |\alpha|^2 + 1 - 72 g^2 t^2 |\alpha|^6}, \tag{71}$$

thus equations (69)–(71) show that for a fixed value of $\langle N \rangle$ as the value of $[\Delta N]^2$ decreases, minimum total noise increases which indicates the presence of quantum state.

4. Conclusion

Comparison of non-classical parameters like phase fluctuation, antibunching and minimum total noise have been done in seven and eight wave mixing interaction and third harmonic generation nonlinear optical processes. Figs. 1–4 show that reduction of phase fluctuation parameters U, S, Q and antibunching increases with increasing mean photon number $|\alpha|^2$. After comparing Figs. 1–4, we can conclude that rate of reduction of parameters U, S, Q and antibunching is maximum in third harmonic generation as compared to eight wave mixing and seven wave mixing. Equations (30)–(32), (44)–(46), (58)–(60) show that the parameter U is independent of θ while S and Q parameters can be tuned by varying the values of t and θ. The result also indicates that higher the rate of reduction of phase fluctuation parameter, higher will be the antibunching.

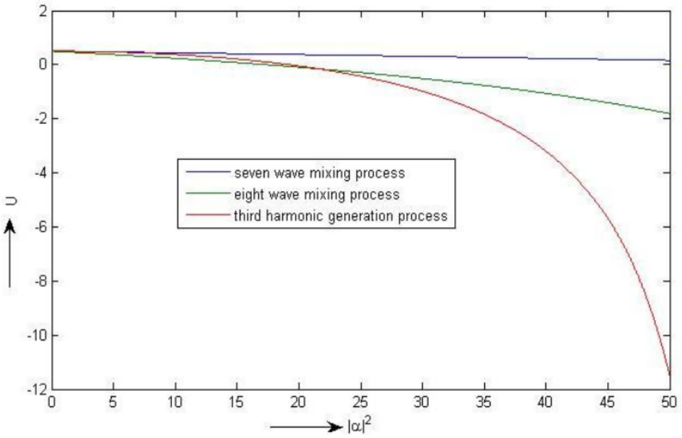

FIG. 1. Variation of phase fluctuation parameter U with $|\alpha|^2$ for seven wave mixing, eight wave mixing and for third harmonic generation (taking $g^2t^2 \approx 10^{-4}$)

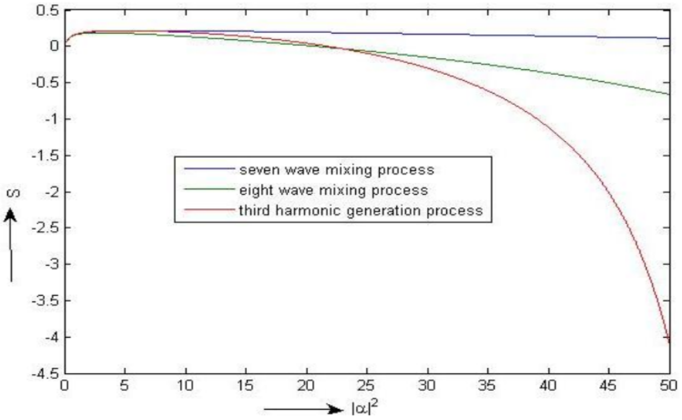

FIG. 2. Variation of phase fluctuation parameter S with $|\alpha|^2$ for seven wave mixing, eight wave mixing and for third harmonic generation (taking $g^2t^2 \approx 10^{-4}$ and $\theta = 0$)

Figures 4 and 5 show the variation of antibunching and minimum total noise with $|\alpha|^2$ and we observe that more is the antibunched state (sub-Poissonian), more will be the minimum total noise present in the system.

Thus we can conclude that the depth of non-classicality can be directly measured by using the quantum parameters i.e. phase fluctuation, antibunching and minimum total noise present in the system.

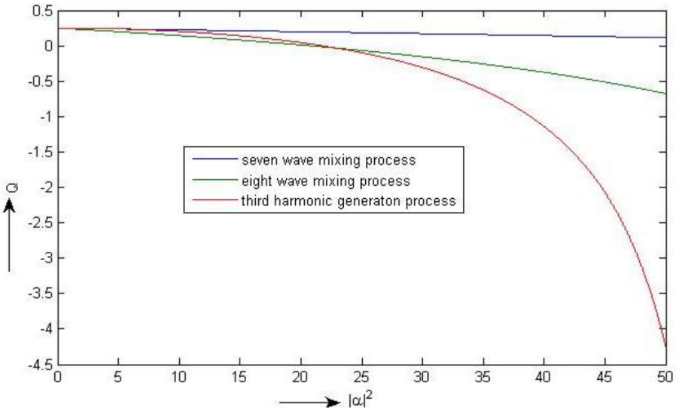

FIG. 3. Variation of phase fluctuation parameter Q with $|\alpha|^2$ for seven wave mixing, eight wave mixing and for third harmonic generation (taking $g^2t^2 \approx 10^{-4}$ and $\theta = 0$)

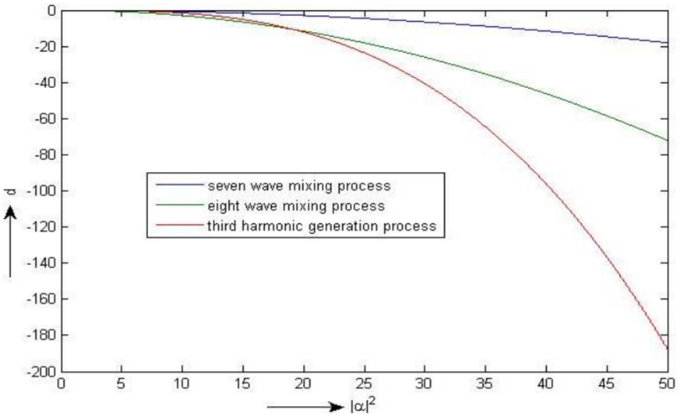

FIG. 4. Variation of d with $|\alpha|^2$ for seven wave mixing, eight wave mixing and third harmonic generation (taking $g^2t^2 \approx 10^{-4}$)

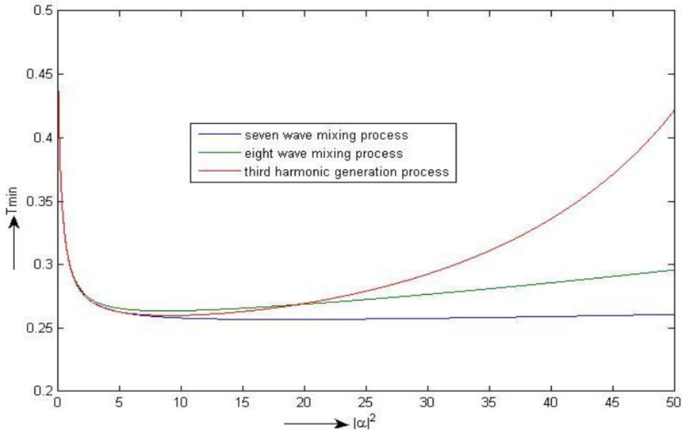

FIG. 5. Variation of $T_{\min}$ in antibunched (sub-Poissonian) state with $|\alpha|^2$ for seven wave mixing, eight wave mixing and for third harmonic generation (taking $g^2t^2 \approx 10^{-5}$)

References

[1] Meystre P., Sargent III M. *Elements of quantum optics*, Second ed., Springer, Berlin, 1999.

[2] Dodunov V.V. *Theory of nonclassical states of light*. Monko V.I. (Eds.), Taylor and Francis, New York, 2003.

[3] Orlowski A. Classical entropy of quantum states of light. *Phyical Review A*, 1993, **48** (1), P. 727–731.

[4] Lynch R. The quantum phase problem: a critical review. *Physical Review*, 1995, **256** (6), P. 367–436.

[5] Perinova V., Luks A., Perina J. *Phase in optics*, Chapter 4. World Scientific, Singapore, 1998.

[6] Ficek Z., Wahidd M.R. *Quantum optics fundamental and applications*, Chapter 4. IIUM Kuala Lumppur, 2004.

[7] Barnett S.M., Pegg D.T. Phase in quantum optics. *Journal of Physics A: Mathematical and General*, 1986, **19** (18), P. 3849–3862.

[8] Pegg D.T., Barnett S.M. Phase properties of the quantized single model electromagnetic field. *Physical Review A*, 1989, **39** (4), P. 1665–1675.

[9] Susskind L., Glogower J. Quantum mechanical phase and time operator. *Physics Physique Fizika*, 1964, **1** (1), P. 49–61.

[10] Vaccaro J.A., Pegg D.T. On measuring extremely small phase fluctuations. *Optics Commnication*, 1964, **105** (5–6), P. 335–340.

[11] Lynch R. Phase fluctuations in the coherent light anharmonic oscillator systems via measured phase operators. *Optics Communication*, 1988, **67** (1), P. 67–70.

[12] Pegg D.D., Vaccaro J.A. Phase properties of squeezed states of light. *Optics communication*, 1989, **70** (6), P. 529–534.

[13] Sanders C., Barnett S.M., Knight P.L. Phase variables and squeezed states. *Optics Communication*, 1986, **58** (4), P. 290–294.

[14] Tsui Y.K. Josephson tunneling between superconductors in the angle-operator formalism. *Physical Review B: Condensed Matter*, 1993, **47** (18), P. 12296–12299.

[15] Lynch R. Phase fluctuations in a squeezed state using measured phase operators. *Optical Society of America B*, 1987, **4** (10), P. 1723–1726.

[16] Carruthers P., Nieto M.M. Phase and angle variables in quantum mechanics. *Review Modern Physics*, 1968, **40** (2), P. 411–440.

[17] Yao D. Phase properties of squeezed states of light. *Phys. Lett. A*, 1987, **122** (2), P. 77–83.

[18] Fan H.Y., Zaidi H.R. An exact calculation of the expectation values of phase operators in squeezed states. *Optics Communication*, 1988, **68** (2), P. 143–148.

[19] Pathak A., Mandal S. Phase fluctuations of coherent light coupled to a nonlinear medium of inversion symmetry. *Physics Letter A*, 2000, **272** (5–6), P. 346–352.

[20] Verma A., Pathak A. Reduction of quantum phase fluctuation in intermediate states. *Physics Letter A*, 2009, **373** (16), P. 1421–1428.

[21] Kreibig U., Vollmer M. Optical properties of metal clusters. *Springer Series in Materials Science*, 1995, **25**, P. 278–279.

[22] Seongmin J.U., Wateker P.R., Jeong S. Nonlinear optical properties of zinc doped germane silicate glass optical fibre. *Journal Nonlinear Optical Physics Matter*, 2011, **19**, P. 791–799.

[23] Xie R.H. *Handbook of advanced electronic and photonic materials and devices*. H.S. Nalwa (Ed.), Elsevier, 2000, 9, P. 267–307.

[24] Xie R.H., Rao Q., Jensen L. *Encyclopedia of nanoscience and nanotechnology*, H.S. Nalwa (Ed.), Elsevier, 2003.

[25] Stentz A.J., Boyd R.W. *Hanbook of photonics*, M.C. Gupta (Ed.), Chapter 5. CRC Press, 1997.

[26] Wang Q., Jianfeng Xu, Xie R.H. Nonlinear optics of nanoparticles and nanocomposites. *Encyclopedia of nanoscience and nanotechnology*, H.S. Nalwa (Ed.), 2004, **8**, P. 101–111.

[27] Danilin S., Lebedev A.V. Quantum enhanced magnetometry by phase estimation algorithms with a single artificial atom. *NPJ Quantum Information*, 2018, **4**, P. 1–7.

[28] Chakraverty B.K. Quantum phase fluctuation in high $T)c$ superconductors. *Physica C*, 2000, **341–348** (1), P. 75–78.

[29] Radkevich A., Semenov A.G., Zaikin A.D. Quantum phase fluctuations and density of states in superconducting nanowires. *Physical Review B*, 2017, **96** (8), 085435.

[30] Faccioli M., Salasnich L. Gaussian quantum fluctuations in thesuperfluid Mott insulator phase transition. *Physical Review A*, 2019, **99** (2), 023614.

[31] Hillery M., Total noise and nonclassical states. *Physical Review A*, 1989, **39** (6), 2994.

NANOSYSTEMS: PHYSICS, CHEMISTRY, MATHEMATICS, 2020, 11 (2), P. 171–175

Shannon entropy associated with electrochemically generated ion concentration gradients

N. V. Ryzhkov, V. Yu. Yurova, E. V. Skorb*
ITMO University, Lomonosova, 9, St. Petersburg, 191002, Russia
*skorb@itmo.ru

PACS 82.35.Rs, 82.39.Wj, 82.45.Fk, 82.60.Lf, 89.70.+c **DOI 10.17586/2220-8054-2020-11-2-171-175**

In this work, we discuss Shannon entropy in relation to ion distribution in solutions. Shannon entropy is a key concept of information theory. Discussion of ion solutions informational entropy is essential for consideration of ions as information carriers in iontronic devices. We studied entropy associated with ions redistribution using model electrochemically triggered local ion fluxes. For this purpose, we utilized bare gold electrodes as well as covered by polyelectrolyte layers and lipids. Modification of the electrode surface leads to a change of ion flux triggered by hydroquinone oxidation. Consequently, various distribution of ions in solution can be obtained. Shannon entropy was evaluated for diverse ion distributions.

Keywords: Shannon entropy, proton fluxes, layer by layer assemblies, electrochemistry.

Received: 30 December 2019

Revised: 17 February 2020

1. Introduction

Entropy is a function that quantifies the number of microstates available to a system. Thus, thermodynamic entropy growth is a driving force for many physicochemical processes. In solutions, the number of microstates at high concentrations is less than for low concentrations. For charged species, the electrostatic driving force opposes the entropic one.

Local ion signals can easily be generated using the electrochemical approach. Spatial propagation of protons produced during hydroquinone oxidation is supposed to be a three-dimensional pH wave described by Fick's laws [1]. The driving force for ion movement is the dispersal of energy into a more probable distribution. The quinone/hydroquinone redox process is characterized by relatively low redox potential, and both compounds are chemically stable. Due to this, quinones are widely used for electrochemically controlled generation and consumption of protons [2–4].

The diffusion of oxidation products is highly affected by the structure of the electrode surface [5, 6]. Polyelectrolyte modified electrodes are of high interest [7, 8]. Layer-by-layer (LbL) polyelectrolyte assemblies containing many charged moieties do not allow ions freely pass through. Polyelectrolyte protonation/deprotonation phenomenon is involved in ion pathways. A wide variety of applications are offered for LbL-assembled coatings and capsules. The LbL approach provides a versatile instrument for multilayer formation with the incorporation of variously charged compounds [8, 9]. Polyelectrolyte multilayers are widely used in the design of biomaterial surface coatings [10, 11], membranes for separation, as well as cargoes for drug encapsulation and delivery [12].

Thus, polyelectrolyte LbL assemblies can be considered as a convenient tool for regulation of ion signal transduction. Polyelectrolyte layers in multi-layered structures are not perfectly stratified, and polymer chains of polycations and polyanions are significantly interpenetrated [13]. Much attention is attracted to the dynamics and internal structure of polyelectrolyte multilayers and the phenomenon of internal diffusion [14, 15]. Various parameters, such as ionic strength [16], charge density [17], pH, and temperature [18], affect polyelectrolyte film internal structure, and several diffusion models in ultrathin polyelectrolyte films are described [19, 20]. Except for permeability and non-permeability, ions accumulation mode was also identified. Polyelectrolyte membrane permeability depends not only on the thickness, but also on film composition [21]. Multilayers composed solely of weak polyelectrolytes tend to transport small molecules or ions more preferably than ones assembled from strong polyelectrolytes [22]. Ion flux through polyelectrolyte membrane is also significantly affected by its stoichiometry, and excess of some component (polycation, or polyanion) affects ion permeability significantly [23]. Thus, the spatial and temporal distribution of electrochemically generated ionic fluxes can be easily tuned by polyelectrolyte membrane assembled from molecules with different molecular weights, strength, specific functional moieties.

Signal generation, storing and transmission via spatial and temporal ion distribution is a basis of iontronics, an emerging technology utilizing precise ion manipulation for information processing. An essential concept of information theory is Shannon entropy, which is a measure of the uncertainty amount. This study is devoted to establishing the relationship between ionic concentration in solution and Shannon entropy. Protons and hydroxide ions seem to be promising for the implementation of a chemical computer. These complementary particles neutralize each other when they are present simultaneously. Thus, it is possible to introduce a subtraction operation atypical for ‘chemical arithmetic’ [24]. Shannon entropy of solutions with various proton and hydroxide content is evaluated here.

2. Materials

Branched PEI (Mw 70 kDa) 30 % water solution purchased from Alfa Aesar; poly(sodium 4-styrene sulfonate) (PSS, Mw 500 kDa) purchased from Polysciences Inc.; liquid soya lecithin Lecisoy 400 containing mostly phosphatidylcholines obtained from Cargill, USA; reagent grade NaCl (99.5 %) obtained from Merck and hexane from Ekos-1, Russia. All chemicals were used as received without any additional purification. Gold wire, 0.2 mm in diameter, was purchased from Agar (UK). Pieces of gold wire of 2 – 3 cm length were embedded in epoxy resin so that circular cross-section of gold wire exposed to outside media on the flat surface of the obtained holder (Fig. 1a). The deposition of the polyelectrolyte cushion onto the gold microelectrode embedded in the epoxy resin was performed using the classical LbL technique. 2 mg/ml each PEI and PSS was dissolved in 0.5 M aqueous NaCl to make polycation and polyanion solutions, respectively. A total of seven layers were deposited, resulting in a $[PEI/PSS]_3/PEI$ polyelectrolyte multilayer. Lecithin vesicles were obtained according to classical rehydration technique [25]. And lipid bilayer deposited from vesicles suspension [25] forming a continuous bilayer.

3. Ion concentration measurements

Proton flux was triggered at the solid-liquid interface by the oxidation of 60 mM hydroquinone solutions in 150 mM KNO_3 at a constant electric current of 5 mA at gold microelectrode embedded in epoxy resin. The concentration of protons close to the surface of gold microelectrode was investigated using Scanning Ion-Selective Electrode Technique (SIET). This instrumentation is based on potentiometric principles which allows characterizing local ionic currents in solution and ion concentration gradient measurement [26] (Fig. 1b). A glass capillary microelectrode filled by an ion-selective membrane in the tip scans the surface, measuring extremely low concentrations of a particular ion with micrometer spatial resolution (Fig. 1c). A system from Applicable Electronics (USA) modulated by an ASET program (Sciencewares, USA) was used to perform SIET measurements. SIET pH measurements were carried out using glass capillary microelectrodes filled with Hydrogen Ionophore Cocktail I (Sigma) and KCl + KH_2PO_4 internal solution. Ag/AgCl/KCl (sat) was used as the external reference electrode.

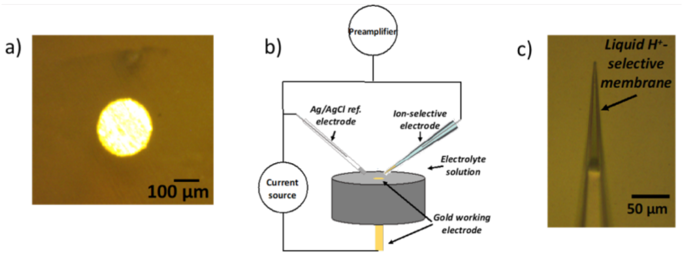

FIG. 1. a) Top view of gold electrode embedded in epoxy resin, b) Scheme of SIET measurement, c) microphotography of glass capillary proton-sensitive electrode

The pH-selective microelectrodes were calibrated using commercially available pH buffers. The local activity of H^+ was detected 25 mm above the surface and mapped on an 11×11 grid.

4. Results and discussion

Electron transfer in the quinone-hydroquinone system is associated with proton transfer. When hydroquinone is oxidized electrochemically, acidification of the near-electrode region occurs. A two-step hydroquinone oxidation was performed at a gold microelectrode surface (Fig. 2a).

Cyclic voltammetry curves were not affected by the further deposition of polyelectrolyte layers and lipid layer formation (Fig. 2a). Since molecules of hydroquinone and quinone are rather small and uncharged, they can pass freely through polyelectrolyte/lipid layer, and multilayer assembly on top of electrodes leads to no change in redox processes at the electrode/hydroquinone solution interface.

Zwitterionic lipids can adsorb protons;thus, at neutral conditions, phosphate groups exist in a deprotonated state. As some components of soy lecithin, in this case, carry an only negative charge, which is not compensated by the positive amine group (e.g., phosphatidylinositol and phosphatidic acid) [27], there is a net negative charge for the lipid

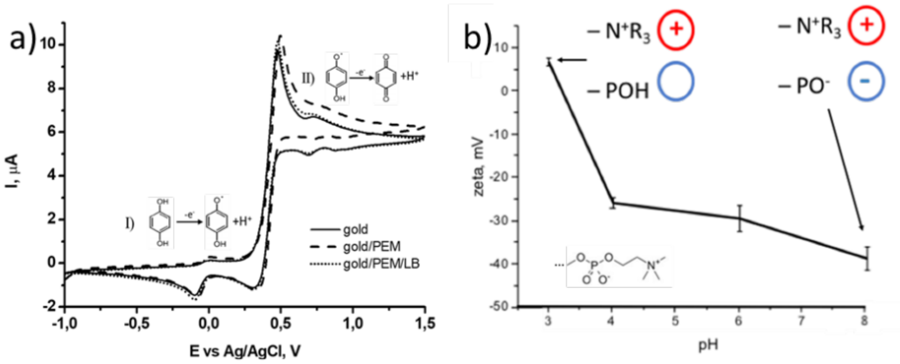

FIG. 2. a) Cyclic voltammetry curves of hydroquinone on a pure gold electrode and a gold electrode covered by a polyelectrolyte multilayer and polymer cushioned lipid layer, b) ζ-potential of lipid vesicles obtained from soy lecithin at different pH adjusted by diluted HCl and NaOH solutions

structures. In acidic media, due to protonated phosphate groups, a positive net charge occurs. The pH-dependence lipid's charge was demonstrated by vesicles ζ-potential measurements (Fig. 2b).

SIET measured ion concentration and obtained pH maps were recalculated to entropy maps for pristine gold working electrode (WE) (Fig. 3a), WE covered with polyelectrolyte multilayers gold/(PEI/PSS)$_3$/PEI (Fig. 3b), and WE covered with polyelectrolyte multilayers and lipid layer on top gold/(PEI/PSS)$_3$/PEI/lipid (Fig. 3c).

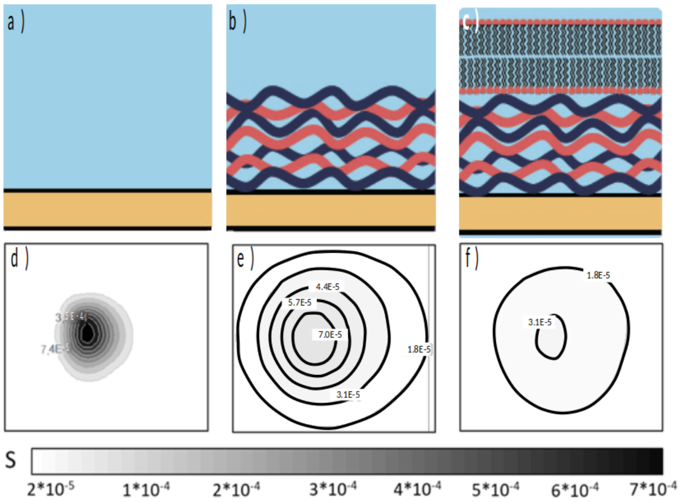

FIG. 3. a) Pristine gold electrode, b) gold electrode covered by polyelectrolyte multilayer gold/(PEI/PSS)$_3$/PEI, c) polyelectrolyte modified gold electrode with lipid bilayer deposited on top gold/(PEI/PSS)$_3$/PEI/LB, d–f) recalculation of pH maps registered by SIET into Shannon's entropy for (d) pristine gold working electrode, e) gold working electrode covered with polyelectrolytes gold/(PEI/PSS)$_3$/PEI, and f) gold working electrode covered with polyelectrolytes and lipid bilayer gold/(PEI/PSS)$_3$/PEI/LB; process occurring at electrode is oxidation of hydroquinone associated with proton flux; lines connect points with equal measured entropy values

Shannon's entropy is a fundamental concept of information theory. This value is a measure of unpredictability of the state, which is equal to its average information content. Since ions are good candidates to perform chemical calculations, we consider electrochemically generated ion fluxes in terms of Shannon entropy, which is a crucial concept of information theory.

Self-organization processes are closely related to entropy change [6]. Entropy change usually relates to a change of thermodynamic parameters such as temperature and pressure or chemical parameters. In the case of electrochemically driven ion flux, the changes in temperature and pressure in the system are negligible, while ion-distribution in the solution is disturbed

Spatial redistribution of protons takes place self-consistently and occurs together with a redistribution of local electric potential during the minimization of the system free-energy. Therefore, the self-organization and the redistribution of pH-fields are directly associated with each other and, thus, the change of entropy can be illustrated using the fields of pH.

Shannon's entropy is defined as:

$$S = -\sum_{i=1}^{n} p_i \log_2 p_i, \tag{1}$$

where $0 \leq p_i \leq 1$ is the probability of measuring some observable value i [28].

For instance, p can be related to the probability of some molecular dipole orientation or electric charge in case of electric systems, an electron spin orientation or magnetic polarization in magnetic systems, a particular state of photons in optical systems, or concentration of chemicals in reacting systems [29]. In the same manner, this approach could be naturally expanded to solutions, to consider p in sense of probability that an observed ion in the solution is an H^+ or OH^- ion (whose concentrations are related with each other). The physical sense of the probability p depends on the particular system's nature. We are interested in a system of H, OH and non-dissociated water only. In accordance with this, we will consider the Shannon entropy for this subsystem only. From the concentration of ions, we can calculate the probability p_H and p_{OH} of finding them at a certain point. In other words, we may use the parts of H^+ and OH^- ions as the probabilities p_H and p_{OH}, to calculate corresponding contributions to the Shannon's entropy associated with the pH in a given spatial area of measurement. Hence, considering only the entropy subsystem containing H, OH and water, Shannon's entropy associated with the measured pH in a particular spatial area can be calculated as follows:

$$S = -\Big(p_H \log_2 p_H + p_{OH} \log_2 p_{OH} + (1 - p_{OH} - p_H) \log_2 (1 - p_{OH} - p_H)\Big). \tag{2}$$

The last term takes into account the contribution provided by other molecules which we do not measure in experiment (H_2O).

The probability of observing proton, hydroxide-ion or non-dissociated water in a solution is related to its concentration, i.e. pH as:

$$p_H = C_H / C_0 = 10^{-pH}, \tag{3}$$

where $C_0 = 1M$ is a normalizing concentration. For OH^- anions, we have:

$$p_{OH} = C_{OH} / C_0 = 10^{-pOH} = 10^{pH-14}, \tag{4}$$

since $pH + pOH = 14$ in water solutions and $p_{H_2O} = 1 - p_H - p_{OH}$. From here, by substitution of these expressions for p into the equation (2), we obtain Shannon's entropy contribution associated with p_H measured in a small volume:

$$S = -\Big(10^{-pH} \log_2 10^{-pH} + 10^{pH-14} \log_2 10^{pH-14} + (1 - 10^{pH-14} - 10^{-pH}) \log_2 (1 - 10^{pH-14} - 10^{-pH})\Big). \tag{5}$$

The first two terms here are associated with the H and OH subsystems, whereas the last one is due to the (subsystem of) non-dissociated water molecules. In vicinity of the neutral pH, the last term provides about 6 %, while the main contribution is provided by:

$$S \approx -(10^{-pH} \log_2 10^{-pH} + 10^{pH-14} \log_2 10^{pH-14}), \tag{6}$$

that we used for the illustration of the experiments in Fig. 3, without losses of the conclusion generality related to the engineering of a given pH distribution with polyelectrolytes.

Usually, as a substance becomes more dissipated, the thermal energy carried by this substance also spreads over volume, followed by entropy. Meanwhile, Shannon entropy associated with pH being dependent on complementary proton and hydroxide-ion concentration is not a monotonous function. The function described by the equation above exhibits a local minimum at pH = 7. The summation of Shannon entropy values can estimate overall entropy for the particular spatial distribution of protons (i.e., distribution of the system states) overall points of the system.

The approach based on the equation above is convenient for analysis of self-organization phenomena (related to change in pH-distributions) and their interpretation in terms of entropy fields. This can be illustrated using the results of our measurements of pH fields in different systems.

Considering the system described above, we can easily vary ion distribution. For instance, taking the spatial distribution of cations determined experimentally in cases of a bare electrode, as well as for electrode covered by polyelectrolyte multilayer $(PEI/PSS)_3$ and lipid bilayer, we obtained the spatial distributions of entropy $S(x, y)$ represented in Figs. 3(a–c). Interestingly, a huge difference is observed for obtained the spatial distributions of entropy that can be associated with various soft matter components for controlling ion fluxes.

5. Conclusion

A model electrochemical system creating local ion-fluxes was demonstrated. The LbL assembly of polyelectrolyte multilayers is suggested as an instrument to control horizontal and vertical ion propagation with the ability to correlate it with the spatial distributions of entropy. In contradistinction to thermodynamic entropy, informational Shannon entropy associated with decreased ionic redistribution with solution dilution. The spatial distribution of Shannon entropy was studied for ion fluxes generated electrochemically.

Acknowledgements

This work is supported by RSF Grant No. 17-79-20186. EVS also thanks the ITMO Fellowship Professorship Program for Infrastructural Support. The authors thank Prof. Stanislav O. Yurchenko (BMSTU, Moscow) for the discussion of entropy analysis.

References

[1] Fomina N., Johnson C.A., et al. An electrochemical platform for localized pH control on demand. *Lab Chip.*, 2016, **16**, P. 2236–2244.

[2] Garnier T., Dochter A., et al. Surface confined self-assembly of polyampholytes generated from charge-shifting polymers. *Chem. Commun.*, 2015, **51**, P. 14092–14095.

[3] Dochter A., Garnier T., et al. Film Self-Assembly of Oppositely Charged Macromolecules Triggered by Electrochemistry through a Morphogenic Approach. *Langmuir*, 2015, **31** (37), P. 10208–10214.

[4] Ryzhkov N.V., Mamchik N.A., Skorb E.V. Electrochemical triggering of lipid bilayer lift-off oscillation at the electrode interface. *J. R. Soc. Interface*, 2019, **16** (150), 20180626.

[5] Maza E., Tuninetti J.S., et al. pH-responsive ion transport in polyelectrolyte multilayers of poly(diallyldimethylammonium chloride) (PDADMAC) and poly(4-styrenesulfonic acid-co-maleic acid) (PSS-MA) bearing strong- and weak anionic groups. *Phys. Chem. Chem. Phys.*, 2015, **17**, P. 29935–29948.

[6] Ryzhkov N.V., Nesterov P., et al. Localization of ion concentration gradients for logic operation. *Front. Chem.*, 2019, **7**, 419.

[7] Ryzhkov N.V., Andreeva D.V., Skorb E.V. Coupling pH-Regulated Multilayers with Inorganic Surfaces for Bionic Devices and Infochemistry. *Langmuir*, 2019, **35** (26), P. 8543–8556.

[8] Ryzhkov N.V., Brezhneva N., Skorb E.V. Feedback mechanisms at inorganic polyelectrolyte interfaces for applied materials. *Surf. Innov.*, 2019, **7** (3–4), P. 145–167.

[9] Decher G., Eckle M., Schmitt J., Struth B. Layer-by-layer assembled multicomposite films. *Curr. Opin. Colloid Interface Sci.*, 1998, **3** (1), P. 32–39.

[10] Zhukova Y., Hiepen C., et al. The Role of Titanium Surface Nanostructuring on Preosteoblast Morphology, Adhesion, and Migration. *Adv. Healthc. Mater.*, 2017, **6** (15), 1601244.

[11] Rmaile H.H., Farhat T.R., Schlenoff J.B. pH-gated Permeability of Variably Charged Species through Polyelectrolyte Multilayer Membranes. *J. Phys. Chem. B*, 2003, **107** (51), P. 14401–14406.

[12] Nikitina A.A., Ulasevich S.A., et al. Nanostructured Layer-by-Layer Polyelectrolyte Containers to Switch Biofilm Fluorescence. *Bioconjug. Chem.*, 2018, **29** (11), P. 3793–3799.

[13] Schönhoff M. Self-assembled polyelectrolyte multilayers. *Curr. Opin Colloid Interface Sci.*, 2003, **8** (1), P. 86–95.

[14] Selin V., Ankner J.F., Sukhishvili S.A. Nonlinear Layer-by-Layer Films: Effects of Chain Diffusivity on Film Structure and Swelling. *Macromolecules*, 2017, **50** (16), P. 6192–6201.

[15] Fares H.M., Schlenoff J.B. Diffusion of Sites versus Polymers in Polyelectrolyte Complexes and Multilayers. *J. Am. Chem. Soc.*, 2017, **139** (41), P. 14656–14667.

[16] Steitz R., Leiner V., Siebrecht R., Klitzing R. Influence of the ionic strength on the structure of polyelectrolyte films at the solid/liquid interface. *Colloids Surfaces A Physicochem. Eng. Asp.*, 2000, **163** (1), P. 63–70.

[17] Steitz R., Jaeger W., Klitzing R. Influence of charge density and ionic strength on the multilayer formation of strong polyelectrolytes. *Langmuir*, 2001, **18** (4), P. 1408–1412.

[18] Karg M., Pastoriza-Santos I., et al. Temperature, pH, and ionic strength induced changes of the swelling behavior of PNIPAM-poly(allylacetic acid) copolymer microgels. *Langmuir*, 2008, **24** (12), P. 6300–6306.

[19] Klitzing R., Möhwald H. A realistic diffusion model for ultrathin polyelectrolyte films. *Macromolecules*, 1996, **29** (21), P. 6901–6906.

[20] Farhat T.R., Schlenoff J.B. Ion transport and equilibria in polyelectrolyte multilayers. *Langmuir*, 2001, **17** (4), P. 1184–1192.

[21] Hoshi T., Saiki H., Anzai J.I. Amperometric uric acid sensors based on polyelectrolyte multilayer films. *Talanta*, 2003, **61** (3), P. 363–368.

[22] Fu J., Fares H.M., Schlenoff J.B. Ion-Pairing Strength in Polyelectrolyte Complexes. *Macromolecules*, 2017, **50** (3), P. 1066–1074.

[23] Kelly K.D., Fares H.M., Abou Shaheen S., Schlenoff J.B. Intrinsic Properties of Polyelectrolyte Multilayer Membranes: Erasing the Memory of the Interface. *Langmuir*, 2018, **34** (13), P. 3874–3883.

[24] Banda P., Teuscher C., Stefanovic D. Training an asymmetric signal perceptron through reinforcement in an artificial chemistry. *J. R. Soc. Interface*, 2014, **11** (93), 20131100.

[25] Diamanti E., Gregurec D., et al. Lipid layers on polyelectrolyte multilayers: Understanding lipid-polyelectrolyte interactions and applications on the surface engineering of nanomaterials. *J. Nanosci. Nanotechnol.*, 2016, **16** (6), P. 5696–5700.

[26] Souto R.M., Lamaka S.V., González S. Uses of Scanning Electrochemical Microscopy in Corrosion Research. In: *Microscopy: Science, Technology, Applications and Education*, 2010.

[27] Scholfield C.R. Composition of Soybean Lecithin. *J. Am. Oil Chem. Soc.*, 1981, **58** (10), P. 889–892.

[28] Shannon C.E. A Mathematical Theory of Communication. *Bell Labs Tech. J.*, 1948, **27** (3), P. 379–423.

[29] Haken H. *Information and Self-Organization. A Macroscopic Approach to Complex Systems*. Springer, Berlin, 2006, 257 p.

NANOSYSTEMS: PHYSICS, CHEMISTRY, MATHEMATICS, 2020, 11 (2), P. 176–182

Electronic transport in penta-graphene nanoribbon devices using carbon nanotube electrodes: A computational study

M. Shunaid Parvaiz[1,2], Khurshed A. Shah[1,*], G. N. Dar[2], Sugata Chowdhury[3], Olasunbo Farinre[3], Prabhakar Misra[3]

[1]Department of Physics, S. P. College Campus, Cluster University, Srinagar, J&K-190001, India

[2]Department of Physics, University of Kashmir, Srinagar, J&K-190006, India

[3]Department of Physics and Astronomy, Howard University, Washington, DC 20059, USA

*drkhursheda@gmail.com

DOI 10.17586/2220-8054-2020-11-2-176-182

Electronic transport properties of pristine, homogenously and heterogeneously boron-nitrogen doped saw-tooth penta-graphene nanoribbon (SPGNR) with carbon nanotube electrodes have been studied using Extended Huckel Theory in combination with the non-equilibrium Green's function formalism. CNT electrodes produce a remarkable increase in current at higher bias voltages in pristine SPGNR. The current intensity is maximum at higher bias voltages, while the nitrogen-doped model shows current from the onset of the bias voltage. However, there are also considerable differences in the I-V curves associated with the pristine model and other models doped homogenously as well as heterogeneously with boron and nitrogen. The doped models also exhibit a small negative differential resistance effect, with much prominence in the nitrogen-doped model. In summary, our findings show clearly that doping can effectively modulate the electronic and the transport properties of penta-graphene nanoribbons that have not been studied and reported thus far.

Keywords: Penta-graphene nanoribbon, CNT, NEGF, EHT, Doping, ATK.

Received: 10 March 2020

Revised: 23 March 2020

1. Introduction

Carbon is one of the most interesting elements, having a number of allotropes like graphite, diamond, fullerene, nanotube, C_{60} and graphene [1]. After the successful synthesis of graphene, significant research has been conducted in characterizing carbon-based nanomaterials [2–5]. A large number of 2D carbon allotropes are being studied. Although some of the polymorphs, such as graphdiyne, are metastable compared with graphene, they have been successfully synthesized [6]. Some of the 2D allotropes of carbon are being researched for their interesting properties that are an improvement on graphene, such as anisotropic Dirac cones, ferromagnetic nature, high catalytic behavior and high superconductivity, due to the high density of states at the Fermi level [7–9]. These results reveal that the novel properties of carbon allotropes are related to the topological arrangement of carbon atoms and thus highlight the importance of structure-property relationships [10].

Carbon nanostructures are based on two important structural motifs, namely pentagons and hexagons. The hexagon is the building block of zero-dimensional nanoflakes, nanotube, graphene, graphite and metallic carbon phases [11–13]. Carbon materials composed of pentagons are rarely found. Carbon pentagons are generally known as topological defects, or geometrical frustrations, as stated in the well-known "isolated pentagon rule" (IPR) for fullerenes, where pentagons must be separated from each other by neighboring hexagons to reduce the steric stress [14, 15]. For example, C_{60} is made up of 12 pentagons separated by 20 hexagons resembling the shape of a soccer ball, explaining the IPR rule perfectly. In some examples, the existence of carbon pentagons is also accompanied by carbon heptagons, which are separated from one another [14]. The synthesis of pentagon-based C_{20} cage has inspired many researchers and considerable research has been done to stabilize pentagon-based and non-IPR carbon materials of different dimensionalities [16]. Some non-IPR fullerenes have also been experimentally synthesized [15]. During the growth of 2D carbon sheets, a "pentagon first" mechanism was brought into play in order to transform sp carbon chains to sp^2 carbon rings [17]. Therefore, we wanted to pursue the idea of building a penta-graphene carbon sheet using fused pentagons as structural motivation. The dynamical, thermal, and mechanical stability of such a structure has been confirmed in a series of publications [18–24]. Moreover, Zhang and coworkers [12] have reported the thermal and mechanical stability of pentagon-based carbon nanotubes (CNTs). Additionally, Avramov et al. [25] have reported the binding energy per atom for (n, n) penta-graphene based carbon nanotubes (CNTs), confirming that the (7,7) penta-graphene based CNT is the most energetically stable structure. Pentagraphene is an attractive material for optoelectronic applications, because it is a semiconductor with a quasi-direct band gap. Additionally, it has a reduced thermal conductivity as compared to graphene and is an auxetic material which means it has a negative Poisson's ratio.

Furthermore, many properties of pentagraphene can be tuned by doping and functionalization, therefore it will be an exciting material in the coming times.

In the present work, we investigate the electrical property of a new carbon allotrope, penta-graphene, consisting entirely of pentagons, within the framework of Extended Huckel theory (EHT). As far as we are aware, we show for the first time that the penta-graphene nanoribbon contacted with CNT electrodes exhibit higher current and conductance values as compared to similar pristine pentagraphene nanoribbon (PGNR) with PGNR electrodes as reported by Tien, et. al. [26]. Also, its boron-nitrogen doped versions sandwiched between two carbon nanotube electrodes exhibit interesting electronic properties that are different than those reported in previous studies cited earlier. The current paper is organized from here on as follows: Section II describes the models and methods employed in the study, Section III presents the results and discussion, and concluding remarks are presented in Section IV.

2. Models and methods

In the present study, we have modeled a saw-tooth penta-graphene nanoribbon (SPGNR) based on a two-probe system attached with two (4,0) zig-zag CNT electrodes using the Atomistic Toolkit (ATK) (version P-2019.03) software and its graphical interface virtual nanolab [27], as shown in Fig. 1. CNT electrodes have been used in previous research work designed to study the electronic properties of various devices [28].

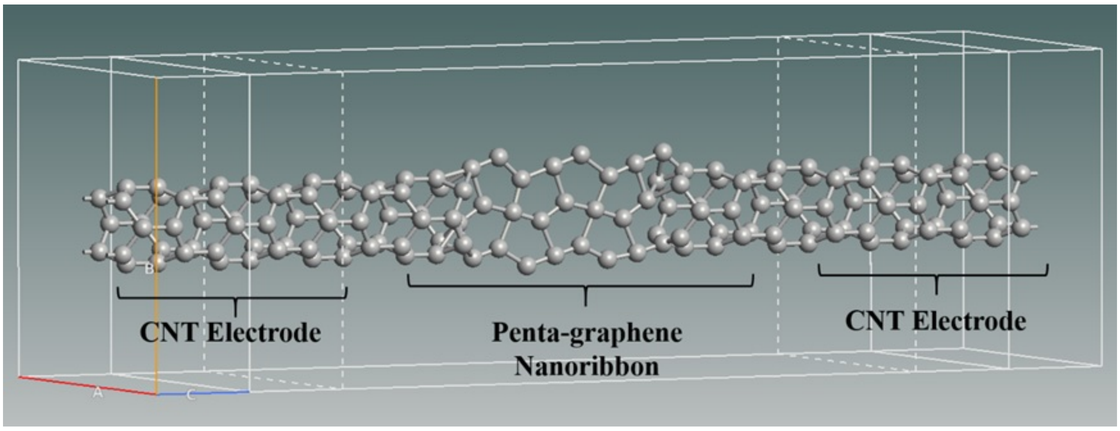

FIG. 1. The computational model of SPGNR with CNT electrodes

In order to understand the behavior of the PGNR-based system for comparative studies, we substitutionally doped the scattering region of the device with 4 atoms of boron and nitrogen, both homogenously and heterogeneously, as illustrated in Fig. 2(a,b,c). In all simulated models, both electrodes consist of 16 atoms each, and the central scattering region consists of 120 atoms. The central scattering region was taken as 30 Å and the length of the two electrodes was set at 4.263 Å each. To overcome the scattering losses, 10% of the length of electrodes was considered as the scattering region.

Here, we have based our hypothesis on the Non-Equilibrium Green's Function (NEGF) formalism and used the single particle approach based on the Landauer–Buttiker formalism to determine the current [29]

$$I = \frac{2e}{h} \int\limits_{-\infty}^{+\infty} T(E, V_b) \left[f(E - \mu_L) - f(E - \mu_R) \right] dE, \tag{1}$$

where $T(E, V_b)$ is the transmission function at energy E and voltage V_b, and $f(E-\mu_L)$ and $f(E-\mu_R)$ are the Fermi distribution functions of the left and right electrodes, respectively.

The models used in the study were simulated using Huckel parameters with an electrode temperature of 300 K. The Density mesh cut-off was set to 55 Hartee. The set of k-points were chosen as 1, 1, 125 for appropriate sampling. The maximum range for the interaction was taken as 10 Å and the Fourier2D solver was adopted as the Poisson solver for the boundary conditions. The applied bias across the two electrodes was varied from 0 to 2 V in order to analyze the current and the transmission spectra. Table 1 summarizes the calculation parameters used for the simulation associated with the model.

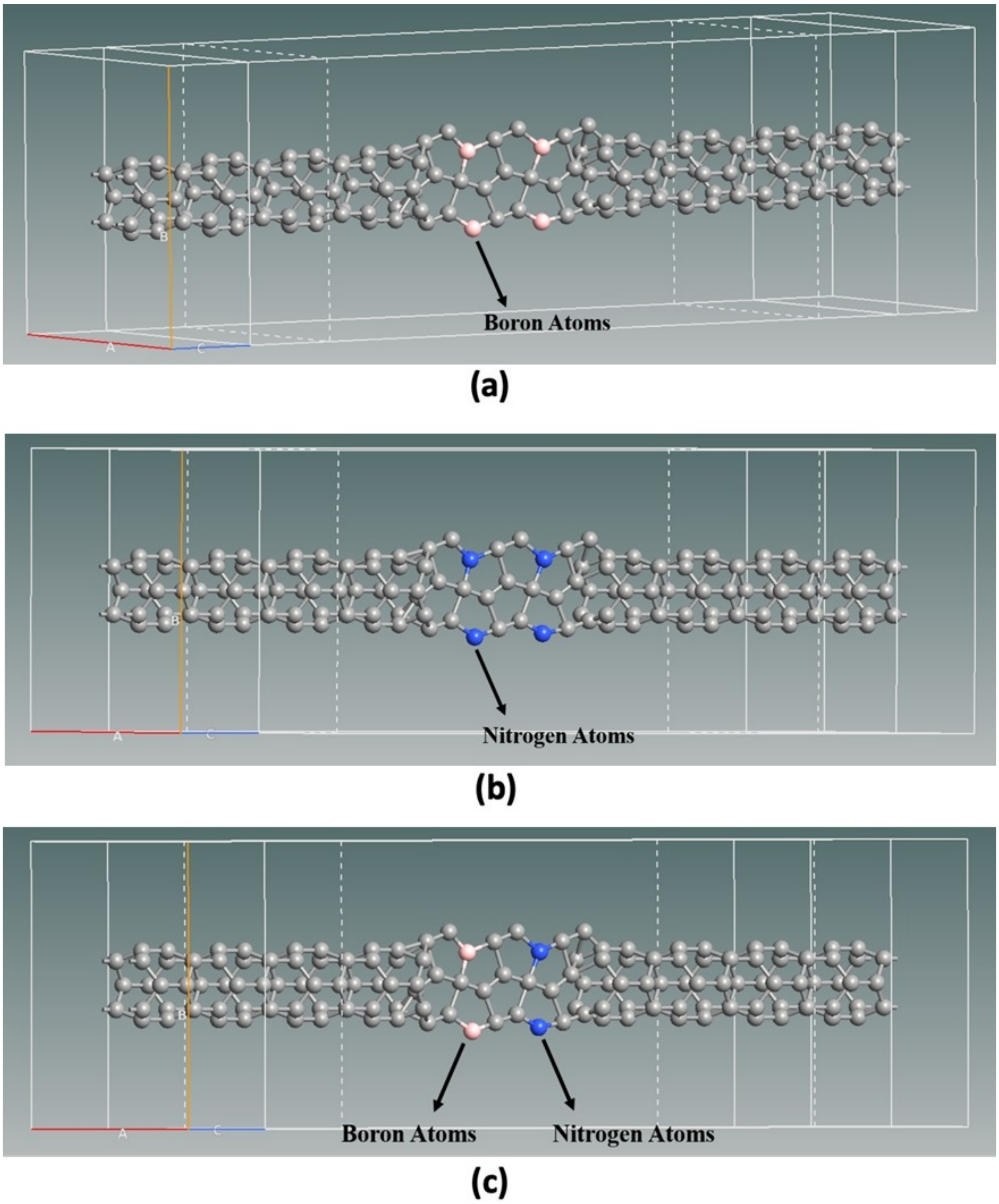

FIG. 2. PGNR models doped with (a) boron atoms, (b) nitrogen atoms, and (c) both boron and nitrogen atoms

TABLE 1. Simulation parameters associated with the model

Parameter	Value
Calculator	Semi Empirical
Formalism	Extended Huckel Theory (EHT)
Density mesh cut-off	55 Hartree
k-point sampling	1 × 1 × 125
Maximum Steps	100
Step Size	0.01 nm
Poisson Solver	Fourier2D solver
Electrode Temperature	300 K
Device Algorithm Formalism	Non-equilibrium Green's Function (NEGF)

3. Simulation results

All the proposed models were simulated in device mode using the ATK software and its graphical interface, Virtual Nanolab, in order to study the transport properties and the effect of different doping atoms on the conductance of the CNT contacted PGNR two-probe system. All of the structures were fully relaxed in order to make the residual forces on each atom smaller than 0.05 eV/Å. In order to achieve the requisite results, we analyzed the projected device density of states (PDDoS) and transmission spectra of all models and plotted the I-V curves and conductance curves under different bias voltages. Fig. 3 shows the projected PDDoS of the proposed models. In case of pristine SPGNR, the states of C atoms are almost non-existent in the energy zone, with a similar trend in all models doped with B. In the case of N-SPGNR, new electronic states of N atoms are observed in the energy zone corresponding to the band gap of the pristine SPGNR, and thereby reducing the band gap. This in turn also results in the change of the band structure leading to a high current in N-SPGNR at low applied voltages. It is observed that the alteration in band structure is mainly dependent upon the doped element and not on the electronic distribution from the dopants [30].

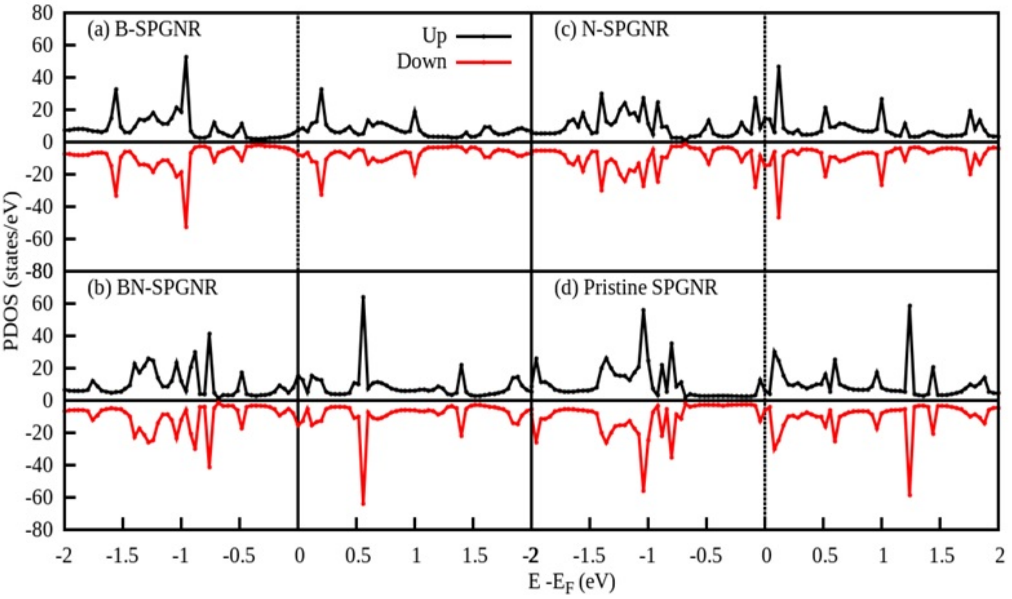

FIG. 3. Projected Device Density of States (PDDoS) for (a) B-SPGNR (b) BN-SPGNR (c) N-SPGNR, and (d) Pristine SPGNR

Figure 4(a) shows the I–V curves of pristine, boron-doped, nitrogen-doped and heterogeneously boron-nitrogen doped systems, respectively. The results show that the pristine SPGNR model produces the maximum current at higher applied voltages, while the nitrogen- doped model produces a high current at lower applied voltages. Using CNT electrodes results in a remarkable increase in current at higher bias voltages in pristine SPGNR, as compared to other reports [26]. The possible mechanism for this behavior is due to the fact that the CNT exhibits a ballistic transport property and acts as an efficient charge injecting electrode in this model due to negligible contact resistance associated with the C-C bonds of the CNT electrodes and the SPGNR scattering region. At higher applied voltages, the charge transfer from the CNT electrodes is so high that a bandgap reduction takes place in the SPGNR, resulting in high output current. For pristine, boron-doped and heterogeneously boron-nitrogen doped models, the current changes slightly as the bias voltage increases from 0 V to 0.6 V. The current behavior of the pristine penta-graphene system starts to increase at a bias voltage of 0.8 V, reaches its maximum at 1.6 V and then decreases afterwards. In the boron-doped model, the first peak appears at 1.0 V, followed by a sharp increase in current reaching its maximum value at 1.6 V and then decreasing to its minimum at 2.0 V. A similar trend is observed in the BN-doped model, where the current starts to increase at 0.8 V, forming one peak at 1.4 V and then reaching up to the highest value at 1.8 V. However, the current intensity in these three models is high with peak intensity of 13.774 μA in the pristine model. On the other hand, the current intensity of the nitrogen-doped model increases linearly with the bias voltage from 0 V to 0.8 V; the current then decreases at 1.0 V and subsequently increases again at 1.2 V and remains almost constant with the rest of the bias voltage. This variation of current with the bias voltage is due to the difference in electronic scattering of different dopant atoms. Nitrogen has five outer electrons, which means that it will have free electrons in the doped penta-graphene nanoribbon configuration; this in turn results in a high electron density, thereby explaining the high value of current at low bias.

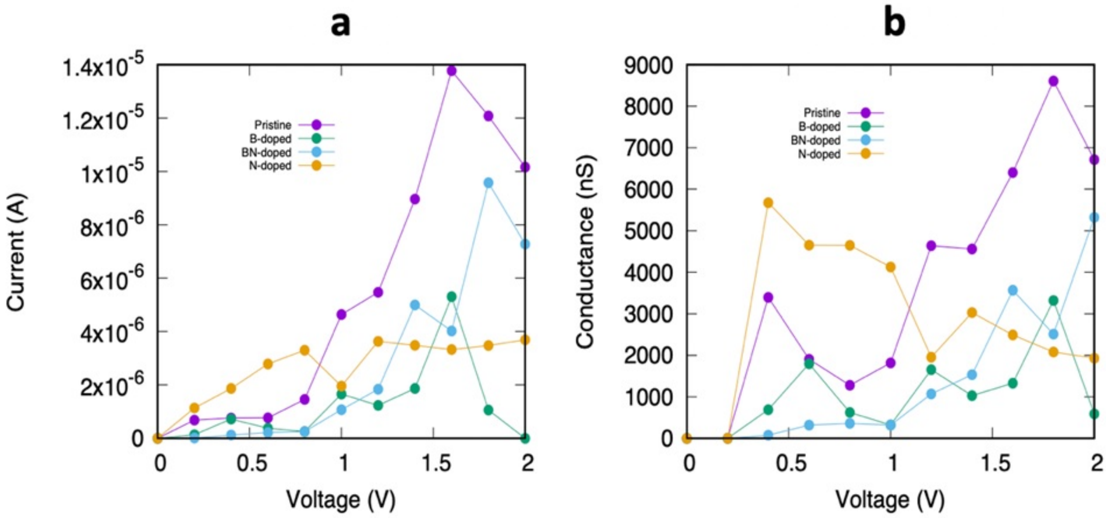

FIG. 4. (a) I–V curves of Pristine SPGNR, B-SPGNR, BN-SPGNR and N-SPGNR (b) Conductance curves of Pristine SPGNR, B-SPGNR, BN-SPGNR and N-SPGNR

Figure 4(b) gives a comparison between the conductance of the proposed models, showing that the nitrogen-doped model has a higher conductance at low voltages while the pristine model shows increased conductance at higher bias voltages. It is important to mention here that penta-graphene is an indirect band-gap semiconductor with a band gap of 3.25 eV and the electronic states near the Fermi level originate from the sp^2 hybridized carbon atoms. The sp^3 hybridized carbon atoms spatially separate the p$_z$ orbitals of the sp^2 hybridized carbon atoms, which screens the full electron delocalization leading to a finite bandgap. The non-dispersive partially degenerate valence bands give high density of states near the Fermi level, thereby leading to high conductance.

In order to further understand the obtained I–V curves of the studied systems, we examined the transmission spectra of the modelled systems at a bias voltage of 0.8 V, as shown in Fig. 5. $T(E)$ almost remains unchanged with the increasing bias voltage to 0.8 V. Nevertheless, there exist higher coefficients at the bias windows from 1.0 V that leads to the current fluctuation. The outcomes show a strong influence of the transmitted spectrum on the I–V characteristics of the two-probe system. In the nitrogen-doped model, it is observed that the transmittance peaks are present in all the displayed voltages, as compared to other models, showing a strong impact of the transmission spectrum on the I–V characteristics of the two-probe model.

Furthermore, our results show a small negative differential resistance (NDR) behavior in the doped penta-graphene models. The NDR effect is most prominent in the nitrogen doped model. As the voltage is applied, the current arises due to the electrons in the pertinent states and the transmission coefficient in the bias range. The transmission occurs due to the electronic band-to -band tunneling, which is possible only when the bands are shifted in the order of the semiconductor energy gap. In the present investigation, we are using the semiconducting penta-graphene nanoribbon

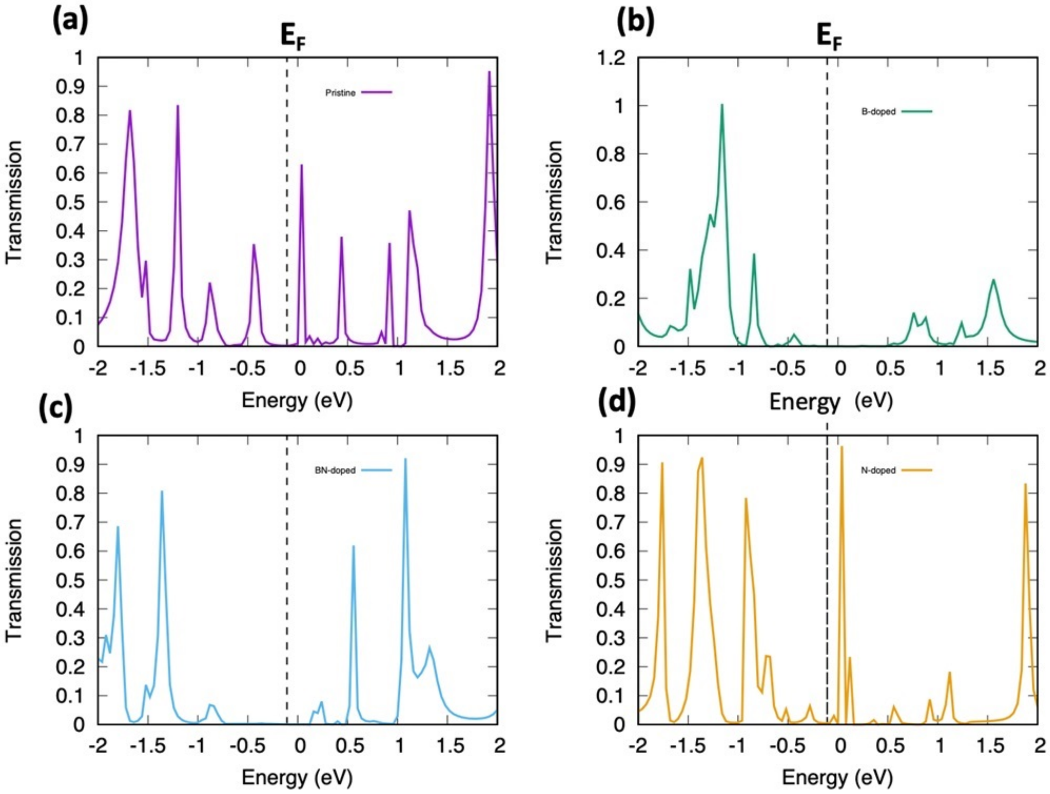

FIG. 5. Transmission spectra of (a) pristine SPGNR, (b) B-doped SPGNR, (c) BN-doped SPGNR and (d) N-doped SPGNR at a bias voltage of 0.8 V

and the nitrogen doping makes band-to-band tunneling feasible by appropriately shifting and aligning of the bands with respect to the Fermi level, and thereby giving rise to the NDR region.

4. Conclusion

In conclusion, by analyzing the electronic and transport characteristics of pristine and doped penta-graphene nanoribbons with CNT electrodes, we have observed that using CNT electrodes results in a remarkable increase in current at higher bias voltages in pristine SPGNR as compared to other cited reports. Doping also significantly affects the I–V characteristics and transmission spectra of the two-probe systems. Specifically, the operating voltage of the nitrogen-doped model is significantly reduced as compared to the pristine, homogenously boron-doped and heterogeneously boron-nitrogen doped models. Moreover, the results show that the magnitude of the current in the pristine penta-graphene model is maximum at higher bias voltages. The behavior of the computed transmission spectrum completely matches the I–V characteristics. The small but perceptible NDR behavior is also observed in doped penta-graphene models, especially in the nitrogen-doped model.

Acknowledgement

This work is supported by the Department of Science and Technology, Science and Engineering Research Board (DST-SERB), New Delhi, India, funded project (Grant No. EMR/002866/2017).

References

[1] Kroto H.W., Heath J.R., OBrien, S.C., Curl R.F., Smalley R.E. C_{60}: Buckminsterfullerene. *Nature*, 1985, **318**, P. 162–165.
[2] Shah K.A., Parvaiz M.S. Computational comparative study of substitutional, endo and exo BN Co-Doped single walled carbon nanotube system. *Superlattices and Microstructures*, 2016, **93**, P. 234–241.
[3] Shah K.A., Parvaiz M.S. Negative differential resistance in BN co-doped coaxial carbon nanotube field effect transistor. *Superlattices and Microstructures*, 2016, **100**, P. 375–380.
[4] Shah K.A., Parvaiz M.S., Dar G.N. Photocurrent in single walled carbon nanotubes. *Physics Letters A*, 2019, **383**, P. 2207–2212.
[5] Zwanenburg F.A., Van der Mast D.W., et. al. Electric Field Control of Magnetoresistance in InP Nanowires with ferromagnetic Contacts. *Nano Letters*, 2009, **9**, P. 2704–2709.

[6] Li Y., Xu L., Liu H. Chem, Graphdiyne and graphyne: from theoretical predictions to practical construction. *Chem. Soc. Rev.*, 2014, **43**, P. 2572–2586.

[7] Malko D., Neiss C., Vines F., Gorling A. Competition for Graphene: Graphynes with Direction-Dependent Dirac Cones. *Phys. Rev. Lett.*, 2012, **108**, P. 086804.

[8] Mina M., Susumu O. Two-Dimensional sp^2 Carbon Network of Fused Pentagons: All Carbon Ferromagnetic Sheet. *Appl. Phys. Express*, 2013, **6**, P. 095101.

[9] Terrones H., et al. New Metallic Allotropes of Planar and Tubular Carbon. *Phys. Rev. Lett.*, 2000, **84**, P. 1716–1719.

[10] Xu L.C., et al. Two dimensional Dirac carbon allotropes from graphene. *Nanoscale*, 2014, **6**, P. 1113–1118.

[11] Bucknum M.J., Hoffmann R. A Hypothetical Dense 3,4-Connected Carbon Net and Related B_2C and CN_2 Nets Built from 1,4-Cyclohexadienoid Units. *J. Am. Chem. Soc.*, 1994, **116**, P. 11456–11464.

[12] Zhang S., Wang Q., Chen X., Jena P. Stable three-dimensional metallic carbon with interlocking hexagons. *Proc. Natl. Acad. Sci.*, 2013, **110**, P. 18809–18813.

[13] Omachi H., Nakayama T., Takahashi E., Segawa Y., Itami K. A grossly warped nanographene and the consequences of multiple odd-membered-ring defects. *Nat. Chem.*, 2013, **5**, P. 739–744.

[14] Deza M., Fowler P.W., Shtogrin M., Vietze K. Pentaheptite Modifications of the Graphite Sheet. *J. Chem. Inf. Comput. Sci.*, 2000, **40**, P. 1325–1332.

[15] Tan Y.Z., Xie S.Y., Huang R.B., Zheng L.S. The stabilization of fused-pentagon fullerene molecules. *Nat. Chem.*, 2009, **1**, P. 450–460.

[16] Prinzbach H., et al. Gas-phase production and photoelectron spectroscopy of the smallest fullerene, C_{20}. *Nature*, 2000, **407**, P. 60–63.

[17] Wang Y., et al. Template Effect in the Competition between Haeckelite and Graphene Growth on Ni(111): Quantum Chemical Molecular Dynamics Simulations. *J. Am. Chem. Soc.*, 2011, **133**, P. 18837–18842.

[18] Yagmurcukardes M., Sahin H., Kang J., Torun E., Peeters F.M., Senger R.T. Pentagonal monolayer crystals of carbon, boron nitride, and silver azide. *J. Appl. Phys.*, 2015, **118**, P. 104303–104306.

[19] Yu Z.G., Zhang Y.W. A comparative density functional study on electrical properties of layered penta-graphene. *J. Appl. Phys.*, 2015, **118**, P. 165706.

[20] Xu W., Zhang G., Li B. Thermal conductivity of penta-graphene from molecular dynamics study. *J. Chem. Phys.*, 2015, **143**, P. 154703–154706.

[21] Cranford S.W. When is 6 less than 5? Penta-to hexa-graphene transition. *Carbon*, 2016, **96**, P. 421–428.

[22] Lopez-Bezanilla A., Littlewood P.B. σ–π-Band Inversion in a Novel Two-Dimensional Material. *J. Phys. Chem. C*, 2015, **119**, P. 19469–19474.

[23] Stauber T., Beltran J.I., Schliemann J. Tight-binding approach to penta-graphene. *Sci. Rep.*, 2016, **6**, P. 22672–22680.

[24] Rajbanshi B., Sarkar S., Mandal B., Sarkar P. Energetic and electronic structure of pentagraphene nanoribbons. *Carbon*, 2016, **100**, P. 118–125.

[25] Avramov P., Demin V., Luo M., Choi C.H., Sorokin P.B., Yakobson B., Chernozatonskii L. Translation Symmetry Breakdown in Low-Dimensional Lattices of Pentagonal Rings. *J. Phys. Chem. Lett.*, 2015, **6**, P. 4525–4531.

[26] Tien N.T., Thao P.T.B., Phuc V.T., Ahuja R. Electronic and transport features of sawtooth penta-graphene nanoribbons via substitutional doping, *Physica E: Low-dimensional Systems and Nanostructure*, 2019, **114**, P. 113572.

[27] Quantum ATK version P-2019.03, Synopsis Quantum ATK (www.synopsys.com/silicon/quantumatk.html).

[28] Baughman R.H., Zakhidov A.A., de Heer W.A. Carbon nanotubes–the route toward applications. *Science*, 2002, **297**, P. 787–792.

[29] Landauer R. Spatial Variation of Currents and Fields Due to Localized Scatterers in Metallic Conduction. *IBM J. Res. Dev.*, 1957, **1**, P. 223–231.

[30] Berdiyorov G., Dixit G., Madjet M. Band gap engineering in penta-graphene by substitutional doping: first-principles calculations, *J. Phys.: Condensed Matter*, 2016, **28**, P. 475001–475010.

NANOSYSTEMS: PHYSICS, CHEMISTRY, MATHEMATICS, 2020, 11 (2), P. 183–188

Dynamics of polarons in branched conducting polymers

K. K. Sabirov[1], J. R. Yusupov[2], Kh. Sh. Matyokubov[3]

[1]Tashkent University of Information Technologies, 108 Amir Temur Str., 100200, Tashkent Uzbekistan

[2]Turin Polytechnic University in Tashkent, 17 Niyazov Str., 100095, Tashkent, Uzbekistan

[3]Urgench State University, 14 H. Olimjon Str., 220100, Urgench, Uzbekistan

karimjonsabirov80@gmail.com

PACS 82.35.Cd, 71.38.-k **DOI 10.17586/2220-8054-2020-11-2-183-188**

In this paper, we study polarons in branched conducting polymers. For the description of polarons dynamics in such a polymers, we use the modified SSH-model in combination with quantum graph concept. Applications and possible extensions of the model are discussed.

Keywords: quantum graph, SSH model, conducting polymers, polaron dynamics.

Received: 20 March 2020

Revised: 3 April 2020

1. Introduction

Conducting polymers have attracted much attention in the context of organic electronic and third generation photovoltaics as basic functional materials. Effective practical implementation of such materials requires understanding their electronic properties, especially, charge transport. To solve such a task, one needs to develop highly accurate and realistic models for charge dynamics in conducting polymers. The main charge carriers in conducting polymers are charged solitons, excitons and polarons. The latter is an electron or hole trapped by phonon cloud. Polarons as charge carriers appear in different conducting polymers, when the latter is doped or has defects. The dynamics of polarons in conducting polymers are nicely described within the Su–Schrieffer–Heeger (SSH) model, which is a one dimensional analog of tight-binding models of the solid state physics. Applying the SSH model allows one to calculate band structure and transport characteristics of polarons in conducting polymers. So far, different aspects of charge transport in conducting polymers have been studied within the SSH-model and its modifications (see, Refs. [1–11] for review). However, despite the certain progress made in the study of charge transport in conducting polymers, some aspects of the topic are still far from the research focus area. This mainly concerns branched conducting polymers. These are three or more linear polymer chains connecting to each other at the branching areas. Such polymers have several advantages compared to the linear (unbranched) ones. In particular, by choosing optimal branching architecture, one can tune the functional properties of the materials and devices made of such polymers. Such polymers attracted certain attention over the past decade. A considerable number of papers have been published in the literature during past two decades on the synthesis of different branched polymers and study of their optical, electronic and mechanical properties (see, e.g., [12–29]). A review of the chemistry and physics of hyperbranched polymers is presented in [15]. In [19], a synthesis strategy for a hyperbranched sulfonated polydiphenylamine was developed and electronic properties have been studied. Synthesis and light-emitting applications of several conjugated polymers have been reviewed in [21].

In this paper, we address the problem of polaron dynamics in branched conducting polymers. The system is modeled by means of the quantum graph concept and SSH-model, i.e., by constructing extended version of the latter. This allows one to derive a system of wave equations on metric graphs. We note that the linear wave equations on metric graphs have been extensively studied in the Refs. [30–35] and soliton dynamics in networks has been the topic for extensive research during the past decade (see, e.g., Refs. [36–45]). Modeling such structures in terms of metric graphs provides powerful tool for effective description of the wave dynamics in branched structures appearing in different areas of physics. The graph itself is determined as a set of branches, which are connected to each other at the vertices (branching points) according to some rule. This rule is called the topology of a graph. When branches of a graph are assigned length it is called metric graph. The topology of a graph is given in terms of the adjacency matrix, which is defined, e.g., in [30–34].

The paper is organized as follows. In the next section we briefly recall SSH model on a real line. Section 3 presents extension of the SSH-model on graphs and exact solution of the obtained wave equations. Finally, section 4 presents some concluding remarks.

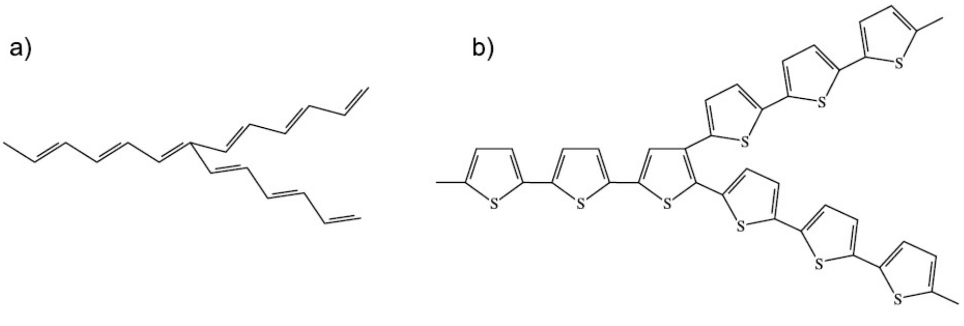

FIG. 1. Sketch of branched conducting polymers

2. Polaron dynamics on a linear polymers

Before treating the problem of branched conducting polymers, we briefly recall the linear counterpart of the problem, following the Ref. [6]. The Hamiltonian of SSH model for linear polymer can be written as: [6,7]

$$\begin{aligned}H(t) = &\frac{i}{2}\int \left(u(x,t)\partial_t u^*(x,t) - u^*(x,t)\partial_t u(x,t)\right) dx + \\ &+\frac{i}{2}\int \left(v(x,t)\partial_t v^*(x,t) - v^*(x,t)\partial_t v(x,t)\right) dx + \\ &+\gamma\int \left[\frac{d\Delta(x,t)}{dt}\right]^2 dx + \theta\int \Delta^2(x,t)dx - \\ &-i\beta\int \left(u^*(x,t)\partial_x u(x,t) - v^*(x,t)\partial_x v(x,t)\right) dx + \\ &+\int \Delta(x,t)\left(u^*(x,t)v(x,t) + v^*(x,t)u(x,t)\right) dx,\end{aligned} \tag{1}$$

where β is the effective electron-phonon coupling constant and the pair of the wave functions $u(x,t)$ and $v(x,t)$ describe effective electron-phonon interaction.

The wave equations following from this Lagrangian can be written as:

$$\begin{aligned}-i\partial_t u + i\beta\partial_x u - \Delta(x)v = 0, \\ -i\partial_t v - i\beta\partial_x v - \Delta(x)u = 0.\end{aligned} \tag{2}$$

Using substitutions $u(x,t) = \exp(i\epsilon t)u(x)$, $v(x,t) = \exp(i\epsilon t)v(x)$, one can separate time and space variables in these equations:

$$\begin{aligned}\epsilon u = -i\beta\partial_x u + \Delta(x)v, \\ \epsilon v = i\beta\partial_x v + \Delta(x)u.\end{aligned} \tag{3}$$

Explicit form of the band gap parameter can be written as

$$\Delta(x) = \Delta_0 - k_0\beta\left[\tanh k_0(x + x_0) - \tanh k_0(x - x_0)\right].$$

For this system of equations the electron wave functions for the positive-energy localized state can be written as [6,7]

$$\begin{aligned}u_0(x) = N_0\left[(1 - i)\text{sech}k_0(x + x_0) + (1 + i)\text{sech}k_0(x - x_0)\right], \\ v_0(x) = N_0\left[(1 + i)\text{sech}k_0(x + x_0) + (1 - i)\text{sech}k_0(x - x_0)\right],\end{aligned} \tag{4}$$

with $N_0 = \frac{\sqrt{k_0}}{4}$. These wave functions are normalized as

$$\int \left(u_0^2 + v_0^2\right) dx = 1, \tag{5}$$

and k_0 is found by solving equation $\tanh(2k_0x_0) = k_0\beta/\Delta_0$. For the above wave functions one can estimate polaron width x_0 and polaron binding energy E_0 [6,7]:

$$2x_0 \approx 8.9a, \quad E_0 = 0.1\Delta_0,$$

where a is the lattice constant. In the next section we extend this model for branched conducting polymer.

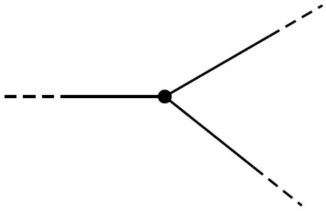

FIG. 2. Star graph

3. Polarons in branched conducting polymers

Polarons in conducting polymers appear both as a result of photo-generation, as well as a charge carrier in organic electronic devices when a voltage is applied. An effective way for modeling of polaron dynamics in conducting polymers is the SSH-model, which treats a polymer chain as a 1D lattice and applies nonlinear version of the tight-binding model. Here, we consider dynamics of polarons in a branched conducting polymers consisting of three (linear) polymer chains, which are connected to each other at single monomer (see, Fig.1). The branching is assumed to be in the form of Y-junction (see, Fig.1). Such system can be mapped onto the basic star graph presented in Fig.2. Assuming that the length of polymer is much longer than its width, the dynamics of polaron can be described in terms of the SSH-Hamiltonian given on a star graph with branches $b_j,\ j = 1,2,3,\ b_1 \sim (-\infty;0],\ b_{2,3} \sim [0;+\infty)$. The SSH-Hamiltonian on this star graph is given as:

$$H = \sum_{j=1}^{3}\int_{0}^{+\infty} H_j(t)dt, \tag{6}$$

where:

$$\begin{aligned} H_j(t) = \frac{1}{\beta_j}\Bigg[& \frac{i}{2}\int_{b_j}\big(u_j(x,t)\partial_t u_j^*(x,t) - u_j^*(x,t)\partial_t u_j(x,t)\big)\,dx + \\ & +\frac{i}{2}\int_{b_j}\big(v_j(x,t)\partial_t v_j^*(x,t) - v_j^*(x,t)\partial_t v_j(x,t)\big)\,dx + \\ & +\gamma_j\int_{b_j}\left[\frac{d\Delta_j(x,t)}{dt}\right]^2 dx + \theta_j\int_{b_j}\Delta_j^2(x,t)dx - \\ & -i\beta_j\int_{b_j}\big(u_j^*(x,t)\partial_x u_j(x,t) - v_j^*(x,t)\partial_x v_j(x,t)\big)\,dx + \\ & +\int_{b_j}\Delta_j(x,t)\big(u_j^*(x,t)v_j(x,t) + v_j^*(x,t)u_j(x,t)\big)\,dx\Bigg]. \end{aligned} \tag{7}$$

Here, β_j is the effective electron-phonon coupling constant for branch b_j. Using this Hamiltonian, one can derive wave equations for polaron in branched polymer, as well as boundary conditions at the branching point. The latter is derived from the energy conservation, given by $\dot{H} = 0$. Requiring the first variation of (6) should be zero, and using $\delta u_j = 0,\ \delta v_j = 0$ at $t = 0$ and $t \to +\infty$, $u_1,\ v_1 \to 0$ at $x \to -\infty$, $u_{2,3},\ v_{2,3} \to 0$ at $x \to +\infty$ we have wave equations and boundary conditions on the star graph presented in Fig.2:

$$\begin{aligned} -i\partial_t u_j + i\beta_j\partial_x u_j - \Delta_j v_j = 0, \\ -i\partial_t v_j - i\beta_j\partial_x v_j - \Delta_j u_j = 0, \end{aligned} \tag{8}$$

$$\begin{aligned} u_1^*\delta u_1|_{x=0} = u_2^*\delta u_2|_{x=0} + u_3^*\delta u_3|_{x=0}, \\ v_1^*\delta v_1|_{x=0} = v_2^*\delta v_2|_{x=0} + v_3^*\delta v_3|_{x=0}. \end{aligned} \tag{9}$$

Using $u_j(x,t) = \exp(i\epsilon t)u_j(x),\ v_j(x,t) = \exp(i\epsilon t)v_j(x),\ \frac{1}{\alpha_1}\delta u_1\Big|_{x=0} = \frac{1}{\alpha_2}\delta u_2\Big|_{x=0} + \frac{1}{\alpha_3}\delta u_3\Big|_{x=0}$ and $\alpha_1\delta v_1|_{x=0} = \alpha_2\delta v_2|_{x=0} = \alpha_3\delta v_3|_{x=0}$ one can separate space and time-variables in the wave equation, so that the wave equation

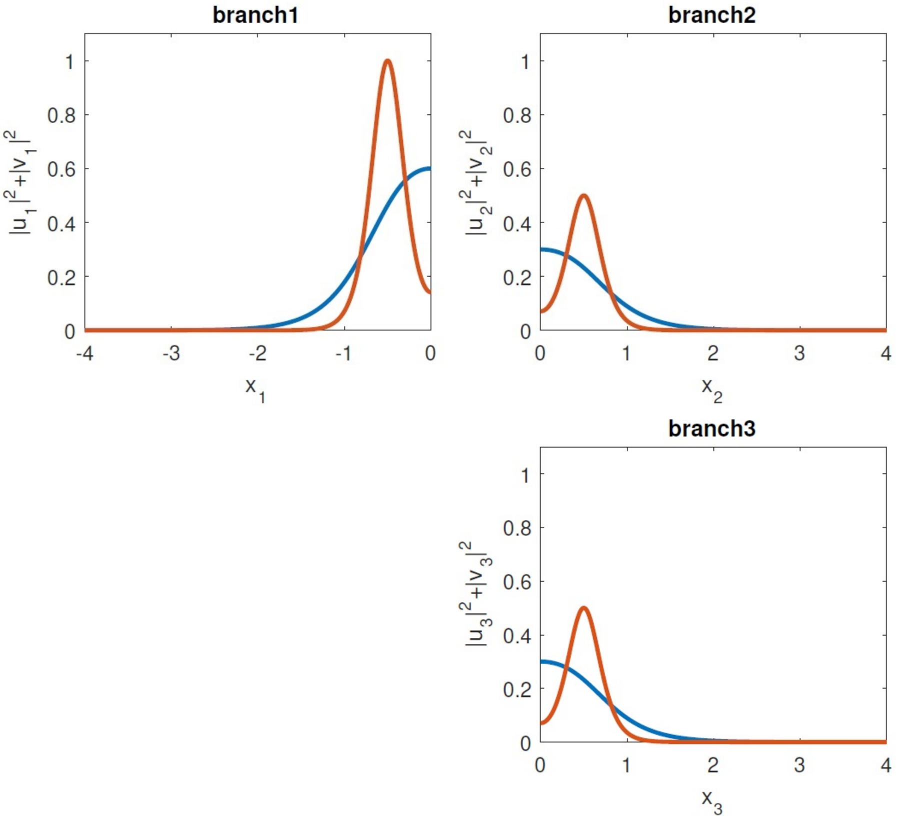

FIG. 3. (Color online) The profile of the squared modulus of the polaron wave function on a branched conducting polymer for the values of β_j fulfilling the sum rule in Eq.(16): $\beta_1 = 1; \beta_2 = \beta_3 = \sqrt{2}$. The values of x_0 and σ are chosen as $x_0 = 1/3,\ \sigma = 2$ (blue) and $x_0 = 1/2,\ \sigma = 4$ (red)

takes the forms:

$$\begin{aligned} \epsilon u_j &= -i\beta_j \partial_x u_j + \Delta_j v_j, \\ \epsilon v_j &= i\beta_j \partial_x v_j + \Delta_j u_j, \end{aligned} \tag{10}$$

with:

$$\begin{aligned} &\alpha_1 u_1|_{x=0} = \alpha_2 u_2|_{x=0} = \alpha_3 u_3|_{x=0}, \\ &\frac{1}{\alpha_1} v_1\bigg|_{x=0} = \frac{1}{\alpha_2} v_2\bigg|_{x=0} + \frac{1}{\alpha_3} v_3\bigg|_{x=0}. \end{aligned} \tag{11}$$

α_j are nonzero real constants, which will be determined below. We note that in real applications to polymers they can be chosen on the basis of certain physical properties.

Let us introduce the following notations:

$$u_j(x) = \frac{u_0(x)}{\beta_j},\ v_j(x) = \frac{v_0(x)}{\beta_j}. \tag{12}$$

Then, exact analytical solution of the problem given by Eqs.(10) and (11) can be written as:

$$\begin{aligned} u_0(x) &= N\left[(1-i)\mathrm{sech} k_0(x+x_0) + (1+i)\mathrm{sech} k_0(x-x_0)\right], \\ v_0(x) &= N\left[(1+i)\mathrm{sech} k_0(x+x_0) + (1-i)\mathrm{sech} k_0(x-x_0)\right], \\ \Delta_j(x) &= \Delta_{0j} - k_0\beta_j\left[\tanh k_0(x+x_0) - \tanh k_0(x-x_0)\right], \end{aligned} \tag{13}$$

where k_0 is found by solving equation $\tanh(2k_0x_0) = k_0/\sigma$, and $\Delta_{0j} = \sigma\beta_j$, $j = 1, 2, 3$. Requiring that the solutions given by (13) should fulfill the vertex boundary conditions (11), we get the following constraints for α_j:

$$\frac{\alpha_1}{\beta_1} = \frac{\alpha_2}{\beta_2} = \frac{\alpha_3}{\beta_3}, \tag{14}$$

$$\frac{1}{\alpha_1\beta_1} = \frac{1}{\alpha_2\beta_2} + \frac{1}{\alpha_3\beta_3}, \tag{15}$$

which make Eq.(13) to be the exact solution of the problem given by: Eqs. (10) and (11):

$$\frac{1}{\beta_1^2} = \frac{1}{\beta_2^2} + \frac{1}{\beta_3^2}, \tag{16}$$

and $N = \frac{\beta_1\sqrt{k_0}}{4}$.

The exact solutions given by Eq.(13) present the wave function of polaron in branched conducting polymer having the form of Y-junction. In Fig. 3 the plot of the squared modulus of the wave function is presented for the values of parameters $\beta_1 = 1$, $\beta_2 = \beta_3 = \sqrt{2}$.

4. Conclusions

We studied polarons in branched conducting polymers. A model based on the use of a modified SSH-model leading to the linear wave equations system for polarons dynamics is used in combination with quantum graph concept. Explicit wave function of the polaron on branched conducting polymer having Y-junction type branching is obtained. The model proposed in this work can be extended to the case of more complicated branching topologies. Also, it can be applied for modeling of exciton migration in polymer based thin film organic solar cells, where polymer chains packed on the cell create complicated branched structures.

References

[1] Heeger A.J., and R. Pethig. Charge Storage and Charge Transport in Conducting Polymers: Solitons, Polarons and Bipolarons [and Discussion]. *Philosophical Transactions of the Royal Society of London. Series A, Mathematical and Physical Sciences*, 1985, **314**(1528), P. 17–35.

[2] Heeger A.J. Nobel Lecture: Semiconducting and metallic polymers: The fourth generation of polymeric materials, *Rev. Mod.Phys.*, 2001, **73**, P. 681.

[3] Heeger A.J., Kivelson S., Schrieffer J.R., Su W.-P. Solitons in conducting polymers. *Rev. Mod.Phys.*, 1988, **60**, P. 781.

[4] Su W.P., Schrieffer J.R., Heeger A.J. Solitons in Polyacetylene. *Phys. Rev. Lett.*, 1979. **42**, P. 1698.

[5] Brazovskii S.A. *JETP Lett.*, 1978, **28**, P. 20.

[6] Campbell D.K. and Bishop A.R. Solitons in polyacetylene and relativistic-field-theory models. *Phys. Rev. B*, 1981, **24**, P. 8.

[7] Campbell D.K. and Bishop A.R. Soliton Excitations in Polyacetylene and Relativistic Field Theory Models. *Nuclear Physics B*, 1982, **200**[FS4], P. 297–328.

[8] Horovitz B. Soliton Lattice in Polyacetylene. Spin-Peierls Systems, and Two-Dimensional Sine-Gordon Systems. *Phys. Rev. Lett.*, 1981, **46**, P. 11.

[9] Horovitz B. The mixed peierls phase and metallic polyacetylene. *Solid State Communications*, 1980, **34**, P. 61–64.

[10] Horovitz B. Solitons in polyacetylene: A comment. *Phys. Rev. B.*, 1980, **22**, P. 2.

[11] Krumhansl J.A., Horovitz B., and Heeger A.J. Amplitude solitons in incommensurate Peierls systems: Implications for TTF-TCNQ. *Solid State Communications*, 1980, **34**, P. 945–948.

[12] Wallace D.S., Stoneham A.M., Hayes W., Fisher A.J. and Testa A. Theory of defects in conducting polymers. II. Application to polyacetylene. *J. Phys.: Condens. Matter*, 1991, **3**, P. 3905.

[13] Fujii M., Ari K. and Yoshino K. Branching Patterns of a Conducting Polymer Polymerized Electrochemically with a ConstantCurrent Source, *J. Electrochem. Soc.*, 1993, **140**, P. 7.

[14] Jurkiewicz J. and Krzywicki A. Branched polymers with loops. *Phys. Lett. B*, 1997, **392**, P. 291–297.

[15] Inoue K. Functional dendrimers, hyperbranched and star polymers. *Prog. Polym. Sci.*, 2000, **25**, P. 453.

[16] Dai L., Winkler B., Dong L., Tong L. and Mau A.W.H. Conjugated Polymers for LightEmitting Applications, *Adv. Mater.*, 2001, **13**, P. 12–13.

[17] Wu D.T., *Synth. Met.*. Theory for conductivity in conducting star polymer blends, 2002, **126**, P. 289.

[18] Gao C. and Yan D. Hyperbranched polymers: from synthesis to applications. *Prog. Polym. Sci.*, 2004, **29**, P. 183.

[19] Hua F. and Ruckenstein E. Hyperbranched Sulfonated Polydiphenylamine as a Novel Self-Doped Conducting Polymer and Its pH Response. *Macromolecules*, 2005, **38**, P. 888.

[20] Ch. Wu, Malinin S.V., Tretiak S., Chernyak V.Y. Exciton scattering and localization in branched dendrimeric structures. *Nature Physics*, 2006, **2**, P. 631–635.

[21] Lee R.-H., Chen W.-Sh., and Wang Y.-Y. Synthesis and electroluminescence properties of a series of hyper-branched light-emitting polymers. *Thin Solid Films*, 2009, **517**, P. 5747.

[22] Hirao A. and Yoo H.-S. Dendrimer-like star-branched polymers: novel structurally well-defined hyperbranched polymers. *Polymer J.*, 2011, **43**, P. 2.

[23] Hutchings L.R. Complex Branched Polymers for StructureProperty Correlation Studies: The Case for Temperature Gradient Interaction Chromatography Analysis. *Macromolecules*, 2012, **45**, P. 5621.

[24] Pan L., Yu G., Zhai D., et.al. Hierarchical nanostructured conducting polymer hydrogel with high electrochemical activity. *Proc. Natl. Acad. Sci. U.S.A.*, 2012, **109**, P. 9287.

[25] Li H., Malinin S.V., Tretiak S., and Chernyak V.Y. Effective tight-binding models for excitons in branched conjugated molecules. *J. Chem. Phys.*, 2013, **139**, P. 064109.

[26] Ohshita J., Tominaga Y., Tanaka D., Mizumo T., Fujita Y., Kunugi Y. Synthesis and optical properties of organosiliconoligothiophene branched polymers. *J. Org. Chem.*, 2013, **50**, P. 736.

[27] Otrokhov G.V., Morozova O.V., Vasileva I.S., Shumakovich G.P., Zaitseva E.A., Khlupova M.E., and Yaropolov A.I. Biocatalytic synthesis of conducting polymers and prospects for its application. *Biochemistry*, 2013, **78**, P. 1539.

[28] Goll M., Ruff A., Muks E., Goerigk F., Omiecienski B., Ruff I., Gonzalez-Cano R. C., Navarrete J. T. L., Delgado M. C. R. and Ludwigs S. Functionalized branched EDOT-terthiophene copolymer films by electropolymerization and post-polymerization click-reactions. *Beilstein J. Org. Chem.*, 2015, **11**, P. 335.

[29] Soganci T., Gumusay O., Soyleyici H. C., Ak M. Synthesis of highly branched conducting polymer architecture for electrochromic applications, *Polymer*, 2018, **134**, P. 187.

[30] Kostrykin R., Schrader R., Kirchhoffs rule for quantum wires. *J. Phys. A: Math. Gen.*, 1999, **32**, P. 595.

[31] Kottos T. and Smilansky U. Periodic Orbit Theory and Spectral Statistics for Quantum Graphs. *Ann.Phys.*, 1999, **274**(1), P. 76–124.

[32] Kuchment P. Waves in Random Media, 2004, **14** P. S107.

[33] Gnutzmann S. and Smilansky U. Quantum graphs: Applications to quantum chaos and universal spectral statistics. *Adv.Phys.*, 2006, **55**(5-6), P. 527–625.

[34] Exner P. and Kovarik H. *Quantum waveguides.* Springer, 2015.

[35] Gnutzmann S., Keating J.P. and Piotet F. Eigenfunction statistics on quantum graphs. *Ann.Phys.*, 2010, **325**(12) P. 2595–2640.

[36] Sobirov Z., Matrasulov D., Sabirov K., Sawada S., and Nakamura K. Integrable nonlinear Schrdinger equation on simple networks: Connection formula at vertices. *Phys. Rev. E*, 2010, **81**, P. 066602.

[37] Sobirov Z., Matrasulov D., Sawada S., and Nakamura K. Transport in simple networks described by an integrable discrete nonlinear Schrdinger equation. *Phys.Rev.E*, 2011, **84**, P. 026609.

[38] Adami R., Cacciapuoti C., Finco D., Noja D. Fast Solitons on Star Graphs. *Rev.Math.Phys*, 2011, **23**, P. 4.

[39] Sabirov K.K., Sobirov Z.A., Babajanov D., and Matrasulov D.U. Stationary nonlinear Schrödinger equation on simplest graphs. *Phys.Lett. A*, 2013, **377**, P. 860.

[40] Caputo J.-G., Dutykh D. Nonlinear waves in networks: Model reduction for the sine-Gordon equation. *Phys. Rev. E*, 2014, **90**, P. 022912.

[41] Uecker H., Grieser D., Sobirov Z., Babajanov D. and Matrasulov D. Soliton transport in tubular networks: Transmission at vertices in the shrinking limit. *Phys. Rev. E*, 2015, **91**, P. 023209.

[42] Noja D. Nonlinear Schrödinger equation on graphs: recent results and open problems. *Philos. Trans. R. Soc. A*, 2014, **372**, P. 20130002.

[43] Noja D., Pelinovsky D., and Shaikhova G. Bifurcations and stability of standing waves in the nonlinear Schrödinger equation on the tadpole graph. *Nonlinearity*, 2015, **28**, P. 2343.

[44] Sobirov Z., Babajanov D., Matrasulov D., Nakamura K., and Uecker H. Sine-Gordon solitons in networks: Scattering and transmission at vertices, *EPL*, 2016, **115**, P. 50002.

[45] Sabirov K.K., Rakhmanov S., Matrasulov D. and Susanto H. The stationary sine-Gordon equation on metric graphs: Exact analytical solutions for simple topologies. *Phys.Lett. A*, 2018, **382**, P. 1092.

NANOSYSTEMS: PHYSICS, CHEMISTRY, MATHEMATICS, 2020, 11 (2), P. 189–194

One-dimensional photonic crystals (Si/SiO$_2$) for ultrathin film crystalline silicon solar cells

S. Saravanan, R. S. Dubey

Advanced Research Laboratory for Nanomaterials & Devices, Department of Nanotechnology, Swarnandhra College of Engineering & Technology, Seetharampuram, Narsapur – 534 280, West Godavari, Andhra Pradesh, India

shasa86@gmail.com

PACS 73.50.h, 84.60.Jt **DOI 10.17586/2220-8054-2020-11-2-189-194**

The performances of ultrathin film silicon solar cells are limited due to low light absorption and poor collection of charge carriers. In this work, we have designed and studied the one-dimensional photonic crystals (1DPCs) and thin film silicon solar cells. For the simulation, the plane wave method (PWM) and rigorous coupled wave analysis (RCWA) methods were used. First, we explored the analysis of bandgap, field distribution and the reflectivity of 1DPCs. Later, the optimized Si/SiO$_2$ 1DPC was integrated with the crystalline silicon solar cell as the back reflector and simulation was performed. The performance of designed solar cells showed the strong influence of 1DPC. The solar cell is integrated with the three distributed Bragg reflectors (5DBRs) at the bottom showed the best performance with its enhanced short circuit current and cell efficiency.

Keywords: PWM, 1DPC, bandgap, RCWA, cell efficiency.

Received: 30 November 2019

Revised: 26 December 2019

1. Introduction

Renewable energy resources are needed to save the environment and for clean energy production (electricity). Researchers and environmentalists have been focusing on photonic crystals (PCs) which are nothing than artificial periodic dielectric structures. Such PCs possesses the different refractive indices of their materials. A properly designed and fabricated photonic crystal prohibits the propagation of the electromagnetic waves. The photonic crystals are classified as one- (1D), two- (2D) and three-dimensional (3D) according to their periodicity. Over last few decades, the dielectric layers have been in wide demand for use in several applications, such as thin film solar cells, LEDs, thermal collector, optical filter, reflective coatings, optical buffer, and optical computers [1–8]. The performance of the photonic crystals has been studied by using various simulation techniques such as plane wave method (PWM), rigorous coupled-wave analysis (RCWA), transfer matrix method (TMM), finite-difference time-domain (FDTD) and Finite element method (FEM) [9–11]. Use of 1DPC as the back reflector in thin film solar cells showed the improved light absorption. Dubey and Ganesan (2017) experimentally prepared and studied the SiO$_2$/TiO$_2$ based multilayer structures by using sol-gel spin coating method. The refractive indices of SiO$_2$ and TiO$_2$ layers were 1.43 and 2.0 with layer thicknesses of 230 and 70 nm each. They achieved $\sim$ 78 % reflectance with the composition of six low and high dielectric layers of SiO$_2$ and TiO$_2$ respectively at center wavelength (λ) 829 nm [12]. Chen at al. (2014) designed and demonstrated the one-dimensional photonic crystals as the back reflectors for thin-film silicon solar cells. The plane wave expansion (PWE) and the FDTD method were used to study the photonic bandgap properties. Further, the optical properties of reflection and absorption of 1DPCs were studied. They reported the reflectivity $\sim$ 97 % by using five distributed Bragg reflectors (5DBRs). The designed solar cell with 5DBRs showed the influence of refractive index contrast and the thickness of the layers and produced 13.41 % mA/cm^2 [13]. Sheng et al. (2010) presented the silicon solar cells with the integration of porous aluminum and distributed Bragg's reflector (DBR) as the back reflectors. This design showed an improvement in photovoltaic performance more than 50 % as compared to reference cell [14]. Again Sheng et al. (2012) demonstrated the design of thin-film solar cell structures by using various back reflectors. The DBR was consisting of amorphous-Si and SiO$_2$ films with their corresponding refractive indices 3.6 and 1.45 designed at center wavelength at 800 nm. However, the improved solar cell performance was attributed to the diffraction grating and DBR integrated at the bottom of solar cell [15]. In this paper, we present the design of Si/SiO$_2$ 1DPCs and ultrathin film crystalline silicon solar cells. The use of DBR showed the enhancement in light absorption and hence, the cell efficiency. The designing of 1DPCs and ultrathin crystalline silicon solar cells are presented in Section 2 while the simulated results are discussed in Section 3. Finally, paper is summarized in Section 4.

2. Designing approach

Figure 1 shows the proposed design of ultrathin crystalline silicon solar cells. This solar cell design was consist of Si_3N_4 antireflection coating (ARC), Al substrate, SiO_2 buffer layer, Al/ITO dual gratings (bottom & top) and 1DPCs (Si/SiO_2). The thicknesses of each component was as below: ARC 70 nm (t_8), top grating 50 nm (t_7), Silicon absorber 41 nm (t_6), bottom grating 159 nm (t_5) and buffer layer 57 nm (t_4) whereas the thicknesses of Si and SiO_2 were 57 nm (t_3) and 137 nm (t_2) respectively. The substrate thickness of Al was 200 nm (t_1).

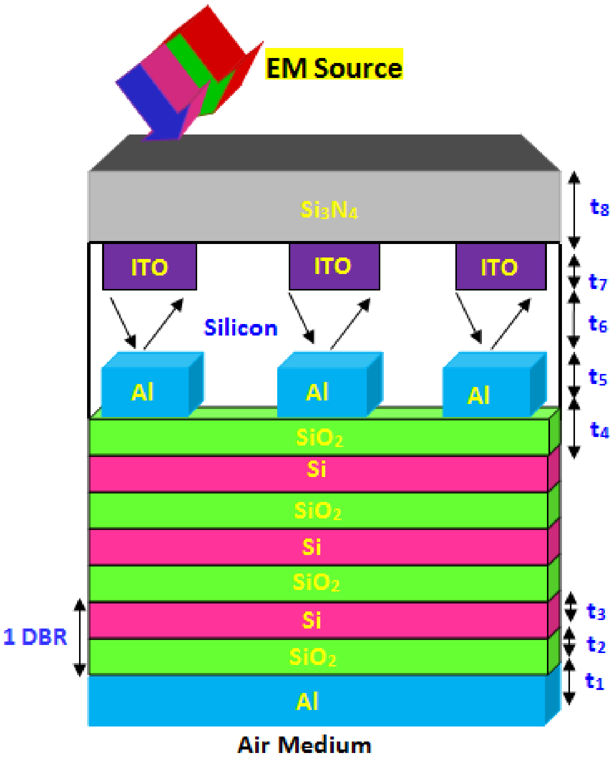

FIG. 1. The schematic diagram of DBR integrated with ultrathin amorphous silicon solar cell

The absorbing material was crystalline silicon with a thickness of approximately 41 nm. Here, the SiO_2 buffer layer was integrated between the DBR and the crystalline silicon absorbing layer. The FDTD technique is widely used for electromagnetic wave analysis. This technique divides the time and space at regular spatial grid size intervals and the simulation time evolve in the field. For the simulation, periodic boundary conditions for X- and Y-axis and the perfect matched layer for Z-axis were applied. Using the optimized design of 1DPC by using plane wave method (PWM), we have presented the solar cells design with the integration of DBR at the bottom and the various analyses were explored using RCWA method.

3. Results and discussion

Figure 2 shows the photonic bandgap (PBG) diagram of 1DPCs by varying the number of stacks (S) of Si/SiO_2 and the thicknesses 57 (t_3) and 137 nm (t_2) respectively designed at center wavelength 800 nm. The choice of a large dielectric contrast material is desirable have a wider bandgap. Here, our chosen materials are Si ($n_1 = 3.4$) and SiO_2 ($n_2 = 1.45$), because of their large refractive index contrast. For the simulation of 1DPC, we applied the periodic boundary conditions (PBC) in the Z-axis and the perfect matched layers (PML) in the X- and Y-axis. In the PBG diagram, as shown in Fig. 1, the X-axis represents the K-wave vector, whereas, the Y-axis represents the eigen frequencies ($\omega a/2\pi c$). Here, ω is the frequency, c is the speed of light in a vacuum, and a is the lattice constant. We can clearly observe the effect of increased number of stacks. As the thickness was increased the bandwidth of the photonic band was decreased. Table 1 shows the analysis of PBG by varying the number of stacks and their reflection bandwidth.

As much as 99 % reflectivity was achieved from the photonic crystals (PCs) based on 5 stacks of Si/SiO_2 layers. The PBGs are strongly dependent on the different variables, for example, the refractive index (n), period (N), dielectric constant (ε) etc. To realize the field distribution in the number of stacks, we have plotted the diagram Fig. 3. We can

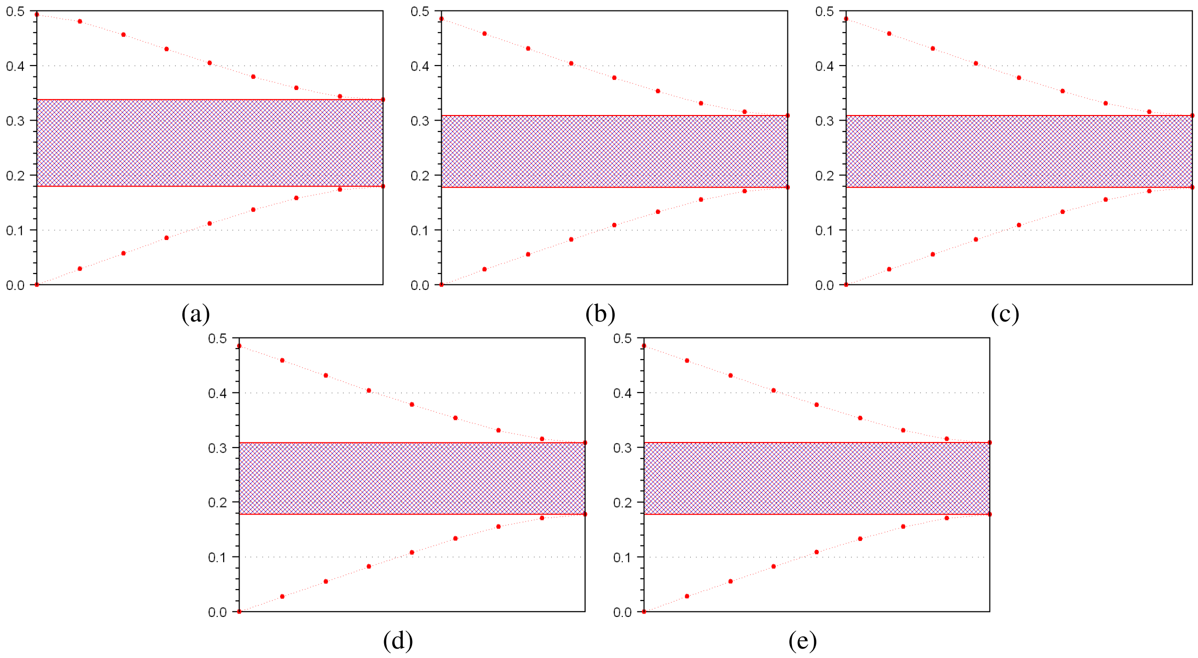

(a) (b) (c)

(d) (e)

FIG. 2. Photonic bandgap of 1DBR (a), 2DBR (b), 3DBR(c), 4DBR (d) and 5DBR (e)

TABLE 1. The photonic bandgap, reflection and field intensity of Si/SiO 1DPC structures

DBR	Photonic Band Gap / Frequency ($\omega a/2\pi c = a/\lambda$)	Reflection (%)	Field Intensity
1S	0.16	49.3	1.70
2S	0.13	87.8	1.92
3S	0.13	96.8	1.98
4S	0.13	98.5	1.98
5S	0.13	98.8	1.98

assume that the light was irradiated from the left side and the field distribution was studied within the 1S, 2S, 3S, 4S and 5S of Si/SiO_2 stacks. The RCWA method is useful for the field distribution analysis and the reflectivity of the various stacks as shown in Fig. 3. The incident light on the dielectric medium shows the partial reflection and partial transmission the light. Consequently, the transmission of light was decreased due to the total internal reflection of incident light with the increased number of stacks. This phenomenon plays a key role when 1DPC is integrated as a back reflector in thin film solar cell. It gives the folding of unabsorbed light passed through the active region and therefore, increases the light absorption in longer wavelength.

Referring to Fig. 3(a–e), we can observe the field distribution or gradual decrease in the light intensity from the left to right side. The red and pink color strips can be understood as the high and low intensity of field from left to right side as shown in Fig. 3(a–e). We can observe the shifting and widening of reflection band with the increased of the number of stacks as shown in Fig. 3(f). As much as about 99 % reflection was observed from the photonic crystal based on 5 stacks. The reflectivity corresponding to 1S, 2S, 3S, 4S and 5S were 49.3, 87.8, 96.8, 98.5, 98.85 %. Table 1 summarizes the bandgap, reflectivity and field intensities. With this analysis of reflection using N-stacks, we have integrated this structure at the bottom of solar cell as represented in Fig. 1.

Figure 4 shows the bar diagram of cell efficiency of various solar cells by varying the number of 1DPC stacks as the back reflector. We can clearly observe the enhancement in the cell efficiency with respect to the increased Si/SiO_2 stacks as compare to designed solar cell without photonic crystals or back reflector for the transverse electric mode (TE). Generally, the thin-film solar cells do not have the capability to absorb light in the longer wavelength region and therefore it severely affects the conversion efficiencies of solar cells. The role of 1DPCs is to act as back reflector for the wavelength region which could not be absorbed in the absorbing medium. Similar trends are observed for the transverse magnetic (TM) waves. However, for the case of TM wave the cell efficiency was better than the transverse electric (TE) wave case. This enhancement is attributed to the bottom metal (Al) grating which generated the surface

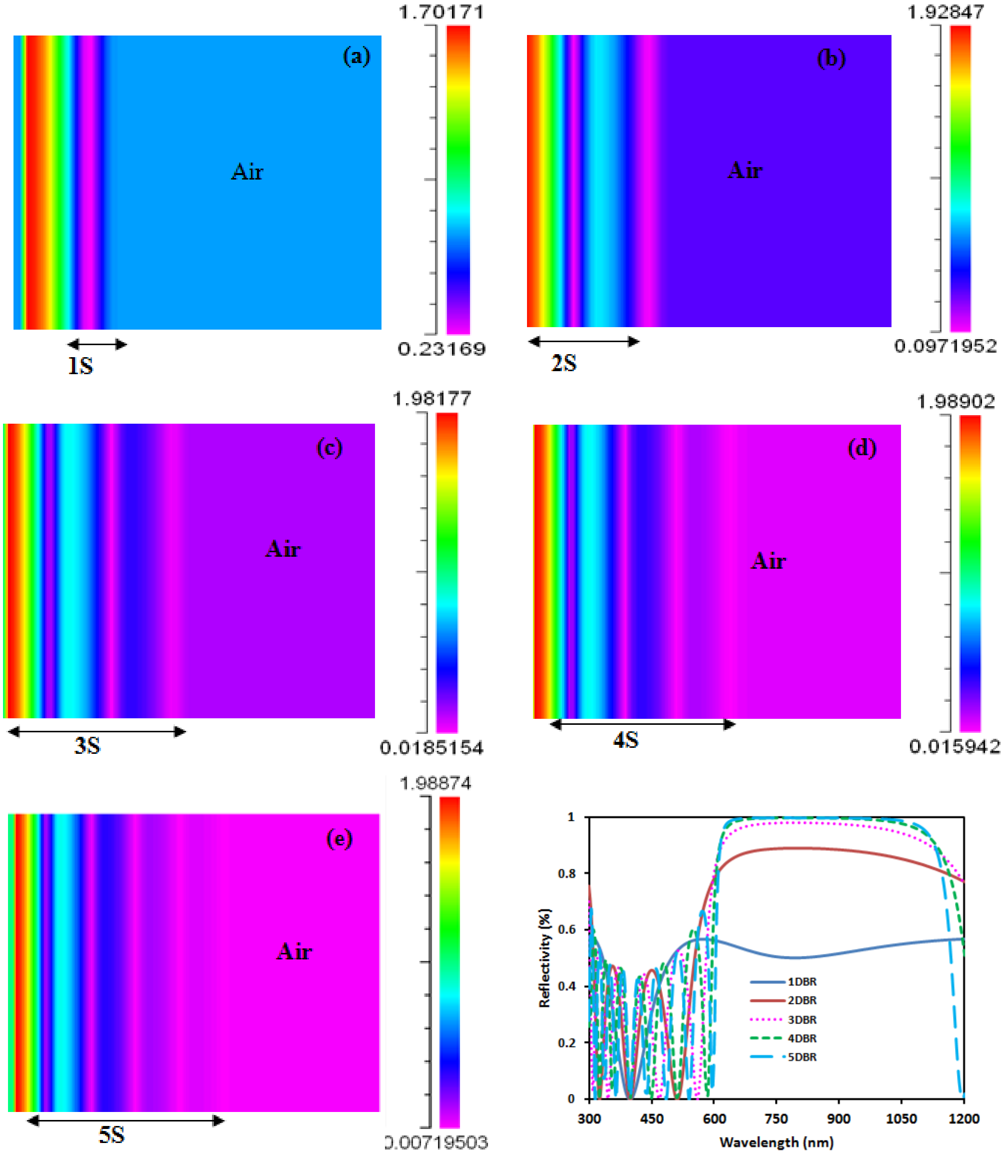

FIG. 3. Transverse electric (TE) field distribution of 1S (a), 2S (b), 3S (c), 4S (d), 5S (e) with intensity profile and reflectivity (f)

plasmons and localization of the field. The designed solar cell using 1DPC based on three stacks showed the maximum photovoltaic performance i.e. short-circuit current (J_{SC}) 19.69 and 25.54 mA/cm^2 while cell efficiency (η) 16.8 and 19.5 % for the case of TE and TM waves respectivey. The light trapping plasmonic nanostructures are the important factor to enhance the optical performance [16].

The use of 1DPC is to enhance the light absorption by folding the light back to the Si absorber region. In this context, we have studied the light absorption for the case of TE and TM waves which is plotted in Fig. 5. From this figure, we can clearly observe the enhancement of light absorption in the solar cell based on 3S-1DPC. Comparably, the light absorption for the TM case is dominant which is due to the induced surface plasmons with the localized field at the tip of the Al grating as shown in the inset of Fig. 5 at the right-hand side. The use nanograitngs were found to be important in order to enhance the light trapping in the multiple junctions [17–19]. Here, the Al and ITO gratings are supposed to have the scattering of light with the large diffraction angle for prolonging the photon pathlength. The analysis of TE and TM depicts the nature of light within the simulated structure. The electric field distribution at 460 nm shows the Fabry–Perot resonance and guided modes in the absorber region due to the back reflector, remarkably. Similarly, magnetic field distribution at wavelength 840 nm confirmed the localized surface

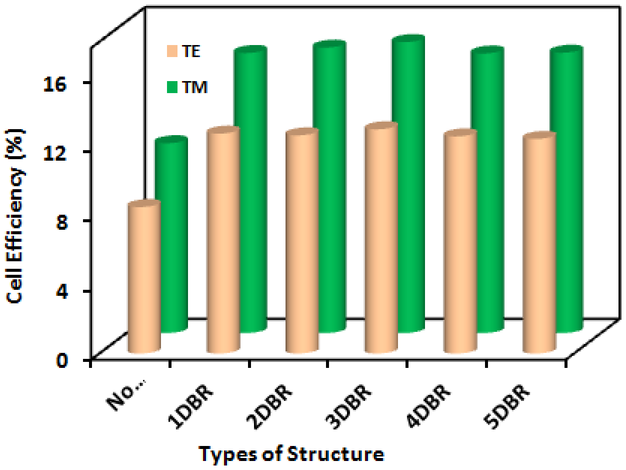

FIG. 4. Bar diagram of solar cell efficiency (TE & TM cases) of various solar cells

plasmons and the surface guided modes observed in the absorber region. It represents significant enhancement of light trapping due to the combined photonic and plasmonic effects.

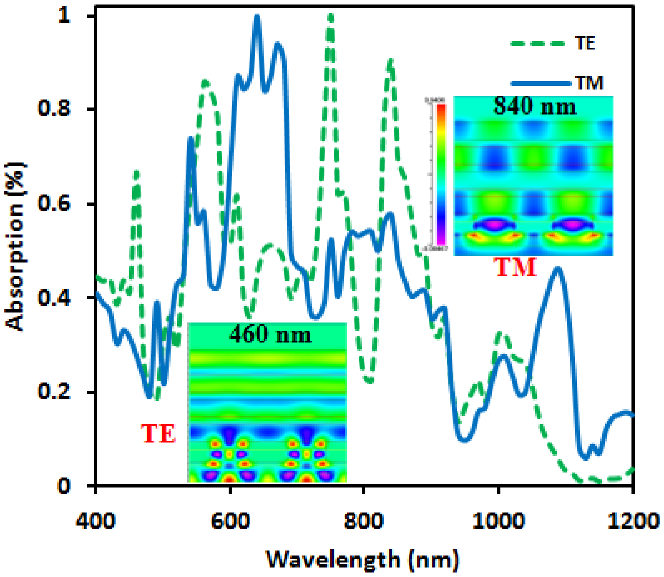

FIG. 5. The absorption spectrum of 3-stacks based ultrathin silicon solar cell in both polarization modes

4. Conclusion

In this work, designing of 1DPC with respect to the number of stacks and thin-film silicon solar cell has been presented. The photonic bandgap was found to be shifted towards the longer wavelength with its widening as a function of increased number of stacks. The proposed design of solar cell based on 3S-1DPC showed the enhanced short-circuit current density and solar cell efficiency. This enhancement was attributed to the light trapping mechanism supported by the 1DPC as the back reflector and the guiding of light by the diffraction grating of ITO on the top and Al at the bottom. For the TM case, the field distribution was significantly enhanced due to the induced surface plasmons which could contribute to the enhanced photovoltaic performance. Finally, the proposed design of thin film solar cell is useful for the enhancement of light absorption assisted by the photonic and plasmonic modes.

References

[1] Banerjee A. Novel applications of one-diemnsional photonic crystal in optical buffering and optical time divison multiplexing. *Optik*, 2001, **122** (4), P. 355–357.

[2] Saravanan S., Dubey R.S., Kalainathan S. Design and optimization of ultrathin crystalline silicon solar cells using an efficient back reflector. *AIP advances*, 2015, **5**, 057160-10.

[3] Yong K., Yu H.K., et al. Flexible top-emitting diodes with a functional dielectric reflector on a metal foil substrate. *RSC advances*, 2018, **8**, P. 26156–26160.

[4] Mu C., Cornelissen H.J., Bociort F., Liebig T. Dielectric multilayer angular filters for coupling LEDs to thin light guides. *Proceedings of SPIE*, 2011, **8170**, 817001-1-6.

[5] Kumar M., Kumari N., et al. Multilayer dielectric thin-film optical filters for beam folding applications. *Proceedings of SPIE*, 2015, **9654**, 96540-1-5.

[6] Yamamoto Y., Kamiys T., Yanai H. Characteristic of optical guided in multilayer metal-clad planar optical guide with low-index dielectric buffer layer. *IEEE Journal of Quantum Electronics* 1975, **11** (9), P. 729-736.

[7] Young L. Multilayer reflection coatings on a metal mirror. *Applied Optics*, 1963, **2**, P. 445–447.

[8] Chizari A., Abdollahramezani S., Jamali M.V., Salehi J.A. Analog optical computing based on a dielectric met-reflect array. *Optics Letters*, 2016, **41**, P. 3451–3453.

[9] Meade R.D., Rappe A.M., et al. Accurate theoretical analysis of photonic bandgap materials. *Physics review B*, 1993, **48**, P. 843–8437.

[10] Dubey R.S., Gautam D.K. Development of simulation tools to study optical properties of one-dimensional photonic crystals. *Journal of electromagnet waves and applications*, 2012, **22** (5–6), P. 849–860.

[11] Axmann W., Kuchment P. An efficient finite element method for computing spectra of photonic and acoustic bandgap materials. *Journal of Computational Physics*, 1999, **150**, P. 467–481.

[12] Dubey R.S., Ganesan V. Reflectance modulation using SiO_2/TiO_2multilayer structures prepared by sol-gel spin coating process for optical applications. *Superlattice and Microstructures*, 2017, **111**, P. 1099–1103.

[13] Chen P., Hou G., et al. Optimal desing of on-dimensional photonic crystals back reflectors for thin film silicon solar cells. *Journal of Applied Physics*, 2014, **116**, 064508.

[14] Sheng X., Johnson S.G., et al. Integrated photonic structures for light trapping in thin film Si solar cells. *Applied Physics Letters*, 2012, **100**, 111110-1-3.

[15] Sheng X., Liu J., et al. Integration of self-assembled porous alumina and distributed Bragg reflector for light trapping in Si photovoltaic devices. *IEEE photonics technology letters*, 2010, **22** (18), P. 1394–1396.

[16] Zeng L., Yi Y., et al. Efficiency enhancement in Si solar cells by textured photonic crystal back reflector. *Applied Physics Letters*, 2006, **89**, 111111-1-3.

[17] Sheng X., Liu J., et al. Integration of self-assembled porous alumina and distributed reflector for light trapping in Si photovoltaic devices. *IEEE photonics technology letters*, 2010, **22** (18), P. 1394–1396.

[18] Krc J., Zeman M., Luxembourg S.L., Topic M. Modulated photonic crystal structures as broadband back reflectors in thin-film solar cells. *Applied Physics Letters*, 2001, **94**, 153501-1-3.

[19] Dubey R.S., Sarojini P.L. Light trapping mechansim in one-dimensional (1D) photonic crystals for silicon-based solar cells. *Journal of Electromagnetic Waves and applications*, 2012, **27**, P. 1–9.

NANOSYSTEMS: PHYSICS, CHEMISTRY, MATHEMATICS, 2020, 11 (2), P. 195–204

Synthesis and characterisation of CZTSe bulk materials for thermoelectric applications

Yogeshchandra Sharma

Department of Physics, Vivekananda Global University, Jaipur–303012, Rajasthan, India
yc.sharma.vit@gmail.com,
+919664075093, +917597776818, https://orcid.org/0000-0003-3532-6097

PACS 85.80.Fi, 72.20.Pa, 72.20.My, 82.80.Gk, 82.80.Pv, 61.05.cp, 74.25.Fy

DOI 10.17586/2220-8054-2020-11-2-195-204

Quaternary Copper Zinc Tin Selenide (CZTSe) is a preferred candidate as an absorber layer in solar cells due to its non-toxicity and the abundancy of its constituents. This material also has thermoelectric properties suitable for solar thermal energy conversion and waste heat recovery. The preparation of bulk thermoelectric materials is a tedious, multistep task and requires considerable time and energy consumption for tuning of desired properties. Here one step solid state reaction has been used for synthesis of bulk CZTSe materials in five different ratios of elemental precursors: Cu, Zn, Sn and Se. Atomic Force Microscopy (AFM), X-Ray Photoelectron Spectroscopy (XPS) and X-ray diffraction (XRD) techniques have been used for structural and compositional analysis of the materials. AFM analysis shows significant difference in roughness parameters and grain size with respect to Cu/Zn variations. The XRD spectra of various samples show the formation of CZTSe materials. Raman spectra verifies absence of secondary phases. XPS analysis reveals constituent atoms display chemical valences of $+1$, $+2$, $+4$, and -1 for Cu, Zn, Sn, and Se, respectively. The stoichiometric sample, $Cu_2ZnSnSe_4$, exhibited the maximum power factor 0.30 mW·m^{-1}K^{-2}, having carrier concentration in the range of 10^{18} – 10^{19} cm^{-3} and resistivity in the range of 0.21 to 0.24 Ω·cm.

Keywords: thermoelectric devices, thermoelectric effects in semiconductors and insulators, Hall effect in semiconductors, Raman spectroscopy in chemical analysis, photoelectron spectroscopy in chemical analysis, powder diffraction X-ray, transport properties (electric and thermal conductivity, thermoelectric effects, etc.).

Received: 20 December 2019

Revised: 28 February 2020

1. Introduction

The use of thermoelectric technology will increase as it can build solid state devices having better reliability and power density. In future, it will be main technology behind the sustainable energy applications which will be able to overcome ever growing energy demand and depleting fossil fuels. Although, most high performance thermoelectric materials are tellurides or antimonides but these contain toxic and rare earth elements. Higher cost and toxicity are major issues which are hindering the wide use of thermoelectric devices in areas like household heating and cooling, medical applications and automobiles. Besides the discovery of new materials it is sometimes of interest to investigate known materials that show promise in different domains; like quaternary chalcogenides, which are composed of earth abundant materials and have been studied for a variety of different applications like, solar-cell absorbers [1–3], photocatalysts for solar water splitting [4], nonlinear optics [5], topological insulators [6], and magneto-optic and magneto-ferroics [7,8]. In these materials, the transport of carriers is often disturbed and impeded by grain boundaries and the interfaces between the matrix and composites. Recently, certain multinary compounds like, CZTS, CZTSe and others have attracted great interest as thermoelectric materials because their physical properties can be tuned by varying the elemental composition.

For a thermoelectric material, the energy conversion efficiency, $ZT = S^2T/k$, where T is the absolute temperature, S is the Seebeck coefficient, σ is the electrical conductivity, and κ is the thermal conductivity which consists of electronic thermal conductivity (κ_e) and lattice thermal conductivity (κ_L). Simultaneous increase of σ and reduction of κ are preferred for the ZT enhancement but these factors have trade-off relationship with each other.

Conventional TE materials are narrow band gap semiconductors in which a bipolar effect may reduce the TE efficiency [9]. The TE properties of quaternary chalcogenides CZTS, CZTSe, $Cu_2ZnGeSe_4$, $Cu_2CdSnSe_4$ and Cu_2FeSnS_4 have been studied by various workers [10–20]. Their band gaps are wide enough to avoid the bipolar effect and these have low thermal conductivities due to the complexity of the crystallographic structures; this enables them to be a potentially outstanding class of TE materials. Although the ZT values obtained for these are still about 0.9, these are still lower than those for ternary compounds. It has been reported that for quaternary materials, relatively low thermal conductivity and good electrical properties could be achieved by appropriate doping [21–24]. It has been reported by various workers that modification of electrically conducting units by doping of Cu^{2+} create more hole carriers and extra conducting pathways [25–27]. The structural disruption through doping units effectively enhances the σ values without significantly affecting the electrical thermal conductivity, which ultimately enhances the ZT value. The experiments have further shown that the total thermal conductivity of Cu-based quaternary chalcogenides with chalcopyrite derived structures is very low as compared to well-optimized TE material like Bi_2Te_3 alloy. This is due to the fact that the total thermalconductivity in these compounds is dominated mainly by phonon thermal conductivity than electrical thermal conductivity, along with a possibility of random distribution of cations and anions in the unit cell, which may gave rise to structural anisotropy, responsible for lowering of thermal conductivity. Similar studies have been reported for other structural forms of these quaternary chalcogenides such as wurtzite, orthorhombic, stannite and stannite-kuramite etc. [28–31].

Similar electronic behavior as well as transport properties have been observed as a function of temperature, doping level and crystal symmetry for CZTX (X = S, Se and Te), imparting similar thermoelectric behavior in all three. The results obtained in the reports give a way to explore high performance thermoelectric materials with the family of widely existing tetrahedrally bonded semiconductors. Among these materials CZTSe has been explored as high performance thermoelectric material with ZT value of 0.28 at 700 K by Shi et al [32], which further improves to 0.95 at 850 K by indium doping in the material $Cu_2ZnSn_{0.90}In_{0.10}Se_4$, owing to the lower thermal conductivity of the doped material. The work by Chen et al [33] on Cu-doped CZTSe polygon like nanocrystals suggests that, the substitution of Zn^{2+} with Cu^{+} while Cu-doping introduces extra holes as charge carrier in CZTSe, which enhances the electrical conductivity. On the other hand, the intensive phonon scattering at the small grain boundaries of the polygon shaped nanocrystals reduces the thermal conductivity.

CZTSe has a band gap in the range of 1.4 – 1.5 eV, also has thermoelectric properties useful in energy conversion technologies. A number of methods have been used for the synthesis of CZTSe thin films and bulk materials, like Aqueous Synthesis method [34], RF-DC sputtering method [35, 36], thermal co-evaporation [37], electro deposition method [38], Molecular beam epitaxy [39] and solid state reaction [40–51] etc.

In this work, CZTSe bulk materials have been synthesised by one step solid state reaction of its elemental constituents at 850 °C in a rocking furnace. This approach that has proven successful for other chalcogenide materials, herein the synthesis and study of structural properties have been reported. The materials are analyzed for formation of CZTSe along with various phases by AFM, XRD and Raman spectroscopic techniques while uniformity of elemental distribution was analyzed using XPS technique. To understand electrical behavior Hall effect and thermoelectric measurements have also been performed.

2. Experimental details

2.1. Materials synthesis

Quartz ampoules were etched in acetone and cleaned with DI water for 30 minutes to remove impurities. High purity Cu, Zn, Sn and Se (99.99 %) powders were weighed and mixed in an agate mortar according to the stoichiometry reported in Table 1. These were then loaded in five different cleaned quartz ampoules, which were sealed under vacuum at $\sim 1 \times 10^{-6}$ torr. These ampules were then placed one by one in a vertical rocking furnace, in which these were heated to 850 °C (at a rate of 50 °C per hour) and then held up for four hours. After cooling down to room temperature the ampoules were broken to extract the solid samples. The bulk materials obtained were grinded again with agate mortar and the process of solid state reaction was repeated for five times. After the completion of fifth cycle these chunks were separated from ampoules. For performing the electrical measurements small parts of the chunks were grinded into square shape and polished. The bulk densities of the samples were measured by employing the Archimedes principle. Stoichiometry variations in the ratio of solid state reacted CZTSe compounds and their densities have been given in the Table 1.

2.2. XRD analysis

Crystalline quality and epitaxial nature of bulk materials were determined from XRD measurements, which were performed using the synchrotron beam at angle-dispersive X-ray diffraction (ADXRD) beamline (BL-12) of Indian synchrotron source "Indus-2" at Raja Ramanna Centre for advanced Technology (RRCAT), Indore. Wave length of 0.78765 Å for angle dispersive x-ray diffraction experiments was selected from the white light using a Si (111) channel cut monochromator. The monochromatic beam is then focused on to the sample with a Kirkpatrick–Baez (K–B) mirror. A MAR345 image plate detector (Mar345 area detector with 0.1×0.1 mm^2 pixel) was used to collect 2D diffraction data. Sample to detector distance and the wavelength of the beam were calibrated using NIST standards LaB_6 and CeO_2. 2D diffraction data were then integrated using FIT2D software to get desired 1D intensity versus 2θ data.

TABLE 1. Stoichiometry variations in the ratio of various samples and their bulk densities

Sample	Stoichiometry	Cu/Zn	Cu/Sn	Se/(Cu+Zn+Sn)	Cu/(Zn+Sn)	Density (gm/cm^3)
Sample 1	$Cu_2ZnSnSe_4$	2.0	2.0	1.0	1.0	5.67
Sample 2	$Cu_2ZnSnSe_{5.6}$	2.0	2.0	1.4	1.0	5.68
Sample 3	$Cu_2ZnSnSe_{5.2}$	2.0	2.0	1.3	1.0	5.64
Sample 4	$Cu_{1.8}ZnSnSe_{5.2}$	1.8	1.8	1.36	0.9	5.62
Sample 5	$Cu_2Zn_{1.1}SnSe_{5.2}$	1.818	2.0	1.26	0.95	5.60

2.3. Raman analysis

The Raman spectroscopy measurements were performed at room temperature using a DPSS semiconductor Laser (make: Action spectrapro, sp-2500) as an excitation. The wavelength of the laser is 532 nm, to avoid laser heating the beam power was kept at 15 mW. The monochromator grating used was having 600 lines per mm. The spectra were recorded for 30 seconds at different locations. The lens used was having magnification of 20×. Raman spectra were recorded with a monochromator system in backscattering configuration with a microscope and a motorized XY stage.

2.4. Atomic force microscopy (AFM) analysis

The samples were placed on the surface of a nickel disk (1.2 cm^2) using double-sided adhesive tape and placed it on the AFM scanner (Multi-Mode/Nanoscope 8 scanning probe microscope, Bruker, USA). Measurements were performed in air under ambient conditions ($T = 25$ °C, RH = 21 %) using the J-scanner ($\min xy = 5$ μm). Scanning was performed in tapping mode using Si cantilevers with integrated tips ($t = 3.75$ μm, $l = 125$ μm, $w = 35$ μm, $F_0 = 300$ kHz, $k = 40$ Nm^{-1}) and an RMS amplitude of 1.5 V. The images were processed and dimensions measured using Nanoscope Analysis software (V9, Bruker).

2.5. XPS analysis

X-ray photoelectron spectroscopy measurements were carried using synchrotron radiation facility hard x-ray photoelectron spectroscopy (HAXPES) beamline BL-14, Indus-2 [52] which has double-crystal monochromator [Si (111)] with excitation energy of 4.311 keV and equipped with Hemispherical analyzer and detector system (Phoibos 225, Specs make). The typical pressure in the experimental station is 5×10^{-9} mbar.

2.6. Electrical measurements

The electrical conductivity (σ) was measured using the four probe set up and the thermoelectric measurement set up.Conductivity measurements were done with the help of Hall set up (HMS 5000 from Ecopia Corp., South Korea) at room temperature (RT) with a $0.5T$ magnetic field in the van der Pauw configuration. The HMS-5000 Hall Measurement System is a complete system for measuring the carrier concentration, carrier mobility (μ) and resistivity of materials. The HMS-5000 includes software with current–voltage curve capability for checking the ohmic integrity of the user made sample contacts.

2.7. Thermoelectric measurements

The setup for measuring Seebeck coefficient of thermoelectric materials is a designed sample holder, which consists two cuboid shaped copper blocks mounted on a rectangle shaped copper block with top cylinder shaped for temperature dependent measurements (shown in Fig. 1 below). For Seebeck coefficient measurement the sample is placed on two cuboid shaped copper blocks and the sample bridges the two blocks. The heater is used to generate the temperature gradient along the sample, the two PT100 devices have been connected to temperature controller are used to measure the temperature of the copper blocks; these are inserted into the holes provided in copper blocks. The voltage generated as a result of temperature gradient is determined by taking out the two separated contacts on the sample. The setup can measure Seebeck coefficient of both bulk and thin film thermoelectric materials up to a wide range of temperature (RT to 300 °C). The process of measurement can also be done in high vacuum, for that the whole system of sample holder is placed in a cylinder shaped case of steel provided with vacuum valve and vacuum lock at the top end. The vacuum arrangement consists of rotary pump and diffusion pump which can create vacuum. The measurements on copper and silicon were measured accurately hence confirms the reliability of the setup.

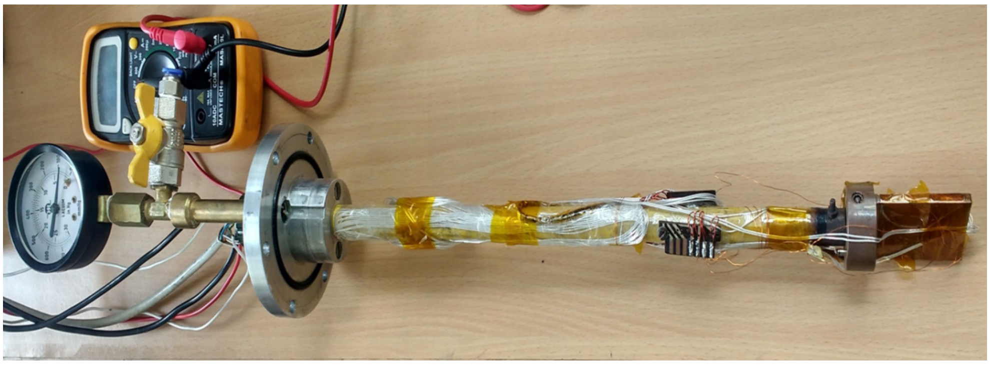

FIG. 1. Various parts of the thermoelectric measurement set up developed in our laboratory

3. Results and discussion

3.1. XRD analysis

From the XRD results, it has been found that the reaction among the elemental powders (Cu, Zn, Sn, and Se) occurred. A possible reason for the reaction is the melting of reactant powders. During the solid state reaction, the maximum reaction temperature (850 °C) is much higher than the melting points of Zn (420 °C), Sn (232 °C), and Se (221 °C). In this case as the reaction temperature is very high most reactants occur as liquid. The availability of the liquid phases increases the contacting area among different intermediate species formed and facilitates the mass transportation. Mixing at high temperature increases the reaction rate and well mixing of different constituents is obtained.

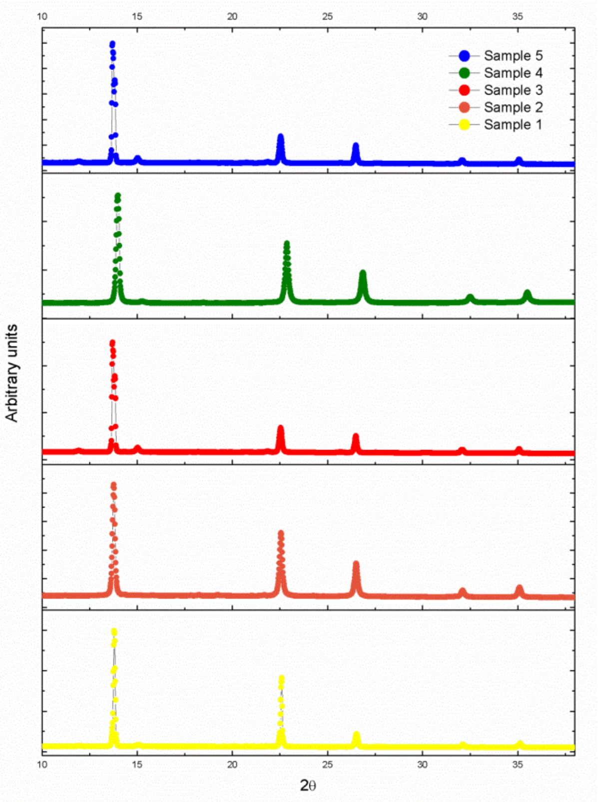

FIG. 2. XRD plots of various samples

The XRD pattern for the Bulk materials synthesized has been shown in Fig. 2. The appearance of prominent peaks confirm the formation of nanocrystalline CZTSe material. Average crystallite size obtained for the different materials have been shown in the third column of the Table 2. The crystallite size were calculated from the FWHM for the peaks at various angles (2θ) namely, at 13.77, 22.56, 26.51 and 32.11° which corresponds to the reflections from (112), (204), (312) and (316) planes, respectively. A significant variation in the values of crystallite size from 16 to 34 nm have been seen in the samples which may be due to variation in the stoichiometry's of various sample. All the peaks in the XRD data were indexed with reference to the standard data for the CZTSe compound ICDD file No. 04-003-8817.

TABLE 2. Crystallite size of various samples by XRD data

Sample	Stoichiometry	Crystallite size (nm)
Sample 1	$Cu_2ZnSnSe_4$	31
Sample 2	$Cu_2ZnSnSe_{5.6}$	24.9
Sample 3	$Cu_2ZnSnSe_{5.2}$	33.6
Sample 4	$Cu_{1.8}ZnSnSe_{5.2}$	18.1
Sample 5	$Cu_2Zn_{1.1}SnSe_{5.2}$	15.8

3.2. Raman analysis

Because the main three diffractions of CZTSe have Bragg angles similar to those of the diffractions of ZnSe and CTSe, it is necessary to investigate the samples by Raman spectroscopy. Figure 3 shows the Raman spectra of various samples in which the vibration modes corresponding CZTSe are present at 191, 217 and 246 cm^{-1}, revealing no secondary phases, such as Cu_2SnSe_3 with a tetragonal or cubic structure, and very similar lattice constants to those of CZTSe. The peaks of tetragonal Cu_2SnSe_3 appear at 178 cm^{-1}, corresponding to the CZTSe A1-mode; however, no distinct peaks appear at 204, 231 and 291 cm^{-1} corresponding to A2-mode of Cu_2SnSe_3. Also, no major ZnSe peaks – which would appear at 206 and 252 cm^{-1}, and no other possible secondary phases appear, such as Cu–Se- and Sn–Se-related compounds.

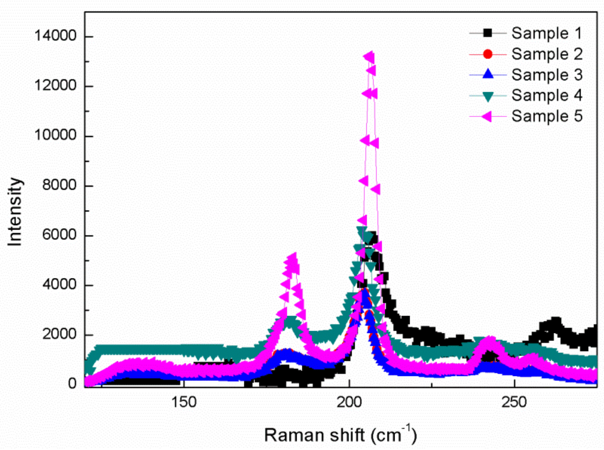

FIG. 3. Raman spectra of various samples

3.3. AFM analysis

Atomic force microscopic analysis is ideal for quantitatively measuring the nanometric dimensional surface roughness and for visualizing the surface nano-texture of the materials prepared. Three-dimensional (3D) AFM images of the five different materials have been shown in Fig. 4.

Roughness is the key feature in application of photovoltaic technology as physical and chemical properties are directly affected by this parameter. A small variation in value of average roughness of five different sample of CZTSe is observed with respect to their stoichiometry change. Sample 2 with ratio Se/(Cu+Zn+Sn) = 1.4 i.e. $Cu_2ZnSnSe_{5.6}$ with

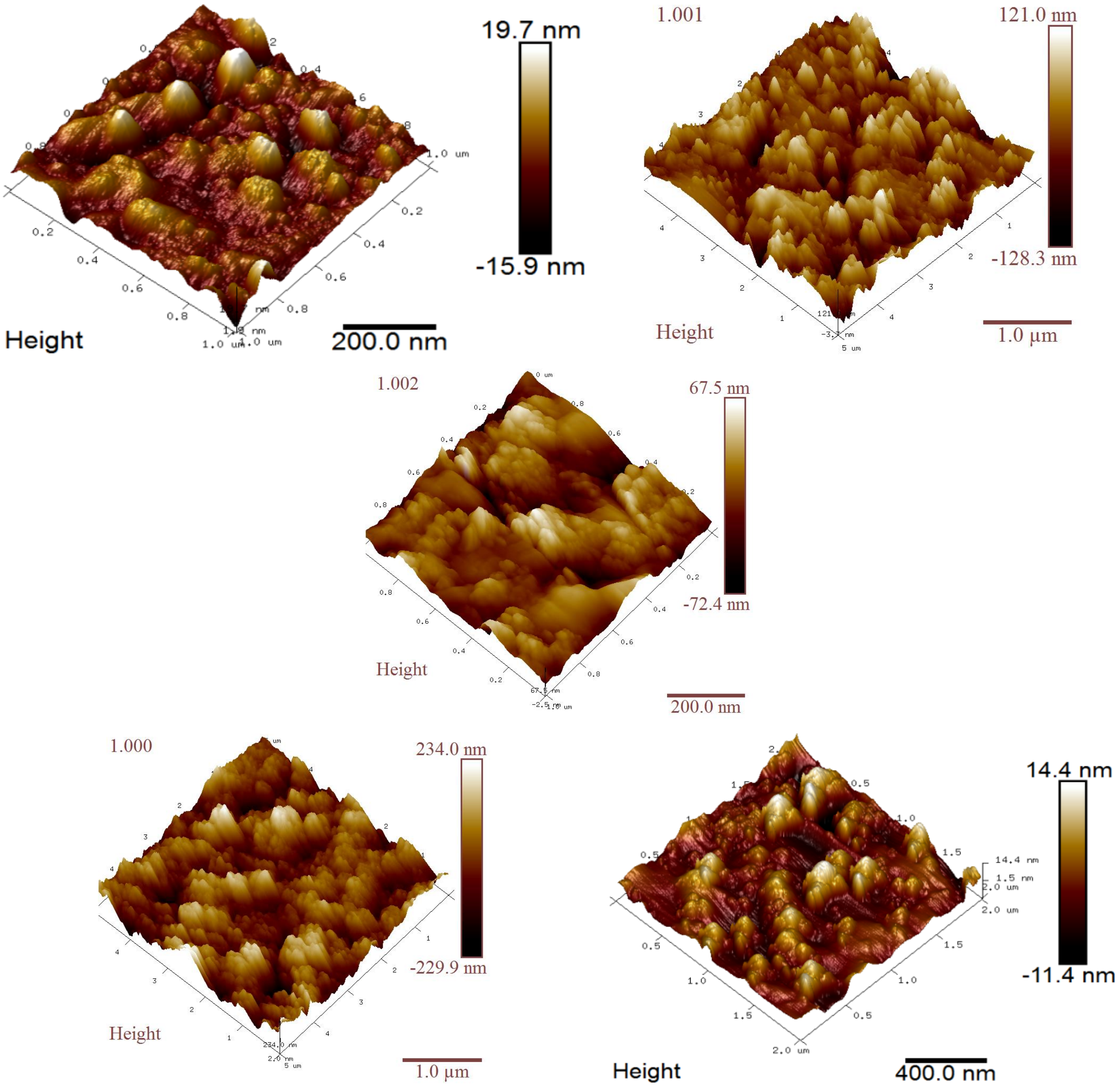

FIG. 4. Three-dimensional (3D) AFM images of various samples

TABLE 3. Roughness parameters of various samples

Sample ID	R_a (nm)	R_q (nm)	R_z (nm)	R_{ku}/R_a	R_{ku}	R_{sk}
Sample 1	51.8	65.24	650	1.259	6.02	0.932
Sample 2	49.4	63.8	636	1.2914	3.41	0.105
Sample 3	51.8	65.1	427	1.2561	2.88	0.0750
Sample 4	51.1	64.8	521	1.2681	3.01	0.0542
Sample 5	50.9	64.2	590	1.2612	3.17	0.0458

40 % excess of Se exhibits the lowest value of average roughness 49.4 nm while Sample 1 with perfect stoichiometry $Cu_2ZnSnSe_4$ and Sample 3 with 30 % excess of Se, $Cu_2ZnSnSe_{5.2}$ exhibited same value of roughness 51.8 nm. Table 3 illustrates that the variations in RMS roughness (R_q) values observed for all CZTSe samples are exactly have the same trend as exhibited by average roughness values (R_a) and ten point mean height R_z values.

3.4. XPS analysis

Figure 5 shows the XPS spectra of all the samples synthesized. The Cu 2p spectrum shows two narrow symmetric peaks at 932 eV ($2p^{3/2}$) and 952 eV ($2p^{1/2}$) with a peak splitting of 20 eV, which is characteristic of Cu (I). The Zn 2p peaks appearing at 1021 eV ($2p^{3/2}$) and 1044 eV ($2p^{1/2}$) with a peak splitting of 23 eV correspond to Zn (II). The Sn 3d peaks appearing at 486 eV ($3d^{5/2}$) and 495 eV ($3d^{3/2}$) with a peak splitting of 9 eV can be assigned to Sn (IV). The Se 3p peaks appearing at 160 eV ($3p^{3/2}$) and 166 eV ($3p^{1/2}$) with a peak splitting of 6 eV can be assigned to Se (IV) indicates Se with a valence of -1. Similar XPS spectra were observed for all the samples, confirming the chemical valence of $+1$, $+2$, $+4$, and -1 for Cu, Zn, Sn, and Se, respectively.

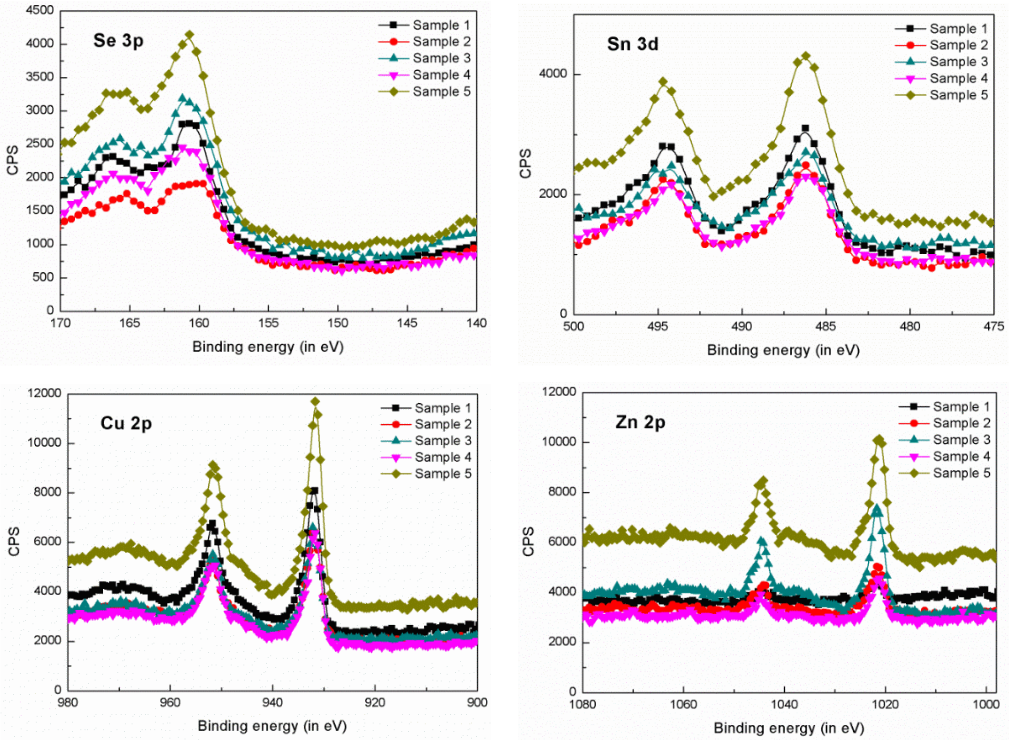

FIG. 5. XPS core level peaks of various samples

3.5. Electrical measurements

The electrical transport properties of the synthesized bulk materials are measured in the temperature range of 300 – 600 K. The electrical conductivities of the samples fall in the ranges of 12500 – 16000 $S{\cdot}m^{-1}$ and 4200 – 4800 $S{\cdot}m^{-1}$ at 300 and 600 K, respectively. For all the samples, the electrical conductivity decreases the exact reason for this transition of the σ-T dependence is unknown to author at present. Among the materials, the Cu-excessive sample ($Cu_2ZnSnSe_4$) shows the largest electrical conductivity, in the temperature range 300 – 600 K. This behavior may be attributed to the creation of holes (Cu^{2+} $3d^9$ vs. Cu^+ $3d^{10}$) and the conversion of electrically insulating paths to electrically conducting paths. As reported by some workers, the electrical conductivity is little changed in Se excess doping, it has been observed that with increase in the Se content electrical conductivity decreases, having a minimum value of 4200 $S{\cdot}m^{-1}$ for the $Cu_{1.8}ZnSnSe_{5.2}$ stoichiometry. The synthesized bulk materials exhibit positive Seebeck coefficients, confirming their p-type character. The Seebeck coefficients of the samples increase with increasing temperature, having the values in the ranges of 40 – 55 $\mu V{\cdot}K^{-1}$ and 185 – 250 $\mu V{\cdot}K^{-1}$ at 300 and 600 K, respectively. By comparing the five samples, it has been found that both Cu-excess and Se-excess lead to an enhancement of Seebeck coefficients. With high electrical conductivity and large Seebeck coefficient, the Cu-excessive sample ($Cu_2ZnSnSe_4$) exhibits the maximum power factor in the whole temperature range, which reaches 0.30 $mW{\cdot}m^{-1}K^{-2}$ at 600 K.

The stoichiometric sample $Cu_2ZnSnSe_4$, shows highest power factor while the Cu-deficient sample, $Cu_{1.8}ZnSnSe_{5.2}$, shows the lowest power factor at highest temperature 600 K. The other three samples show similar values in electrical conductivity, Seebeck coefficient, and power factor at 600 K (shown in Fig. 6).

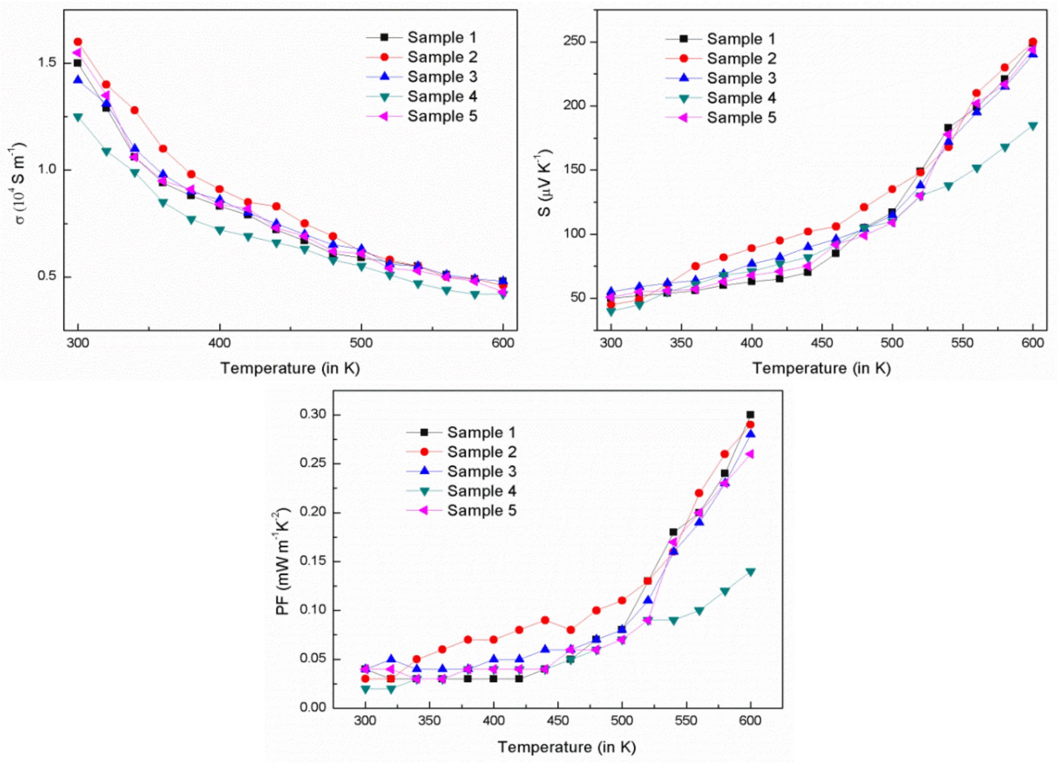

FIG. 6. Temperature dependence of thermal conductivity, Seebeck coefficient and power factors of various samples

TABLE 4. Electrical properties of various samples by Hall measurements

Sample	Carrier concentration (cm^{-3})	Resistivity (Ω, cm)	Mobility ($cm^2V^{-1}s^{-1}$)
Sample 1	1.8×10^{18}	0.21	1.01
Sample 2	2.2×10^{19}	0.22	0.64
Sample 3	2.1×10^{19}	0.21	0.59
Sample 4	1.7×10^{18}	0.24	1.20
Sample 5	2.0×10^{18}	0.23	0.99

Table 4 presents the electrical properties of CZTSe materials characterized by four probe Hall measurements at room temperature. The measurements were used to estimate the mobility, carrier concentration and resistivity of the materials. All materials had p-type conductivity based on the positive sign of the Hall coefficient. Carrier concentration was found in the range of 10^{18} – 10^{19} cm^{-3}. There was an increment in carrier concentration with the increase in Se concentration while resistivity and mobility values decreased i.e. the trend of change in mobility and resistivity with increase in Se content was opposite to the carrier concentration. Since there are some binary and ternary compounds in the samples; these compounds cause a decrease of the carrier concentration. Decrease in mobility could be related to increase in grain size. Moreover the electrical properties were in good agreement with the reports published earlier for kesterite materials.

4. Conclusions

Despite the challenging objective, CZTSe bulk materials were prepared by solid state reaction of the elemental constituents. The structure, morphology, thermoelectric and electrical properties were investigated. Analysis of AFM images revealed a significant difference has been observed in roughness parameters and grain size with respect to Cu/Zn variations, and it can be concluded that Cu deficiency and excess of Zn in the samples caused a decrease in mean grain size with respect to perfect stoichiometric sample of CZTSe. These observations have been analyzed and verified in terms of XRD and Raman scattering studies. The appearance of prominent peaks in the XRD spectrum confirms the formation of nanocrystalline CZTSe materials. Raman spectra of various samples have the vibration mode peaks corresponding to CZTSe, revealing no secondary phases in the materials. XPS analysis of all the samples confirmed the chemical valences of $+1$, $+2$, $+4$, and -1 for Cu, Zn, Sn, and Se, respectively.The stoichiometric sample, $Cu_2ZnSnSe_4$, exhibited the maximum power factor 0.30 $mW{\cdot}m^{-1}K^{-2}$, having a carrier concentration in the range of 10^{18} – 10^{19} cm^{-3} and resistivity in the range of 0.21 to 0.24 $\Omega{\cdot}cm$. The electrical and thermoelectric behaviors shown by various samples arein accordance with earlier studies.

Acknowledgements

Author is sincerely thankful to Director and Dr. Jasaram, Defence Laboratory, Jodhpur; Director, MRC, MNIT, Jaipur; Dr. A. K. Sinha, Dr. M. K. Tiwari, Dr. V. Srihari (beam time for XRD at BL-11) and U. Gautam (beam time for BL-14) at INDUS-II, Raja Rammanna Center for Advanced Technology (RRCAT), Indore; Dr. K. Ashokan and Sh. R. C. Meena from IUAC, New Delhi for their experimental and technical support.

References

[1] Kush P., Deka S. Multifunctional copper-based quaternary chalcogenide semiconductors toward state-of-the-art energy applications. *Chem. Nano Mat.*, 2019, **5** (4), P. 373–402.

[2] Tanaka K., Oonuki M., Moritake N., Uchiki H. Cu_2ZnSnS_4 thin film solar cells prepared by Non-vacuum Processing. *Sol. Energy Mater. Sol. Cells*, 2009, **93**, 583.

[3] Guo Q., Ford G.M., et al. Fabrication of 7.2% Efficient CZTSSe Solar Cells using CZTS Nanocrystals. *J. Am. Chem. Soc.*, 2010, **132**, 17384.

[4] Tsuji I., Shimodaira Y., et al. Novel Stannite-type Complex Sulfide Photocatalysts AI–Zn–AIV–S4 (AI = Cu and Ag; AIV = Sn and Ge) for Hydrogen Evolution under Visible-Light Irradiation. *Chem. Mater.*, 2010, **22**, 1402.

[5] Samanta L.K., Bhar G.C. Optical Nonlinearity of Some Stannite and Famatinite Crystals. *Phys. Status Solidi A*, 1977, **41**, 331.

[6] Chen S., Gong X.G., et al. Band Structure Engineering of Multinary Chalcogenide Topological Insulators. *Phys. Rev. B*, 2011, **83**, 245202.

[7] Fries T., Shapira Y., et al. Magnetic ordering of the antiferromagnet Cu_2MnSnS_4 from magnetization and neutron-scattering measurements. *Phys. Rev. B*, 1997, **56**, 5424.

[8] Nenert G., Palstra T.T.M. Magnetoelectric and Multiferroic Properties of Ternary Copper Chalcogenides $Cu_2MIIMIVS_4$. *J. Phys.: Cond. Matter*, 2009, **21**, 176002.

[9] Liu M.L., Huang F.Q., Chen L.D., Chen I.W. A wide-band-gap P-type thermoelectric material based on quaternary chalcogenides of Cu_2ZnSnQ_4 (Q=S,Se). *Appl. Phys. Lett.*, 2009, **94**, 202103.

[10] Ibanez M., Cadavid D., et al. Composition control and thermoelectric properties of quaternary chalcogenide nanocrystals: The case of Stannite $Cu_2CdSnSe_4$. *Chem. Mater.*, 2012, **24**, 562.

[11] Dong Y., Khabibullin A.R., et al. Synthesis, Transport properties, and Electronic Structure of $Cu_2CdSnTe_4$. *Appl. Phys. Lett.*, 2014, **104**, 252107.

[12] Dong Y., Wang H., Nolas G.S. Synthesis and thermoelectric properties of Cu excess $Cu_2ZnSnSe_4$. *Phys. Status Solidi RRL*, 2014, **8**, 61.

[13] Wang B., Xiang H., et al. Theoretical investigation on thermoelectric properties of Cu-based chalcopyrite compounds. *Phys. Rev. B*, 2017, **95**, 035201.

[14] Raju C., Falmbigl M., et al. Thermoelectric properties of chalcogenide based $Cu_{2+x}ZnSn_{1-x}Se_4$. *AIP Adv.*, 2013, **3**, 032106.

[15] Yang H., Jauregui L.A., et al. Nontoxic and abundant copper zinc tin sulfide nanocrystals for potential high-temperature thermoelectric energy harvesting. *Nano Lett.*, 2012, **12**, 540.

[16] Fan F.J., Wang Y.X., et al. Large-scale colloidal synthesis of non-stoichiometric $Cu_2ZnSnSe_4$ nanocrystals for thermoelectric applications. *Adv. Mater.*, 2012, **24**, 6158.

[17] Liu M.L., Chen I.W., Huang F.Q., Chen L.D. Improved thermoelectric properties of Cu-doped quaternary chalcogenides of $Cu_2CdSnSe_4$. *Adv. Mater.*, 2009, **21**, 3808.

[18] Ibáñez M., Cadavid D., et al. Composition control and thermoelectric properties of quaternary chalcogenide nanocrystals: The case of stannite $Cu_2CdSnSe_4$. *Chem. Mater.*, 2012, **24**, 562.

[19] Fan F.J., Yu B., et al. Colloidal synthesis of $Cu_2CdSnSe_4$ nanocrystals and hot-pressing to enhance the thermoelectric figure-of-merit. *J. Am. Chem. Soc.*, 2011, **133**, 15910.

[20] Paul S., Gulyas I., et al. Carrier transport properties in a thin-film $Cu_2ZnSnSe_4$ solar cell. *Thin Solid Films*, 2019, **675**, 103.

[21] Zeier W.G., LaLonde A., et al. Influence of a nano phase segregation on the thermoelectric properties of the p-Type doped stannite compound $Cu_{2+x}Zn_{1-x}GeSe_4$. *J. Am. Chem. Soc.*, 2012, **134**, 7147.

[22] Goto Y., Naito F., et al. Enhanced thermoelectric figure of merit in stannite-kuramite solid solutions $Cu_{2+x}Fe_{1-x}SnS_{4-y}$ (x =0–1) with anisotropy lowering. *Inorg. Chem.*, 2013, **52**, 9861.

[23] Dong Y., Wang H.S., Nolas G. Synthesis and thermoelectric properties of Cu excess $Cu_2ZnSnSe_4$. *Phys. Status Solidi RRL*, 2014, **8**, 61.

[24] Chiang M.H., Fu Y.S., et al. Effects of Zn precursors on solvothermal synthesis of $Cu_2ZnSnSe_4$ nanocrystals. *Mater. Lett.*, 2012, **83**, 192.

[25] Shi X., Xi L., et al. CuSe Bond Network and Thermoelectric Compounds with Complex Diamondlike Structure. *Chem. Mater.*, 2010, **22**, 6029.

[26] Cui Y., Deng R., Wang G., Pan D. A general strategy for synthesis of quaternary semiconductor Cu_2MSnS_4 (M = Co^{2+}, Fe^{2+}, Ni^{2+}, Mn^{2+}) nanocrystals. *J. Mater. Chem.*, 2012, **22**, 23136.

[27] Du Y.F., Zhou W.H., et al. Solvothermal synthesis and characterization of quaternary $Cu_2ZnSnSe_4$ particles. *Mater. Sci. Semi. Proced.*, 2012, **15**, 214.

[28] Wei T., Qin Y., et al. Copper chalcogenide thermoelectric materials. *Sci. China Mater.*, 2019, **62**, 8.

[29] Fan C.M., Regulacio M.D., et al. Colloidal nanocrystals of orthorhombic Cu_2ZnGeS_4: phase-controlled synthesis, formation mechanism and photocatalytic behaviour. *Nanoscale*, 2015, **7**, 3247.

[30] Wei K., Nolas G.S. Synthesis and Characterization of Nanostructured Stannite $Cu_2ZnSnSe_4$ and $Ag_2ZnSnSe_4$ for Thermoelectric Applications. *ACS Appl. Mater. Interfaces*, 2015, **7**, 9752.

[31] Xue D.J., Jiao F., et al. Synthesis of Wurtzite $Cu_2ZnGeSe_4$ Nanocrystals and their Thermoelectric Properties. *Chem. – An Asian J.*, 2013, **8**, 2383.

[32] Shi X.Y., Huang F.Q., Liu M.L., Chen L.D. Thermoelectric properties of tetrahedrally bonded wide-gap stannite compounds $Cu_2ZnSn_{1x}In_xSe_4$. *Appl. Phys. Lett.*, 2009, **94**, 122103.

[33] Chen D., Zhao Y., et al. Hot-Injection Synthesis of Cu-Doped $Cu_2ZnSnSe_4$ Nanocrystals to Reach Thermoelectric ZT of 0.70 at 450 °C. *ACS Appl. Mater. Interfaces*, 2015, **7** (44), 24403.

[34] Ritchie C., Chesman A., Jasieniak J., Mulvaney P. Aqueous Synthesis of $Cu_2ZnSnSe_4$ Nanocrystals. *Chem. Mater.*, 2019, **31** (6), 2138.

[35] Zoppi G., Forbes I., et al. $Cu_2ZnSnSe_4$ thin film solar cells produced by selenisation of magnetron sputtered precursors. *Progress in Photovoltaics: Research and Applications*, 2009, **17** (5), 315.

[36] Fan P., Zhao J., et al. Effects of annealing treatment on the properties of CZTSe thin films deposited by RF-magnetron sputtering. *Journal of Alloys and Compounds*, 2015, **625**, 171.

[37] Redinger A., Hönes K., et al. Detection of a ZnSe secondary phase in coevaporated $Cu_2ZnSnSe_4$ thin films. *Applied Physics Letters*, 2011, **98** (10), 101907.

[38] Gremenok V.F., Juskenas R., et al. Growth and properties of $Cu_2ZnSnSe_4$ films on flexible metallic substrates. *Proceedings of the 33rd European Photovoltaic Solar Energy Conference and Exhibition*, 2017, P. 1081.

[39] Stanchik V., Gremenok V.F., et al. Effects of selenization time and temperature on the growth of $Cu_2ZnSnSe_4$ thin films on a metal substrate for flexible solar cells. *Sol. Ener.*, 2019, **178**, 142.

[40] Urazov K.A., Dergacheva M.B., Gremenok V.F., Mit K.A. AFM Investigation of CZTS and CZTSe thin films. *Physics, Chemistry And Application Of Nanostructures: Reviews And Short Notes To Nanomeeting*, 2017, **406**.

[41] Kumar B.R., Rao T.S. AFM Studies on surface morphology, topography and texture of nanostructured zinc aluminum oxide thin films. *Digest Journal of Nanomaterials and Biostructures*, 2012, **7** (4), 1881.

[42] Sharma Y.C., Prajapat R. Study of mixing behaviour of Cu, Zn, Sn and Se multilayer structure by annealing. *Mater. Res. Express*, 2019, **6**, 086418.

[43] Li J., Ma T., et al. The $Cu_2ZnSnSe_4$ thin films solar cells synthesized by electrodeposition route. *Appl. Sur. Sci.*, 2012, **258**, 6261.

[44] Wibowo R.A., Kim W.S., et al. Single step preparation of quaternary $Cu_2ZnSnSe_4$ thin films by RF magnetron sputtering from binary chalcogenide targets. *J. Phy. Chem. Sol.*, 2007, **68**, 1908.

[45] Farva U., Park C. Quaternary Chalcogenide Nanocrystals: Synthesis of $Cu_2ZnSnSe_4$ by Solid State Reaction and their Thermoelectric Properties. *MRS Online Proceedings Library Archive*, 2013, **1543**, 137.

[46] Bishop D.M., McCandless B.E., et al. Fabrication and electronic properties of CZTSe single crystals. *IEEE Journal of Photovoltaics*, 2015, **5**, 390.

[47] Wibowo R.A., Jung W.H., et al. Crystallization of $Cu_2ZnSnSe_4$ compound by solid state reaction using elemental powders. *Materials Chemistry and Physics*, 2010, **124**, 1006.

[48] Wibowo R.A., Jung W.H., Kim K.H. Synthesis of $Cu_2ZnSnSe_4$ compound powders by solid state reaction using elemental powders. *J. Phy. Chem. Sol.*, 2010, **71**, 1702.

[49] Curé Y., Pouget S., Reita V., Boukari H. $Cu_2ZnSnSe_4$ thin films grown by molecular beam epitaxy. *Scripta Materialia*, 2017, **130**, 200.

[50] Choubrac L., Lafond A., et al. The stability domain of the selenide kesterite photovoltaic materials and NMR investigation of the Cu/Zn disorder in $Cu_2ZnSnSe_4$ (CZTSe). *Phys. Chem. Chem. Phys.*, 2015, **17**, 15088.

[51] Gurieva G., Levcenco S., et al. Investigation of Detection Limits of ZnSe and Cu_2SnSe_3 Secondary Phases in $Cu_2ZnSnSe_4$. *Physica Status Solidi C*, 2017, **14**, 1700166.

[52] Jagannath, Goutam U.K., et al. HAXPES beamline PES-BL14 at the Indus-2 synchrotron radiation source. *J. Synchrotron Rad.*, 2018, **25**, P. 1541–1547.

NANOSYSTEMS: PHYSICS, CHEMISTRY, MATHEMATICS, 2020, 11 (2), P. 205–213

Cryometry and excess thermodynamic functions in water soluble of the fullerenol $C_{60}(OH)_{24}$

N. A. Charykov[1,5], K. N. Semenov[1,2,6], V. A. Keskinov[1], N. A. Kulenova[3], Z. K. Shaimardanov[3],
B. K. Shaimardanova[3], L. V. Gerasimova[1], Ayat Kanbar[1], D. G. Letenko[4]

[1]St. Petersburg State Technological Institute (Technical University),
Moskovsky prospect, 26 Saint-Petersburg, 190013, Russia

[2]St. Petersburg State University,7/9 Universitetskaya emb., Saint-Petersburg, 199034, Russia

[3]D. Serikbayev East Kazakhstan state technical university,
A. K. Protozanov Street, 69, Ust-Kamenogorsk city, 070004,The Republic of Kazakhstan

[4]St. Petersburg State University of Architecture and Civil Engineering (SPSUACE),
2-nd Krasnoarmeiskaya St. 4, 190005 St. Petersburg, Russia

[5]St. Petersburg Electrotechnical University "LETI", ul. Professora Popova 5, 197376 St. Petersburg, Russia

[6]Pavlov First Saint Petersburg State Medical University
L'va Tolstogo str. 6-8 Saint Petersburg, 197022, Russia

keskinov@mail.ru

PACS 61.48.+c **DOI 10.17586/2220-8054-2020-11-2-205-213**

The temperature of water-ice crystallization initiation decreases (ΔT) were determined in the binary water solutions of water soluble fullerenol: $C_{60}(OH)_{24} - H_2O$ at 272.85–273.15 K. Solution concentrations (in molar fractions) vary over a wide range $x_{nano-cluster} = 5.0 \cdot 10^{-6} \div 1.6 \cdot 10^{-4}$ a.un. Liquidus temperatures were determined with the help of Beckman thermometer with a linear resolution of the device scale $\frac{\Delta T}{\Delta h} \approx 0.01$ K/mm (h – height of Hg capillary raising). For the thermodynamic description of the discussed systems, we have elaborated an original semi-empirical model, the virial decomposition asymmetric model (VD-AS), with assistance from partial molar functions of nano-clusters (activities and activity coefficients) were calculated. The Gibbs energies for the solutions and miscibility gap concentration regions were calculated. VD-AS model excellently describes pre-delamination or micro-heterogeneous-structure formation in the considered solutions. These calculations are confirmed by the dynamic light scattering data.

Keywords: fullerenol $C_{60}(OH)_{24}$, water solutions, cryometry, excess functions, delamination.

Received: 19 February 2020

Revised: 1 March 2020

1. Introduction

The article is the development of the investigations, devoted to the synthesis, identification and investigation of physico-chemical properties of water soluble derivatives of light fullerene C_{60} and C_{70}, such as: complexes of eithertwo-based dicarboxylic acids (malonates, oxalates), poly-hydroxylated forms (fullerenols), amino-acid derivatives (arginine, alanine) some other derivatives [1–32]. In these works, in particular, such physical-chemical properties of water solutions of light fullerene derivatives, depending on the solutions concentration, were investigated: polythermal solubility and crystal hydrate compositions; volume properties (density, average and partial components molar volumes); refraction indices, specific and molar refractions; conductivity and hydrogen indicator (seeming dissociation degrees and concentration dissociation constants); associates dimensions and electro-kinetic ζ–potentials, some others.

The investigation of the excess thermodynamic functions in such systems (activities, activity coefficients, excess (or mixing) Gibbs energies (enthalpies, entropies) etc, as authors know, until this time was not provided, except for some original works [33–38]. In these articles, in the binary systems with the help of cryometry investigations, the authors determined the decrease of the temperatures of the beginning of ice crystallization (liquidus temperatures), water activities, water activity coefficients, and then, numerically solving the Gibbs-Duhem equation – activities and activity coefficients of fullerene derivatives. No other data, concerning excess function in considered systems, obtained, for example by isopiestic method, were not found, unfortunately. Meanwhile, such data may be very scientifically interesting, because these water solutions have very specific and rare consistent hierarchical type of association (vide infra).

2. Cryometry data in the binary water solutions of water soluble derivatives of light fullerenes

The temperature of water-ice crystallization initiation decreases (ΔT) were determined in the binary water solutions of water soluble derivative of light fullerenes: $C_{60}(OH)_{24}$–H_2 at 272.85–273.15 K. Solution concentrations (in molar fractions) vary in the wide range $X_{nano-cluster} = 5.0 \cdot 10^{-6} \div 1.6 \cdot 10^{-4}$ rel.un. Liquidus temperatures were determined with the help of Beckman thermometer with the linear resolution of the device scale $\frac{\Delta T}{\Delta h} \approx 0.01$ K/mm (h – height of Hg capillary raising). Cryometry data $\Delta T(x_{nano-cluster})$ are depicted in the Fig. 1 and in Table 1.

TABLE 1. Cryometry data and excess thermodynamic functions in the binary system bis-adduct of light fullerene C_{70} and amino-acid – lysine V at 272.99–273.15 K

Molar fraction of $C_{60}(OH)_{24}$ in the solution $X_{C_{60}(OH)_{24}}$ (rel.un.)	Temperature of the beginning of ice crystallization decrease ΔT (K)	$\ln a_{H2O}$ ln(water activity) (rel.un.)	$\ln \gamma_{H2O}$ ln(water activity coefficient) (rel.un.)	$\ln \gamma^{as}_{C_{60}(OH)24}$ ln(activity coefficient of $C_{60}(OH)_{24}$ (rel.un.)
0.000	0.000	0.000	0.000	0.000
$1.083 \cdot 10^{-6}$	0.005	$-5.86 \cdot 10^{-5}$	$-5.75 \cdot 10^{-5}$	3.38
$2.166 \cdot 10^{-6}$	0.013	$-1.44 \cdot 10^{-4}$	$-1.42 \cdot 10^{-4}$	6.65
$4.332 \cdot 10^{-6}$	0.020	$-2.22 \cdot 10^{-4}$	$-2.18 \cdot 10^{-4}$	12.9
$8.66 \cdot 10^{-6}$	0.030	$-3.33 \cdot 10^{-4}$	$-3.25 \cdot 10^{-4}$	24.3
$1.73 \cdot 10^{-5}$	0.050	$-5.49 \cdot 10^{-4}$	$-5.32 \cdot 10^{-4}$	42.2
$3.46 \cdot 10^{-5}$	0.075	$-8.22 \cdot 10^{-4}$	$-7.87 \cdot 10^{-4}$	66.0
$6.92 \cdot 10^{-5}$	0.11	−0.00122	−0.00116	72.5
$1.38 \cdot 10^{-4}$	0.16	−0.00178	−0.00164	73.1

One can see, that all dependencies $\Delta T(x_{nano-cluster})$ are sharply nonlinear, which prove very high positive deviations of the solutions from ideality for all solutions, even when very diluted. In the Fig. 1 for the comparison by the arrow is represented the value ΔT^{id} for the ideal non-electrolyte solution. We can see the experimental ΔT exceeds ΔT^{id} one-two orders (for comparable concentrated and diluted solutions, correspondingly). So, one should expect probably gigantic positive deviations of the solution from the ideality in thermodynamic sense.

3. Calculation of water excess functions

For the calculation of water activity we have used well-known equation, got from the equality of the chemical H_2O potentials in pure solid ice and non-ideal liquid solution [34–38]:

$$\frac{-\Delta H_W^f \Delta T - \Delta C_P \Delta T^2}{R\left(T_0^f - \Delta T\right) T_0^f} = \ln a_{H2O}, \tag{1}$$

where $\Delta H_W^f = 5990$ J/mole, $\Delta C_P = -38.893$ J/mole·K, $T_0^f = 273.15$ K heat, temperature of ice fusion and change of heat capacity in the process of ice fusion, correspondingly. Equation (1) was displayed in the symmetrical normalization scale for thermodynamic functions for both solution components:

$$a_{H2O}(x_{H2O} = 1) = \gamma_{H2O}(x_{H2O} = 1) = 1, \tag{2}$$

$$a_{nano-cluster}\,(x_{nano-cluster} = 1) = \gamma_{nano-cluster}(x_{nano-cluster} = 1) = 1, \tag{3}$$

where x_i and a_i, γ_i – molar fraction, activity and activity coefficient of i-th component.

Calculated data $\ln[a_{H2O}(x_{nano-cluster})]$ are represented in Fig. 2 and Table 1.

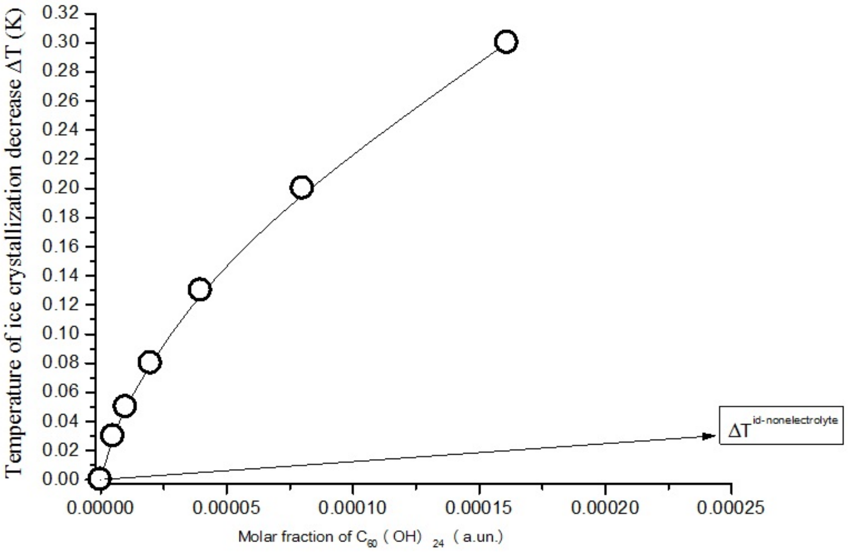

FIG. 1. Temperature of water-ice crystallization beginning (liquidus temperature) decrease (ΔT) against molar fraction concentration in the binary solutions: $C_{60}(OH)_{24}$–H_2O at 272.85–273.15 K. Arrow shows ΔT-function for the ideal non-electrolyte solution

Further authors [33–38] calculated concentration dependencies $\ln\gamma_{H2O}$, derivatives $\frac{d\ln\gamma_{H2O}}{dx_{nano-cluster}}$ (numerically). Then, authors [33–38] (especially [36]) calculated the dependencies $\frac{d\ln\gamma_{nano-cluster}}{dx_{nano-cluster}}$, (according to classical differential Gibbs-Duhem differential equation) also numerically and at the end by numerical integration the dependencies $\ln\gamma_{nano-cluster}$ ($x_{nano-cluster}$) were calculated. As a result, as was expected earlier, significant positive deviations of the solution from the ideality for the functions $\ln\gamma_{nano-cluster}$ were obtained $\ln\gamma_{nano-cluster} \approx$ n($10^0 \div 10^1$) (see Table 1 and lower – Fig. 4). Naturally, in all likelihood, no currently existing thermodynamic model can describe such non-trivial behavior of nano-cluster thermodynamic functions.

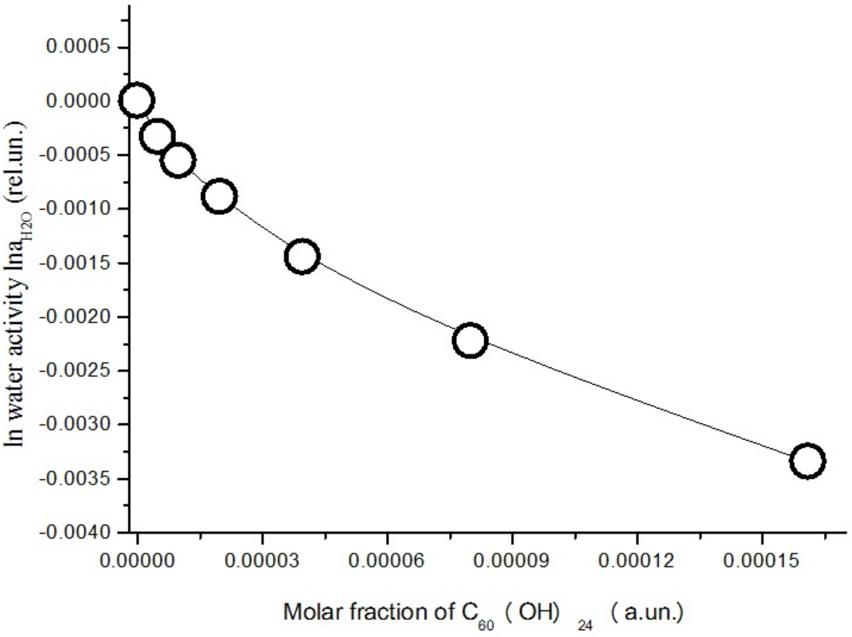

FIG. 2. Logarithm of water activity ($\ln a_{H2O}$) against molar fraction concentration in the binary solutions: $C_{60}(OH)_{24}$–H_2O at 272.85–273.15 K

4. Virial Decomposition Asymmetric Model – VD–AS

For the description of such nontrivial thermodynamic behavior of considered water solutions, we have elaborated semi-empirical model VD-AS (Virial Decomposition Asymmetric Model), based on the virial decomposition of excess molar Gibbs energy on the solution for the components molar fractions. This technique has often been used for the thermodynamic description of binary and multicomponent systems with the different physical-chemical nature, such as: electrolyte solutions [39–42], non-electrolyte (semiconductor) melts [43–46], isovalent substitution solid solutions [47–49]. If one takes only one term in the decomposition for the binary system (corresponding to the invariant second virial coefficient), – see later equation (4) well-known strictly regular solutions model – RSM, is realized. Under the assumption of the temperature dependence for the only virial coefficient, the quasi-regular solution model – QRSM is realized. If one uses third virial coefficients for the decomposition, the sub-regular solution model – SRSM, is realized. Finally, when one additionally takes into account the contribution of the electrostatic non-specific interactions (according to Debye-Huckel theory) Pitzer's model in different variants is realized.

So, let the following numeration: 1 – is the number of the dissolved component (nano-cluster in our case), 2 – is the number of the solvent (H_2O). Let us postulate the following expression:

$$\frac{G^{ex}}{RT} = (n_1 + n_2)\sum_{i=1}\sum_{j=1} X_1^i X_2^j * \lambda_{ij} = \frac{\sum_{i=1}\sum_{j=1} n_1^i n_2^j * \lambda_{ij}}{(n_1+n_2)^{i+j-1}}, \tag{4}$$

where G^{ex} – full molar excess solution Gibbs energy, $R = 8.31$ J/K, T – temperature (K), n_i and X_i – molar number and molar fraction of i-th component, correspondingly, λ_{ij}–ij-th virial coefficient in the decomposition of G^{ex}/RT on the component molar numbers. In other words, λ_{ij} are naturally identified as divided by RT specific energy of interaction of i particles of the 1-st component and j particles of the 2-nd component. If one takes into account huge (two orders of magnitude) differences in components molar masses (1-st are heavy) and it's linear dimensions (almost one order – nanoclusters in our case are hollow), it is quite clear, that if upper limit of the summation according to the 1-st component is small natural number (not more than 4-6), that if upper limit of the summation according to the 2-st component may be more on one-two order.

Let us calculate excess thermodynamic functions of the components $\ln\gamma_i$:

$$\ln\gamma_1 = \frac{\partial(G^{ex}/RT)}{\partial n_1} = \sum_{i=1}\sum_{j=1}[i - (i+j-1)X_1]X_1^{i-1}X_2^j * \lambda_{ij}, \tag{5}$$

$$\ln\gamma_2 = \frac{\partial(G^{ex}/RT)}{\partial n_2} = \sum_{i=1}\sum_{j=1}[j - (i+j-1)X_2]X_1^{i}X_2^{j-1} * \lambda_{ij}. \tag{6}$$

In our case molar fractions f the components are incomparable:

$$X_2 >> X_1, X_2 > 0.999 \approx 1 X_1 << 1. \tag{7}$$

So, equations (5), (6) may be simplified:

$$\ln\gamma_2 \approx \sum_{i=1}(1-i)X_1^i\sum_{j=1}\lambda_{ij} = \sum_{i=2}(1-i)X_1^i\sum_{j=1}\lambda_{ij}. \tag{8}$$

From the systems (5), (6), (8) one can see that, they are agreed in thermodynamic sense, i.e. Gibbs-Duhem equation is valid at T,P = const:

$$X_1 d\ln\gamma_1 + X_2 d\ln\gamma_2 = 0, \tag{9}$$

or, for example from the equations (7) and (8), we can get identity:

$$X_1\sum_{i=1} i(i-1)X_1^{i-2}\lambda_{ij}dX_1 + \sum_{i=1}(1-i)iX_1^{i-1}\lambda_{ij}dX_1 = 0. \tag{10}$$

Let us transfer system (7), (8), denoting as Λ_i summary virial coefficients:

$$\sum_{j=1}\lambda_{ij} = \Lambda_i(T), \tag{11}$$

So, in our conditions of consideration:

$$\ln\gamma_1 \approx \sum_{i=1} i\Lambda_i X_1^{i-1} \tag{12}$$

$$\ln\gamma_2 \approx \sum_{i=1}(1-i)\Lambda_i X_1^i = \sum_{i=2}(1-i)\Lambda_i X_1^i. \tag{13}$$

One can see, that, if $\Lambda_1 \neq 0$, then logarithms of the limit activity coefficients – $\ln\gamma_i^0 = \lim_{X1\to 0}\ln\gamma_i$, correspond to symmetrical method or normalization of the excess thermodynamic functions, namely:

$$\ln\gamma_1^0 = \Lambda_1 \neq 0, \quad \gamma_1(X_1 \to 0) = \gamma_1^0 \neq 1, \tag{14}$$

$$\ln\gamma_2^0 = 0, \quad \gamma_2(X_1 \to 0) = 1. \tag{15}$$

In our case incomparable more conveniently is to use asymmetrical normalization scale, (for this one should only demand the performing of the single condition $\Lambda_1 = 0$):

$$\ln\gamma_1^0 = 0, \quad \gamma_1\left(X_1 \to 0\right) = \gamma_1^0 = 1. \tag{16}$$

$$\ln\gamma_2^0 = 0, \quad \gamma_2\left(X_1 \to 0\right) = 1, \tag{17}$$

$$\ln\gamma_1^{ass} \approx \sum_{i=2} i\Lambda_i X_1^{i-1}, \tag{18}$$

$$\ln\gamma_2^{ass} \approx \sum_{i=2}\left(1-i\right)\Lambda_i X_1^i. \tag{19}$$

This normalization scale will be used by us always default.

Let us introduce the function $\frac{G^{mix}}{RT}$ (divided by RT molar Gibbs energy of mixing), the second isothermal – isobaric concentration derivative of which is equal to the full solution molar Gibbs energy:

$$\frac{G^{mix}}{RT} = X_1\ln X_1 + X_2\ln X_2 + X_1\ln\gamma_1 + X_2\ln\gamma_2, \tag{20}$$

$$\frac{\partial\left[G^{mix}/RT\right]}{\partial X_1} = \frac{1}{X_1} + \frac{1}{X_2} - \left(\ln X_2 + 1\right) + \sum_{i=1} i^2\Lambda_i X_1^{i-1} + \sum_{i=2}\left(1-i\right)\Lambda_i\left[i\left(i-1\right)X_1^{i-2} - \left(i+1\right)X_1^{i-1}\right] \tag{21}$$

$$\frac{\partial^2\left[G^{mix-ass}/RT\right]}{\partial X_1^2} \approx \frac{1}{X_1} + \sum_{i=2} i\left(i-1\right)\Lambda_i X_1^{i-2}. \tag{22}$$

Absolutely similarly we can calculate (divided by *RT*) first isothermal – isobaric concentration derivative of the chemical potential or logarithm of the activity of the 1-st component - μ_1 and $\ln a_1$, correspondingly:

$$\frac{1}{RT}\frac{\partial\mu_1}{\partial X_1} = \frac{\partial\ln a_1}{\partial X_1} \approx \frac{1}{X_1} + \sum_{i=2} i\left(i-1\right)\Lambda_i X_1^{i-2}. \tag{23}$$

So, the equation of the diffusional (spinodal) stability loss will be the following:

$$G_{11}^{mix-ass} = \frac{\partial^2\left[G^{mix-ass}/RT\right]}{\partial X_1^2} = \frac{\partial\ln a_1}{\partial X_1} \approx \frac{1}{X_1} + \sum_{i=2} i\left(i-1\right)\Lambda_i X_1^{i-2} = 0. \tag{24}$$

5. Application of VD-AS model to the description water soluble derivatives of light fullerenes water solutions. Calculation of nanoclusters excess functions. Miscibility gaps

Preliminary calculation shows that the 3-term approximation in VD-AS – model (i.e. $i = 2, 3, 4$) is sufficient for more or less successful for the excess thermodynamic functions calculation with the satisfactory accuracy:

$$\ln\gamma_1^{ass} \approx 2\Lambda_2 X_1 + 3\Lambda_3 X_1^2 + 4\Lambda_4 X_1^3, \tag{25}$$

$$\ln\gamma_2^{ass} \approx -\Lambda_2 X_1^2 - 2\Lambda_3 X_1^3 - 3\Lambda_4 X_1^4. \tag{26}$$

So, the equation of the diffusional (spinodal) stability loss will be the following:

$$12\Lambda_4 X_1^3 + 6\Lambda_3 X_1^2 + 2\Lambda_2 X_1 + 1 = 0, \tag{27}$$

or is elementary explicitly solved relatively X_1 (according to Cardano formula) cubic equation.

All calculated parameters of VD-AS – model is represented in Table 2.

In all considered binary systems we calculated concentration dependencies $\ln\gamma_{H2O}$ (see Table 1):

$$\ln\gamma_2 = \ln_{H2O} = \ln a_{H2O} - \ln X_{H2O} = \ln a_{H2O} - \ln\left(1 - X_1\right), \tag{28}$$

and from these functions $\ln\gamma_2(X_1)$ according to equation (26) we determined parameters of VD-AS model: (Λ_2, Λ_3, Λ_4) (see Table 2).

Formally, the huge values of summary virial coefficients Λ_i, in general, are not surprising, if we remember that, according to the physical sense, the last ones are the sums of the rows, consist of probably thousands terms, responsible for the energies of interactions of few nano-clusters with very large number of water molecules.

TABLE 2. Parameters of model VD-AS (Λ_2, Λ_3, Λ_4) and concentration boards of diffusion instability regions ($X^{diff-instab}$) in the binary system: $C_{60}(OH)_{24}$– H_2O 272.85–273.15 K

VD-AS model parameters (rel.un.)			
Λ_2 (aun.)	Λ_3 (aun.)	Λ_4 (aun.)	$\approx X^{diff-instab}$ (a.un.)
$2.10 \cdot 10^6$	$-1.58 \cdot 10^{10}$	$3.99 \cdot 10^{13}$	$6.0 \cdot 10^{-5}$

Then, according to the equation (24) we calculated concentration dependencies $\ln \gamma_1^{ass}(X_1)$ (See Table 1 and Fig. 3). From Fig. 3 one can see that some dependencies $\ln \gamma_1^{ass}(X_1)$ will cross through the maximum at the values: $X_1 \approx 1.5 \cdot 10^{-4}$ rel.un. (in our case, it lays slightly beyond the investigated concentration range). Maximum state may be determined easily, form the equation (24), solving square equation:

$$\frac{1}{2}\frac{d\ln \gamma_1^{ass}}{dX_1} = \Lambda_2 + 3\Lambda_3 X_1^{+} 6\Lambda_4 X_1^2 = 0. \tag{29}$$

In our opinion, it interesting to compare cryometry data in these system $C_{60}(OH)_{24}$ – H_2O (pure derivative without any traces on Na-substituted fulerenol forms, such as $C_{60}(OH)_{23}ONa$) and in the system fullerenol-d – H_2O (mix of $C_{60}(OH)_{22}$, $C_{60}(OH)_{23}$, $C_{60}(OH)_{24}$ etc with the traces of sodium mono-substituted forms – nearly 10^{-3} mol. %). If Fig. 3 one can observe very good agreement between our data and data from [36], despite on some inconsistency in the composition.

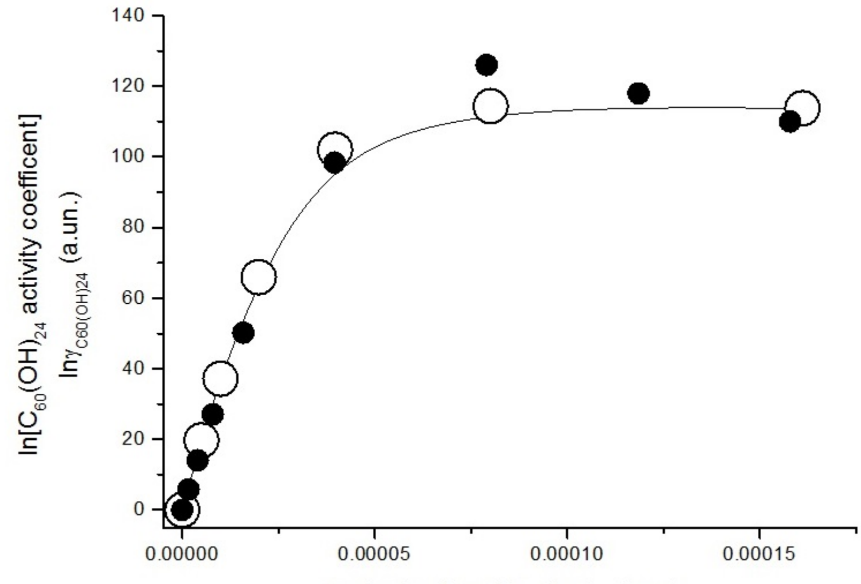

FIG. 3. Logarithm of light fullerene water soluble derivative activity $C_{60}(OH)_{24}$ – H_2O at 272.85–273.15 K (open points – our calculation; solid points symbolize experimental cryometry data from [36] in the related system fullerenol-d – H_2O)

Then, according to the equation (27), we determined the boards of diffusional stability loss - X^{diff} (see Table 2 and Fig. 4), solving cube equation:

$$F = 12\Lambda_4 X_1^3 + 6\Lambda_3 X_1^2 +^2 \Lambda_2 X_1 + 1 = 0. \tag{30}$$

As one can see from Table 2, all cubic equations (27) for our considered systems have real positive roots in real concentration ranges, which correspond to the existence of liquid solutions of nano-clusters in water. From this fact, one can conclude, in some concentration range: $X_1^{diff} \approx 6.0 \cdot 10^{-5}$ rel.un. system begins to flake or may be preflake (see later). In the Fig. 4 the concentration dependencies of the diffusional instability functions $F^{diff-instab} = 12\Lambda_4 X_1^3 + 6\Lambda_3 X_1^2 +^2 \Lambda_2 X_1 + 1 = 0$ is represented. From Fig. 4, we see that almost all functions $F^{diff-instab}(X_1)$ have the initial intersection with the abscissa axis (red point), which corresponds to the diffusional stability loss.

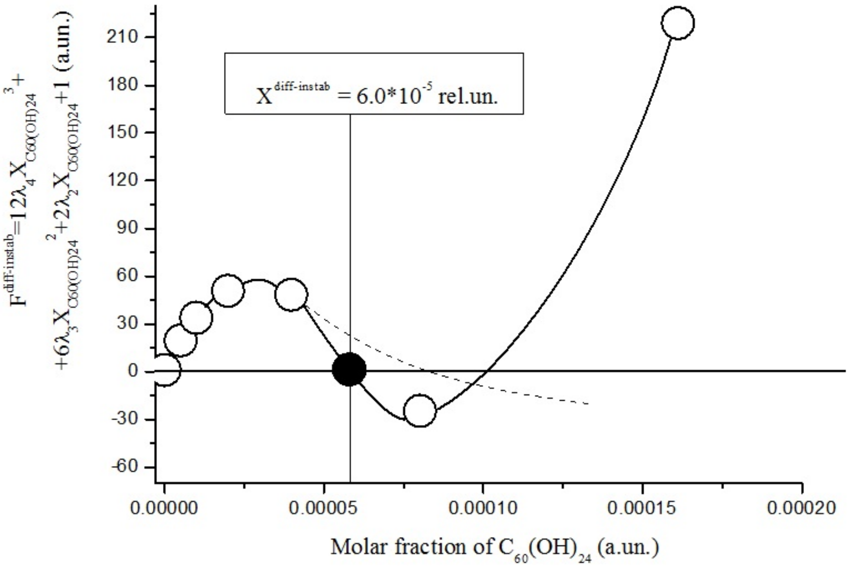

FIG. 4. Instability board function F against molar fraction concentration in the binary solutions: $C_{60}(OH)_{24}$–H_2O at 272.85–273.15 K (solid point corresponds to the border of solutions instability region, dash curve corresponds to the border of solutions instability region from [36])

As expected, even such minor amounts of Na-substituted forms considerably stabilized phase instable nano-cluster solutions.

6. Conclusions

Thus, the water soluble fullerenol $C_{60}(OH)_{24}$ demonstrated very high positive deviations from the ideality, which in turn caused formation of micro-heterogeneous system or pre-delamination in the liquid phase. VD-AS semi-empirical thermodynamic model provided a sufficiently accurate description of the concentration dependence of excess thermodynamic functions in this system.

Acknowledgements

This work was supported by Russian Foundation for Basic Research (RFBR) (Projects Nos. 18-08-00143 A, 19-015-00469 A, and 19-016-00003 A).

References

[1] Li J., Takeuchi A., Ozawa M. et al. C_{60} fullerol formation catalysed by quaternary ammonium hydroxides. *J. Chem.Soc.Chem. Commun.*, 1993, **23**, P. 1784.

[2] Chiang L.Y., Bhonsle J.B., Wang L. et al. Efficient one-ask synthesis of water-soluble fullerenes. *Tetrahedron*, 1996, **52**, P. 4963.

[3] Chiang L.Y., Upasani R.B., Swirczewski J.W. Versatile nitronium chemistry for C_{60} fullerene functionalization. *J.Am.Chem. Soc.*, 1992, **114**, P. 10154.

[4] Meier M.S., Kiegiel J. Preparation and characterization of the fullerene diols 1,2-$C_{60}(OH)_2$, 1,2-$C_{70}(OH)_2$, and 5,6-$C_{70}(OH)_2$. *Org. Lett.*, 2001, **3**, P. 1717.

[5] Szymanska L., Radecka H., Radecki J. et al. Electrochemical impedance spectroscopy for study of amyloid-peptide interactions with (-) nicotine ditartrate and (-) cotinine. Biosens. *Bioelectron*, 2001, **16**, P. 911.

[6] Mirkov S.M., Djordjevic A.N., Andric N.L. et al. Modulating activity of fullerol $C_{60}(OH)_{22}$ on doxorubicin-induced cyto-toxicity. Nitric Oxide, 2004, **11**, P. 201.

[7] Kokubo K., Matsubayashi K., Tategaki H. et al. Facile synthesis of highly water-soluble fullerenes more than half-covered by hydroxyl groups. *ACS Nano*, 2008, **2**(2), P. 327.

[8] Yang J.M., He W., Ping H. et al. The scavenging of reactive oxygen species and water soluble fullerene synthesis. *Chinese. J. Chem.*, 2004, **22**(9), P. 1008.

[9] Sheng W., Ping H., Jian Min Z. et al. Novel and efficient synthesis of water-soluble [C_{60}] fullerenol by solvent-free reaction. *Synthetic Communications*, 2005, **35**(13), P. 1803.

[10] Chiang Long Y. Fullerene Derivatives as Free Radical Scavengers. US patent 5648523. July 15, 1997.

[11] Lamparth I., Hirsch A. Water-soluble malonic acid derivatives of C_{60} with a deffined three-dimensional structure *J. Chem. Soc. Chem. Commun.*, 1994, P. 1727–1728.

[12] Liang Bing GAN, Chu Ping LUO. Water-soluble fullerene derivatives, synthesis and characterization of alanine C_{60} adducts. Chinese Chemical letters, 1994, 5(4), P. 275278.

[13] Kotelnikova R.A., Kotelnikov A.I., Bogdanov G.N., Romanova V.S., Kuleshova E.F., Parnes Z.N., Vol'pin M.E. Membranotropic properties of the water soluble amino acid and peptide derivatives of fullerene C_{60}. FEBS Lett., 1996, **389**, P. 111–114.

[14] Hu Z., Guan W., Wang W., Huang L., Tang X., Xu H., Zhu Z., Xie X., Xing H. Synthesis of amphiphilic amino acid C_{60} derivatives and their protective effect on hydrogen peroxide-induced apoptosis in rat pheochromocytoma cells. *Carbon*, 2008, **46**, P. 99–109.

[15] Kumar A., Rao M.V., Menon S.K. Photoinduced DNA cleavage by fullerene-lysine conjugate. *Tetrahedron Lett.*, 2009, **50**, P. 6526–6530.

[16] Jiang G., Yin F., Duan J., Li G. Synthesis and properties of novel water-soluble fullerene glycine derivatives as new materials for cancer therapy. *J. Mater. Sci: Mater. Med*, 2015, **26**, P. 1–7.

[17] Grigoriev V.V., Petrova L.N., Ivanova T.A., Kotel'nikova R.A., Bogdanov G.N., Poletayeva D.A., Faingold I.I., Mishchenko D.V., Romanova V.S., Kotel'nikov A.I., Bachurin S.O. Study of the neuroprotective action of hybrid structures based onfullerene C_{60}. *Biology Bull*, 2011, **38**, P. 125–131.

[18] Kotel'nikova R.A., Faingol'd I.I., Poletaeva D.A., Mishchenko D.V., Romanova V.S., Shtol'ko V.N., Bogdanov G.N.,Rybkin A.Yu., Frog E.S., Smolina A.V., Kushch A.A., Fedorova N.E., Kotel'nikov A.I. Antioxidant properties of water-soluble amino acid derivatives of fullerenes and their role in the inhibition of herpes virus infection. *Rus. Chem. Bull.*, 2011, **6**, P. 1172–1176.

[19] Leon A., Jalbout A.F., Basiuk V.A. Fullerene-amino acid interactions. A theoretical study. *Chem. Phys. Lett.*, 2008, **452**, P. 306314.

[20] Hu Y.H., Ruckenstein E. Steam reforming products used as a hydrogen resource for hydrogen storage in Li_2N. *J. Mol. Struct. Theochem.*, 2008, **865**, P. 94–97.

[21] Semenov K.N., Charykov N.A., Postnov V.N., Sharoyko V.V., Murin I.V. Phase equilibria in fullerene-containing systems as a basis for development of manufacture and application processes for nanocarbon materials. *Rus. Chem. Rev.*, 2016, **85**, P. 38–59.

[22] Semenov K.N., Charykov N.A., Murin I.V., Pukharenko Yu.V. Physico-Chemical Properties of $C60_{60}$-tris-malonic-derivative Water Solutions. J. of Molecular Liquids, 2015, **202**, P. 50–58.

[23] Semenov K.N., Charykov N.A., Murin I.V., Pukharenko Yu.V. Physico-chemical properties of the fullerenol-70 water solutions. *J. of Molecular Liquids*, 2015, **202**, P. 1–8.

[24] Nikolay A. Charykov, Konstantin N. Semenov, Enriqueta R. Lypez, Josefa Fernndez^c, Evgeny B. Serebryakov, Viktor A. Keskinov^a, Igor V. Murin. Excess thermodynamic functions in aqueous systems containing soluble fullerene derivatives. *J. of Molecule Liquids*, 2018, **256**, P. 305–311.

[25] Serebryakov E.B., Semenov K.N., Stepanyuk I.V., Charykov N.A., Mescheryakov A.N., Zhukov A.N., Alexey V. Chaplygin A.V., Murin I.V. Physico-chemical properties of the C_{70}-L-lysine aqueous solutions. *J. of Molecule Liquids*, 2018, *256*, P. 507–518.

[26] Yur'ev G.O., Lelet M.I., Pochkayeva E.A., Petrov A.V., Semenov K.N., Charykov N.A., Podolskiy N.E., Dulneva L.L., Sharoyko V.V., Murin I.V., Thermodynamic and thermal properties of the C_{60}-L-Arg derivative. J. Chem. *Thermodynamics*, 2018, **127**, P. 39–44.

[27] Podolsky N.E., Marcos M.A., Cabaleiro D., Semenov K.N., Luis Lugo, Petrov A.V., Charykov N.A., Sharoyko V.V., Vlasov T.D., Murin I.V. Physico-chemical properties of C_60(OH)22-24 water solutions: density, viscosity, refraction index, isobaric heat capacity and antioxidant activity. *J. of Mol. Liq*, 2019, **278**, P. 342–355.

[28] Podolsky N., Lelet M., Ageev S., Novikov A., Petrov A., Mazur A., Semenov K., Charykov N., Vasina L., Murin I. Thermodynamic properties from calorimetry and density functional theory and the thermogravimetric analysis of the fullerene derivative $C_{60}(OH)_{40}$. *Journal of Chemical & Engineering Data*, 2019, **64**(4), P. 1480–1487.

[29] Serebryakov E.B., Zakusilo D.N., Semenov K.N., Charyov N.A., Akentiev A.V., Noskov B.A., Petrov A.V., Podolsky N.E., Mazur A.S., Dul'neva L.V., Murin I.V. Physico-chemical properties of C_{70}-l-threonine bisadduct $(C_{70}(C_4H_9NO_2)_2)$ aqueous solutions. *Journal of Molecular Liquids*, 2019, **279**, P. 687–699.

[30] Petrenko V.V., Charykov N.A., Semenov K.N., Keskinov V.A., Kurilenko A.V., Semenyuk V.A., Saf'annikov N.M. Synthesis, Identification and Physical-Chemical Properties of Bis-Adduct of C_{60} with Histidine. Nanotechnology Science and Technology. *Applied Aspects of Nanophysics and Nano-engineering*, 2019, P. 1-6.

[31] Semenyuk V.A., Semenov K.N., Charykov N.A., Keskinov V.A., Petrenko V.V., Kurilenko A.V., Saf'annikov N.M. Tris-Adduct of light Fullerene C_{70} with Indespensible Aminoacide Lysine. *Nanotechnology Science and Technology. Applied Aspects Of Nanophysics and Nano-engineering*, 2019, P. 7–12.

[32] Nikolaev D.N., Podolsky N.E., Lelet M.I., Iamalova N.R., Shemchuk O.S., Ageev S.V., Petrov A.V., Semenov K.N., Charykov N.A., Piotrovskiy L.B., Murin I.V. Thermodynamic and quantum chemical investigation of the monocarboxylated fullerene C_{60}CHCOOH. *J. Chem. Thermodynamics*, 2020, **140**, P. 105898.

[33] Matuzenko M.Yu., Shestopalova A.A., Semenov K.N., Charykov N.A., Keskinov V.A. Cryometry and excess functions of the adduct of light fullerene C_{60} and arginine $C_{60}(C_6H_{12}NAN_4O_2)_8H_8$ aqueous solutions. *Nanosystems: Physics, Chemistry, Mathematics*, 2015, **6**(5), P. 715–725.

[34] Matuzenko M.Yu., Tyurin D.P., Manyakina O.S., Semenov K.N., Charykov N.A., Ivanova K.V., Keskinov V.A. Cryometry and excess functions of fullerenols and trismalonates of light fullerenes $C_{60}(OH)_{22-24}$ and $C_{70}[=C(COOH)_2]_3$, aqueous solutions. *Nanosystems: Physics, Chemistry, Mathematics*, 2015, **6**(4), P. 704–714.

[35] Charykov N.A., Semenov K.N., Keskinov V.V., Garamova P.V., Tyurin D.P., Semenyuk I.V., Petrenko V.V., Kurilenko V.V., Matuzenko M.Yu., Kulenova N.A., Zolotarev A.A., Letenko D.G. Cryometry data in the binary systems bis-adduct of C_{60} and indispensable aminoacids – lysine, threonine, oxyproline. *Nanosystems: Physics, Chemistry, Mathematics*, 2017, **8**(3), P. 397–405.

[36] Safyannikov N.M., Charykov N.A., Garamova P.V., Semenov K.N., Keskinov V.A., Kurilenko A.V., Cherepcova I.A., Tyurin D.P., Klepikov V.V., Matuzenko M.Yu., Kulenova N.A., Zolotarev A.A. Cryometry data in the binary systems bis-adduct of C_{60} and indispensable aminoacids – lysine, threonine, oxyproline. *Nanosystems: Physics, Chemistry, Mathematics*, 2018, **9**(1), P. 46–49.

[37] Charykov N.A., Semenov K.N., Lypez E.R., Fernndez J., Serebryakov E.B., Keskinov V.A., Murin I.V. Excess thermodynamic functions in aqueous systems containing soluble fullerene derivatives. *J. of Molecule Liquids*, 2018, **256**, P. 305–311.

[38] Semenov K.N., Kurilenko A.V., Charykov N.A., Keskinov V.A., Vorob'ev A.L., Shaimardanov Zh.K., Kulenova N.A., Onalbaeva Zh.S., and Letenko D.G. Solubility, Thermal analysis and association of bis-adducts of light fullerene C_{60} and amino-acids: lysine, threonine and oxyproline in water solutions. *Russian Journal of Physical Chemistry A*, 2019, **93**(7), P. 1258–1265.

[39] Pitzer K.S., Pitzer K.S. *J.Phys.Chem.*, 1973, **77**(2), P. 268–277.

[40] Pitzer K.S., Kim J.J. Activity and osmotic coefficients for mixed electrolytes. *J.Amer.Chem.Soc.*, 1974, **96**(28), P. 5701–5707.

[41] Filippov V.K., Charykov N.A., Rumyantsev A.V. The generalization of Pitzer's method on the system with complex formation in the solutions. *Rep. Rus. Acad. Sciences*. Seria: Physics-Chemistry, 1987, **296**(3), P. 665–668.

[42] Carykova M.V., Charykov N.A. *Thermodynamic modeling of evaporate sedimentation processes*. SPb: Nauka, 2003, 257 p.

[43] Charykov N.A., Litvak A.M., Mikhailova M.P., Moiseev K.D., Yakovlev Yu.P. Solid solution $\mathrm{In}_x\mathrm{Ga}_{1-x}\mathrm{As}$ $\mathrm{ySb}_z\mathrm{P}_{1-y-z}$. New material of IR opto-electronics. I. Thermodynamic analysis of production conditions for solid solutions, iso-periodic to the substrates InAs and GaSb, by liquid phase epitaxy method. *Rus. Phys. and Tech. Semic.*, 1997, **31**(4), P. 410–415.

[44] Litvak A.M., Charykov N.A. New thermodynamic method of calculation of melt-solid phase equilibria (for the example of A3B5 systems). *Rus.J.Phys.Chem.*, 1990, **64**(9), P. 2331–2335.

[45] Litvak A.M., Moiseev K.D., Charykov N.A., Yakovlev Yu.P. Hetero-structures $\mathrm{InlxGa}_{1-x}\mathrm{As}_y\mathrm{Sb}_{1-y}$/InAs production by LPE method. *Rus. Tech. Phys. Lett.*, 1990, **16**(13), P. 41-45.

[46] Baranov A.N., Guseinov A.A., Litvak A.M., Popov A.A., Charykov N.A., Sherstnev V.C., Yakovlev Yu.P. Production of solid solutions $\mathrm{InxGa}_{1-x}\mathrm{As}_y\mathrm{Sb}_{1-y}$, iso-periodic to GaSb, nearby miscibility gap. *Rus. Tech. Phys. Lett.*, 1990, **16**(5), P. 33–38.

[47] Stringfellow G.B. Calculation of energy band gaps in quaternary III-IV alloys. *J.Elecrctron. Mat.*, 1981, **10**(5), P. 919–936.

[48] Stringfellow G.B. Calculation of ternary and quaternary III-V phase diagrams. *J.Cryst.Growth*, 1982, **58**, P. 194–202.

[49] Litvak A.M., Charykov N.A. Melt-solid phase equilibria in the system Pb-InAs-InSb. *Rus.J.Neorg.Chem.*, 1990, **35**(12), P. 3059–3062.

NANOSYSTEMS: PHYSICS, CHEMISTRY, MATHEMATICS, 2020, 11 (2), P. 214–222

Synthesis of porous graphene nanocomposite and its excellent adsorption behavior for Erythromycin antibiotic

Fateme Bahmei[1], Nader Bahramifar[1*], Habibollah Younesi[1], Valeri Tolstoy[2]

[1]Department of Environmental Science, Faculty of Natural Resources, Tarbiat Modares University, Tehran, Iran

[2]Department of Chemistry, Saint Petersburg State University,
Peterhof, 198504, Saint Petersburg, Russia

f.bahmei@modares.ac.ir, *n.bahramifar@modares.ac.ir, hunesi@modares.ac.ir, v.tolstoy@spbu.ru

PACS 81.05.ue, 81.07.Wx, 87.64.Je, 82.65.+r **DOI 10.17586/2220-8054-2020-11-2-214-222**

The purpose of this study was to evaluate the efficiency of porous magnetic graphene (PMG) for removal of Erythromycin (ER) from aqueous solutions. PMG was prepared from banana peel residue, which was considered as a discarded material. As-synthesized nanocomposite was characterized by SEM, AFM, FTIR, RAMAN and BET analysis. The optimum conditions were obtained at pH of 3, contact time of 30 min, initial antibiotic concentration of 200 mg/L, and adsorbent dose of 0.35 g/L. In equilibrium, the Langmuir isotherm model was the best fit to the experimental data for the kinetics study, the adsorption process developed the pseudo-second-order model. According to the results, nanosheet had high adsorption capacity (286 mg/g) and can be considered as an acceptable adsorbent for the removal of ER from aqueous solutions.

Keywords: Porous magnetic graphene, Erythromycin, adsorption, kinetic.

Received: 3 March 2020

1. Introduction

Drugs, such as antibiotics are non-biodegradable. They can maintain their structure in the aquatic environment for a long time Erythromycin is one of the common types of antibiotics used for many infections. This antibiotic, like Erythromycin, is included in a macrolide antibiotic, so it can be used as a substitute for penicillin for patients who are allergic to beta-lactam antibiotics. Some antibiotics can't be removed through conventional wastewater treatment and they will reach surface water, groundwater and drinking water. Due to the necessity of eliminating antibiotics in the environment, there are various methods for removing them by researchers that each has its advantages and disadvantages [1]. Physical operations such as liquid phase extraction, adsorption, and membrane removal have been used to remove antibiotics. Biological processes, chemical processes such as electrochemistry, sound waves, chemical oxidation, and advanced oxidation have also been reported to be useful for antibiotic treatment. In physical methods, pollutants are generally separated from sewage or polluted by a physical mechanism and no change in the chemical structure of the contaminant. Therefore, these methods are more suitable for condensation as a pre-purification process [2].

Methods that are mainly effective in removing hormone and antibiotic compounds and, according to some evidence, other antibiotic compounds can be advanced techniques such as adsorption by activated carbon, reverse osmosis and oxidation by chlorine. The adsorption methods are simple and practical and have no toxic by-products and are low cost. One of them is Activated carbon that has high porosity and specific surface area and very high adsorption capacity that is widely used to remove organic pollutants from polluted waters and wastewater [3]. Graphene is another adsorbent that used to completely remove antibiotics from aqueous solutions. It is a new adsorbent in wastewater treatment [4]. In theory, it is not new, as it is the Fundamental structural building block of graphite and has been believed to occur for almost 100 years. Graphene sheets are made up of carbon atoms. On a graphene plate, each carbon atom is bonded to the other three carbon atoms. These three links are on one plate and the angles between them are equal to 120°. In this case, the carbon atoms are positioned to form a network of regular hexagons. The carbon-carbon bond length in graphene is about 0.142 nm [5].

Graphene is differed from other conventional 2D materials and has different structural properties. It is a terrific pure material that has unique and remarkable features due to it's simple and orderly structure (rising from the tight arrangement of carbon atoms), which can each make a significant revolution in the various fields of science and industry. Graphene is known as a transparent and flexible material [6]. Among the adsorbents, because of their easily of separation, magnetic adsorbents are more common. Therefore, the combination of nanotechnology and magnetic separation together has helped dramatically the complete elimination of antibiotics [7].

There are various methods of producing graphene. Such as reduction of graphene oxide [8, 9], thermal decomposition of 6HSiC single crystal [10], chemical exfoliation, chemical vapor deposition (CVD), and other chemical synthesis [11]. In this investigation, porous magnetic graphene (PMG) synthesized naturally by using lignocellulosic biowastes such as banana peel, in addition to being a simple and cost-effective and straightforward, also introduces a little pollution into the environment. Then, the adsorption efficiency of as synthesized graphene were evaluated by removal of Erythromycin from synthetic wastewater. The parameters of solution pH, temperature, adsorbent dosage, and primary concentration of Erythromycin which affect the omission process were explored.

2. Experimental

2.1. Materials

The Banana peel was used as a precursor for synthesis of graphene. Ferric chloride hexahydrate ($FeCl_3.6H_2O$-Merck), Sodium acetate ($C_2H_3NaO_2$-Merck), Potassium hydroxide(KOH-Merck), Ethylene glycol ($C_2H_6O_2$-Merck), and Ethanol (C_2H_5OH-Merck) were used in the synthesis of PMG. Erythromycin ($C_{37}H_{67}NO_{13}$) used in the current study was purchased from sigma.

2.2. Synthesis of graphene

For the preparation of graphene, Banana peels were first crushed and then have been washed well to remove pollutants. Then they were dried in an oven at 70 °C. To obtain the uniform particle size, it has been milled and passed from the sieve 10 g of the dried material was carbonated in a muffle furnace at a temperature of 600 °C with a rate of 10 °C min^{-1} with the attendance of argon gas for 1 hour. 5 g of carbonized sample was mixed with 25 g KOH (1:5 ratio) and stirred for 1 hour on a magnetic stirrer. Then it will dry for 24 hours (at 110 °C). To get the graphene, the activated sample was moved to the furnace and heated at 900 °C for 2 hours at a temperature rate of 10 °C min^{-1}. Then, the sample will cool in the presence of argon gas flow. To remove extant potassium, sample was leach with distilled water until the pH of the washed water became 6 to 7. Finally, the sample was dried in an oven at 110 °C for 24 hours. The pictorial representation of the procurement of graphene is given in Fig. 1.

FIG. 1. Process of graphene preparation

2.3. Synthesis of PMG

Graphene (0.5 g) was exfoliated in 70 ml ethyleneglycol (EG) for 3 h using ultrasonic. Ferric chloride hexahydrate (1/5 g) and sodium acetate (3 g) was added to the above mixture and stirred at 500 rpm for 30 minutes. Next the mixture was transferred into a 100 mL Teflon-lined stainless-steel autoclave and kept at 200 °C for 10 h. The sample was washed with distilled water and ethanol (4 to 6 steps), and finally were vacuumed at 60 °C for 6 h until complete drying [12].

3. Characterization methods

G and PMG samples were defined by X-ray diffraction (XRD) measurements using a Philips X'PERT MPD. The Fourier Transform Infrared spectroscopy (FTIR) of the samples was obtain using a Shimadzu FT-IR spectrophotometer in the range of 400–4000 cm^{-1}. The measurement and preparation method is KBr Pellet Method. VSM measurements were carried out by using a Vibrating Sample Magnetometer (Meghnatis Daghigh Kavir Co. Kashan, Iran). Raman spectra were taken with Raman Spectrometer Teksan P50C0R. Raman spectrometers use LASER wavelengths of 533 and 633 nm during characterizing Graphene. Specific surface area values of samples were calculated by the Brunauer-Emmett-Teller (BET) method. The morphology and microstructure of the samples were observed using a scanning electron microscope (SEM) (LEO 1455 VP, Cambridge, U.K.). Atomic force microscope (AFM) image was taken by AFM- Park Scientific CP-Research model (VEECO).

4. Result and discussion

4.1. Characterization of the adsorbent

AFM is a powerful tool for measuring sample thickness. The height profile of the synthesized G sheet from banana peels is presented in AFM images of Fig. 2. From AFM cross-section analysis, it can be observed that the synthesized graphene possesses thickness in the range of 1 to 2.8 nm [13].

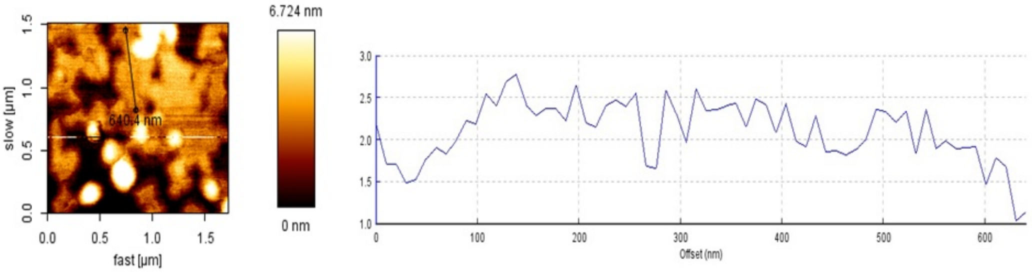

FIG. 2. The AFM images of graphene and its cross-section analysis

Raman spectroscopy is one of the most potent experiments to identify carbon derivatives such as graphene. Raman spectroscopy is an effective method to show the properties of single and multilayer graphene. Graphene structure can be determined by examining the location and intensity of the peaks. The Raman spectrum obtained from the graphene was shown in Fig. 3.

The Raman spectrum shows a fundamental vibrational band in the range between 1300–1700 cm^{-1}. The two significant groups are introduced as G and 2D bands. Besides, a third band will also appear if there is a defect in the carbon network in the graphene (D band). The 2D band of the Raman spectrum has been more sensitive to graphene sheets accumulation [14]. The 2D band position of the graphene monolayer is 2670 cm^{-1}, whereas for several graphene layers (containing 2-4 layers), the 2D band position shifts to larger numbers. The proportion of $\frac{\mathrm{I}_{2D}}{\mathrm{I}_G}$ for single-layer graphene without defects will be 1/6-2. In this study, 2D band at 2619 cm^{-1}, indicating the presence of two- and three-layer graphene sheets in the as-synthesized graphene [15, 16].

The outcomes of the FTIR spectrum of synthesized graphene and PMG nanocomposite are shown in Fig. 4. The functional groups -OH (at nearly 3436 cm^{-1}), C-H (between 2848–2923cm^{-1}) C=C (about 1535 cm^{-1}), and C-O-C groups (about 1050 cm^{-1}) perceived on the surface for both graphene and magnetic graphene. FTIR spectrum of Magnetic graphene gives new bands at 593 cm^{-1}, which can be attribute to Fe-O bond and provides the witness with successful procurement of magnetic graphene [17, 18].

SEM is predominantly used to study the morphology of the synthesized sample and to interpret the results of the synthesis on a micron or nanometer scale. Fig. 5(a) shows the synthesized graphene. The SEM image of graphene

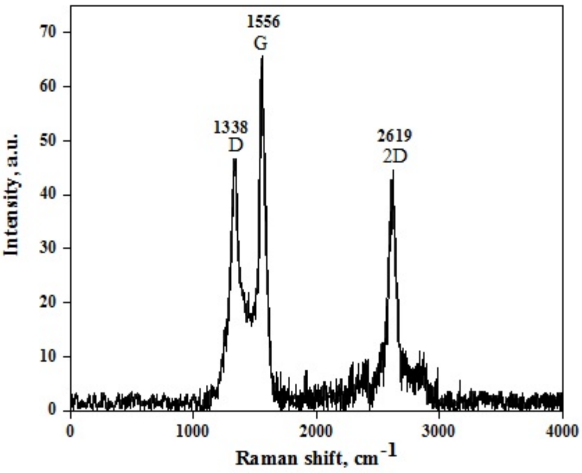

FIG. 3. Raman spectrum from the synthesized graphene

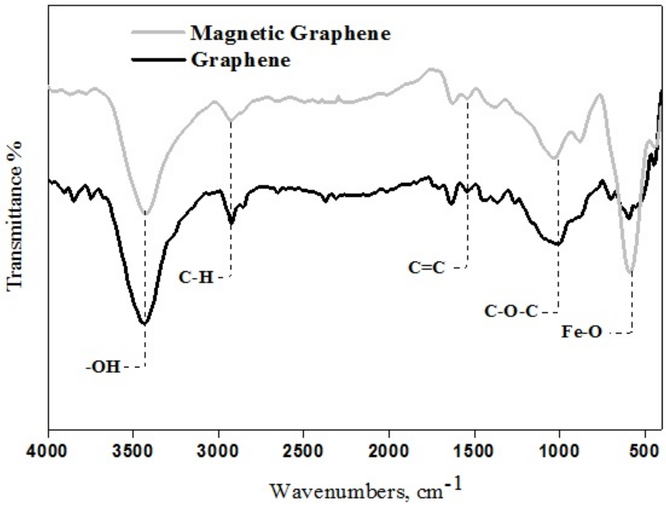

FIG. 4. The FTIR spectrum of synthesized graphene and magnetic graphene

illustrates the few layered structure. Fig. 5(b) shows spherical Fe_3O_4 nanoparticles that are well located on graphene layers and have relatively uniform sizes between 50 and 100 nm [19].

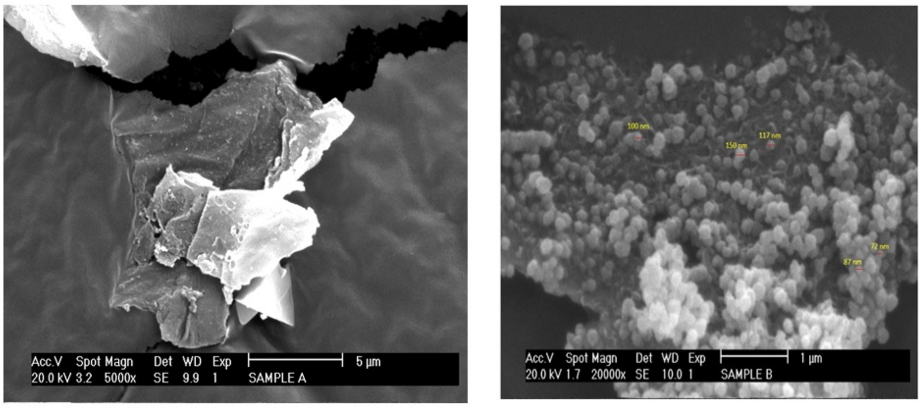

FIG. 5. SEM images of the graphene (a) and magnetic graphene(b)

One of the most critical methods for accurately measuring the total area of porous samples is the BET method, which is based on the adsorption of individual molecular species in the gas state on their surface. From Fig. 6, the significant consequence of the activation parameters in the progression of the porosity by N_2 isotherms shows a type I isotherm for N_2 adsorption on graphene according to the IUPAC classification. It indicates the characteristic of a mainly microporous material. The BJH (Barrett, Joyner, and Halenda) and MP (Microporisity Plot) diagrams showed that the graphene and PMG synthesized mostly contained micro-spherical structures (Fig.7). The percentage of micro-cavity structures in graphene was 96% and for magnetic graphene 87%. In previous studies, the theoretical specific surface area of graphene has been expressed as approximately 2630 m^2g^{-1}. The specific surface area of synthesized graphene is obtained at 2317.5 m^2g^{-1} and is very close to the theoretical value. In addition to the specific surface area of synthesized graphene, other features such as micropore volume (V_{mic}), mesopore volume (V_{mes}), total volume (V_{total}) and cavity radius (R) are given in Table 1. The results show that both graphene and porous magnetic graphene mainly comprise microporous structures [11].

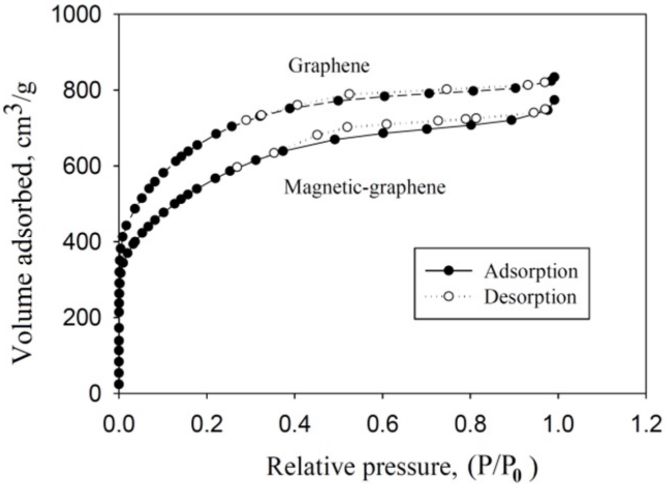

FIG. 6. Nitrogen Adsorption-desorption isotherm of graphene and PMG

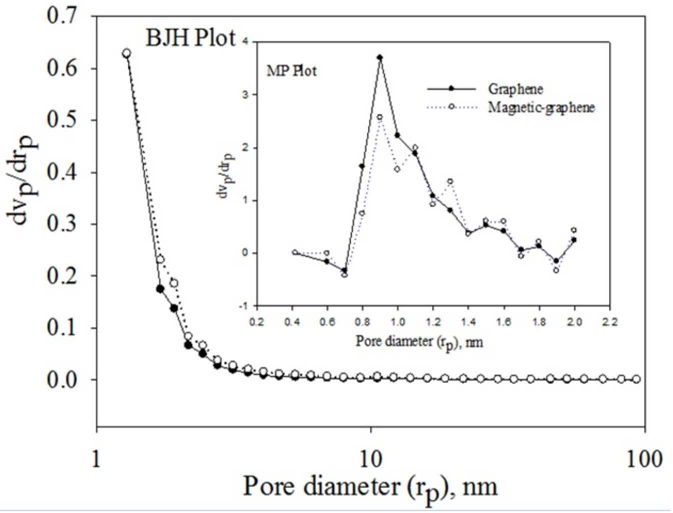

FIG. 7. Pore size distribution of graphene and PMG by using MP and BJH method

4.2. Adsorption experiments

The ER adsorption virtues of PMG were studying at initial pH values between 3 and 9 (Fig. 8). When the pH value is 3, the adsorption capacity of PMG is high. At pH higher than 3 the ER molecule has been negative charge and its tendency to adsorb onto adsorbent has been decreased. The optimal pH value was considered to be 5. In

TABLE 1. Structural properties of the graphene and PMG

Sample	S_{BET}, m^2g^{-1}	V_{mic}, cm^3g^{-1}	V_{mes}, cm^3g^{-1}	V_{total}, cm^3g^{-1}	R, nm
Graphene	2317.5	1.23	0.05	1.28	1.29
Magnetic Graphene	1905.5	1.05	0.14	1.19	1.29

this pH range, the percentage of antibiotic removal was 55%, respective [20]. The effect of reaction time is shown in Fig. 8(a). In the present study, as the contact time increased, the adsorption capacity was increased due to the increased probability of the antibiotic molecule being used to adsorb surface. The adsorption of antibiotic was very rapid in the early minutes and decreased rapidly over time, which may be due to the filling of the adsorbent pores or the problematic access of the antibiotic molecules to the active sites on the adsorbent surface. The rapid adsorption of antibiotics at the initial contact time can be assigned to the high surface area of PMG. The equilibrium contact time of the antibiotic adsorption was 30 minutes, with the elimination rate at this time being approximately 83% for Erythromycin (Fig. 8(b)). [21]. The results of adsorbent dosage on the removal percentage and equilibrium adsorption capacity of the antibiotic molecules studied are presented in Fig. 8(c). As shown in the figure, the percentage of ER removal increased from 32 to 85 as the adsorbent increased. The optimum dose of adsorbent was 35 mg/L. As shown in Fig. 2(d), with increasing concentration, the equilibrium adsorption capacity for ER increased. The maximum absorption capacity of Erythromycin was 286 mg/g at 200 mg/L ER concentration. The results show, as the initial concentration of the contaminant increased, the adsorption efficiency decreased [22].

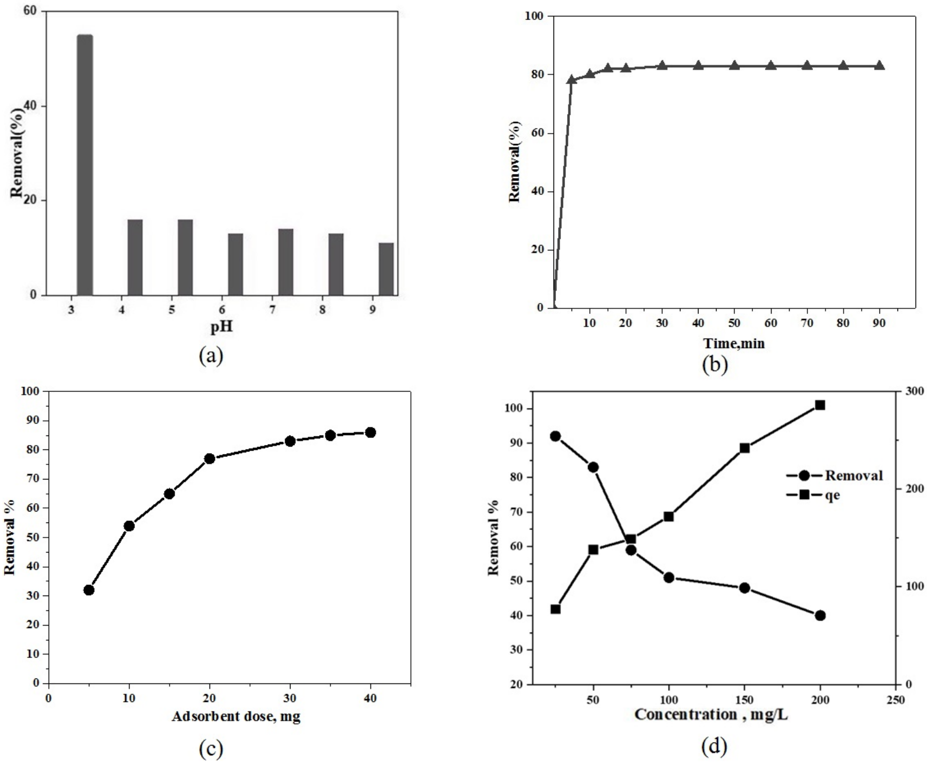

(a) (b) (c) (d)

FIG. 8. (a) Effect of pH on the removal of ER by using adsorbent dosage =20 mg, initial concentration =50 mg/L, at 25°, (b) Effect of contact time on the removal of ER by using pH=3, adsorbent dosage =30 mg, initial concentration 50 mg/L, at 25°, (c) Effect of adsorbent dosage of PMG on the removal of ER by using pH=3, initial concentration 50 mg/L, at 25°, (d) Effect of the initial concentration of ER on removal efficiency and equilibrium adsorption capacity by using pH=3, adsorbent dosage =30 mg, at 25°

4.3. Adsorption kinetics

To discern the dynamics of the adsorption reaction, data can be explained by the adsorption kinetics. In the current study, to obtain these purposes, the Pseudo-first-order (Eq.1) and pseudo-second-order (Eq.2) kinetics model were investigated. According to the achieved results, the mean correlation coefficient (R^2) in the 2-nd order kinetic model was higher than that of the 1st-order kinetic model. Consequently, the experimental data demonstrate that the adsorption of ER on PMG fitted well the 2nd-order kinetic model (Fig. 9(a,b)):

$$\log(q_e - q_t) = \log q_e - \frac{k_1}{2.303}t \tag{1}$$

$$\frac{t}{q_t} = \frac{1}{k_2 q_e^2} + \frac{t}{q_e} \tag{2}$$

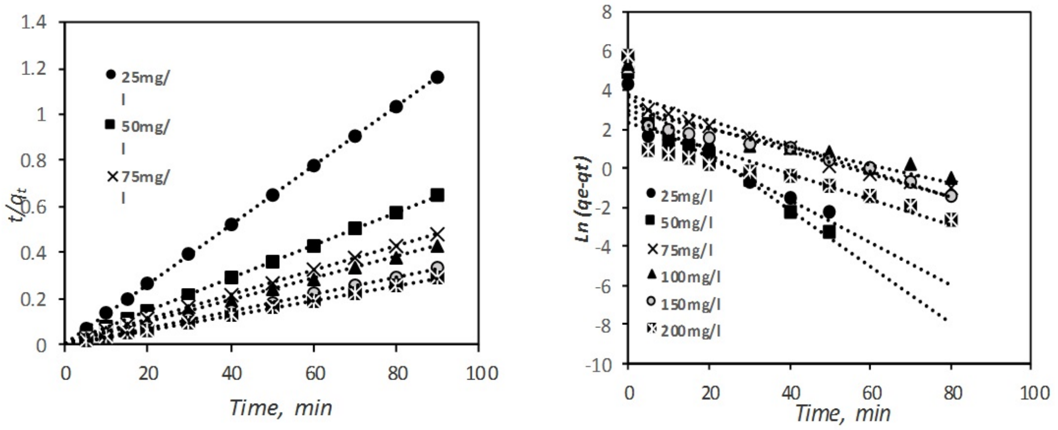

(a) (b)

FIG. 9. Adsorption kinetics of ER onto PMG: (a) pseudo-first-order, (b) pseudo-second-order model

The relevant kinetic parameters calculatedand are listed in Table 2. The results show that the calculated adsorption capacity (qe_2) of the pseudo-second order model for ER absorption is closer to the experimental adsorption capacity [23, 24].

TABLE 2. Kinetic parameters for pseudo-first-order and pseudo-second-order

ER		Pseudo-first-order			Pseudo-second-order		
Concentration(mg/L)	q_e^{exp}(mg/g)	k_1(min^{-1})	q_{e1}(mg/g)	R^2	k_2 (g $mg^{-1}min^{-1}$)	q_{e2}(mg/g)	R^2
25	77.24	0.109	15.98	0.8712	0.031	77.52	0.9999
50	138.80	0.143	36.75	0.9394	0.001	129.87	0.9999
75	187.01	0.065	42.74	0.9113	0.005	188.67	0.9999
100	210.46	0.045	18.57	0.6571	0.011	212.77	0.9999
150	272.44	0.059	26.41	0.7758	0.010	270.27	0.9999
200	310.44	0.065	10.42	0.6785	0.034	312.52	0.9999

4.4. Adsorption isotherms

To study the adsorbate distribution over solid/liquid boundaries, the adsorption isotherm is the basic tool [25] In the current study, commonadsorption isotherm models such as Langmuir, Freundlich and Sips were used to obtain detailed information about the interactions between the surface of the PMG and ER. The equations of these models are 3, 4 and 5 Equations:

$$q_e = \frac{q_m + bC_e}{1 + bC_e} \tag{3}$$

$$q_e = k_f C_e^{1/n} \tag{4}$$

$$q_e = \frac{Q_L K_L C_e^{n_s}}{1 + k_s C_e^{n_s}} \tag{5}$$

where, C_e and q_e represent the equilibrium concentration in the soluble (mg/l) and solid (mg/g), q_m showed maximum adsorption capacity (mg/g) and b, n and k parameters are isotherms constants Fig. 10 demonstrates the plots of adsorption isotherm models and isotherm parameters are shown in Table 3 [26].

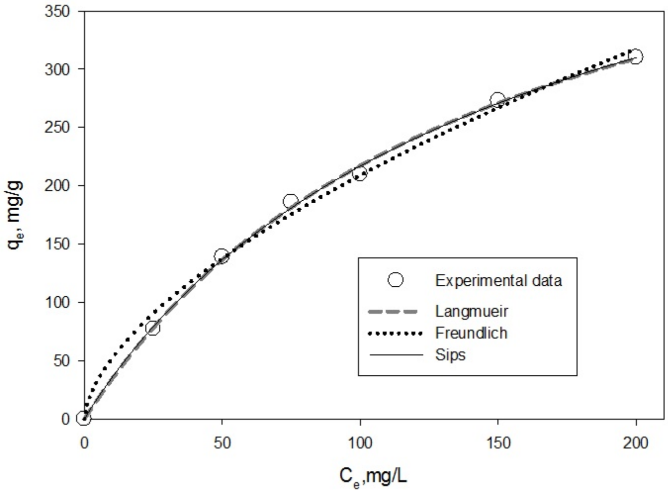

FIG. 10. Adsorption isotherms of ER onto PMG

By comparing the correlation coefficients among isotherm models, it was found that the Langmuir isotherm could describe the experimental data better than the other models. This result showed that the process is homogeneous and monolayer adsorption [27].

TABLE 3. Langmuir, Freundlich and SIPS adsorption isotherm fitting parameters of ER on PMG

Adsorption isotherm	Parameter	Value	R2
Langmuir	q_m	534	0.9973
	$b_{(l.mg)}$	0.0005	
Freundlich	K_F	13.03	0.9798
	n	1.65	
Sips	q_m	561	0.7291
	K_s	0.0062	
	n	1.03	

4.5. Conclusions

The primary objective of this study was to synthesize high-quality graphene from the banana peel with low chemical consumption For better separation from aqueous solution, porous magnetic graphene was synthesized. Then, it was confirmed by AFM, Raman, FTIR, SEM, and BET analyses Based on the morphological results, the porous surface was confirmedand it is demonstrated that suggested adsorbent has the ability to remove antibiotic. The optimum condition was provided at pH of 3, contact time of 30 min, and the adsorbent dose of 0.35 g/L. Also, the results exposed that the Langmuir isotherm and pseudosecond-order kinetics model better describes the adsorption of Erythromycin. According to the results, PMG nanoparticle adsorbent can be considered as an acceptable absorbent for the removal of antibiotics from aqueous solutions.

References

[1] Li MF, Liu YG, Zeng GM, Liu N, Liu SB. Graphene and graphene-based nanocomposites used for antibiotics removal in water treatment: a review. *Chemosphere*, 2019.

[2] Koyuncu I., Arikan O.A., Wiesner M.R., Rice C. Removal of hormones and antibiotics by nanofiltration membranes. *Journal of membrane science*, 2008, **309**(1-2), P. 94–101.

[3] Moussavi G., Allahabad A., Yaghmaeian K., Eskandari M. Preparation, characterization and adsorption potential of the NH_4Cl-induced activated carbon for the removal of amoxicillin antibiotic from water. *Chemical engineering journal*, 2013, **217**, P. 119–128.

[4] Yi J.W., Park J., Kim K.S., Kim B.H. pH-Responsive self-duplex of Py A-substituted oligodeoxyadenylate in graphene oxide solution as a molecular switch. *Organic and biomolecular chemistry*, 2011, **9**(21), P. 7434–7438.

[5] Dhinakaran V., Lavanya M., Vigneswari K., Ravichandran M., Vijayakumar M.D. Review on exploration of graphene in diverse applications and its future horizon. *Materials Today: Proceedings*, 2020.

[6] Yousefi N., Lu X., Elimelech M., Tufenkji N. Environmental performance of graphene-based 3D macrostructures. *Nature nanotechnology*, 2019, **14**(2), P. 107–119.

[7] Zhu J., Wei S., Gu H., Rapole S.B., Wang Q., Luo Z., Haldolaarachchige N., Young D.P., Guo Z. One-pot synthesis of magnetic graphene nanocomposites decorated with core@ double-shell nanoparticles for fast chromium removal. *Environmental science and technology*, 2012, **46**(2), P. 977–985.

[8] Dideikin A.T., Vul A.Y. Graphene oxide and derivatives: the place in graphene family. *Frontiers in Physics*, 2019, **6**, P. 149.

[9] Shanmugam S., Nanjan S. In-situ conversion of rgo from graphene oxide based on solar mediated enhanced characterization properties. *Nanosystems: Physics, Chemistry, Mathematics*, 2019, **10**(5), P. 579–584.

[10] Lebedev S.P., Davydov V.Y., Usachov D.Y., Smirnov A.N., Levitskii V.S., Eliseyev I.A., Guschina E.V., Dunaevsckiy M.S., Vilkov O.Y., Rybkin A.G., Lebedev A.A. Graphene on silicon carbide as a basis for gasand biosensor applications. *Nanosystems: Physics, Chemistry, Mathematics*, 2018, **9**(1), P. 95–97.

[11] Ekhlasi L., Younesi H., Rashidi A., Bahramifar N. Populus wood biomass-derived graphene for high CO_2 capture at atmospheric pressure and estimated cost of production. *Process Safety and Environmental Protection*, 2018, **113**, P. 97–108.

[12] Ai L., Zhang C., Chen Z. Removal of methylene blue from aqueous solution by a solvothermal-synthesized graphene/magnetite composite. *Journal of hazardous materials*, 2011, **15**, **192**(3), P. 1515–1524.

[13] Lin L.Y., Kim D.E., Kim W.K., Jun S.C. Friction and wear characteristics of multi-layer graphene films investigated by atomic force microscopy. *Surface and Coatings Technology*, 2011, **205**(20), P. 4864–4869.

[14] Villar-Rodil S., Paredes J.I., Martínez-Alonso A., Tascón J.M. Preparation of graphene dispersions and graphene-polymer composites in organic media. *Journal of Materials Chemistry*, 2009, **19**(22), P. 3591–3593.

[15] Calizo I., Balandin A.A., Bao W., Miao F., Lau C.N. Temperature dependence of the Raman spectra of graphene and graphene multilayers. *Nano letters*, 2007, **7**(9), P. 2645–2649.

[16] Ferrari A.C. Raman spectroscopy of graphene and graphite: disorder, electron–phonon coupling, doping and nonadiabatic effects. *Solid state communications*, 2007, **143**(1-2), P. 47–57.

[17] Xue B., Zhu J., Liu N., Li Y. Facile functionalization of graphene oxide with ethylenediamine as a solid base catalyst for Knoevenagel condensation reaction. *Catalysis Communications*, 2015, **64**, P. 105–109.

[18] Lü M., Li J., Yang X., Zhang C., Yang J., Hu H., Wang X. Applications of graphene-based materials in environmental protection and detection. *Chinese Science Bulletin*, 2013, **58**(22), P. 2698-710.

[19] Guo X., Du B., Wei Q., Yang J., Hu L., Yan L., Xu W. Synthesis of amino functionalized magnetic graphenes composite material and its application to remove Cr (VI), Pb (II), Hg (II), Cd (II) and Ni (II) from contaminated water. *Journal of hazardous materials*, 2014, **278**, P. 211-20.

[20] Ou H., Chen Q., Pan J., Zhang Y., Huang Y., Qi X. Selective removal of erythromycin by magnetic imprinted polymers synthesized from chitosan-stabilized Pickering emulsion. *Journal of hazardous materials*, 2015, **289**, P. 28–37.

[21] Moussavi G., Alahabadi A., Yaghmaeian K., Eskandari M. Preparation, characterization and adsorption potential of the NH_4Cl-induced activated carbon for the removal of amoxicillin antibiotic from water. *Chemical engineering journal*, 2013, **217**, P. 119-28.

[22] Budyanto S., Soedjono S., Irawaty W., Indraswati N. Studies of Adsorption Equilibria and Kinetics of amoxicillin from simulated wastewater using activated carbon and natural bentonite. *Journal of environmental protection science*, 2008, **2**, P. 72–80.

[23] Shafiee M., Akbari A., Ghiassimehr B. Removal of Pb (II) From Wastewater Using Henna; Optimization of Operational Conditions. *Iranian Journal of Chemical Engineering*, 2018, **15**(4), P. 17–26.

[24] Peer F.E., Bahramifar N., Younesi H. Removal of Cd (II), Pb (II) and Cu (II) ions from aqueous solution by polyamidoamine dendrimer grafted magnetic graphene oxide nanosheets. *Journal of the Taiwan Institute of Chemical Engineers*, 2018, **87**, P. 225-40.

[25] Beltrame K.K., Cazetta A.L., de Souza P.S., Spessato L., Silva T.L., Almeida V.C. Adsorption of caffeine on mesoporous activated carbon fibers prepared from pineapple plant leaves. *Ecotoxicology and environmental safety*. 2018. **147**, P. 64–71.

[26] Rostamian R., Behnejad H. A comparative adsorption study of sulfamethoxazole onto graphene and graphene oxide nanosheets through equilibrium, kinetic and thermodynamic modeling. *Process Safety and Environmental Protection*, 2016, **102**, P. 20-9.

[27] Budyanto S., Soedjono S., Irawaty W., Indraswati N. Studies of Adsorption Equilibria and Kinetics of amoxicillin from simulated wastewater using activated carbon and natural bentonite. *Journal of environmental protection science*, 2008, **2**, P. 72–80.

NANOSYSTEMS: PHYSICS, CHEMISTRY, MATHEMATICS, 2020, 11 (2), P. 223–229

Effect of bath temperature on morphological and optical properties of ZnS films prepared by electrochemical deposition technique

Jitendra Borse, Arun Garde
Department of Physics, Late Pushpadevi Patil Arts and Science College, Risod, India
Department of Physics, S P H Arts, Science and Commerce College Nampur, Nashik, India
jaborse@gmail.com, arungarde@yahoo.co.in

DOI 10.17586/2220-8054-2020-11-2-223-229

Zinc sulfide thin films were synthesized by means of cyclic voltammetry technique onto stainless steel substrate. The electrolyte bath of aqueous solution containing 0.1 N Zinc sulfate ($ZnSO_4{\cdot}7H_2O$) and 0.1 N sodium thiosulfate ($Na_2S_2O_3.5H_2O$) with 0.1 N Triethanolamine was used as complexing agent. Cyclic voltammetry was employed to measure its ranges of deposition voltages and thickness of ZnS thin films can be controlled by number of voltage cycles applied during deposition. Also we obtained hysteresis curve that imply its potential application. The bath temperatures were varies from 30°C to 60°C. The Influence of bath temperatures on optical properties and morphology has been investigated in details. The electrochemical deposited ZnS thin films were characterized by UV-visible spectroscopy and the field emission scanning electron microscopy (FESEM). The UV-visible spectroscopy analysis showed that energy gap varied between 3.99 to 3.79 eV depending on bath temperatures. The FESEM analysis showed that ZnS thin film deposited at various bath temperatures are polycrystalline nature, homogenous, uniform with randomly oriented nanoflakes and nanorods. The good quality of zinc sulphide thin film could be prepared in the presence of triethanolamine.

Keywords: electrodeposition, bath temperature, ZnS-thin film, morphological and optical properties.

Received: 12 March 2020

Revised: 29 March 2020

1. Introduction

Zinc sulfide (ZnS) is one of the direct II–VI semiconductor compounds with large band gap energy of ~ 3.65 eV at room temperature exhibits a wide optical transparency from the ultraviolet to the infrared region [1]. The material crystallizes in both cubic and hexagonal forms and it is used a material of reference to test several theoretical models in condensed material physics [2]. Most of the times it shows mixed phase crystal structure. While cubic structure of ZnS has been reported to have a wide direct band gap of ~ 3.6 eV at optimum temperature, hexagonal structure of ZnS has been reported to have a bandgap of ~ 3.91 eV [3]. The material has been huge potential application in both thick and thin film form in various photovoltaic and optoelectronic devices [4] This optical transparency combined with chemical and thermal stability makes zinc sulfide used as key material for solar control coating, window layer solar cell, electroluminescence devices, optoelectronic devices, sensors and others [5]. Zinc sulfide is a promising material to be used in solar cell as passivation layer for better photovoltaic properties [6]. Due to its high refractive index of material (~ 2.3), it can be used as an antireflective coating [7]. Zinc sulfide is also an important phosphor host lattice material used in preparation of electroluminescent devices (ELD). This is because of its large band gap that is enough to emit visible light without absorption and the efficient transport of high energy electrons [8]. Recently, investigation has shown that, layered type semiconducting cadmium chalcogenides group (CdSe, CdS,ZnS, CdTe) which absorb ultraviolet and near infrared light. These materials are particularly promising materials for photo electrochemical solar energy conversion [9]. Various types of physical, chemical and growth techniques have been used to deposit ZnS thin films on to different substrates. While physical deposition methods such as physical vapor deposition, sputtering, molecular beam epitaxy, pulsed laser deposition atomic layer epitaxy, cathodic arc deposition and metal organic chemical vapor deposition demand the use of either vacuum conditions or complex equipment. Growth methods such as layer by layer, layer plus island etc are used for thin film deposition. Chemical techniques are simpler, inexpensive and cost effective. Thus they have become more popular in recent times. ZnS thin film has been grown by using electrodepositon and various chemical techniques [10] such as Sol-gel [1], Spin coating [5], Spray Pyrolysis [11], chemical vapor deposition and chemical bath deposition [12] etc. The technique of electrodepositon is simple, inexpensive and can be adaptable to large area processing with low fabrication cost. The ZnS thin films have been deposited by two electrode or three electrode cyclic voltammetry electrochemical deposition techniques [13]. Using chemical bath deposition techniques, many researchers have reported different characterization results for thin films with different temperatures [14]. The deposition of ZnS thin film on the substrate as cathode is given by following reaction:

$$\mathrm{Zn}^{+2} + 2e^- + S \rightarrow \mathrm{ZnS}\ \text{(Thin Layer)}. \tag{1}$$

Cyclic voltammetry is a very important electrochemical and linear sweep technique. It is used potentiodynamic electrochemical measurement and to study the redox behavior of compounds and to determine mechanisms and rates of oxidation/ reduction reaction. Also it is generally used to study the electrochemical properties of an analyte in solution or of a molecule that is adsorbed onto the electrode. In a cyclic voltammetry experiment, the working electrode's potential is ramped in the opposite direction to return to the initial potential. These cycles of ramps in potential may be repeated as many times as needed. The current at the working electrode is plotted versus the applied voltage (that is, the working electrode's potential to give the cyclic voltammogram trace. In the present study we report the synthesis of ZnS, three electrodes potentiostatic electrodeposition technique with different electrolyte bath temperature was employed to prepare ZnS thin films and their morphological and optical properties [15, 16].

2. Experimental work

The deposition of ZnS on stainless steel substrate by three electrode cyclic voltammetry technique.The electrolyte was prepared by mixing solution of AR grade Zinc Sulfate ($ZnSO_4$), Sodium Thiosulfate ($Na_2S_2O_3$) of 0.1 N in the volume ratio of 1:1 respectively, with 2 % of total volume of electrolyte bath. Here 0.1 N Triethanolamine was taken as a complexing agent [17].

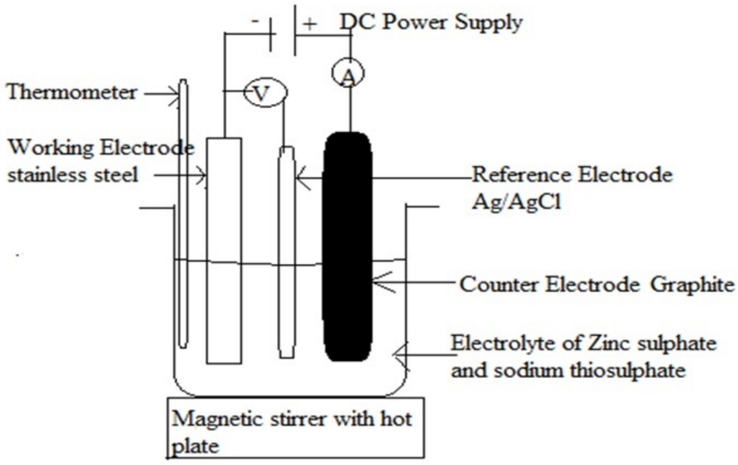

FIG. 1. Schematic of Electrodeposition method used in the present study of deposition of ZnS thin films with various bath temperatures

Figure 1 show a standard cyclic voltammetry experiment consists of a cell with three electrodes such as reference electrode, working electrode and counter electrode. This combination is sometimes referred to as a three-electrode setup. Electrolyte was added to the sample solution to ensure sufficient conductivity. The solvent, electrolyte, and material composition of the working electrode will determine the potential range that can be accessed during the experiment. It was employed to measure its ranges of deposition voltages [13]. Distilled water was used for preparation of aqueous solution of above precursor chemicals. The pH of electrolyte solution was maintained fixed at 3.5 by dilute hydrochloric acid. By using magnetic stirrer with hot plate while other parameters being kept constant, the electrolyte bath temperatures were adjusted from 40 to 65 °C. Before deposition the substrate was thoroughly cleaned with double distilled water and acetone. The distance between the working electrode and counter electrode was kept constant as 1 cm during deposition of materials. The deposition parameters were adjusted such as deposition time 20 min and bath temperatures adjusted 30 – 60 °C. It was observed that a formation of uniform and well adherent black ZnS films were obtained on the substrate. The film was dried under IR lamp for 10 min. We obtain that thickness of ZnS films was controlled by number of voltage cycles applied during deposition. The thicknesses of films with different bath temperatures were measured [18]. Also we obtained hysteresis curve that imply its potential application. We conclude that, the variation of bath temperatures do affect the structure, surface morphology and optical properties of thin films.

3. Results and Discussion

3.1. Cyclic Voltammetry

In a cyclic voltammetry experiment, for reaction mechanisms that involve the transfer of electrons, the working electrode's potential was ramped in the opposite direction to return to the initial potential. These cycles of ramps in potential may be repeated as many times as needed. Accordingly this process was repeated. The current at the working electrode was plotted versus the applied voltage (that is, the working electrode's potential) to give the cyclic voltammogram trace.

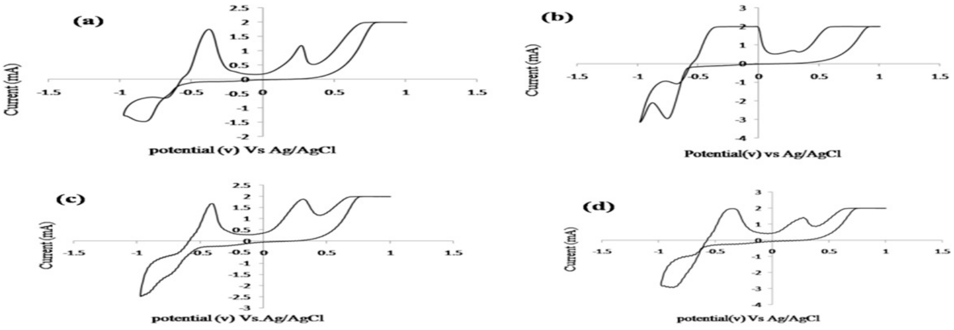

FIG. 2. Cyclic voltammogram of measured current versus applied potential of mixed electrolyte bath of 0.1 N $ZnSO_4$ and 0.1 N of $Na_2S_2O_3$ with different scan speed at a) 25 mV/s, b) 50 mV/s, c) 75 mV/s, d) 100 mV/s

Figure 2 shows variation of the cyclic voltammetry of mixed electrolyte bath with different scan speeds at different electrode potentials. The cyclic voltammetry of these mixtures were performed at different scan speeds to find suitable deposition potential for ZnS film [19].The first and second anodic peak $+0.25$, $+0.80$ V was found at scan speed 25 mV/s indicating dissolution of sulphide and zinc ions in to the solution respectively. At that time, cathodic potential reached -0.80 V against the Ag/AgCl (Reference Electrode) and deposition of ZnS occurred [20]. Anodic potential at range $+0.55$ to $+0.99$ V was found at scan speed 50 mV/s due to dissolution of deposited materials in to the solution and materials deposited at -0.743 V against Ag/AgCl (Reference Electrode). Anodic potential peaks were found at $+0.29$, $+0.75$ V at scan speed 75 mV/s due to the dissolution of sulfide and zinc ions in to the solution respectively. That times the cathodic potential reached at -0.94 V the material deposition take place. However, Fig. 2(d) The anodic potential peaks were found at $+0.23$, $+0.63$ V at scan speed 100 mV/s indicating the dissolution of sulfide and zinc in the solution respectively, When the deposition take place at cathodic potential -0.85 V versus Ag/AgCl (Reference Electrode), the film deposited at cathodic potential range from -0.74 to -0.94 V against Ag/AgCl shows optimized value of deposing potential [20]. Fig. 3 shows linear sweep voltammetry of mixed electrolyte bath. The potential increases with small increase in current. After 0.74 volts, potential continuously increases with saturated peak current.

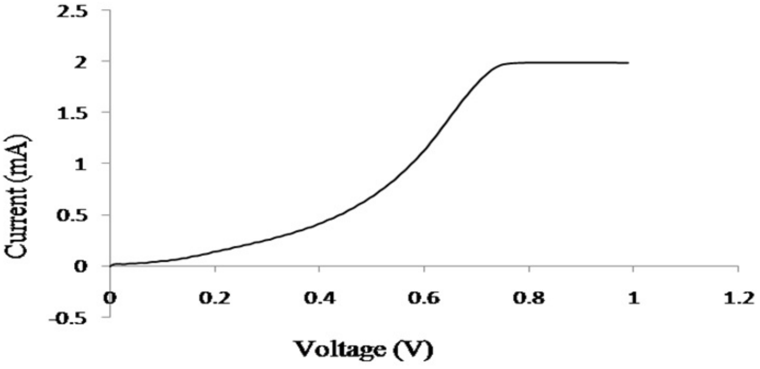

FIG. 3. Linear Sweep Voltammetry measured current versus applied potential of mixed electrolyte bath of 0.1 N of $ZnSO_4$ and $Na_2S_2O_3$

Figure 4 shows the chronoamperometry of mixed electrolyte bath. The variation of current with time of solutions indicated that the current increases linearly as a function of time. After 20 seconds, the current was saturated with continuously increase in time.

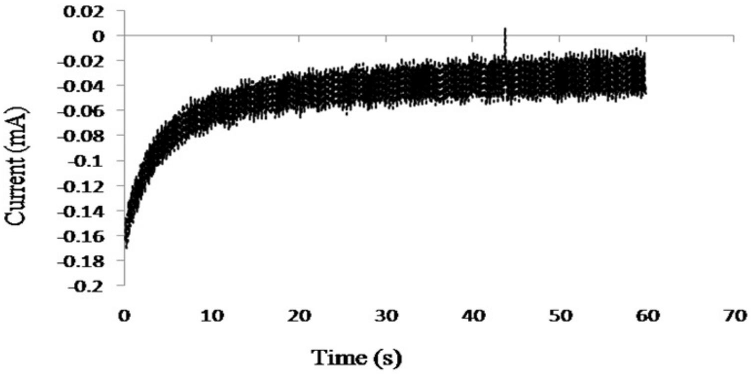

FIG. 4. Chronoamperometry of mixed electrolyte bath of 0.1 N of $ZnSO_4$ and $Na_2S_2O_3$

3.2. Film thickness estimation

The thickness variation of ZnS deposited by using electrodepositon was measured by using mass difference method [21, 22].

$$t = \frac{\Delta m}{\Lambda \rho}, \tag{2}$$

where Δm is mass difference of before deposition and after deposition, t is thickness of film, Λ is area of deposition, ρ is density of deposited material.

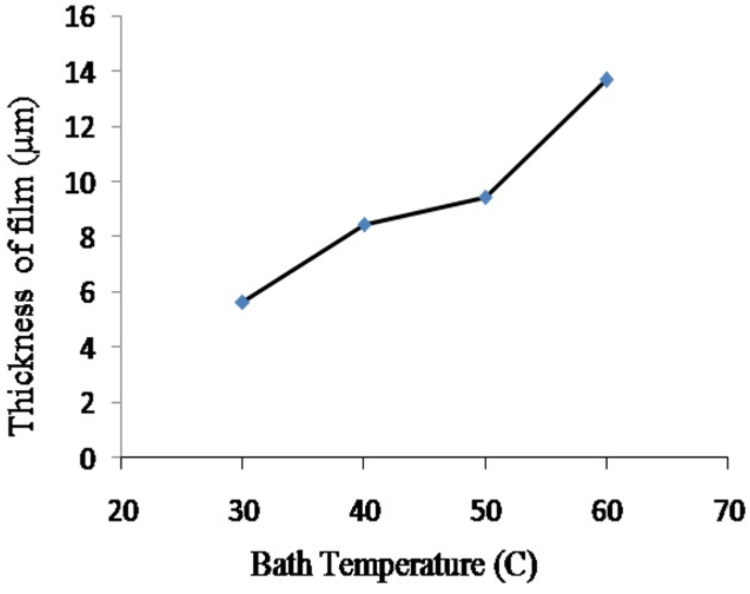

FIG. 5. Thickness Variation of ZnS thin films deposited at different bath temperatures

The variation of film thickness as a function of electrolyte bath temperature is shown in Fig. 5. The ZnS film thickness linearly increases with an increase in bath temperature. The thickness of films increased from 5.65 to 13.69 μm when bath temperature rose from 30 to 60 °C. However, in this technique, we have controlled the thickness of ZnS film by adjusting the bath temperature.

3.3. UV- visible spectroscopy

The optical absorption measurement was carried out by using UV visible spectrophotometer (BSR-UV-1900) in the range of 190–400 nm.

Figure 6 shows the absorption band edge was found at 311, 317, 322 and 327 nm at bath temperatures 30, 40, 50, and 60 °C respectively. The band gaps of ZnS films were found to be 3.99, 3.91, 3.85, 3.79 eV at 30, 40, 50, and 60 °C

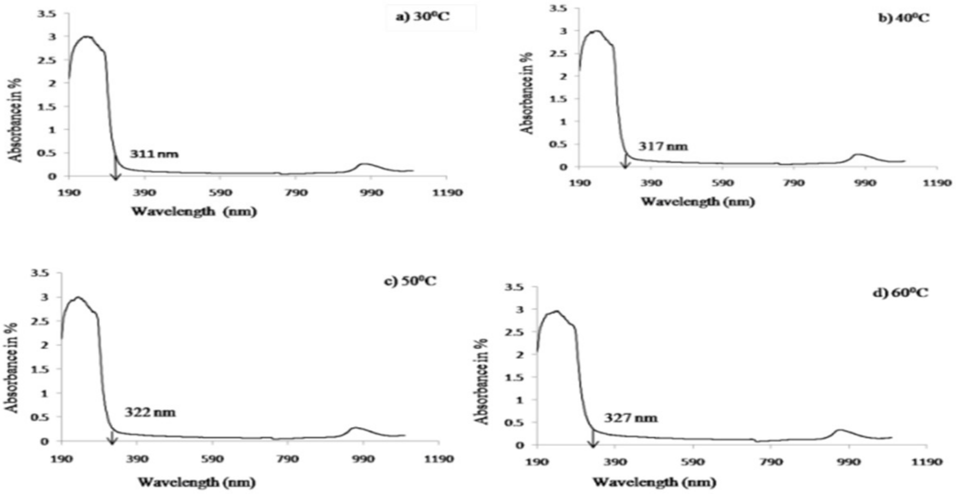

FIG. 6. UV-Visible absorption spectra of ZnS thin film at Bath temperatures a) 30 °C, b) 40 °C, c) 50 °C and d) 60 °C

respectively. The UV visible absorption spectra show the band gap energy varies inversely with crystallites sizes. As a result, it was found that band gap energy of ZnS decreased with increased bath temperature [14].

3.4. Energy dispersive analysis by X-ray spectroscopy

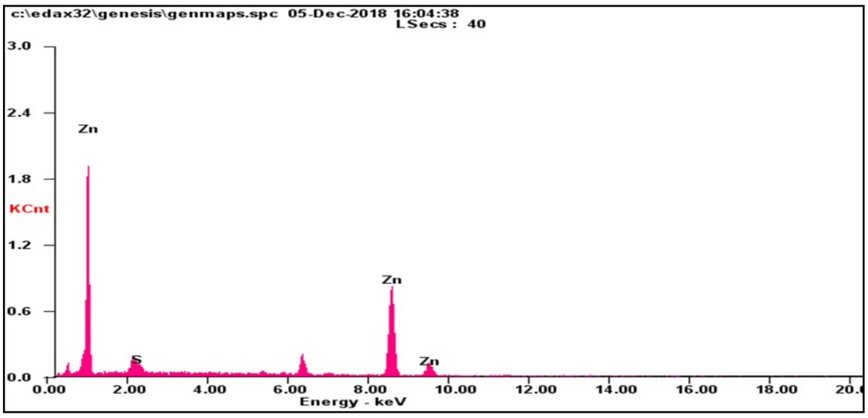

FIG. 7. Energy Dispersive analysis by X-ray Spectroscopy of ZnS thin film

EDS spectra of deposited ZnS thin film shows in Fig. 7. It confirm the successful formation of ZnS. That grown thin film composed of only Zn and S elemental composition. No impurity peaks are observed in this spectrum.

3.5. Field emission scanning electron microscopy

The FESEM was carried out to study the effect of different bath temperature on the surface morphology of ZnS thin films.

Figure 8 FESEM photographs shows ZnS films at bath temperatures 30, 40, 50 and 60 °C. The surface morphology of ZnS thin films changes significantly with increasing bath temperature [20]. The ZnS films' morphologies also show the size of ZnS nanorods was increased with an increase in bath temperature [23]. The crystallinity of ZnS thin film is higher at bath temperature 60 °C indicated that the film was dense and pinhole free. The crystallinity of ZnS thin films layer is increases with increase in bath temperature [24]. The variation of average crystallite size of the film sample with bath temperatures are listed in Table 1.

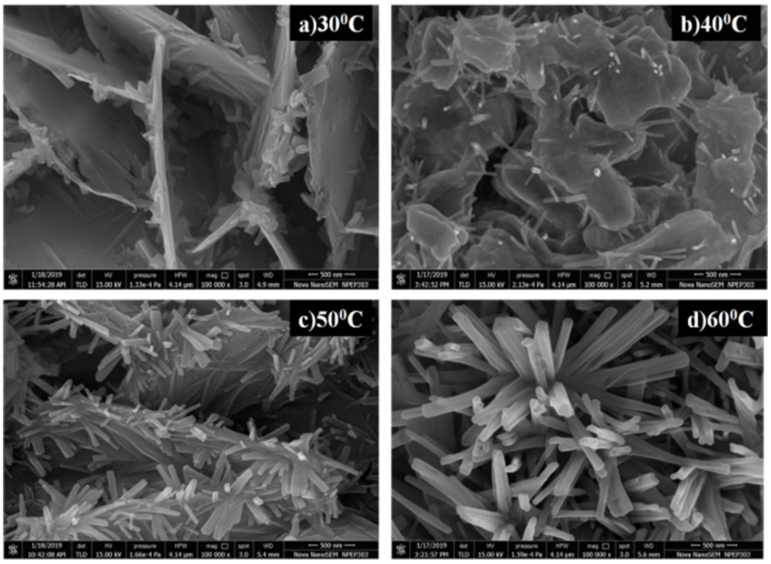

FIG. 8. FESEM micrograph of the ZnS thin films at bath temperatures a) 30 °C, b) 40 °C, c) 50 °C, d) 60 °C

TABLE 1. Estimated values of Average crystallite size and band gap of ZnS at different bath temperatures

Bath temperature (°C)	Average Crystallite size (nm)	Energy Band gap (eV)
30 °C	40.15 nm	3.99
40 °C	60.10 nm	3.91
50 °C	80.08 nm	3.85
60 °C	160.06 nm	3.79

4. Conclusion

The synthesis of ZnS films has been carried out by cyclic voltammetry technique. ZnS has been successfully deposited on stainless steel substrates. The influence of bath temperature on optical properties has been investigated systematically. The ZnS film thickness linearly increases with increase in bath temperature. The ZnS films shows absorption band edges 311 to 327 nm with band gap varies in the range between 3.99 to 3.79 eV. The UV visible absorption spectra show the band gap energy varies inversely with crystallites sizes. The surface morphology of the films shows that films are smooth and uniform with randomly oriented nanorods. The crystallinity of ZnS films layer is increases with increase in bath temperature.

Acknowledgment

The author thanks authorities of Physics Research Centre M.S.G college Malegaon camp, Nashik for providing all the required Laboratory and infrastructural facilities for doing this work. Also thanks to CIF laboratory, Pune and SAIF IIT Chennai For characterization facilities.

References

[1] Ayan Mukherjeea, Partha Mitraa, Characterization of Sn Doped ZnS Thin Films synthesized by CBD. *Materials Research*, 2017, **20**(2), P. 430–435.

[2] Rawlins T.G.R., Woodward R.J. Sputtered Zinc Sulphide Films on Silicon. *Journal of Materials Science*, 1972, **7**(3), P. 257–264.

[3] Nasr T.B., Kamoun N., Kanzari M., Bennaceur R. Effect of pH on the properties of ZnS thin films grown by chemical bath deposition. *Thin Solid Films*, 2006, **500**(1-2), P. 4–8.

[4] Shinde M.S., Ahirrao P.B., Patil I.J., Patil R.S. Studies on nanocrystalline ZnS thin films prepared by modified chemical bath deposition method. *Indian Journal of Pure & Applied Physics*, 2011, **49**(11), P. 765–768.

[5] Thi T.M., Hien N.T., Thu D.X., Trung V.Q. Thin films containing Mn-doped ZnS nanocrystals synthesised by chemical method and study of some of their optical properties. *Journal of Experimental Nanoscience*, 2012, **8**(5), P. 694–702.

[6] Hachiya S., Shen Q., Toyada T. Effect of ZnS coatings on the enhancement of the photovoltaic properties of PbS quantum dot-sensitized solar cells. *Journal of Applied Physics*, 2012, **111**(10), P. 104315.

[7] Tec-Yam S., Rojas J., Rejón V., Oliva A.I. High quality antireflective ZnS thin films prepared by chemical bath deposition. *Materials Chemistry and Physics*, 2012, **136**(2-3), P. 386–393.

[8] Pawar M.J., Nimkar S.D., Nandurkar P.P., Tale A.S., Deshmukh S.B., Chaure S.S. Effect of Sn_2+ Doping on Optical Properties of Thiourea Capped ZnS Nanoparticles. *Chalcogenide Letters*, 2010, **7**(2), P. 139–143.

[9] H.M.M.N.Hennayaka, Hoseong, Lee. Structural and optical properties of ZnS thin film grown by pulsed electrodeposition. *Thin solid films*, 2013, **548**, P. 86–90.

[10] Baranski A.S., Bennet M.S., Fawcett W.R. The physical properties of CdS thin films electrodeposited from aqueous diethylene glycol solutions. *Journal of Applied Physics*, 1983, **54**(11), P. 6390–6394.

[11] Djelloul A., Adnane M., Larbah Y., Sahraoui T., Zegadi C., Maha A., Rahal B. Properties study of ZnS Thin films Prepared by Spray Pyrolysis Method. *Journal of Nano & Electronics Physics*, 2015, **7**(4), P. 04045.

[12] Agawane G.L., Shin S.W., Moholkar A.V., Gurav K.V., Yun J.H., Lee J.Y., et al. Non-toxic complexing agent Tri-sodium citrate's effect on chemical bath deposited ZnS thin films and its growth mechanism. *Journal of Alloys and Compounds*, 2012, **535**, P. 53–61.

[13] Mohammad Lamido Modugu, Olajide Ibukun-oluOlusola, Obi Kingsley Echendu, Burak adem, ImyhamyMudiyDharmadasa. *Journal of electronic materials*, 2016, **45**(6), P. 2710–2717.

[14] Sachin Rondiya, Avinash Rokade, Sandesh Jadkar, Effect of Bath temperature on optical and Morphology properties of CdS thin films grown by chemical bath deposition Energy. *Procedia*, 2017, **110**, P. 201–209.

[15] Noemie Elgrishi, Kelley. J. Rountree, Brian D. McCarthy, Eric S. Rountree, Thomas T. Eisenhart,and Jillian L. Dempsey. A Practical Beginner's Guide to Cyclic Voltammetry, *J.Chem.Educ*, 2018, **95**, P. 197–206.

[16] Yongkuk Kim, Jaegoo Jung, Seunghun Kim and Won-Seok Chae, Cyclic Voltammetric and Chronoamperometric Deposition of CdS, *Materials Transactions*, 2013, **54**(8), P. 1467–1472.

[17] HoS.M. Role of complexing agent in chemical bath deposition of thin films. *Australian Journal of Basic & Applied Sci.*, 2015, **9**(31), P. 625–629.

[18] Haddad H., Chelouche A., Talantikite D., Merzouk H., Djouadi D. Effects of deposition time in chemically deposited ZnS films in acidic solution. *Thin Films*, 2015, **589**(8), P. 451–456.

[19] Sarvanan Naglingam,Geok Bee The, Rong-fuhLouh and Kai Tung Chee Cyclic. Voltammetry studies of cadmium zinc sulphide aqueous solution. *International Journal of Physical Sciences*, 2011, **6**(31), P. 7166–7170.

[20] Dergacheva M.B., Urazov K.A., Khussurova G.M. and Leontyeva K.A. New method of Electrodeposition of Nanostructure of ZnS films. *Coatings*, 2016, **6**, P. 14.

[21] Mondal S., Mitra P. Preparation of cadmium-doped ZnO thin films by SILAR and their characterization. *Bulletin of Materials Science*, 2012, **35**(5). P. 751–757.

[22] Kale S.S., Mane R.S., Pathan H.M., Shaikh A.V., Joo O.S., Han S.H. Preparation and characterization of ZnTe thin films by SILAR method. *Applied Surface Science*, 2007, **253**(9), P. 4335–4337.

[23] Salim H.I, Olusola O.I, Ojo A.A., Urasov K.A, Dergacheva M.B. and dharmadasa. *Journal of Material Science: Materials in Electronics*, 2016, **27**, **7**, P. 6786–6799.

[24] Tarkeshwar Sinha, Devjyoti Lilhare, Ayush Khare. Effects of Various Parameters on Structural and Optical Properties of CBD-Grown ZnS Thin Films. *A Review Journal of Electronic Materials*, 2018, **47**(2), P. 1730–1751.

NANOSYSTEMS: PHYSICS, CHEMISTRY, MATHEMATICS, 2020, 11 (2), P. 230–236

Electrochemical investigation of hydrothermally induced $MnCo_2S_4$ nanoparticles as an electrode material for high performance supercapacitors

M. Dakshana[1], S. Meyvel[1], M. Malarvizhi[1], P. Sathya[2]

[1]Chikkaiah Naicker College, Erode-63, India

[2]Salem Sowdeswari College, Salem, India

meyvelphd@gmail.com

DOI 10.17586/2220-8054-2020-11-2-230-236

Ternary spinel $MnCo_2S_4$ spherical nanoparticles are prepared through a simple one step hydrothermal approach with precursors followed by an ion exchange reaction. The obtained spherical nanoparticles offers a high specific surface area with mesoporous structure, this aids in providing outstanding electrochemical performance with a specific capacitance of 707.77 F/g at 2 A/g and a good cyclic stability (initial capacitance of 95.15% after 10000 cycles). It offers a high energy density of 78.17 W h Kg^{-1} to satisfy the commercial needs. By the utilization of structural and electrochemical benefits, $MnCo_2S_4$ electrode establishes its significant potential in the field of energy storage system.

Keywords: electrode material, psudeocapacitor, ternary metal sulfides.

Received: 15 March 2020

Revised: 4 April 2020

1. Introduction

Electrical energy is one of the most imperative topics in recent years due to its growing demand on storage in a sustainable way [1]. Among, diverse energy conversion and storage systems, supercapacitor is a new class of electrochemical energy system known for its notable power density, long term stability, superfast charge and discharge efficacy, long cycle life and environmental favorable. Yet they suffer from a low energy density this inhibits them from commercial applications [2]. An electrode material plays a predominant role in determining the supercapacitor performance. According to the previous reported literature several active materials like transition metal oxides, metal hydroxides, metal sulfides, conductive polymers and carbon based materials are effectively studied for supercapacitor applications. Among them, metal sulfides along with mono metal sulfides and bimetal sulfides are considered as promising candidates with remarkable properties in various applications like electro catalyst in hydrogen evolution reaction and as electrode material for energy storage applications. Amid different (NiS, CoS, ZnS) mono metal sulfides, e.g., cobalt sulfides, which appear to exist in different phases, such as $Co_{1-x}S$, Co_9S_8, Co_2S_3, Co_3S_4, provide various oxidation states which enhance their supercapacitor performance but they still suffer from low conductivity, poor mechanical stability and reduced specific capacitance when prepared via conventional methods. Compared to mono metal sulfides, binary metal sulfides have attracted much research attention by their superior capacitive performance and electrochemical activity obtained by its rich redox active sites and intensified charge transfer into different metal ions [3, 4]. Recently, pseudo capacitive bimetal sulfide, e.g., $NiCo_2S_4$, $ZnCo_2S_4$, $CuCo_2S_4$, $MnCo_2S_4$, and $FeCo_2S_4$ [2] offer excellent conductivity than the oxide counterparts. Due to their sulpho spinel structure, they result in low band gap energies which promote enhanced electrical conductivity ~ 100 times superior than oxide counterparts. Moreover, the low elctronegativity of sulfur provides a stable structure by forbidding the structure expansion, hence fast electron transportation is forwarded by its reinforced mechanical flexibility [2, 3] Among various binary metal sulfides, $MnCo_2S_4$ is finely studied as one of the most promising candidates with appreciable capacitive properties and good rate capabilities in supercapacitor applications; that fact is a result of the synergetic effect of cobalt with large oxidation potential and manganese, with more electrons [2, 5, 6].

The porosity level and morphology of the prepared electrode material also plays a vital role in determining its electrochemical performance. In this work, we adopted a one-step hydrothermal approach for the successful preparation of $MnCo_2S_4$ nanoparticles as a supercapacitor electrode material endowed with nanospheres like morphology and specific capacitance of 707.77 F/g at 2 A/g, it provide a high energy density of 78.17 W h Kg^{-1} at a power density of 863.27 W Kg^{-1} they offer an outstanding cyclic stability with a notable capacitance retention of 95.15% after 10000 galvanostatic charge discharge (GCD) cycles, these results suggest that $MnCo_2S_4$ is suitable candidate for high energy density supercapacitor applications.

2. Experimental

In this simple procedure, 0.2 mmol of Mn(NO$_3$)$_2$6H$_2$O and 0.4 mmol of Co(NO$_3$)$_2$6H$_2$O were dissolved in 60 ml of distilled water under uniform stirring for 30 minutes to achieve a homogenous solution, later 0.8 mmol of C$_2$H$_5$NS (thioacetamide) as sulfur source is made to dissolve in 25 ml of ethanol and combined to the above homogenous solution in a drop wise manner, followed by steady stirring for 6 hours. Next, the end solution was transferred into a Teflon- coated stainless autoclave. The autoclave was locked and treated in a hot air oven for 24 hours at 160 °C. After the thermal treatment, the autoclave was naturally cooled down to room temperature. The resultant black precipitate was put into centrifuged (Hamilton Bell v6500 Vanguard centrifuge) at 2600 RPM for 20 minutes and washed thoroughly with deionized water and ethanol by a number of times to remove the residuals and followed by drying in a vaccum oven at 110 °C for 6 hours and finely ground and this successive formation of MnCo$_2$S$_4$ nanoparticles.

3. Material characterization

Philips XPERT-PRO (Cu-K$\alpha\lambda = 1.5418$ Å) instrument were utilized to analyze crystalline nature of the sample via X-Ray Diffraction (XRD) pattern. JEM-2100 (JEOL, JAPAN) was used to obtain TEM images and their associated selected area electron diffraction (SAED) patterns. The chemical state and composition of the prepared sample was examined by XPS Ultra axis instrument (Kratos Analytical). The specific surface area and porous nature of the sample was studied via nitrogen adsorption- desorption analysis using BETSORP MAX (Microtrac BEL, Japan). The electrochemical properties of the gleaned electrode were measured by the instrument CHI 660E electrochemical workstation in a three-electrode cell frame work containing 2.0M KOH electrolyte solution with a potential range 0-0.5V Vs (Ag/Agcl).

4. Framing of electrode

The as-obtained powder sample was integrated as working electrode containing 80% of prepared sample, 15% of carbon black and 5% of PVDF (Polvinylidene Fluoride). A certain amount of N-methylpyrrolidone (NMP) was added to bind as homogenous slurry, the as formed slurry was loaded on to the nickel foam (1×1 cm^2) followed by drying in vacuum oven at 80 °C for 10 hours. The mass loading of electrode/cm^2 was predicted around 1.96 mg/cm^2.

5. Results and discussion

5.1. XRD analysis

Figure 1 shows the XRD pattern of MnCo$_2$S$_4$. Despite the fact, there is no standard pattern for MnCo$_2$S$_4$, the well-defined diffraction peaks located at 2θ = 16.2, 26.6, 30.9, 31.8 and 36.3° were indexed to the (111), (220), (311), (222) and (400) planes of cubic Co$_3$S$_4$ (JCPDS card number 73-1703) [5]. This indicates that addition of Mn to cobalt sulfide does not alter the crystal structure with slight changes in the lattice parameter [2]. Hence, the obtained product was mainly composed of MnCo$_2$S$_4$.

5.2. XPS characterization

The existence of constituent elements and chemical state of MnCo$_2$S$_4$ nanostructures were determined by XPS studies. From Mn2p spectrum (Fig. 2), the peaks positioned at 653.7, 641.5 and 643.6, 654.5 eV were attributed to Mn^{2+} and Mn^{3+} respectively [7]. In order, to conform the oxidation state of Mn, the MnS Spectrum was utilized. As shown in Fig. 3, it holds a binding energy splitting width of about 6.01 eV, which fits the Mn^{2+} oxidation state [3].

Whereas the Co2p spectrum in Fig. 4 showed two spin-orbit doublets of Co^{2+} and Co^{3+} and two shake up satellites. The peak located at 795.9 eV corresponds to Co2p$_{1/2}$ with a shoulder at 801.2 eV and the peak appeared at 779.8 eV related to Co2p$_{3/2}$ with satellite peak at 784.1 eV. The presence of weak satellite peaks indicates that the majority of cobalt is Co^{3+}. The spin separation of Co2p$_{3/2}$ and Co2p$_{1/2}$ is around 15 eV due to co-existence of Co^{3+} and Co^{2+} [8]. The S2p spectrum (Fig. 5) displayed a main peak of metal-sulfur bond at 163.8 eV and shake-up satellite peak at 168.3 eV [9].

5.3. Structural analysis

TEM micrograph images (Fig. 6 and Fig. 7) of MnCo$_2$S$_4$ recognized the non-uniformly dispersed nanospheres resembling structure of surface of size 16–17 nm. This uncommon morphology provides sufficient open space as an electroactive surface. From the high-resolution transmission electron microscope (HRTEM) image (Fig. 8), the inter-planar distance of lattice fringes is measured as 0.321 nm that correspond to (2 2 0) crystallographic planes. These

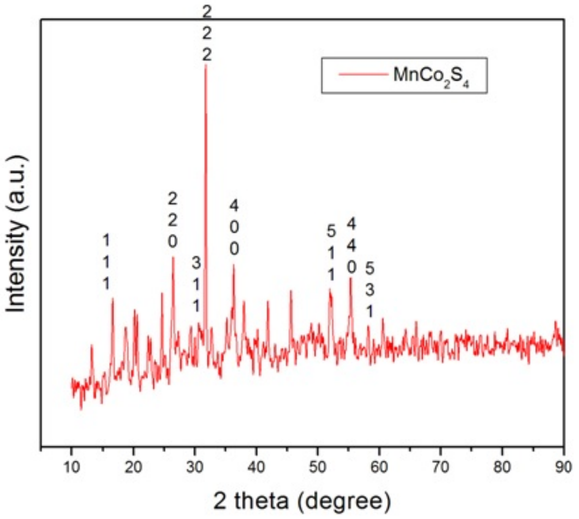

FIG. 1. X-ray diffraction pattern of MnCo$_2$S$_4$

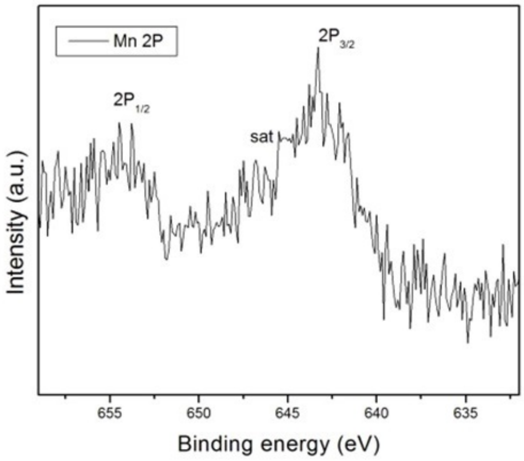

FIG. 2. XPS Spectrum of manganese element

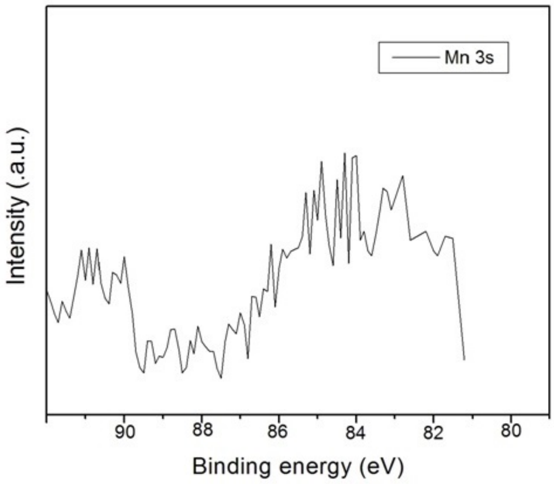

FIG. 3. Mn 3s spectrum

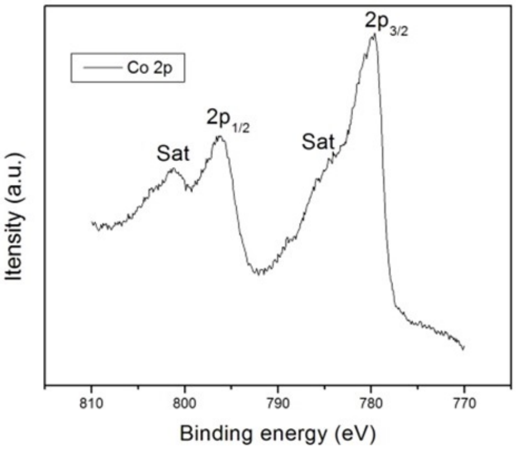

FIG. 4. XPS Spectrum of cobalt element

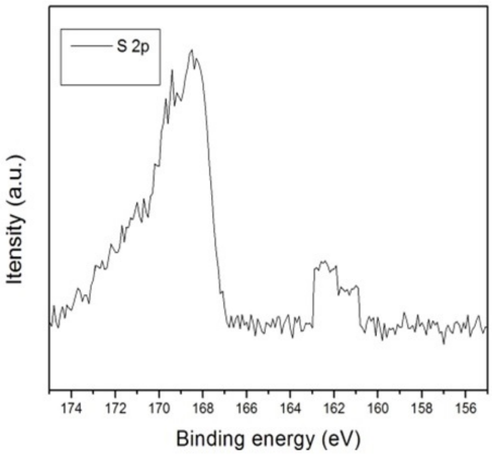

FIG. 5. XPS Spectrum of sulphur element

results are reliable with X-ray diffraction (XRD) analysis and the inset of Fig. 9, shows similar SAED which authenticates its polycrystalline nature. The EDX spectrum of the representative sample illustrated in Fig. 10 confirmed the presence of Mn, Co, and S elements.

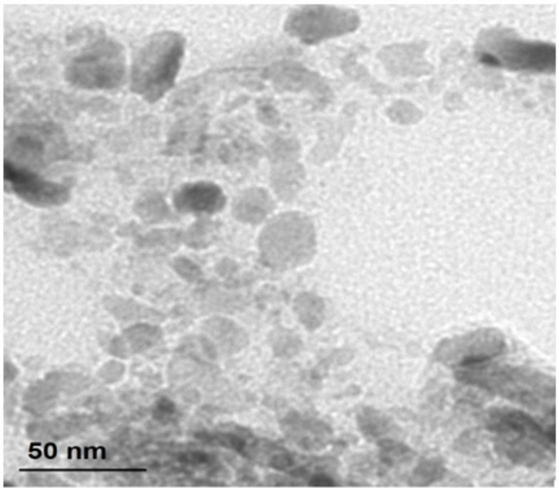

FIG. 6. TEM micrograph images of $MnCo_2S_4$

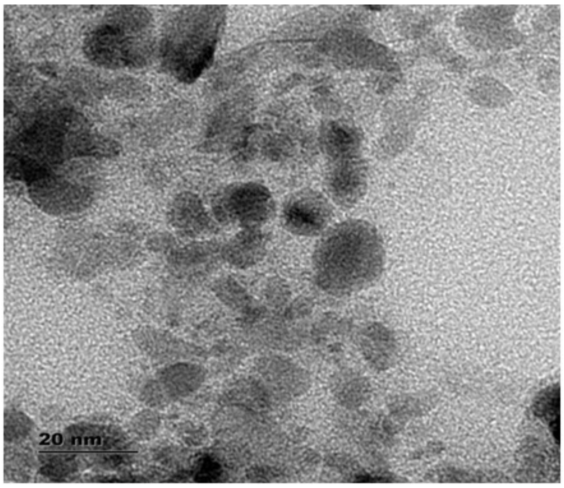

FIG. 7. TEM micrograph images of $MnCo_2S_4$

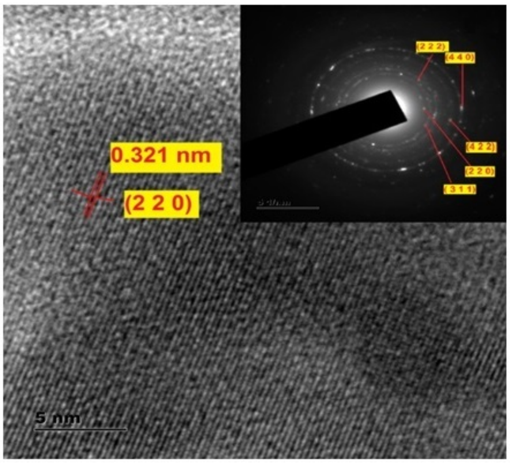

FIG. 8. SAED pattern of $MnCo_2S_4$

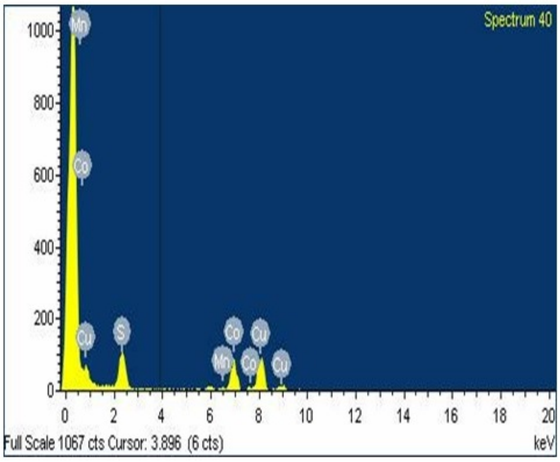

FIG. 9. EDS Spectrum of $MnCo_2S_4$

5.4. Surface area and pore size analysis

The adsorption isotherms shown in Fig. 9 are classified as type IV hysteresis loops that hold to the mesoporous structure [10] of the sample. It can be further confirmed by the Barett–Joyner–Halenda (inset of Fig. 10) pore size distribution data, the resultant pore distribution are narrow and most of the pores are mainly centered in the range of 6.95 nm. They enclose a high surface area of 73.26 m^2g^{-1} due to a typical nanosphere-like architecture. The high specific surface area and mesoporous nature of the prepared sample provides abundant electron-active sites and short diffusion path for charge transport channels this in turn improve electrochemical reactions in the redox process, and results in appreciable specific capacitance.

5.5. Electrochemical properties

5.5.1. Cyclic voltammetry studies. The electrochemical characterization was carried out in a 3-electrode system with $MnCo_2S_4$ electrode as the working electrode. Fig. 11 depicts CV curves at different scan rates, the pair of redox peaks are caused by interaction between sulphospinel materials and electrolyte ions [2, 3]. Redox peaks affirm the reversible faradaic property attributed to the pseudocapacitive behavior of the $MnCo_2S_4$ electrode. The substantial shape maintains of CV curves suggests the good redox reaction reversibility of the electrode [2], moreover, with

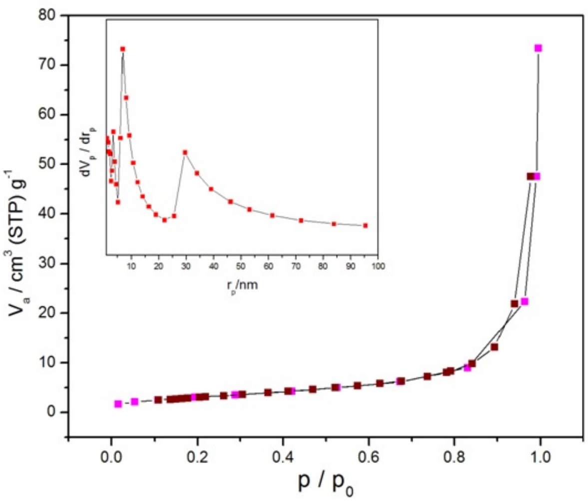

FIG. 10. N_2 sorption isotherms and differential mesopore size distribution ΔV/Δd plots (inset) of $MnCo_2S_4$

respect to the scan rate the anodic and cathodic peak shifts, this corresponds to the fast charge/discharge rates. The interaction between the electrode material and electrolyte ions [11, 12] are given by the following equations [3]:

$$\text{MnS+OH}^- \leftrightarrow \text{MnSOH} + e^- \tag{1}$$

$$\text{CoS+OH}^- \leftrightarrow \text{CoSOH} + e^- \tag{2}$$

$$\text{CoSOH +OH}^- = \text{CoSO+H}_2\text{O} + e^- \tag{3}$$

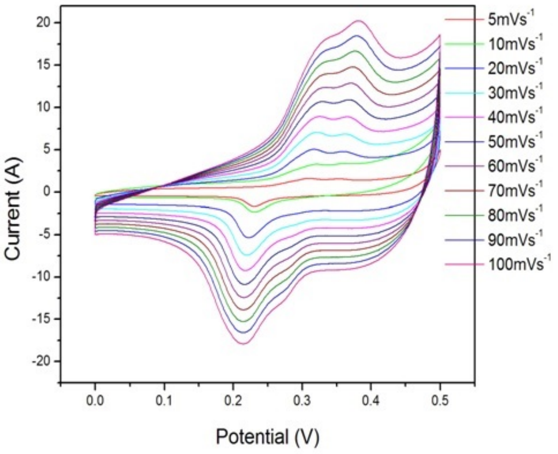

FIG. 11. CV curves of $MnCo_2S_4$ at various scan rates

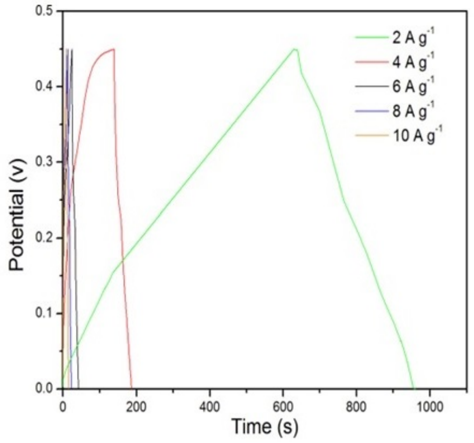

FIG. 12. Charge/Discharge curves of $MnCo_2S_4$ at various current densities

5.5.2. Galvanostatic Charge/Discharge Analysis. The pseudo capacitive property of $MnCo_2S_4$ nanoparicles were established by well-symmetric glavanostatic charge/discharge (GCD) curves (Fig. 12) at a potential window of 0.0–0.5 V with different current densities [4]. The specific capacitance is calculated using the following equation [13]:

$$c_s = \frac{l\Delta t}{m\Delta v}. \tag{4}$$

The superior specific capacitance of 707.77 F/g at 2 A/g is obtained. As shown in Fig. 13, the specific capacitance decreases as current density increases, due to minimum utilization of active material and at high discharge current densities the controlled diffusion presents its inability to maintain the redox transition completely. To determine the cycle ability, the electrodes are subjected to continuous charge/discharge cycles of 10000 cycles at a current density of 10 A/g. The structural stability is a crucial factor in evaluating the cycle ability of the electrode material. Since, the electrode material enclose a porous nanosphere-like morphology which leads to better ionic conductivity and accessibility to reach active sites in electrode material This helps in providing capacitance retention of 95.15% after 10000 GCD cycles (Fig. 14) which is achieved by good structural stability. To satisfy its commercial needs, a Ragone plot of energy density vs. power density profile (Fig. 15) is studied and it is endowed with an appreciable energy density of 78.1 W h Kg^{-1} at a power density 863.27 W Kg^{-1}.

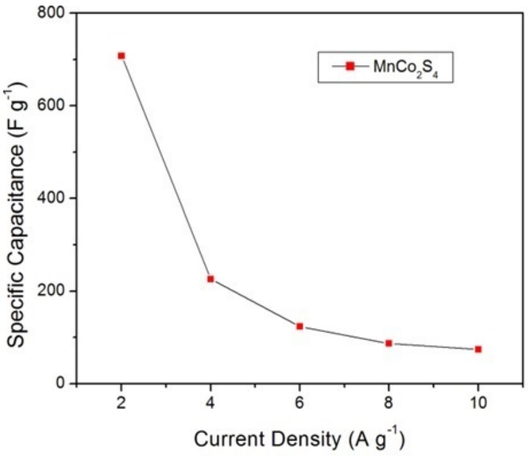

FIG. 13. Current density vs specific capacity plot of $MnCo_2S_4$

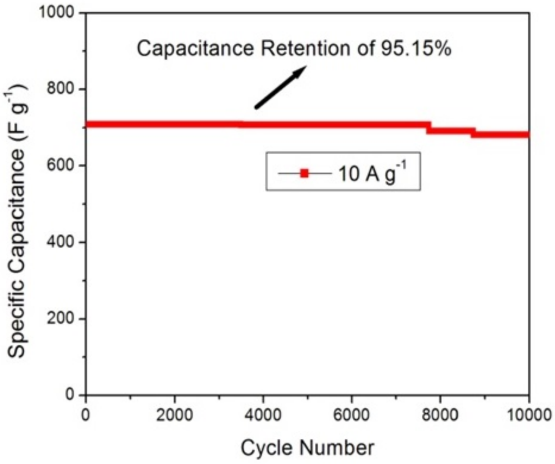

FIG. 14. Cyclic stability of $MnCo_2S_4$ electrodes at 10 Å g^{-1}

5.5.3. EIS characterization. EIS measurements were taken in defining impedance response of $MnCo_2S_4$ electrode materials in the frequency region 100 KHz – 0.01 Hz at an open-circuit potential of amplitude 5 mV and their corresponding Nyquist plot is portrayed in Fig. 16. The straight line at low frequency region specify the capacitive behavior, charge transfer resistance R_{ct} is premeditated from the semi-circle in the high frequency region, negligible semicircle indicates the very lowest charge-transfer resistances, and this improves the speedy electron transfer in the charge-discharge process leading to high-rate capability and notable supercapacitor performance [15, 16].

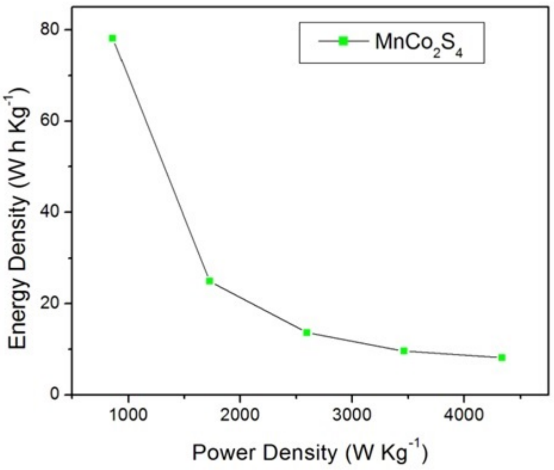

FIG. 15. Ragone plot of $MnCo_2S_4$

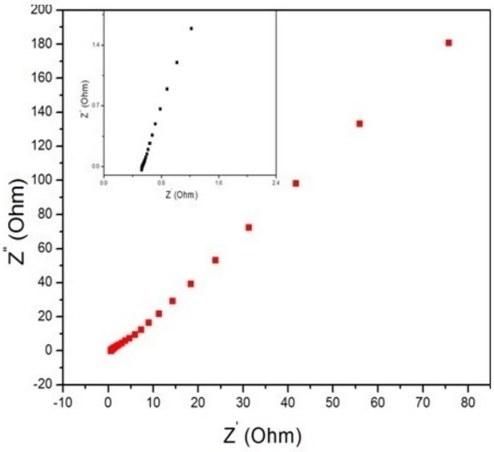

FIG. 16. EIS plot of $MnCo_2S_4$ electrode

6. Conclusion

A $MnCo_2S_4$ supercapacitor electrode with a propitious electrochemical performance was expediently fabricated using a simple one step hydrothermal method. The nanospheres like architecture of size 16–17 nm provide a highly accessible porous structure which assists superior specific capacitance of 707.77 F/g at a current density of 2 A/g; it also has capacitance retention of 95.15% of initial capacitance after 10000 GCD cycles. The excellent performances contributed to the high surface area with mesoporous structure and low charge transfer resistance suggests that the $MnCo_2S_4$ could be utilized in fabricating high competency energy storage device.

References

[1] Bu Yuan,Yu, Xial Wang, Shuyan Song and Xiong Wen (David) Lou. Formation of onion-like $NiCo_2S_4$ particles via sequential ion-exchange for hybrid supercapacitors. *Adv. Mater. United States*, 2016, **29**, P. 1605051.

[2] Hongfei Wang, Hongfei, Zhang, Kefu, Song, Yuqing, Qiu, Jun, Wu, Juan and Yan, Lifeng. $MnCo_2S_4$ nanoparticles anchored to N- and S-codoped 3D graphene as a prominent electrode for asymmetric supercapacitors. *Carbon. United Kingdom*, 2019, **146**, P. 420–429.

[3] Elshahawy, Abdelnaby M., Li, Xin, Zhang, Hong, Hu, Yating, Ho, Kuan Hung, Guan Cao and Wang John. Controllable $MnCo_2S_4$ nanostructures for high performance hybrid supercapacitors. *J. Mater. Chem. A*, 2017, **5**, P. 7494–7506.

[4] Huang, Yunpeng, Cui, Fen, Bao, Jian, Zhao, Yan, Lian, Jiabiao, Liu, Tianxi and Li, Huaming. $MnCo_2S_4$/$FeCo_2S_4$ "lollipop" arrays on a hollow N-doped carbon skeleton as flexible electrodes for hybrid supercapacitors. *J. Mater. Chem. A*, 2019, **7**, P. 20778–20789.

[5] Liu S. and Jun S.C. Hierarchical manganese cobalt sulfide core–shell nanostructures for high-performance asymmetric supercapacitors. *J. Power Sources*, 2017, **342**, P. 629–637.

[6] Jia, Hong, Song, Yingying, Wu, Jie, Fu, Wenwen, Zhao, Jianguo and Liu, Xianming. A novel P-doped $MnCo_2S_4$ nanoneedles assembled dandelion-like structure for high performance hybrid supercapacitors. *Mater. Lett. Netherlands*, 2018, **233**, P. 55–58.

[7] Li, Wenhua, He, Lei, Zhang, Jing, Li, Bin, Chen, Qianqiao and Zhong, Qin. Anchoring spinel $MnCo_2S_4$ on carbon nanotubes as efficient counter electrodes for Quantum Dot Sensitized solar cells. *J. Phys. Chem. C.*, 2019, **123**, P. 21866–21873.

[8] Yin, Jialin, Zhang, Hao, Luo, Jiaqiu, Yao, Mengqi and Hu, Wencheng. High-boiling-point solvent synthesis of mesoporous $NiCo_2S_4$ with high specific surface area as supercapacitor electrode material. *J. Mater. Sci. Mater. Electron*, 2016, **28**, P. 2093–2099.

[9] Gong X.F., Cheng J.P., Ma K.Y., Liu F., Zhang Li and Zhang XiaoBin. Nanostructured nickel-cobalt sulfide grown on nickel foam directly as supercapacitor electrodes with high specific capacitance. *Mater. Chem. Phys.*, 2016, **173**, P. 317–324.

[10] Zhu, Tao, Zhang, Guoxiong, Hu, Tao, He, Zhenni, Lu, Yisheng, Wang, Guiqing, Guo, Haibo, Luo, Jian, Lin, Chuan and Chen, Yigang. Synthesis of $NiCo_2S_4$-based nanostructured electrodes supported on nickel foams with superior electrochemical performance. *J. Mater. Sci.*, 2015, **51**, P. 1903–1913.

[11] Atin Pramanik, Sandipan Maiti, Monjoy Sreemany, and Sourindra Mahanty. Carbon Doped $MnCo_2S_4$ Microcubes Grown on Ni Foam as High Energy Density Faradaic Electrode. *Electrochim. Acta*, 2016, **213**, P. 672–679.

[12] Silambarasan M., Padmanathan N., Ramesh P.S., Geetha D. Spinel $CuCo_2O_4$ Nanoparticles: Facile One-Step Synthesis, Optical, and Electrochemical Properties. *Mater. Res. Express*, 2016, **3**, P. 095021.

[13] Dakshana M., Meyvel S., Malarvizhi M., Sathya P., Ramesh R., Prabhu S. and Silambarasan M. Facile synthesis of $CuCo_2S_4$ nanoparticles as a faradaic electrode for high performance supercapacitor applications. *Vacuum*, 2020, **174**, P. 109218.

[14] Saravanakumar B., Ramachandran S.P., Ravi G., Ganesh V., Sakunthala A. and Yuvakkumar R. Morphology dependent electrochemical capacitor performance of $NiMoO_4$ nanoparticles. *Mater. Lett.* 2017, **209**, P. 1–4.

[15] Wen, Ping, Fan, Mingjin, Yang, Desuo, Wang, Yan, Cheng, Hualei and Wang, Jinqing. An asymmetric supercapacitor with ultrahigh energy density based on nickle cobalt sulfide nanocluster anchoring multi-wall carbon nanotubes. *J. Power Sources*, 2016, **320**, P. 28–36.

[16] Jun Pu, Tingting Wang, Haiyang Wang, Yao Tong, Chenchen Lu, Wei Kong, and Zhenghua Wang. Direct Growth of $NiCo_2S_4$ Nanotube Arrays on Nickel Foam as High-Performance Binder-Free Electrodes for Supercapacitors. *Chem Plus Chem*, 2014, **79**, P. 577–583.

NANOSYSTEMS: PHYSICS, CHEMISTRY, MATHEMATICS, 2020, 11 (2), P. 237–245

Synthesis, characterization and concentration dependant antibacterial potentials of nickel oxide nanoparticles against *Staphylococcus aureus* and *Escherichia coli*

V. Gupta[1,*], V. Kant[2], A. Gupta[3], M. Sharma[1]

[1]Department of Chemistry, University of Jammu, J&K, India

[2]Division of Pharmacology & Toxicology, IVRI, Bareilly, UP, India
(Present address: Department of Veterinary Pharmacology & Toxicology, LUVAS, Hisar)

[3]Department of Physics, University of Jammu, J&K, India

[*]vijayta1gupta@gmail.com

DOI 10.17586/2220-8054-2020-11-2-237-245

Bacterial resistance to antibiotic treatment is a major emerging clinical and public health issue across the globe. Advancements in the field of metal oxide nanomaterials in the last few years have improved the potential of metal oxides in different applications. Metal oxides, of which, nickel oxide (NiO) is one, also possess antibacterial activities. This investigation was planned to synthesize NiO nanoparticles to study their antibacterial potential in comparison with bulk NiO and standard antibiotics at different concentrations. Synthesis and characterization of NiO nanoparticles was done by standard procedures. The antibacterial potentials of different compounds were determined at different concentrations against *S. aureus* and *E. coli*. The diameter of zone of inhibition showed that the antibacterial effect of NiO nanoparticles against *S. aureus* was better than *E. coli* at the same concentration. The concentration-dependent effect of NiO nanoparticles was observed from 0.125 to 128 μg/ml. The effect of NiO nanoparticles was markedly better than bulk NiO at all concentrations. Tetracycline and gentamicin did not show effect below 1.0 μg/ml and 2.0 μg/ml, respectively. The activity index and fold increase of NiO nanoparticles were both higher than 1 and positive, with respect to tetracycline, gentamicin and bulk NiO against *S. aureus* and *E. coli* at all the tested concentrations. In conclusion, the NiO nanoparticles seemed to be a more potent antibacterial agent than their bulk form, tetracycline and gentamicin, and in future, their applications may be extended in biomedical field and other areas to reduce microbial infections and incidences of antibacterial resistance.

Keywords: nickel oxide nanoparticles, *S. aureus*, *E. coli*, Antibacterial activity, activity index, fold increase.

Received: 20 March 2020

Revised: 3 April 2020

1. Introduction

The growth and proliferation of bacteria can occur fruitfully anywhere. Bacterial infections, due to both gram-positive as well as gram-negative bacterial strains, are considered as serious health problems worldwide. Bacterial infectious diseases cause huge morbidity and mortality, thus, there is need to develop effective antimicrobial agents. Over the years, different infections resulting from society as well as hospital atmosphere have been controlled by the use of antibiotics [1]. Exposure of bacteria to several environmental variations such as temperature, osmolarity, radiation, toxins, and limited nutrition make them capable to survive in diverse environments by developing various approaches. Bacterial resistance to antibiotic treatment is emerging a major clinical and public health issue across the globe, which is also a serious concern for physician. Antimicrobial resistance is mainly due to indiscriminate use of antibiotic medications, lack of new strategies for antibacterial resistance development etc. [2]. This problem has added financial burden to the healthcare system. It is also predicted that antibacterial resistance will achieve world-wide epidemic proportions by 2050 and account for approximately 10 million casualties [3, 4]. In view of its global importance, appropriate strategies and actions are needed from governmental sectors, industry, healthcare professions, farmers, society etc. Bacteria can develop resistance to treatments by different pathways, like decreased influx and increased efflux mechanisms, alteration in binding target sites, production of some enzymes etc. Development of more efficient antibacterial agents to overcome the problems of bacterial mutation, antibiotic resistance, outbreaks of pathogenic strains, etc. is demanded in the present era.

Different metals and metal oxides have been used as an antimicrobial agents for thousands of years. Indians have also used copper and silver to preserve food and disinfect water [5]. However, after the discovery of antibiotics in the twentieth century, their antimicrobial properties in a variety of medical applications have rapidly diminished. Recent basic and applied research on various metal oxides has led to their broad scale application in various areas such as catalysis, in semiconductors, sensors, controlled release of drugs and as antimicrobial agents. Advancements in the field of nanobiotechnology in the last few years have also led to the development of various metal oxide nanomaterials, which are emerging as one of the new antibacterial agents. Studies on the synthesis, characterization and applications of nanoparticles as an antimicrobial system is the latest area of interest in the biomedical and healthcare sectors. Nanoparticles are considered better antimicrobial agents than their bulk forms against drug-resistant pathogens due to size effect, doping effect, cost effective and stability, prolonged shelf-life etc. Recently, nanoparticles of many metal oxides like zinc oxide, copper oxide, iron oxide, cobalt oxide, cerium oxide etc. have shown various biological activities including antibacterial activity against Gram-positive and Gram-negative bacteria [6–9]. The bactericidal property by different metal oxide nanoparticles occurs by various mechanisms [10]. Additionally, nanoparticles of cobalt have shown better antibacterial efficacy than its bulk form against *Staphylococcus aureus* (*S. aureus*) and *Escherichia coli* (*E. coli*) [11]. It has also been reported that silver nanoparticles stabilized with neomycin-chitosan has enhanced antimicrobial activity relative to the neomycin-chitosan system and silver nanoparticles alone [12].

Nickel oxide (NiO), a P-type semiconductor transition metal oxide, in bulk and nano size has received significant attention due to its wide range of applications in different fields [13]. The nano NiO possesses significantly different catalytic, optical, electronic, and magnetic properties than its bulk form due to quantum size and surface effects [14, 15]. Although, various investigations have documented the efficient applications and properties of NiO based materials, but the detailed studies on antimicrobial activity of NiO and its nano form are very limited and mostly lacking in comparison of antibacterial actions of NiO nanoparticles with respect to its bulk form as well as standard antibiotics. In view of this, the present investigation sought to prepare NiO nanoparticles to determine their antibacterial action against commonly present bacterial strains i.e. *S. aureus and E. coli*, and their comparison of antibacterial actions to bulk NiO and standard antibacterials (tetracycline and gentamicin) at different concentrations.

2. Materials and method

2.1. Materials used

The different chemicals of analytical grade were used for in this investigations. Nickel nitrate and sodium hydroxide were used for the synthesis of NiO nanoparticles and purchased from Sigma Aldrich, USA. Dimethyl sulfoxide (DMSO) was purchased from SRL. Tetracycline and gentamicin were procured from Sigma Aldrich, USA. The Muller-Hinton Agar (MHA), Muller-Hinton Broth (MHB) and nutrient broth (NB) were purchased from Hi-media, Mumbai, India and used for antibacterial studies. The *S. aureus* (MTCC 1430) and *E. coli* (MTCC 2127) gifted from the Department of Biotechnology, University of Jammu were revived using the nutrient broth (NB) and used two bacterial strains in this study.

2.2. Synthesis of NiO nanoparticles

Aqueous solution of 0.25 M nickel nitrate and 1.25 M sodium hydroxide with constant stirring at 55 °C were reacted for the synthesis of NiO nanoparticles. The complete mixture was magnetically stirred for 2 h at pH 12, forming a green precipitate of nickel hydroxide which was centrifuged, filtered and washed. Thereafter, they were calcined at 600 °C for 3 h to obtain NiO nanoparticles. The synthesized NiO nanoparticles at different concentrations were dispersed in DMSO by employing ultrasonication for further studies. There was no addition of stabilizer during any step in order to avoid its effects on the surface property of the nanoparticle as well as chemical contamination.

2.3. Characterization of NiO nanoparticles

The synthesized nanoparticles were characterized by using various techniques like particle size analyzer (PSA), transmission electron microscopy (TEM) and scanning electron microscopy (SEM). The particle size distribution (PSD) analysis of the synthesized nanoparticles was done by Malvern Instruments Zetasizer Nano-ZS instrument. The transmission electron microscope (Hitachi H-7500) was used to evaluate the size and morphology of nanoparticles. The surface morphology of the particles was observed by a scanning electron microscope (SEM-EDS) using SEM (JEOL JSM - 6390LV).

2.4. Assessment of antibacterial activity

2.4.1. Determination of zone of inhibition by well-diffusion method. Different concentrations of tetracycline, gentamicin, bulk NiO and synthesized NiO nanoparticles were used to evaluate their antibacterial potentials against the gram-positive i.e. *S. aureus* and gram-negative i.e. *E. coli* bacterial strains. The antibacterial activity was determined on Muller-Hinton agar by the agar well diffusion method [16]. The agar used for the study was seeded with overnight cultures of different bacterial strains (10^8 cfu/ml) and then poured (12 ml) in petri plates. Five 6 mm wells of diameter were punched into the agar plates for testing antimicrobial activity of nanoparticles and other compounds. Prepared wells were also sealed with one drop of melted agar (0.8% agar) to prevent the leakage of nanoparticles and other compounds from the bottom of the wells. Using a micropipette, different dilutions of NiO nanoparticles, bulk NiO and antibiotics were poured onto each of five wells on all plates. After overnight incubation at 37 °C, the different diameters of zone of inhibition were measured to quantify the antibacterial activity. In this study, DMSO was used as negative control, and tetracycline and gentamicin were used as positive control to compare the efficacy of the nanoparticles. The same experiment for all the dilutions was conducted in triplicate. The activity index and fold increase for the comparison of antibacterial potentials of NiO nanoparticles with bulk NiO and standard antibiotics was also determined by using values of zone of inhibition.

2.4.2. Activity index for NiO nanoparticles. The activity index was calculated by comparing the resultant zones of inhibition of NiO nanoparticles with the standard antibiotic or bulk NiO by using the following formula:

$$\text{Activity Index (AI)} = \frac{\text{Inhibition zone of the NiO nanoparticles}}{\text{Inhibition zone of the bulk NiO or standard antibiotic}}$$

2.4.3. Fold increase for NiO nanoparticles. Fold increase was also determined by comparing the resultant zones of inhibition of NiO nanoparticles with the standard antibiotic or bulk NiO. The fold increase was calculated by using the following equation:

$$\text{Fold increase}(\%) = \frac{b-a}{a} \cdot 100,$$

where a and b refer to the inhibition zones of antibiotic/ bulk NiO and NiO nanoparticles, respectively.

3. Results and discussion

The PSD of NiO nanoparticles is shown in Fig. 1A and it showed the overall z-average size of 178.6 nm with a polydispersity index of 0.239. This signified that the particle size distribution consisted of a single size mode devoid of aggregates. The TEM (Fig. 1B) and SEM (Fig. 1C) micrographs of NiO nanoparticles showed that the synthesized NiO nanoparticles have the average size of 40–55 nm and almost spherical shape. The SEM micrograph also demonstrated that the majority of the particles displayed little aggregation.

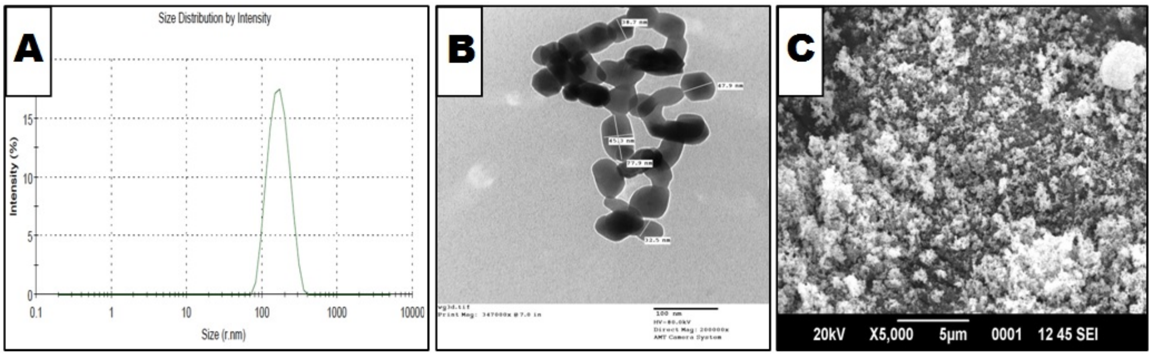

FIG. 1. (A) The particle size distribution (PSD) of NiO nanoparticles. Micrograph of TEM (B) and SEM (C) of NiO nanoparticles

Images of bacterial culture plates of present study evidently showed that tetracycline, gentamicin, bulk NiO and NiO nanoparticles produced zones of inhibition against *S. aureus* and *E. coli* in concentration dependent manners (Fig. 2). The mean diameters of zones of inhibition for different tested compounds at different concentrations are presented in Table 1. It has been previously reported that the inhibition of bacterial growth increases with an increase in concentration of nanoparticles [17]. Earlier, different nanoparticles have been studied for antimicrobial activities against human pathogenic bacteria such as *S. aureus* and *E. coli* [18,19]. The synthesized NiO nanoparticles produced larger zone of inhibition against *S. aureus* in comparison to *E. coli* at the same concentration. It was revealed that NiO nanoparticles have stronger action against *S. aureus* than *E. coli*. These results are in agreement with the earlier studies in which *S. aureus* were more sensitive than *E. coli* to antibacterial actions of Ni nanoparticles [20]. In recent years, also, few studies have shown the antimicrobial actions of NiO nanoparticles prepared by different methods. Khalil et al [21] biologically synthesized NiO nanoparticles by using aqueous leaf extracts of *Sageretia thea*, and observed their antimicrobial properties by in vitro assays. Their study also revealed that the antibacterial activities of NiO nanoparticles were enhanced after UV illumination and *E. coli* as well as B. *subtilis* were the most susceptible strains. Srihasam et al., [22] produced NiO nanoparticles using *Stevia* leaf broth, which showed the antimicrobial actions strongly against gram-negative bacteria. The synthesized nanoparticles in their study ranged from 20 to 50 nm and were spherical in shape. Helan et al [23] prepared the NiO nanoparticles with the help of phytoconstituents present in the neem leaf and observed their antibacterial activity, which was concentration-dependent. In their study,

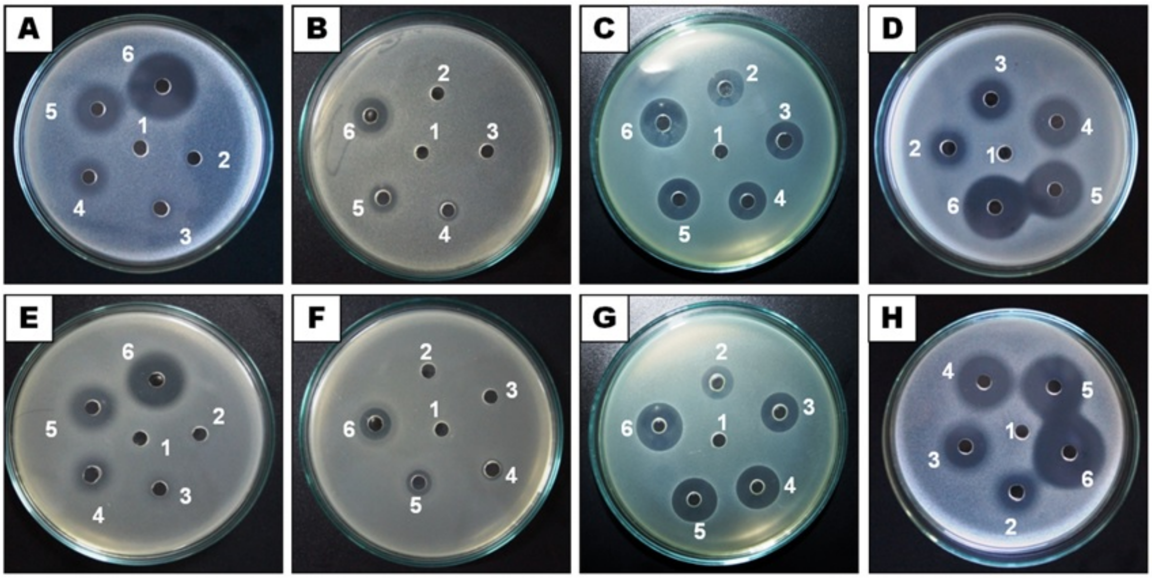

FIG. 2. Zone of inhibitions of tetracycline (A,E), gentamicin (B,F), bulk NiO (C,G) and NiO nanoparticles (D,H) against *S. aureus* (A-D) and *E. coli* as (E-H) at different concentrations i.e. (1) 0.00 μg/ml, (2) 0.125 μ g/ml, (3) 0.5 μg/ml, (4) 2.0 μg/ml, (5) 16.0 μg/ml and (6) 128 μg/ml

morphological analysis revealed oblong shape and 12 nm size of nanoparticles. Abbasi et al [24] also synthesized NiO nanoparticles by an environmentally-benign synthetic method using *Geranium wallichianum* as reducing and capping agent. The NiO nanoparticles in their study were of 21 nm size and nanoparticles showed showed antibacterial potential against different bacterial strains at different concentrations (700–21.875 μg/ml). In their study, the *B. subtilis* (MIC: 21.875 μg/ml) was the most susceptible organism, and *K. pneumonia* (MIC: 175 μg/ml) as well as *P. aeruginosa* (MIC: 175 μg/ml) were the least susceptible bacterial strains with respect to the action of NiO nanoparticles. Bhat et al [25] synthesized face-centered cubic structure of NiO nanoparticles with 30 nm average size by co-precipitation method. In their study, *K. pneumonia* and *B. subtilis* showed maximum zone of inhibition (15 mm) at 40 mg/ml concentration, and minimum inhibitory concentration 62.5 μg/ml. In our present study, the antibacterial actions of synthesized NiO nanoparticles increased with an increase in concentration, and this concentration dependent action was observed only from 0.125 to 128 μg/ml. It was observed in this study that the action of the nanoparticles decreased when the concentration of nanoparticles increased beyond 128 μg/ml. This decreased action at higher concentrations was postulated to be due to the agglomeration of nanoparticles at higher concentrations. Some previous studies have also explained in their findings that nanoparticles possess some optimum concentration at which higher effects are noticed in comparison to more or less concentration [26]. Thus, the optimum concentration for NiO nanoparticles in the present study was 128 μg/ml. Standard antibacterials i.e. tetracycline and gentamicin did not show zones of inhibition at lower concentrations i.e. below 1.0 μg/ml for tetracycline and below 2.0 μg/ml for gentamicin (Table 1) and seemed ineffective at lower concentrations. On the other hand, the bulk NiO and NiO nanoparticles used in this study were effective below these concentrations (Tables 1). It suggested that the range of inhibitory concentration for bulk and nano NiO was broader with respect to both tetracycline and gentamicin. The antibacterial effects of nano form of NiO was observed markedly better than bulk form at all tested concentrations of present study. Hence, NiO nanoparticles can provide antibacterial action for longer duration with less frequency of applications and may be considered as a substitute for tetracycline, gentamicin and bulk NiO in different fields in view of to diminish the occurrence of bacterial resistance.

The size, morphology and concentration of nanoparticles significantly influence their physical and chemical properties, which affect the degree of growth and survival of bacteria. Different previous studies have revealed that metal oxide nanoparticles between 1 and 100 nm size with different shapes are promising antimicrobial agents against infectious diseases [27]. The TEM micrograph in present study showed average size of 40–55 nm and spherical shape of synthesized NiO nanoparticles. So, nanoparticles synthesized in this study could be considered promising antimicrobial agents. The metal oxide nanoparticles induce bacterial toxicity through various mechanisms of actions like, oxidative stress, lipid peroxidation, cell membrane lysis, enzyme inhibition, proteolysis etc. [28]. The overall charge of the bacterial cell at physiological pH is negative due to the dissociation of excess carboxylic groups at the cell surface [29]. Since NiO has a positive surface charge, so, they became electrostatically bound to the negative cell surface,

TABLE 1. Zone of inhibition for tetracycline, gentamicin, bulk NiO and NiO nanoparticles (NPs) against *S. aureus* and *E. coli* at different concentrations

Conc.	Zone of inhibition (mm) against *S. aureus*				Zone of inhibition (mm) against *E. coli*			
(μg/ml)	Tetracycline	Gentamicin	Bulk NiO	NiO NPs	Tetracycline	Gentamicin	Bulk NiO	NiO NPs
128.0	22.17	15.67	18.08	25.17	17.58	12.33	15.33	22.08
64.0	19.17	13.75	17.00	22.83	16.00	11.17	14.25	21.33
32.0	16.50	12.25	16.25	21.00	14.00	10.50	13.42	20.92
16.0	13.08	10.50	15.17	19.50	11.83	8.75	12.42	18.58
8.0	11.50	9.00	14.42	18.50	9.50	7.75	11.17	17.50
4.0	8.83	7.42	12.00	17.67	8.00	7.08	10.67	16.33
2.0	7.50	7.08	11.25	16.00	7.25	7.00	10.25	14.08
1.0	7.25	–	10.58	13.50	7.08	–	9.42	12.58
0.5	–	–	9.50	13.17	–	–	8.67	12.08
0.25	–	–	9.00	11.00	–	–	8.25	10.00
0.125	–	–	8.50	9.83	–	–	7.58	8.83

which hinder the cellular activity. Penetration of NiO into the cell and its toxicity made the cell inactive and dead followed by lysis [30]. The penetration of NiO nanoparticles in bacteria through cell membrane leads to generation of reactive oxygen species (ROS), which leads to damage of cell components [31, 32]. The antibacterial potential of the nanoparticles is mainly governed by the size, shape, dosage, stability, morphology, and treatment time [33]. In the present study, the smaller size of NiO nanoparticles was thought to be responsible for better antibacterial actions than its bulk form, as smaller size usually enhancedby the dispersibility and penetration into the intracellular matrix and interference with intracellular Ca^{2+} absorption leading to cell damage [22]. Attachment of the nickel ions released from the NiO nanoparticles to the cell membrane of the microbes initiate electrostatic interactions, wherein it interferes with cellular physiology leading to their disruption [34]. Further, these damaged cell membranes are more susceptible to further interactions, which lead to more penetration of NiO nanoparticles and leakage of the intracellular organelles [22]. These sequential steps augment the antimicrobial action of the nanoparticles. Additionally, the interactions of penetrated NiO nanoparticles generate the ROS, which has a significant tendency in interfering the microbial electron transport chain, damaging DNA by breaking the phosphate and hydrogen bonds, denaturing the protein by alteration of the tertiary structure, and damaging the mitochondria by oxidative stress [22, 35]. The soluble nickel compounds attack the bacterial cell membrane from outside, whereas nanoparticles (metal/metal oxide) easily get entry through bacterial cell membrane and leading to the death of bacterial cell [36–38]. The schematically possible hypothetical mechanisms of NiO nanoparticles for the antibacterial actions are shown in Fig. 3. So, the direct contact of NiO nanoparticles may be responsible for damaging the cell membrane followed by cell lysis in present study. It has been observed that metal oxide nanoparticles do not generate bacterial resistance and are safe potential antimicrobial alternatives for clinical applications [39, 40]. Most of the nanoparticles also did not inactivate or lose their properties when exposed to sterilization by different ways, like high temperature, gamma irradiation or plasma treatment etc. [41]. The various advantages and unique properties of nanoparticles have led to the incorporation of nano forms of oxides of silver, copper, titanium, zinc, iron etc. into the medical field has emerged as an alternative to new antimicrobial agents in recent years [42, 43]. Further, NiO nanoparticles in comparison to it bulk form undergo marked transformations, which induce significant changes in their structural and physico-chemical properties, which in turn affects its better action.

Consideration of an antimicrobial agent as better than others can be done after the comparison its potential with some standard antimicrobials and its other forms. The calculation of activity index (AI) by using the values of zone of inhibition is considered one of the standard approaches for the comparison of antibacterial potentials of different compounds [44]. The testing drug/compound will be considered better against particular bacteria if it possess value of AI more than one. In the present investigation, the AI for NiO nanoparticles with respect to tetracycline, gentamicin and bulk NiO against *S. aureus* and *E. coli* was calculated at various concentrations, and the values are presented in Table 2. The AI of NiO nanoparticles with respect to tetracycline, gentamicin and bulk NiO against *S. aureus* and *E. coli* were found higher than 1 at all compared concentrations. These values also revealed that the AI of NiO nanoparticles against *S. aureus* and *E. coli* was higher for gentamicin in comparison to tetracycline and bulk NiO at the same concentration. Another method for the comparative studies of different antimicrobials is calculation of

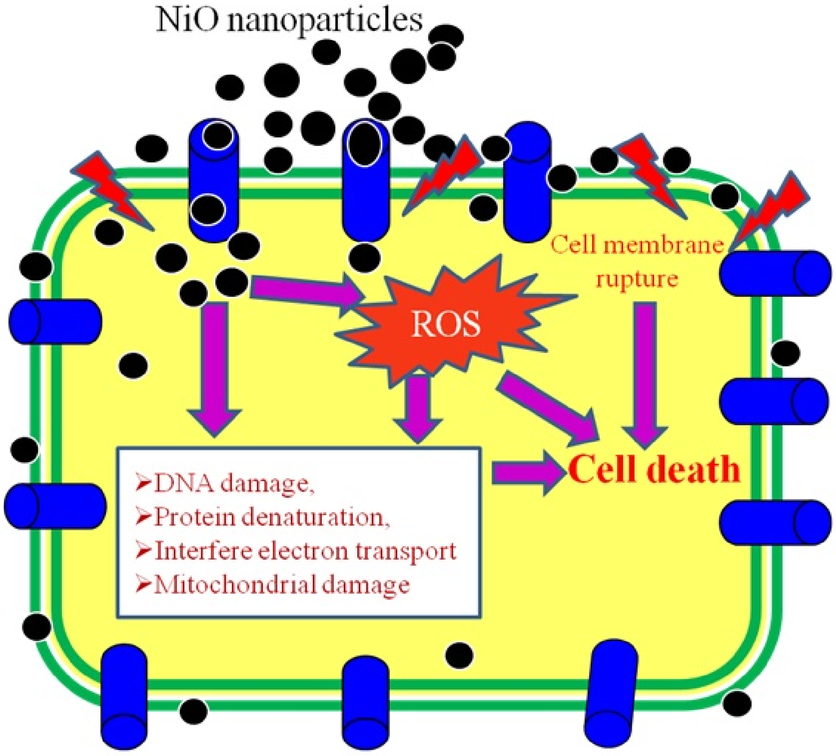

FIG. 3. The schematically possible hypothetical mechanisms of action of NiO nanoparticles for antibacterial activity

TABLE 2. Activity index of NiO nanoparticles with respect to tetracycline, gentamicin and bulk NiO against *S. aureus* and *E. coli* at different concentrations

Conc. (μg/ml)	Activity Index w.r.t. Tetracycline		Activity Index w.r.t. Gentamicin		Activity Index w.r.t. bulk NiO	
	S. aureus	*E. coli*	*S. aureus*	*E. coli*	*S. aureus*	*E. coli*
128.0	1.14	1.26	1.61	1.79	1.39	1.44
64.0	1.19	1.33	1.66	1.91	1.34	1.50
32.0	1.27	1.49	1.71	1.99	1.29	1.56
16.0	1.49	1.57	1.86	2.12	1.29	1.50
8.0	1.61	1.84	2.06	2.26	1.28	1.57
4.0	2.00	2.04	2.38	2.31	1.47	1.53
2.0	2.13	1.94	2.26	2.01	1.42	1.37
1.0	1.86	1.78	–	–	1.28	1.34
0.5	–	–	–	–	1.39	1.39
0.25	–	–	–	–	1.22	1.21
0.125	–	–	–	–	1.16	1.16

fold increase (%). This method represents the relative effect of tested compound in contrast to any standard antibiotic/drug/other compound and the positive value represents the better actions of tested compound. Conversely, the negative value of fold increase indicates that the tested compound is less effective against particular bacteria than standard antibiotic/drug/other compound at the same concentration. In our study, the values of fold increase (%) for NiO nanoparticles with respect to tetracycline, gentamicin and bulk NiO against *S. aureus* and *E. coli* at different concentrations are presented in Table 3. The positive values of fold increase of NiO nanoparticles w.r.t. tetracycline, gentamicin and bulk NiO against *S. aureus* and *E. coli* were evident at all the concentrations in present study (Table 3).

It is well known phrase in biomedical sciences that the prevention is better than cure, so applying/coating of NiO nanoparticles on large active surface area, on cellulose bandages, uniforms, bed linen, medical equipment etc. may be useful preventive measures to control bacterial/microbial infections and will make a considerable input in reducing bacterial contamination, mortality, treatment of costs etc. In recent years, applications of nanotechnology in the biomedical field have given many beneficial results. In the biomedical field, various devices coated with antimicrobial nanomaterials such as heart valves, catheters, and dental implants have been used and in these devices there is delay or inhibition in the adhesion and growth of bacteria such as *Streptococcus mutans*, *S. epidermis*, and *E. coli*. [45]. The application of nanoparticles of different metals and their oxides like zinc, silver, copper or titanium, etc. has increased because of their bactericidal activity against both Gram-positive and Gram-negative bacterial strains. Silver nanoparticles are commonly and widely employed for different purposes like bactericides in catheters, burn wound care, and in the dental practice [46]. But, there are some issues related to the biological safety of silver nanoparticles and pigmentation effect of silver nanoparticles on teeth [47,48]. NiO is cheaper than silver and NiO nanoparticles may replace the silver nanoparticles in the coming years in various application. Additionally, metals oxide nanoparticles are considered better antimicrobial pharmaceuticals due to their durability, high stability, and low mammalian cell toxicity in comparison to organic nanoparticles [49]. The promising antimicrobial actions shown by different metals oxide nanoparticles, including NiO nanoparticles, could have a several therapeutic applications in biomedical field and their use can also be extended to food industry, water purification, textile industry, paint industry, sewage treatments, etc.

TABLE 3. Fold increase (%) of NiO nanoparticles with respect to (w.r.t.) tetracycline, gentamicin and bulk NiO against *S. aureus* and *E. coli* at different concentrations

Conc. (μg/ml)	Fold increase (%) w.r.t. Tetracycline		Fold increase (%) w.r.t. Gentamicin		Fold increase (%) w.r.t. bulk NiO	
	S. aureus	*E. coli*	*S. aureus*	*E. coli*	*S. aureus*	*E. coli*
128.0	13.53	25.59	60.64	79.05	39.17	44.02
64.0	19.13	33.33	66.06	91.04	34.31	49.71
32.0	27.27	49.40	71.43	99.21	29.23	55.90
16.0	49.04	57.04	85.71	112.38	28.57	49.66
8.0	60.87	84.21	105.56	125.81	28.32	56.72
4.0	100.00	104.17	138.20	130.59	47.22	53.13
2.0	113.33	94.25	125.88	101.19	42.22	37.40
1.0	86.21	77.65	–	–	27.56	33.63
0.5	–	–	–	–	38.60	39.42
0.25	–	–	–	–	22.22	21.21
0.125	–	–	–	–	15.69	16.48

4. Conclusions

In conclusion, the NiO nanoparticles were better antibacterial agents than their bulk form and they also seemed better than the standard antibiotics tetracycline and gentamicin, particularly at low concentrations, against both gram positive (*S. aureus*) and gram negative (*E. coli*) bacteria. In future, the strong antibacterial potentials of NiO nanoparticles may be extended its applications in different fields.

Acknowledgements

The authors are thankful to Department of Chemistry and Department of Biotechnology, University of Jammu, for providing necessary facilities and support for conducting present study. The authors also acknowledge the support of SAIF STIC (Kochi), SAIF Chandigarh, CIL Chandigarh for providing the facilities for characterization.

References

[1] Hawkey P.M. The growing burden of antimicrobial resistance. *J. Antimicrob. Chemother*., 2008, **62**, P. i1–i9.

[2] Livermore D.M. The 2018 Garrod lecture: Preparing for the black swans of resistance. *J. Antimicrob. Chemother.*, 2018, **73**, P. 2907–2915.

[3] Sugden R., Kelly R., Davies S. Combatting antimicrobial resistance globally. *Nat. Microbiol.*, 2016, **1**, P. 16187.

[4] O'Neill J. Antimicrobial Resistance: Tackling a Crisis for the Health and Wealth of Nations. *Rev. Antimicrob. Re.*, 2014.

[5] Galib M., Barve M., Mashru C, Jagtap B.J., Patgiri P.K., Prajapati. Therapeutic potentials of metals in ancient India: A review through *Charaka Samhita*. *J. Ayurveda Integr. Med.*, 2011, **2**, P. 55.

[6] Azam A., Ahmed A.S., Oves M., Khan M.S., Habib S.S., Adnan Memic. Antimicrobial activity of metal oxide nanoparticles against Gram-positive and Gram-negative bacteria: a comparative study. *Int. J. Nanomed.*, 2012, **7**, P. 6003–6009.

[7] Bhushan M., Kumar Y, Periyasamy L., Viswanath A.K. Antibacterial applications of α-Fe_2O_3/Co_3O_4 nanocomposites and study of their structural, optical, magnetic and cytotoxic characteristics. *App. Nanosci.*, 2018, **8**, P. 137–153.

[8] Ebadi M., Zolfaghari M.R., Aghaei S.S., Zargar M., Shafiei M., Zahiri H.S., Noghabi K.A. A bio-inspired strategy for the synthesis of zinc oxide nanoparticles (ZnO NPs) using the cell extract of cyanobacterium Nostoc sp. EA03: from biological function to toxicity evaluation. *RSC Adv.*, 2019, **9**, P. 23508.

[9] Khadar Y.A.S., Balamurugan A., Devarajan V.P., Subramanian R., Kumar S.D. Synthesis, characterization and antibacterial activity of cobalt doped cerium oxide (CeO_2:Co) nanoparticles by using hydrothermal method. *J. Mater. Res. Technol.*, 2019, **8**(**1**), P. 267–274.

[10] Parham S., Wicaksono D.H.B., Bagherbaigi S., Lee S.L., Nur H. Antimicrobial treatment of different metal oxide nanoparticles: a critical review. *J. Chin. Chem. Soc.*, 2016, **63**, P. 385–393.

[11] Gupta V., Kant V., Sharma A.K., Sharma M. Comparative assessment of antibacterial efficacy for cobalt nanoparticles, bulk cobalt and standard antibiotics: A concentration dependant study. *Nanosyst. Phys. Chem. Math.*, 2020, **11**(1), P. 78–85.

[12] Preethika R.K., Ramya R., Ganesan M., Nagaraj S., Pandian K. Synthesis and characterization of neomycin functionalized chitosan stabilized silver nanoparticles and study its antimicrobial activity. *Nanosyst. Phys. Chem. Math.*, 2016, **7**(4), P. 759–764.

[13] Deraz N.M., Selim M.M., Ramadan M. Processing and properties of nanocrystalline Ni and NiO catalysts. *Mater. Chem. Phys.*, 2009, **113**, P. 269–275.

[14] Meyer M., Albrecht-Gary A.M., Dietrich-Buchecker C.O., Sauvage J.P. Dicopper(I) trefoil knots: Topological and structural effects on the demetalation rates and mechanism. *J. Am. Chem. Soc.*, 1997, **119**, P. 4599–4607.

[15] Li Y.G., Shi D.H., Zhu H.L., Yan H., Ng S.W. Transition metal complexes (M=Cu, Ni and Mn) of Schiff-base ligands: syntheses, crystal structures, and inhibitory bioactivities against urease and xanthine oxidase. *Inorg. Chim. Acta.*, 2007, **360**(9), P. 2881–2889.

[16] Perez C., Pauli M., Bazerque P. An antibiotic assay by agar-well diffusion method. *Acta Biol. Med. Exp.*, 1990, **15**, P. 113–115.

[17] Rizwan W., Young-Soon K., Amrita M., Soon-Il Y., Hyung-Shik S. Formation of ZnO micro-flowers prepared via solution process and their antibacterial activity. *Nanoscale Res. Lett.*, 2010, **5**, P. 1675–1681.

[18] Yoon K.Y., Byeon J.H., Park J.H., Hwang J. Susceptibility constants of *Escherichia coli* and *Bacillus subtilis* to silver and copper nanoparticles. *Sci. Total Environ.*, 2007, **373**, P. 572–575.

[19] Ruparelia J.P., Chatterjee A.K., Duttagupta S.P., Mukherji S. Strain specificity in antimicrobial activity of silver and copper nanoparticles. *Acta Biomater.*, 2008, **4**, P. 707–716.

[20] Mazumder A., Davis J., Rangari V., Curry M. Synthesis, characterization, and applications of dendrimer-encapsulated zero-valent Ni nanoparticles as antimicrobial agents. *Nanomater.*, 2013,Article ID 843709, 9 pages.

[21] Khalil A.T., Ovais M., Ullah I., Ali M., Shinwari Z.K., Hassan D., Maaza M. *Sageretia thea* (Osbeck.) modulated biosynthesis of NiO nanoparticles and their *in vitro* pharmacognostic, antioxidant and cytotoxic potential. *Artif. Cells Blood Substit. Biotechnol.*, 2018, **46**(4), P. 838–852.

[22] Srihasam S., Thyagarajan K., Korivi M., Lebaka V.R., Mallem S.P.R. Phytogenic generation of NiO nanoparticles using *Stevia* leaf extract and evaluation of their *in-vitro* antioxidant and antimicrobial properties. *Biomolecules*, 2020, **10**, P. 89.

[23] Helan V., Prince J.J., Al-Dhabi N.A., Arasu M.V., Ayeshamariam A., Madhumitha G., Roopan S.M., Jayachandran M.. Neem leaves mediated preparation of NiO nanoparticles and its magnetization, coercivity and antibacterial analysis. *Results Phys.*, 2016, **6**, P. 712–718.

[24] Abbasi B.A., Iqbal J., Mahmood T., Ahmad R., Kanwal S., Afridi S. Plant-mediated synthesis of nickel oxide nanoparticles (NiO) via *Geranium wallichianum*: characterization and different biological applications. *Mater. Res. Express*, 2019, **6**, P. 0850a7.

[25] Bhat S.A., Zafar F., Mondal A.H., Kareem A., Mirza A.U., Khan S., Mohammad A., Haq Q.R., Nishat N. Photocatalytic degradation of carcinogenic Congo red dye in aqueous solution, antioxidant activity and bactericidal effect of NiO nanoparticles. *J. Iran. Chem. Soc.*, 2019.

[26] Ahamed M., Alhadlaq H.A., Khan M.M.A., Karuppiah P., Al-Dhabi N.A. Synthesis, characterization, and antimicrobial activity of copper oxide nanoparticles. *J. Nanomater.*, 2014, Article ID 637858, 4 pages.

[27] Hoseinzadeh E., Makhdoumi P., Taha P., Hossini H., Stelling J., Kamal M.A., Ashraf G.M. A review on nano-antimicrobials: Metal nanoparticles, methods and mechanisms. *Curr. Drug Metab.*, 2017, **18**(2), P. 120–128.

[28] Djurisic A.B., Leung Y.H., Ng A.M., Xu X.Y., Lee P.K., Degger N., Wu R.S. Toxicity of metal oxide nanoparticles: mechanisms, characterization, and avoiding experimental artefacts. *Small*, 2015, **11**(1), P. 26–44.

[29] Stoimenov P.K., Klinger R.L., Marchin G.L., Klabunde K.J. Metal oxide nanoparticles as bactericidal agents. *Langmuir*, 2002, **18**, P. 6679–6686.

[30] Rakshit S., Ghosh S., Chall S., Mati S.S., Moulik S.P., Bhattacharya S.C. Controlled synthesis of spin glass nickel oxide nanoparticles and evaluation of their potential antimicrobial activity: A cost effective and eco friendly approach. *RSC Adv.*, 2013, **3**, P. 19348–19356.

[31] Helen S.M., Rani H.E. Characterization and antimicrobial study of nickel nanoparticles synthesized from *Dioscorea* (elephant yam) by green route. *Int. J. Sci. Res.*, 2015, **4**, P. 216–219.

[32] Ayeshamariam A., Sankaracharyulu G.V., Kashif M., Hussain S., Bououdina M., Jayachandran M. Antibacterial activity studies of Ni and SnO2 loaded Chitosan beads. *Mater. Sci. Forum*, 2015, **833**, P. 110–112.

[33] Jesudoss S.K., Vijaya J.J., Clament N., Selvam S., Kombaiah K., Sivachidambaram M., Adinaveen T., Kennedy L.J. Effects of Ba doping on structural, morphological, optical, and photocatalytic properties of self-assembled ZnO nanosphere. *Clean Technol. Environ. Policy*, 2016, **18**, P. 729–741.

[34] Basak G., Das D., Das N. Dual role of acidic diacetate sophorolipid as biostabilizer for ZnO nanoparticles synthesis and biofunctionalizing agent against *Salmonella enterica* and *Candida albicans*, *J. Microbiol. Biotechnol.*, 2014, **24**, P. 87–96.

[35] Burello E., Worth A.P. A theoretical framework for predicting the oxidative stress potential of oxide nanoparticles. *Nanotoxicology*, 2011, **5**, P. 228–235.

[36] Robison S.H., Cantoni O., Heck J.D., Costa M. Soluble and insoluble nickel compounds induce DNA repair synthesis in cultured mammalian cells. *Cancer Lett.*, 1983, **17**(3), P. 273–279.

[37] Oller A.R. Respiratory carcinogenecity assessment of soluble nickel compounds. *Environ. Health Perspect.*, 2002, **110**(5), P. 841–844.

[38] Schwerdtle T., Hartwig A. Bioavailability and genotoxicity of soluble and particulate nickel compounds in cultured human lung cells. *Materwiss. Werksttech.*, 2006, **37**(6), P. 521–525.

[39] Jan T., Iqbal J., Ismail M., Badshah N., Mansoor Q., Arshad A., Ahkam Q. Synthesis, physical properties and antibacterial activity of metal oxides nanostructures. *Mat. Sci. Semicon. Proc.*, 2014, **21**, P. 154–160.

[40] Kalyani R.L., Venkatraju J., Kollu P., Rao N.H., Pammi S.V.N. Low temperature synthesis of various transition metal oxides and their antibacterial activity against multidrug resistance bacterial pathogens. *Korean J. Chem. Eng.*, 2015, **32**(5), P. 911–916.

[41] Huh A.J., Kwon Y.J. Nanoantibiotics: A new paradigm for treating infectious diseases using nanomaterials in the antibiotics resistant era. *J. Control. Release*, 2011, **156**(2), P. 128–145.

[42] Ling D., Hyeon T. Chemical design of biocompatible iron oxide nanoparticles for medical applications. *Small*, 2013, **9**, P. 1450–1466.

[43] Mahapatra O., Bhagat M., Gopalakrishnan C., Arunachalam K.D. Ultrafine dispersed CuO nanoparticles and their antibacterial activity. *J. Exp. Nanosci.*, 2008, **3**, P. 185–193.

[44] Selvarani M., Prema P. Evaluation of antibacterial efficacy of chemically synthesized copper and zerovalent iron nanoparticles. *Asian J. Pharm. Clin. Res.*, 2013, **6**, P. 223–227.

[45] Wang L., Hu C., Shao L. The antimicrobial activity of nanoparticles: Present situation and prospects forthe future. *Int. J. Nanomed.*, 2017, **12**, P. 1227.

[46] Kim J.S., Kuk E., Yu K.N., Kim J.H., Park S.J., Lee H.J., Kim S.H., Park Y.K., Park Y.H., Hwang C.Y., Kim Y.K., Lee Y.S., Jeong D.H., Cho M.H. Antimicrobial effects of silver nanoparticles. *Nanomed.*, 2007, **3**, P. 95–101.

[47] Sondi I., Salopek-Sondi B. Silver nanoparticles as antimicrobial agent: a case study on *E. coli* as a model for Gram-negative bacteria. *J. Colloid. Interf. Sci.*, 2004, **275**, P. 177–182.

[48] Jain P., Pradeep T. Potential of silver nanoparticle-coated polyurethane foam as an antibacterial water filter. *Biotechnol. Bioeng.*, 2005, **90**, P. 59–63.

[49] Deravi L.F., Swartz J.D., Wright D.W. The biomimetic synthesis of metal oxide nanomaterials. Wiley, 2010.

NANOSYSTEMS: PHYSICS, CHEMISTRY, MATHEMATICS, 2020, 11 (2), P. 246–251

Influence of hydrothermal synthesis conditions on the composition of the pyrochlore phase in the Bi_2O_3–Fe_2O_3–WO_3 system

M. S. Lomakin[1,2], O. V. Proskurina[1,2], V. V. Gusarov[1]
[1]Ioffe Institute, 26, Politekhnicheskaya St., 194021, St. Petersburg, Russia
[2]St. Petersburg State Institute of Technology, 26, Moskovsky pr, 190013, St. Petersburg, Russia
lomakinmakariy@gmail.com

DOI 10.17586/2220-8054-2020-11-2-246-251

The paper deals with a study of the effect which the hydrothermal fluid pH has on the formation of a pyrochlore-structured phase in the Bi_2O_3–Fe_2O_3–WO_3 system. It was shown that at pH of 1 and 8, the formation of pyrochlore-structured phase particles with crystallite sizes of 38 and 118 nm, respectively, is accompanied by the formation of the Bi_2WO_6 compound with the Aurivillius phase structure. At pH values from 2 to 7, only pyrochlore-structured nanocrystalline particles with a variable composition are formed. Under these conditions, the dependence of the average size of crystallites of the pyrochlore-structured phase particles on pH is extreme, as the size increases from $\sim$ 67 nm at pH 2 up to $\sim$ 126 nm at pH 5 and then decreases to $\sim$ 102 nm at pH 7. The samples obtained at pH 3–4 have a composition that is the closest to that specified for the synthesis. When pH increases up to 10, there forms a non-single-phase product that contains the Bi_2WO_6 phase and δ-Bi_2O_3-based phase.

Keywords: hydrothermal synthesis, pyrochlore phase, nanocrystals, crystallite size.

Received: 14 January 2020

Revised: 28 February 2020

1. Introduction

As a rule, the conditions of hydrothermal synthesis (HTS), significantly affect the composition, structure, and size of particles and crystallites of the synthesized products [1–7]. Important factors in this case are the sequence and rate of reagents mixing and the pH of the hydrothermal fluid [8, 9]. Changes in pH usually significantly affect the state and composition of phases resulting from hydrothermal treatment [10, 11]. Another important factor is the effect of pH on the change in the structure of the double electric layer on the surface of solid phase particles, which, in turn, can determine the crystallite growth mechanisms, the possibility and rate of particles aggregation, their shape and size [12, 13]. The pH of the medium has a particularly strong effect on phase equilibria in the systems containing W^{6+} ions, which are characterized not only by changes in the composition and structure of aqueous complexes with a change in pH, but also by the condensation of acid residues into a sparingly soluble isopolyacid in a highly acidic media [14]. Other examples are bismuth (III) and iron (III) hydroxides, the degree of hydration of which depends on the pH of the medium [15,16], and the pH at the onset of hydrates formation varies from $\sim$ 1.5 for iron hydroxide up to $\sim$ 3.2 for bismuth hydroxide [16]. The HTS method application in [17] has for the first time resulted in producing and characterizing a pyrochlore-structured phase with the variable composition $Bi_{y+0.67\delta}Fe_yW_{2-y}O_6O'_\delta$ (BFWO) in two-phase mixtures. The preparation of BFWO-based single-phase samples with a specified composition has encountered a number of synthesizing difficulties that require a systematic study of the influence of phase formation conditions on the composition and structure of the target product.

This work is aimed at establishing optimal pH values of the hydrothermal fluid for the synthesis of BFWO nanocrystalline phases with a specified composition.

2. Materials and methods

2.1. Synthesis section

The molar ratio of the reagents was chosen based on the stoichiometry of the target product, i.e., a pyrochlore-structured phase with the $Bi_{0.5}Fe_{0.36}WO_{4.29}$ composition. The synthesis was carried out in several stages. 2 mmol of crystalline bismuth (III) nitrate pentahydrate, $Bi(NO_3)_3{\cdot}5H_2O$ (puriss. spec.), were dissolved in 30 ml of 1M HNO_3 (puriss. spec.) by stirring with a magnetic stirrer until complete dissolution, and 1.44 mmol of crystalline iron(III) nitrate nonahydrate, $Fe(NO_3)_3{\cdot}9H_2O$ (pur.), were added to the resulting bismuth nitrate solution. The dissolution of the iron salt was very fast. 4 mmol of crystalline hydrate (VI) of sodium tungstate, $Na_2WO_4{\cdot}2H_2O$ (p.a.), were dissolved in 25 ml of distilled water and then added dropwise to the continuously stirred solution of bismuth and iron salt. After an hour of continuous stirring of the resulting suspension, NaOH 4M solution was added dropwise to achieve pH 1 (without adding NaOH), 2, 3, ..., 8, 10. After stirring for some more time, the resulting suspension was transferred to a separate Teflon crucible (80% filling) and placed in a steel autoclave, which was put in a furnace heated up to 200°C. Twenty-four hours later, the autoclave was removed from the furnace and cooled at room temperature. The obtained precipitates were separated in a centrifuge, rinsed with distilled water and dried at 80°C for 24 hours.

2.2. Characterization

The X-ray diffraction (XRD) patterns were recorded at 295 K on a Rigaku SmartLab 3 powder diffractometer ($Co_{K\alpha}$ emission) with the K_β filter in the $2\theta = 15$ to 71° angle range and at a speed of 3°/min. The average size of crystallites was calculated by the Halder–Wagner method. The elemental bulk composition, the morphology and size of the particles were determined using a Tescan Vega 3 SBH scanning electron microscope with an Oxford Instruments X-ray microanalysis attachment. The elemental composition was determined with a 1 mass. % error.

3. Results and discussions

3.1. Obtained samples composition

Bulk compositions of the obtained samples are presented in Table 1. An increase in the hydrothermal fluid pH significantly affects changes in the obtained samples bulk composition.

TABLE 1. Obtained samples bulk composition

Synthesized composition		Bi, at. %	Fe, at. %	W, at. %
		26.9	19.4	53.7
pH	1	28.5	17.2	54.3
	2	27.2	18.5	54.3
	3	26.7	19.4	53.9
	4	26.5	19.7	53.8
	5	27.6	20.1	52.3
	6	30.6	20.0	49.4
	7	32.9	22.6	44.5
	8	37.1	22.9	40.0
	10	45.2	35.9	18.9

The exceptions are the single-phase samples obtained at pH 2, 3, and 4, in which the bismuth/tungsten molar ratio is constant (Bi/W ~ 0.5), and only the amount of iron changes, slightly increasing with the increasing pH. The single-phase samples obtained at pH 5, 6, and 7, demonstrate an increase in the amount of bismuth and iron along with the increasing pH, while the amount of tungsten in the BFWO structure decreases. These facts provide evidence for the presence of a certain region of compositions in the ternary diagram of Bi_2O_3–Fe_2O_3–WO_3, in which the BFWO phase exists, which is thus a phase of variable composition, since a significant change in the elements ratio in the BFWO phase does not lead to the appearance of other phases. It should be noted that the compositions of the samples obtained at pH 3 and 4 correspond to the composition specified for the synthesis to the greatest extent. The bulk compositions of the samples obtained at pH 1, 8, and 10 are found in the non-single-phase region.

3.2. XRD analysis

The crystal structure and phase composition of the obtained samples were analyzed by X-ray powder diffraction technique. The XRD patterns of non-single-phase and single-phase samples are presented in Fig. 1 and Fig. 2, respectively. The XRD pattern of a sample obtained at pH 1 (Fig. 1) shows the presence of the BFWO phase (CSD 1961005) with the average size of crystallites of $\sim$ 38 nm, and of the Bi_2WO_6 phase (ICSD code 73-1126).

Only the BFWO phase is present in the samples obtained at pH 2, 3 and 4 (Fig. 2). The unit cell parameter a of the BFWO phase for these samples varies only slightly and averages 10.3341(5) Å. No other crystalline phases, except for BFWO, were present also in the XRD patterns of the samples obtained at pH 5, 6, and 7 (Fig. 2). The sample obtained at pH 8 mainly consists of the BFWO phase with an average crystallite size of $\sim$ 118 nm, with a small amount of the Bi_2WO_6 phase (Fig. 1). The local microanalysis data for the BFWO phase in the sample obtained at pH 8 does not practically differ from the bulk composition of the sample, since the mass fraction of the Bi_2WO_6 phase in this sample is negligibly small. In this regard, the BFWO phase composition in this sample can be taken equal to the bulk composition of the sample, although with some reservation. The unit cell parameter a of the BFWO phase in the samples synthesized at pH 5, 6, 7, and 8 of the hydrothermal fluid increases with the increasing pH from

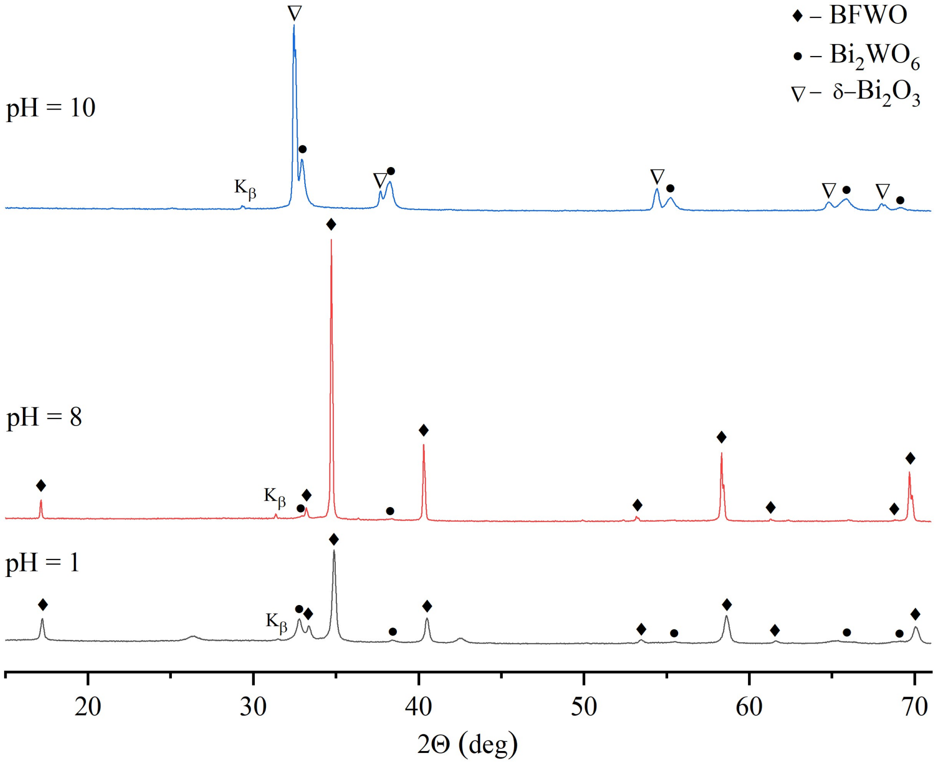

FIG. 1. XRD patterns of the non-single-phase samples obtained at different pH values

10.3394(8) Å (pH 5) up to 10.3848(6) Å (pH 8). The data on the BFWO phase compositions and unit cell parameter are consistent with the data obtained in [17], which state that the unit cell parameter increases with an increase in the amount of bismuth in the pyrochlore structure. According to the X-ray diffraction data on the sample obtained at pH 10 (Fig. 1), two crystalline phases coexist in it, i.e., the Aurivillius-structured Bi_2WO_6 and the δ-Bi_2O_3-based phase (ICSD code 16-654). According to the local microanalysis data, the composition of the δ-Bi_2O_3-based phase is $Bi_{3.35}Fe_{0.68}WO_{9.05}$.

Figure 3 presents the BFWO phase crystallite size as the extreme function of the hydrothermal fluid pH.

3.3. Obtained samples morphology

The SEM data are presented in Fig. 4. The sample obtained at pH 1 consists of particles 100–150 nm in size; individual phases in this sample are morphologically indistinguishable (Fig. 4a). The BFWO phase particles in the samples obtained at pH 2, 3, 4, 6, 7 and 8 have a similar morphology (Fig. 4b). These are spherical agglomerates consisting of crystallites; the size of both depends on the hydrothermal fluid pH. In the sample obtained at pH 5, the agglomerates of the BFWO phase are significantly enlarged and start acquiring the octahedral shape (Fig. 4c). In the sample obtained at pH 8 (Fig. 4d), the Aurivillius phase-structured Bi_2WO_6 compound coexisting with BFWO is represented by spherical agglomerates with a size of $\sim 5\ \mu$m.

According to the data obtained by SEM in backscattered electrons (Fig. 4f), three phases coexist in the sample obtained at pH 10 (Fig. 4e). The δ-Bi_2O_3-based and the Bi_2WO_6 phases are crystalline, since they differ in the XRD pattern of this sample. The particles of the δ-Bi_2O_3-based phase in the sample obtained at pH 10 are regular octahedrons with a size of $\sim 10\ \mu$m, but they are not single crystals, since the peaks of this phase have a significant broadening in the XRD pattern (Fig. 1). Particles of the Bi_2WO_6 phase in this sample are represented by fused plates with no pronounced agglomeration, with an average crystallite size of about 23 nm. The third phase in the sample obtained at pH 10, (marked as XR am-us in Fig. 4f), is X-ray amorphous and, according to the local microanalysis, has the composition $Bi_{2.61}Fe_{2.84}WO_{11.18}$, i.e., it is significantly richer in iron, which is also seen from the phase contrast (Fig. 4f).

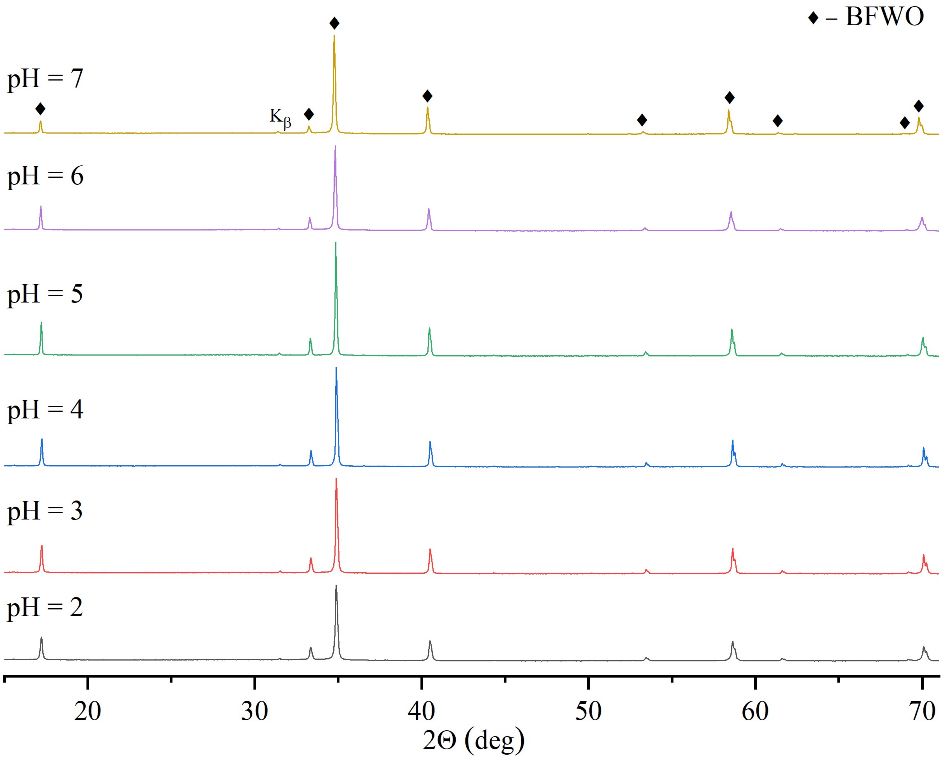

FIG. 2. XRD patterns of the single-phase samples obtained at different pH values

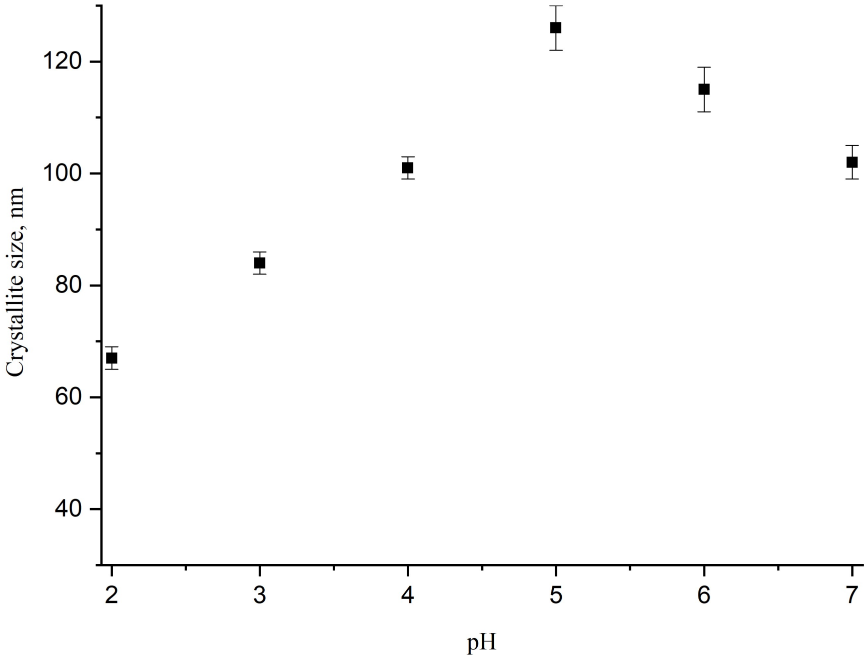

FIG. 3. BFWO phase crystallite size as the function of the hydrothermal fluid pH

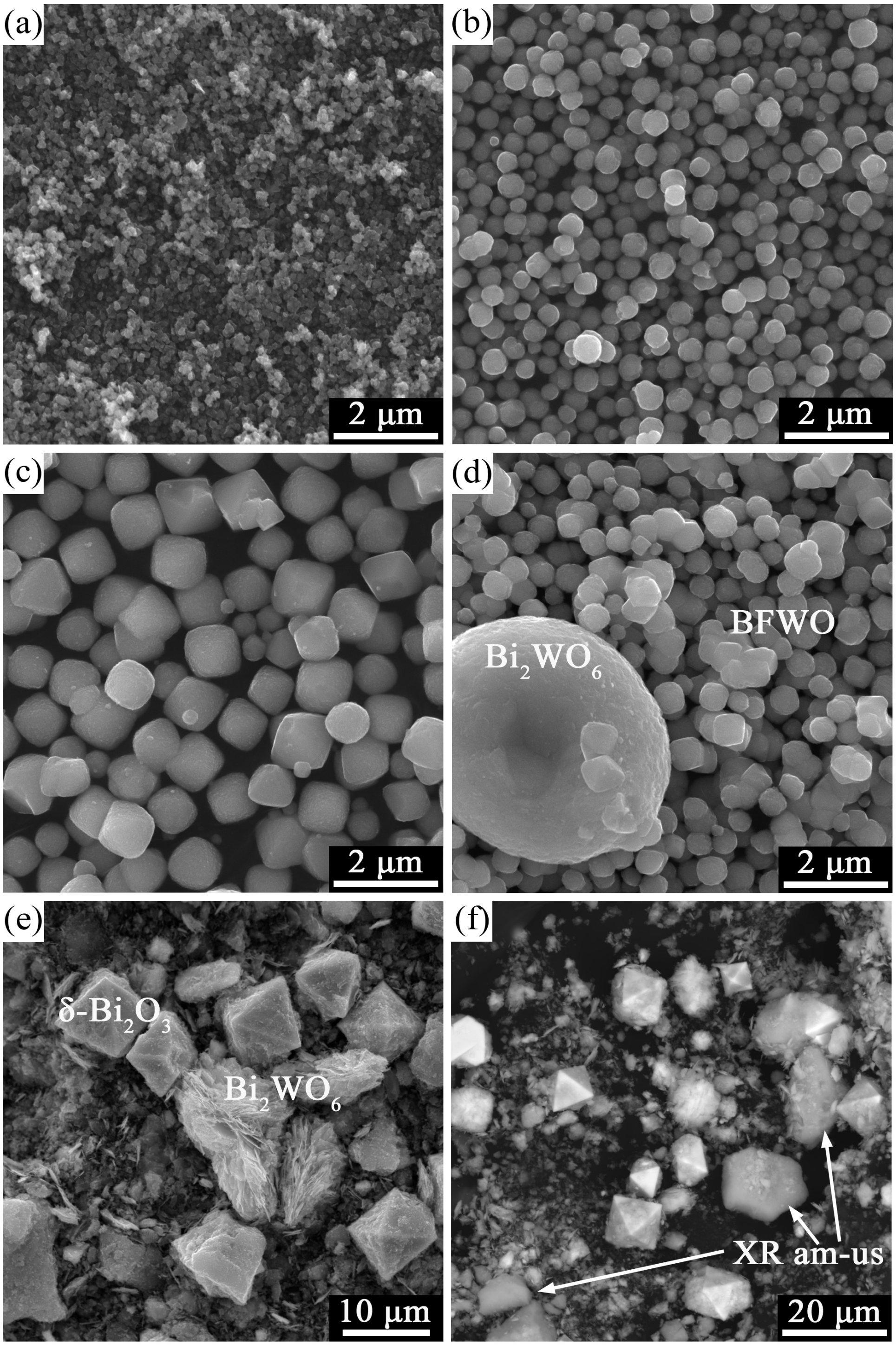

FIG. 4. SEM of the samples obtained at pH 1–(a), 3–(b), 5–(c), 8–(d), 10–(e) and 10–(BSE-detector)–(f)

4. Conclusion

A study of the effect that the hydrothermal fluid pH has on the BFWO phase formation under hydrothermal conditions showed that the phase state and composition of the individual phases in the HTS products in the water-salt system containing all three elements, i.e., Bi^{3+}, Fe^{3+}, and W^{6+}, significantly depend on the pH. It was found that the hydrothermal fluid pH significantly affects both the size of the BFWO phase crystallites and the size of the agglomerates consisting of them. It was shown for the studied initial composition that it is possible to obtain the BFWO phase with a composition specified for the synthesis only when the hydrothermal fluid pH equals 3–4.

Acknowledgments

XRD studies, SEM and EDXMA of samples were performed employing the equipment of the Engineering Center of the St. Petersburg State Institute of Technology.

References

[1] Almjasheva O.V., Smirnov A.V., Fedorov B.A., Tomkovich M.V., Gusarov V.V. Structural features of ZrO_2–Y_2O_3 and ZrO_2–Gd_2O_3 nanoparticles formed under hydrothermal conditions. *Russ. J. Gen. Chem.*, 2014, **84**(5), P. 804–809.

[2] Popkov V.I., Almjasheva O.V. Formation mechanism of $YFeO_3$ nanoparticles under the hydrothermal condition. *Nanosyst.:Phys. Chem. Math.*, 2014, **5**(5), P. 703–708.

[3] Almjasheva O.V., Gusarov V.V. Hydrothermal synthesis of nanosized and amorphous alumina in the ZrO_2-Al_2O_3-H_2O system. *Russ. J. Inorg. Chem.*, 2007, **52**(8), P. 1194–1200.

[4] Al'myasheva O.V., Korytkova E.N., Maslov A.V., Gusarov V.V. Preparation of Nanocrystalline Alumina under Hydrothermal Conditions. *Inorg. Mater.*, 2005, **41**(5), P. 460–467.

[5] Pozhidaeva O.V., Korytkova E.N., Romanov D.P., Gusarov V.V. Formation of ZrO_2 Nanocrystals in Hydrothermal Media of Various Chemical Compositions. *Russ. J. Gen. Chem.*, 2002, **72**(6), P. 849–853.

[6] Pozhidaeva O.V., Korytkova E.N., Drozdova I.A., Gusarov V.V. Phase state and particle size of ultradispersed zirconium dioxide as influenced by condition of hydrothermal synthesis. *Russ. J. Gen. Chem.*, 1999, **69**(8), P. 1219–1222.

[7] Kuznetsova V.A., Almjasheva O.V., Gusarov V.V. Influence of microwave and ultrasonic treatment on the formation of $CoFe_2O_4$ under hydrothermal conditions. *Glass Phys. Chem.*, 2009, **35**(2), P. 205–209.

[8] Proskurina O.V., Tomkovich M.V., Bachina A.K., Sokolov V.V., Danilovich D.P., Panchuk V.V., Semenov V.G., Gusarov V.V. Formation of Nanocrystalline $BiFeO_3$ under Hydrothermal Conditions. *Russ. J. Gen. Chem.*, 2017, **87**(11), P. 2507–2515.

[9] Almjasheva O.V., Krasilin A.A., Gusarov V.V. Formation mechanism of core-shell nanocrystals obtained via dehydration of coprecipitated hydroxides at hydrothermal conditions. *Nanosyst.: Phys. Chem. Math.*, 2018, **9**(4), P. 568–572.

[10] Krasilin A.A. Khrapova E.K. Effect of hydrothermal treatment conditions on formation of nickel hydrogermanate with platy morphology. *Russ. J. Appl. Chem.*, 2017, **90**(1), P. 22–27.

[11] Wang Y., Zhang S., Zhong Q., Zeng Y., Ou M., Cai W. Hydrothermal Synthesis of Novel Uniform Nanooctahedral $Bi_3(FeO_4)(WO_4)_2$ Solid Oxide and Visible-Light Photocatalytic Performance. *Ind. Eng. Chem. Res.*, 2016, **55**(49), P. 12539–12546.

[12] Bugrov A.N., Almjasheva O.V. Effect of hydrothermal synthesis conditions on the morphology of ZrO_2 nanoparticles. *Nanosyst.: Phys. Chem. Math.*, 2013, **4**(6), P. 810–815.

[13] Almjasheva O.V., Lomanova N.A., Popkov V.I., Proskurina O.V., Tugova E.A., Gusarov V.V. The minimum size of oxide nanocrystals: phenomenological thermodynamic vs crystal-chemical approaches. *Nanosyst.: Phys. Chem. Math.*, 2019, **10**(4), P. 428–437.

[14] Matveichuk Yu.V. FTIR-spectroscopic investigation of sodium tungstate and sodium molybdate solutions in wide range of H. *Izv. Vyssh. Uchebn. Zaved. Khim. Khim. Tekhnol.*, 2017, **60**(1), P. 56–63.

[15] Cornell R. M., Giovanoli R., Schneider W. Review of the hydrolysis of iron (III) and the crystallization of amorphous iron (III) hydroxide hydrate. *J. Chem. Tech. Biotechnol.*, 1989, **46**, P. 115–134.

[16] Yukhin Yu.M., Mikhailov Yu.I. Chemistry of bismuth compounds and materials. *SB RAS Publishing House*, Novosibirsk, 2001, 360 p.

[17] Lomakin M.S., Proskurina O.V., Danilovich D.P., Panchuk V.V., Semenov V.G., Gusarov V.V. Hydrothermal Synthesis, Phase Formation and Crystal Chemistry of the pyrochlore/Bi_2WO_6 and pyrochlore/α-Fe_2O_3 Composites in the Bi_2O_3-Fe_2O_3-WO_3 System. *J. Solid State Chem.*, 2020, **282**, 121064.

NANOSYSTEMS: PHYSICS, CHEMISTRY, MATHEMATICS, 2020, 11 (2), P. 252–259

Synthesis of $GdFeO_3$ nanoparticles via low-temperature reverse co-precipitation: the effect of strong agglomeration on the magnetic behavior

Y. Albadi[1,2], K. D. Martinson[3], A. V. Shvidchenko[3], I. V. Buryanenko[4], V. G. Semenov[5], V. I. Popkov[3]

[1]Saint Petersburg State Institute of Technology, St. Petersburg, 190013, Russia
[2]Al-Baath University, Homs, 77, Syria
[3]Ioffe Institute, St. Petersburg, 194021, Russia
[4]Peter the Great St. Petersburg Polytechnic University, St. Petersburg, 195251, Russia
[5]Saint Petersburg State University, Petergof, St. Petersburg, 198504, Russia
albadi.yamen@gmail.com

PACS 81.20.Fw, 61.46.+w, 75.20.-g **DOI 10.17586/2220-8054-2020-11-2-252-259**

Gadolinium orthoferrite ($GdFeO_3$) seems to have potential as a dual-modal contrast agent for magnetic resonance imaging (MRI), thus its preparation in the form of ultrafine superparamagnetic nanoparticles is currently of great interest. In this work, nanocrystalline $GdFeO_3$ was successfully synthesized by the heat treatment (750 °C, 4 h) of gadolinium and iron(III) hydroxides reversely co-precipitated at low temperature (0 °C). Initial and resulting powders were analyzed by EDX, SEM, PXRD, Mössbauer spectroscopy, vibration magnetometry, etc. Gadolinium orthoferrite was formed as isometric nanocrystals with an average size of 23 ± 3 nm, which were strongly agglomerated into clusters of about 200 nm in diameter. It was shown that the individual $GdFeO_3$ nanocrystals are superparamagnetic, but in the cluster form, they exhibit a collective weak ferromagnetic behavior. After ultrasonic-assisted disintegration of $GdFeO_3$ to a colloidal solution form, these clusters remained stable due to their strong agglomeration and low zeta potential value of 1 mV. Thus, it is concluded that the further use of the synthesized $GdFeO_3$ nanoparticles as a basis of MRI contrast agents will be possible only after the suppression of their clustering.

Keywords: gadolinium orthoferrite; nanoparticles; colloidal solutions; magnetic resonance imaging; contrast agents.

Received: 3 April 2020

1. Introduction

The action of contrast agents for magnetic resonance imaging (MRI) is based on the reduction of the longitudinal (T_1) and transverse (T_2) relaxation times of water protons [1]. Shortening the longitudinal relaxation time causes increased signal intensity on T_1-weighted images and the affected regions appear brighter (positive contrast agents), whereas shortening the transverse relaxation time causes decreased signal intensity on T_2-weighted images and the affected regions appear darker (negative contrast agents) [2]. Almost all MRI contrast agents affect both T_1 and T_2 relaxation times, but their effect is usually more pronounced for either the positive or the negative mode of MRI diagnostics; such contrast agents are called single-modal [3]. However, due to the peculiarities of their composition and structure, some substances are capable of exhibiting a hybrid contrast effect and can affect both positive and negative MRI images [4]. Dual-modal (hybrid) contrast agents combine the advantages of single-modal contrast agents and increase diagnostic accuracy, which is carried out in T_1 and T_2 modes within the same procedure of an MRI investigation [5]. Therefore, the development of a new generation of MRI contrast agents has scientific and practical importance.

One of these possible substances is gadolinium orthoferrite ($GdFeO_3$), which has been previously suggested as an MRI contrast agent in the form of nanoparticles [6–9]. The perovskite structure of $GdFeO_3$ contains gadolinium, which is involved in T_1-contrast agents [10, 11], and iron oxide, which is used as a T_2-contrast agent as nanoparticles [12, 13]. Therefore, nanocrystalline gadolinium orthoferrite seems to be promising as a dual-modal $T_1 - T_2$ contrast agent for MRI. A variety of methods have been used in the synthesis of $GdFeO_3$ nanoparticles, including co-precipitation [14], hydrothermal [15], combustion [16], sol-gel [17], microwave [18], and other methods. Among them, the co-precipitation method is a priority for medical applications since it allows the production of gadolinium orthoferrite nanoparticles with minimal chemical impurities. But the traditional direct co-precipitation technique, routinely realized at room temperature, does not allow to obtain superparamagnetic particles of small (<30 nm) size [14]. Thus, new original approaches are required to solve the synthesis problem of gadolinium orthoferrite nanocrystals with the required crystalline, morphological, and magnetic parameters.

In this paper, the low-temperature reverse co-precipitation technique was proposed to synthesize ultrafine superparamagnetic nanoparticles of $GdFeO_3$. A detailed investigation has been performed to determine their structural and morphological features, as well as magnetic behavior. After that, a colloidal solution based on the as-synthesized

GdFeO$_3$ nanoparticles was prepared to estimate its compliance with the basic requirements for the solutions of MRI contrast agents.

2. Experimental

2.1. Synthesis of GdFeO$_3$ nanoparticles

An aqueous solution of stoichiometric amounts of gadolinium nitrate hexahydrate Gd(NO$_3$)$_3$·6H$_2$O (puriss., 99.9%) and iron(III) nitrate nonahydrate Fe(NO$_3$)$_3$·9H$_2$O (pur., 98.0%), with a concentration of 0.01 mol/L for each salt, was used as a source of gadolinium ions Gd^{3+} and iron(III) ions Fe^{3+}. An aqueous solution of ammonia with a concentration of 1 mol/L prepared from aqueous ammonia NH$_4$OH (puriss. spec., 23.5%) was used as the precipitating medium. The co-precipitation was carried out at a temperature close to 0 °C by adding the solution of nitrates in a drop-wise manner to the solution of ammonia which was on a magnetic stirrer. The obtained precipitate was washed several times with distilled water. Then the sample was dried at a temperature of 45 °C for 24 hours. After that, the dried co-precipitated hydroxides were heated at a temperature of 750 °C for 4 hours in the air.

2.2. Characterization of the co-precipitated hydroxides and the heat-treated product

A small amount of the sample of co-precipitated hydroxides was investigated by thermogravimetric analysis (TGA) using a Shimadzu DTG-60 simultaneous thermal analyzer. The content of gadolinium and iron in the co-precipitated hydroxides was determined by energy-dispersive X-ray spectroscopy (EDX) using a TESCAN VEGA3 scanning electron microscope coupled with an x-act EDX microprobe analyzer from Oxford Instruments. The scanning electron microscopy (SEM) images of the co-precipitated hydroxides and the heat-treated product were obtained using the same microscope. The powder X-ray diffraction (PXRD) patterns of the co-precipitated hydroxides and the heat-treated product were obtained using a Rigaku SmartLab 3 diffractometer. The processing of PXRD data was carried out using SmartLab Studio II software. The Brunauer-Emmett-Teller (BET) surface area was determined by nitrogen adsorption-desorption isotherm measurements at 77 K on a Micromeritics ASAP 2020 nitrogen adsorption apparatus. Pore size distributions of the sample were calculated by the Barrett-Joyner-Halenda (BJH) procedure using adsorption-desorption isotherms. The characteristic particle size of GdFeO$_3$ was estimated by spherical morphology approximation using the formula $D = 6 / (S \cdot \rho_{XRD})$, where D – characteristic particle size, S – specific surface area, and ρ_{XRD} – X-ray density of GdFeO$_3$.

The state of Fe atoms in the heat-treated product was studied using a WissEl Mössbauer spectrometer. Measurements were made in the absorption geometry at room temperature (298 K). The isomer shift was evaluated with respect to α-Fe. The magnetic properties of the heat-treated product were measured on a Lake Shore 7400 vibrating magnetometer. The magnetic characteristics according to the hysteresis loop data were calculated using the vibration method built in the magnetometer's software on a Lake Shore 7410 vibration magnetometer.

2.3. Preparation and characterization of the colloidal solution of GdFeO$_3$ nanoparticles

A colloidal solution of the as-synthesized GdFeO$_3$ nanoparticles was prepared by mixing 10 mg of the heat-treated product with 50 mL of distilled water and sonicating the mixture for 4 hours. After that, the colloidal solution was centrifugated at a speed of 1000 rpm for 30 minutes, and the supernatant was collected [7]. The size distribution of particles in the prepared colloidal solution was investigated by dynamic light scattering (DLS) using a ZetaSizer Nano ZS analyzer. The zeta potential of particles in the prepared colloidal solution was determined using the same analyzer.

3. Results and discussion

Gadolinium and iron(III) hydroxides undergo a series of physicochemical processes before forming gadolinium orthoferrite and its formation begins immediately after the completion of weight loss [14], therefore the TGA of the co-precipitated hydroxides was necessary to determine the minimum temperature at which GdFeO$_3$ forms. The TGA and derivative thermogravimetric (DTG) curves are presented in Fig. 1, and the main weight loss effects are indicated by numbers 1-5 on the DTG curve.

The total weight loss was about 23.55%. These weight loss effects may include the evaporation of the physically adsorbed water on the sample surface (effect 1), the dehydration of iron(III) hydroxide (effect 2), the dehydration of gadolinium hydroxide (effect 3), the release of the physically adsorbed carbon dioxide (CO$_2$) on the sample surface (effect 4), and the decomposition of gadolinium carbonate derivatives with the release of CO$_2$ (effect 5). The decomposition mechanism of gadolinium and iron(III) hydroxides was previously considered in detail in [15] and it was shown to be ending completely at a temperature of 447 °C which comparable with ∼500 °C in this work. The appearance of carbonate derivatives in the sample of co-precipitated hydroxides may be due to the active sorption of CO$_2$ from the surrounding air on their surface while preparing the solutions of reactants, washing and drying the

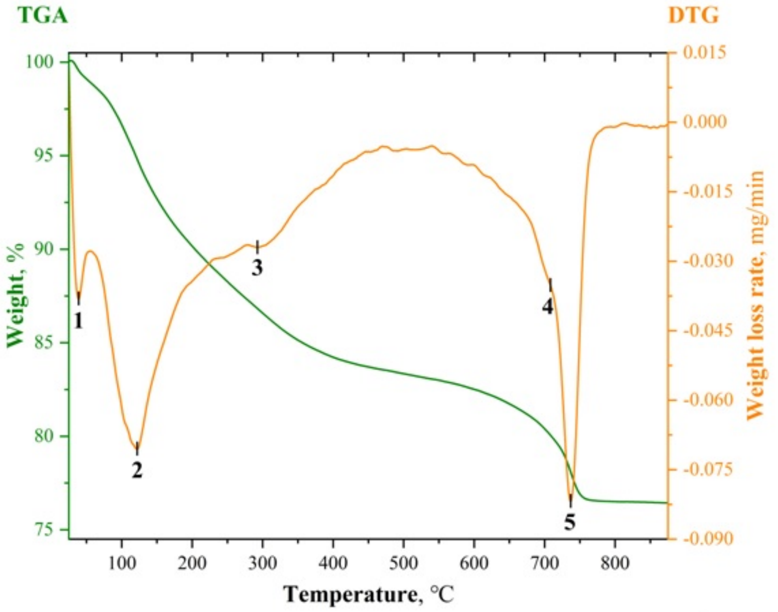

FIG. 1. The TGA and DTG curves of the obtained co-precipitated hydroxides

precipitate. Since the formation of $GdFeO_3$ occurs only after the complete decomposition of gadolinium carbonate derivatives as it was shown in [19] (effect 5, maximum of about 737°C, a temperature of 750°C was chosen as the minimum temperature for the synthesis of $GdFeO_3$ nanoparticles.

The results of EDX, PXRD, and SEM are presented in Fig. 2. The elemental analysis of the obtained sample of the co-precipitated hydroxides by EDX showed that the average stoichiometric gadolinium-to-iron ratio in the obtained sample was 50.31%:49.69% or 1.00:0.99 which is very close to the ratio of 1:1 as in $GdFeO_3$. The detailed EDX results of co-precipitated hydroxides in terms of gadolinium and iron are shown in the table inserted in Fig. 2a.

According to the diffraction pattern of the co-precipitated hydroxides, they were X-ray amorphous (Fig. 2a). The X-ray phase analysis of the heat-treated product showed that it is mainly composed of orthorhombic gadolinium orthoferrite (o-$GdFeO_3$) (Fig. 2b) with a trace amount of a garnet gadolinium ferrite phase called cubic pentairon(III) trigadolinium oxide (c-$Gd_3Fe_5O_{12}$), which is thermodynamically more stable than $GdFeO_3$ [20]. The appearance of this impurity in the sample may be due to the partial carbonization of hydroxides while preparing, which leads to the sample inhomogeneity and, consequently, the formation of another phase along with the main phase after heat treatment. The important role of partial carbonation of the hydroxide precursor on the formation of rare-earth orthoferrites was also previously shown in [21] and [22]. The average crystallite size of the obtained $GdFeO_3$ nanocrystals was calculated by the X-ray line broadening technique based on Scherrer's formula and it is approximately equal to 23 ± 3 nm. The lognormal size distribution of the prepared $GdFeO_3$ nanocrystals based on the broadening of the reflections (111) and (112) is presented as an insert in Fig. 2b. As for (111), the size distribution is sufficiently narrow, i.e. there is no big difference in crystallite sizes, but in the case of (112), a widening towards larger sizes is observed. This can be explained by the fact that unlike (111), (112) overlaps with other reflections in its region, which complicates the calculation of size distribution. Thus, these results indicate that ultrafine gadolinium orthoferrite nanocrystals with a narrow size distribution have been successfully obtained.

The nanoparticles of the co-precipitated hydroxides were relatively isometric as seen on their SEM image (Fig. 2a). After the heat treatment, this isometric morphology remained the same with a marked decrease in the particle size as compared with the co-precipitated hydroxides (Fig. 2b). This decrease in particle size can be explained by the loss of water and CO_2 during the heat treatment (see the TGA results discussed above). The SEM image of the heat-treated product (Fig. 2b) also confirms its narrow crystallite size distribution, i.e. no extra-large particles are observed. These results are in good agreement with the results of the X-ray line broadening analysis given above.

To evaluate the specific surface area of the obtained $GdFeO_3$ nanoparticles, as well as the size and volume of pores in the sample, the low-temperature nitrogen adsorption-desorption measurements were undertaken (Fig. 3).

According to the IUPAC classification, the obtained adsorption isotherm of the heat-treated product belongs to type IV, and the hysteresis loop belongs to type H3, which suggests that a wide distribution of pore sizes in the sample and that slit-shaped pores are the predominant pore types. These facts can be simply explained by the presence

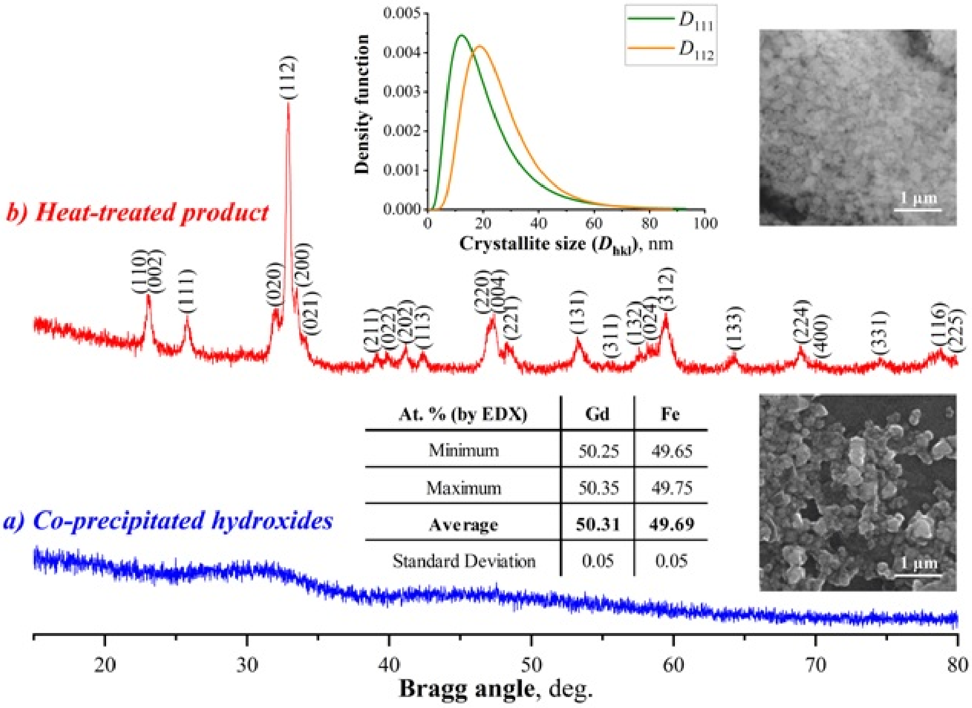

At. % (by EDX)	Gd	Fe
Minimum	50.25	49.65
Maximum	50.35	49.75
Average	**50.31**	**49.69**
Standard Deviation	0.05	0.05

FIG. 2. The PXRD and SEM results of the obtained co-precipitated hydroxides (a) and heat-treated product (b). The insert in (a) shows the EDX results of the co-precipitated hydroxides, and the insert in (b) shows the lognormal size distribution of the prepared $GdFeO_3$ nanocrystals

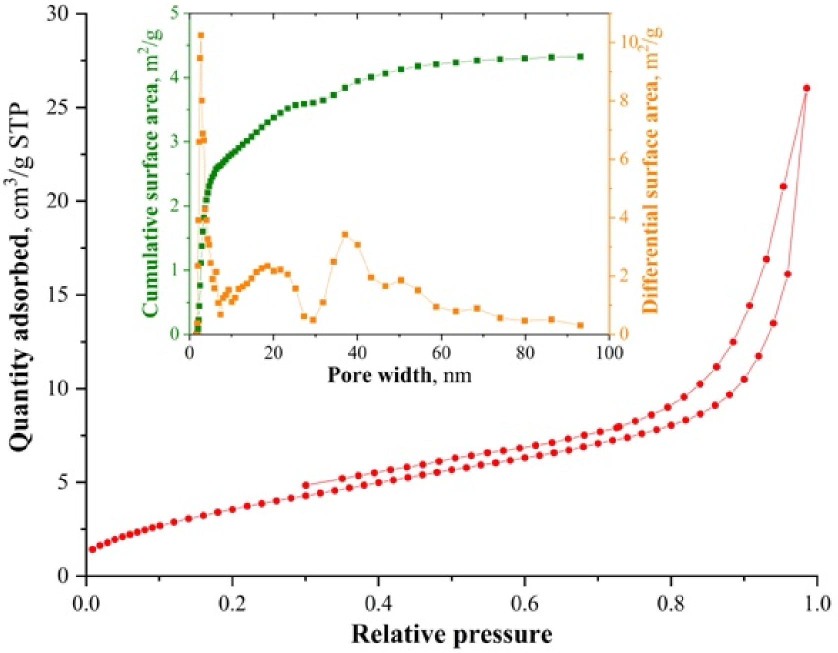

FIG. 3. The nitrogen adsorption-desorption isotherm of the heat-treated product. The insert shows the pore width distribution in the heat-treated product

of pores of different sizes between individual nanocrystals in their agglomerates, which is consistent well with the results of SEM analysis. Based on the adsorption-desorption data obtained, it was found that the BET surface area is about 13.4 m^2/g, the total pore volume is about 40.3 mm^3/g, and the average pore width is approximately 12 nm. The cumulative and differential surface areas are presented as an insert in Fig. 3. The appearance of mesopores and macropores in the analyzed sample is due to the spacings formed by the agglomerates of $GdFeO_3$ nanoparticles. The characteristic size of the nanoparticles obtained based on the specific surface area (13.4 m^2/g) and X-ray density (7.30 g/cm^3) of gadolinium orthoferrite, was found to be about 62 nm. This value is significantly larger than the average crystallite size (23 ± 3 nm) and almost equal to the maximum crystallite size in the lognormal size distribution presented above ($\sim$ 65–70 nm) (see insert in Fig. 2b) which indicates a strong agglomeration of nanocrystals with grain boundaries inaccessible to nitrogen.

For a better understanding of the structural and morphological features of $GdFeO_3$ nanocrystal agglomerates in the synthesized sample, the size distribution of particles in the prepared colloidal solution was analyzed by DLS and it is presented in Fig. 4.

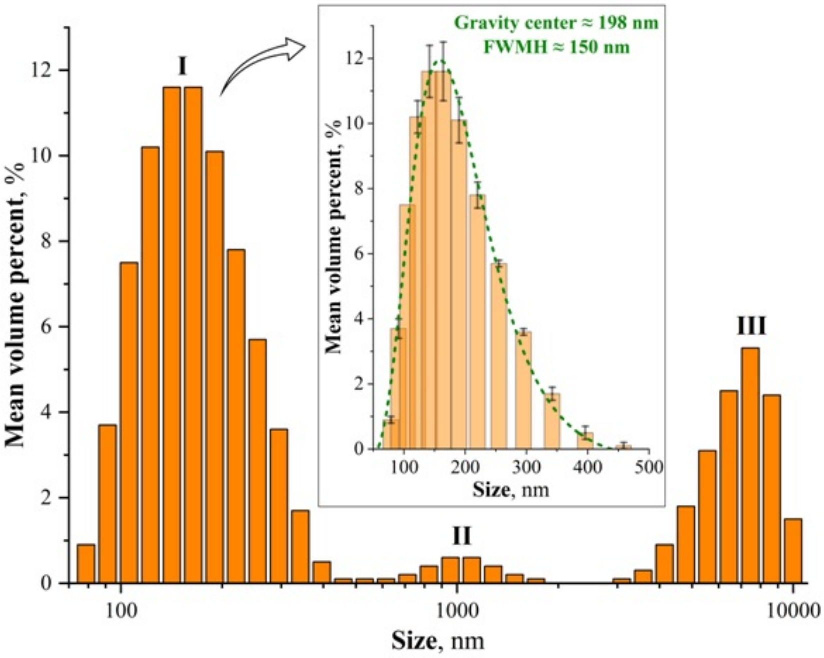

FIG. 4. The size distribution of particles in the prepared colloidal solution of the heat-treated product as shown by DLS

As one can see, the obtained distribution is trimodal, so the particles in the analyzed colloidal solution can be assigned to three peaks: I, II and III, which correspond to primary, secondary and tertiary agglomerates of $GdFeO_3$ nanocrystals, respectively. Approximately 75% of the particles belong to the primary agglomerates (peak I, which has a gravity center of about 198 nm and a full width at half maximum (FWHM) of about 150 nm). The remaining particles have larger sizes and belong to the higher-order agglomerates. These results indicate that the synthesized $GdFeO_3$ nanoparticles tend to agglomerate in the prepared colloidal solution, and the resulting agglomerates, in turn, tend to agglomerate with each other to form larger agglomerates. In other words, the particles that belong to the peak I are agglomerates of the nanoparticles, the particles that belong to the peak II are agglomerates of the particles of peak I, and the particles that belong to the peak III are agglomerates of the particles of peak II. It should be noted that according to the presented results, particles with nanocrystal sizes were not found at all in the prepared colloidal solution, despite the lengthy procedure of high-energy ultrasonic dispergation. This fact indicates that in this sample gadolinium orthoferrite is present in the form of stable clusters of about 198 nm in size of $GdFeO_3$ nanocrystals of about 23 nm. Thus, according to a rough estimate, each such cluster contains about 640 individual nanocrystals. It is worth to be noted that a part of the nanocrystals in these clusters is more tightly coupled, as evidenced by the lower characteristic particle size ($\sim$ 62 nm) estimated from the specific surface area of the sample. The tendency of nanocrystals to form clusters and their high stability can be partially explained by their small absolute value of zeta potential which was found to be equal to 1 mV.

To determine the features of the magnetic structure of the synthesized gadolinium orthoferrite nanocrystals the Mössbauer spectroscopy of the heat-treated product was performed and it is presented in Fig. 5.

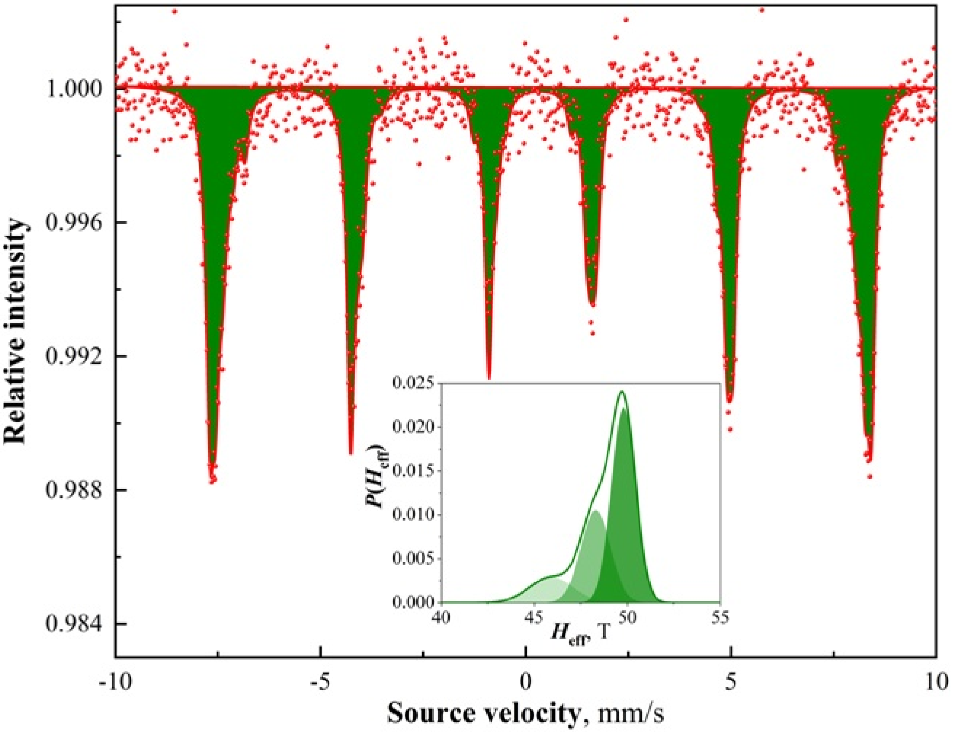

FIG. 5. The results of Mössbauer spectroscopy of the heat-treated product. The insert shows the magnetic hyperfine field distribution

According to the presented results, the heat-treated product contains magnetic (sextet) component. The hyperfine field of the total sextet component corresponds with those of orthorhombic gadolinium orthoferrite [23]. The magnetically ordered phase of *o*-$GdFeO_3$ has a trimodal distribution, as follows from the results presented as an insert in Fig. 5. As it is well-known, gadolinium orthoferrite belongs to the typical antiferromagnets with weak ferromagnetism resulting from a slight distortion of the crystal structure of $GdFeO_3$ from the perovskite structure with the corresponding canting of the Fe^{3+} spins from antiparallelism. Thus, we can assume the presence of two magnetically ordered iron sublattices with close effective magnetic field values, which are the components S1 (49.8±0.1 T) and S2 (48.3±0.1 T) with almost equal amount proportions. But additionally, it is also observed the presence of a third sextet component S3 with a noticeably lower effective magnetic field (45.9±0.1 T), which may correspond to the contribution of the distorted crystal and magnetic structure of the nanoparticle surface. Thus, all of the sextet components belong to the $GdFeO_3$ magnetically ordered phase and related to complex structural and morphological features of synthesized nanocrystals. Detailed characteristics of all the sextet components are summarized in Table 1.

TABLE 1. ^{57}Fe Mössbauer parameters of all the sextet components

Sextet component	Isomer shift, mm/s	Quadrupole splitting, mm/s	Effective magnetic field, T	Total amount, %
$S1$	0.363±0.002	0.008±0.003	49.8±0.1	55.1
$S2$	0.355±0.005	0.011±0.003	48.3±0.1	32.0
$S3$	0.351±0.007	0.038±0.011	45.9±0.1	12.9

The magnetic behavior of the $GdFeO_3$ nanoparticles was investigated at room temperature (298 K) using vibration magnetometry, the results of which are shown in Fig. 6.

The obtained dependence of magnetization on the applied magnetic field has an S-shaped form with an absence of complete saturation even at high values of the applied magnetic field, which in conjunction with low remanent magnetization (0.37 emu/g) is a characteristic feature of superparamagnetic nanoparticles [24]. However, high coercivity

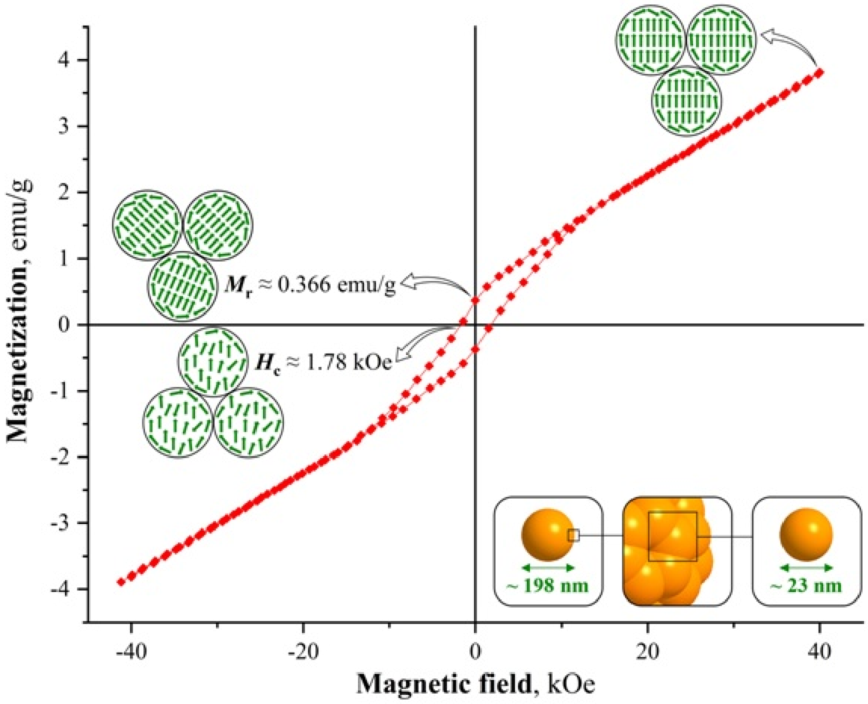

FIG. 6. The magnetization curve of the heat-treated product at 298 K

(1.78 kOe), relatively low magnetization (3.82 emu/g) at the 40 kOe applied field, and an obvious magnetic hysteresis loop indicate a more complex magnetic structure of this substance. The above information on the strong agglomeration of gadolinium orthoferrite nanocrystals allows us to assume that the observed magnetization dependence is the result of the superparamagnetic nanoparticle cluster's behavior but not individual nanoparticles of $GdFeO_3$. In this case, the resulting behavior of the substance in a changing external magnetic field has the characteristic features of both superparamagnetic and ferromagnetic components. When an external magnetic field about 40 kOe (see insert in Fig. 6) is applied to the clusters of superparamagnetic nanoparticles, their inner magnetic moments tend to align along the applied field, leading to a net magnetization, but magnetic saturation does not occur due to disordered surface-associated magnetic moments. When the external magnetic field decreases to zero, a slight residual magnetization (0.37 emu/g) remains, mainly due to the cluster magnetic moment of strongly coupled $GdFeO_3$ nanoparticles that all together behave like a ferromagnet. Then we must apply a significant demagnetizing field (1.78 kOe) to reduce the magnetization of the sample to zero. A schematic representation of the processes occurring with clusters of superparamagnetic nanoparticles under the external magnetic fields as well as a schematic structure of these clusters are presented as inserts in Fig. 6. As one can see, the behavior of clusters of superparamagnetic nanoparticles is markedly different from the magnetic behavior of a collective of independent superparamagnetic nanoparticles [25].

4. Conclusion

Superparamagnetic $GdFeO_3$ nanocrystals with an isometric morphology and an average size of 23±3 nm were successfully synthesized by the low-temperature reverse co-precipitation of gadolinium and iron(III) hydroxides followed by their heat treatment in the air. Analysis results indicate a strong agglomeration of gadolinium orthoferrite nanocrystals in the form of stable clusters with a size of about 200 nm on average. This cluster structure of $GdFeO_3$ possesses its weak ferromagnetic behavior in contrast to the superparamagnetic behavior of individual nanocrystals. Besides, a colloidal solution, produced by water-assisted sonicating of gadolinium orthoferrite nanopowder, contains the first-, second-, and third-order agglomerates of the initial $GdFeO_3$ nanocrystals, and thus a novel approach for colloidal solution preparation should be proposed for further MRI contrast applications.

Acknowledgments

The research was supported by the Russian Science Foundation (project No. 19-73-00286). The study was partially performed on the equipment of the Engineering Center of Saint Petersburg State Institute of Technology. The authors are grateful to Rogozev A. B. for the ^{57}Fe Mössbauer spectroscopy study performed using the equipment of the RITVERC JSC company.

References

[1] Geraldes C.F.G.C., Laurent S. Classification and basic properties of contrast agents for magnetic resonance imaging. *Contrast Media & Molecular Imaging*, 2009, **4**(1), P. 1-23.

[2] Xiao Y.-D. et al. MRI contrast agents: Classification and application (Review). *International Journal of Molecular Medicine*, 2016, **38**(5), P. 1319–1326.

[3] Estelrich J., Sánchez-Martín M.J., Busquets M.A. Nanoparticles in magnetic resonance imaging: From simple to dual contrast agents. *International Journal of Nanomedicine*, 2015, **10**, P. 1727–1741.

[4] Szpak A. et al. T_1–T_2 Dual-modal MRI contrast agents based on superparamagnetic iron oxide nanoparticles with surface attached gadolinium complexes. *Journal of Nanoparticle Research*, 2014, **16**(11), P. 2678.

[5] De M. et al. Hybrid magnetic nanostructures (MNS) for magnetic resonance imaging applications. *Advanced Drug Delivery Reviews*, 2011, **63**(14-15), P. 1282–1299.

[6] Pinho S.L.C. et al. Synthesis and Characterization of Rare-Earth Orthoferrite $LnFeO_3$ Nanoparticles for Bioimaging. *European Journal of Inorganic Chemistry*, 2018, **2018**(31), P. 3570–3578.

[7] Söderlind F. et al. Colloidal synthesis and characterization of ultrasmall perovskite $GdFeO_3$ nanocrystals. *Nanotechnology*, 2008, **19**(8), P. 085608.

[8] Athar T. et al. Super paramagnetic iron oxide and gadolinium ($FeGdO_3$) nanopowder synthesized by hydrolytic approach passes high level of biocompatibility and MRI-based dual contrast property for competent molecular imaging and therapeutic interventions. *Biomedical Physics & Engineering Express*, 2016, **2**(2), P. 025010.

[9] Deka S. et al. Synthesis, characterization and in vitro analysis of α-Fe_2O_3-$GdFeO_3$ biphasic materials as therapeutic agent for magnetic hyperthermia applications. *Materials Science and Engineering: C*, 2018, **92**, P. 932–941.

[10] Caravan P. et al. Gadolinium(III) Chelates as MRI Contrast Agents: Structure, Dynamics, and Applications. *Chemical Reviews*, 1999, **99**(9), P. 2293–2352.

[11] Hermann P. et al. Gadolinium(III) complexes as MRI contrast agents: ligand design and properties of the complexes. *Dalton Transactions*, 2008, **23**, P. 3027–3047.

[12] Zhao X. et al. Ultrasmall Superparamagnetic Iron Oxide Nanoparticles for Magnetic Resonance Imaging Contrast Agent. *Journal of Nanoscience and Nanotechnology*, 2014, **14**(1), P. 210–220.

[13] Dulicska-Litewka J. et al. Superparamagnetic Iron Oxide Nanoparticles—Current and Prospective Medical Applications. *Materials (Basel)*, 2019, **12**(4), P. 617.

[14] Popkov V.I. et al. The Formation of Nanocrystalline Orthoferrites of Rare-Earth Elements $XFeO_3$ (X = Y, La, Gd) Via Heat Treatment of Coprecipitated Hydroxides. *Russian Journal of General Chemistry*, 2017, **87**(11), P. 2516–2524.

[15] Tugova E.A., Zvereva I.A. Formation mechanism of $GdFeO_3$ nanoparticles under the hydrothermal conditions. *Nanosystems: physics, chemistry, mathematics*, 2013, **4**(6), P. 851–856.

[16] Gimaztdinova M.M. et al. Glycine-nitrate combustion synthesis of $GdFeO_3$ nanocrystals. *Condensed Phases and Interfaces*, 2016, **18**(3), P. 422–431.

[17] Li L. et al. Synthesis, Photocatalytic and Electrocatalytic Activities of Wormlike $GdFeO_3$ Nanoparticles by a Glycol-Assisted Sol–Gel Process. *Industrial & Engineering Chemistry Research*, 2013, **52**(26), P. 9130–9136.

[18] Tang P. et al. Preparation of Nanocrystalline $GdFeO_3$ by Microwave Method and Its Visible-light Photocatalytic Activity. *Integrated Ferroelectrics*, 2014, **153**(1), P. 73–78.

[19] Tugova E.A., Karpov O.N. Nanocrystalline perovskite-like oxides formation in Ln_2O_3-Fe_2O_3-H_2O (Ln=La, Gd) systems. *Nanosystems: physics, chemistry, mathematics*, 2014, **5**(6), P. 854–860.

[20] Mathur S. et al. Nanocrystalline Orthoferrite $GdFeO_3$ from a Novel Heterobimetallic Precursor. *Advanced Materials*, 2002, **14**(19), P. 1405–1409.

[21] Popkov V.I., Almjasheva O. V. Formation mechanism of $YFeO_3$ nanoparticles under the hydrothermal conditions. *Nanosystems: physics, chemistry, mathematics*, 2014, **5**(5), P. 703–708.

[22] Popkov V.I. et al. Formation Mechanism of Nanocrystalline Yttrium Orthoferrite under Heat Treatment of the Coprecipitated Hydroxides. *Russian Journal of General Chemistry*, 2015, **85**(6), P. 1370–1375.

[23] Romero M. et al. Synthesis by molten salt method of the $AFeO_3$ system (A=La, Gd) and its structural, vibrational and internal hyperfine magnetic field characterization. *Physica B: Condensed Matter*, 2014, **443**, P. 90–94.

[24] Popkov V.I., Tolstoy V.P., Semenov V.G. Synthesis of phase-pure superparamagnetic nanoparticles of $ZnFe_2O_4$ via thermal decomposition of zinc-iron layered double hydroxysulphate. *Journal of Alloys and Compounds*, 2020, **813**, P. 152179.

[25] Albadi Y., Popkov V.I. Dual-modal contrast agent for magnetic resonance imaging based on gadolinium orthoferrite nanoparticles: synthesis, structure and application prospects. *Medicine: Theory and Practice*, 2019, **4**(S), P. 35–36.

NANOSYSTEMS:

PHYSICS, CHEMISTRY, MATHEMATICS

INFORMATION FOR AUTHORS

The journal publishes research articles and reviews, and also short scientific papers (letters) which are unpublished and have not been accepted for publication in other magazines. Articles should be submitted in English. All articles are reviewed, then if necessary come back to the author to completion.

The journal is indexed in Web of Science Core Collection (Emerging Sources Citation Index), Chemical Abstract Service of the American Chemical Society, Zentralblatt MATH and in Russian Scientific Citation Index.

Author should submit the following materials:

1. Article file in English, containing article title, the initials and the surname of the authors, Institute (University), postal address, the electronic address, the summary, keywords, MSC or PACS index, article text, the list of references.
2. Files with illustrations, files with tables.
3. The covering letter in English containing the article information (article name, MSC or PACS index, keywords, the summary, the literature) and about all authors (the surname, names, the full name of places of work, the mailing address with the postal code, contact phone number with a city code, the electronic address).
4. The expert judgement on possibility of publication of the article in open press (for authors from Russia).

Authors can submit a paper and the corresponding files to the following addresses: nanojournal.ifmo@gmail.com, popov1955@gmail.com.

Text requirements

Articles should be prepared with using of text editors MS Word or LaTex (preferable). It is necessary to submit source file (LaTex) and a pdf copy. In the name of files the English alphabet is used. The recommended size of short communications (letters) is 4-6 pages, research articles– 6-15 pages, reviews – 30 pages.

Recommendations for text in MS Word:

Formulas should be written using Math Type. Figures and tables with captions should be inserted in the text. Additionally, authors present separate files for all figures and Word files of tables.

Recommendations for text in LaTex:

Please, use standard LaTex without macros and additional style files. The list of references should be included in the main LaTex file. Source LaTex file of the paper with the corresponding pdf file and files of figures should be submitted.

References in the article text are given in square brackets. The list of references should be prepared in accordance with the following samples:

[1] Surname N. *Book Title*. Nauka Publishing House, Saint Petersburg, 2000, 281 pp.
[2] Surname N., Surname N. Paper title. *Journal Name*, 2010, **1** (5), P. 17-23.
[3] Surname N., Surname N. Lecture title. In: Abstracts/Proceedings of the Conference, Place and Date, 2000, P. 17-23.
[4] Surname N., Surname N. Paper title, 2000, URL: http://books.ifmo.ru/ntv.
[5] Surname N., Surname N. Patent Name. Patent No. 11111, 2010, Bul. No. 33, 5 pp.
[6] Surname N., Surname N. Thesis Title. Thesis for full doctor degree in math. and physics, Saint Petersburg, 2000, 105 pp.

Requirements to illustrations

Illustrations should be submitted as separate black-and-white files. Formats of files – jpeg, eps, tiff.

NANOSYSTEMS:

PHYSICS, CHEMISTRY, MATHEMATICS

Журнал зарегистрирован
Федеральной службой по надзору в сфере связи, информационных технологий и массовых коммуникаций
(свидетельство ПИ № ФС 77 - 49048 от 22.03.2012 г.)
ISSN 2220-8054

Учредитель: федеральное государственное автономное образовательное учреждение высшего образования
«Санкт-Петербургский национальный исследовательский университет информационных технологий, механики и оптики»

Издатель: федеральное государственное автономное образовательное учреждение высшего образования
«Санкт-Петербургский национальный исследовательский университет информационных технологий, механики и оптики»

Отпечатано в Учреждении «Университетские телекоммуникации»
Адрес: 197101, Санкт-Петербург, Кронверкский пр., 49

Подписка на журнал НФХМ
На второе полугодие 2020 года подписка осуществляется через
ОАО Агентство «Роспечать»
Подписной индекс 57385 в каталоге «Издания органов научно-технической информации»